New structural insights in chloroplast F1FO-ATP synthases

Von der Fakultät für Georessourcen und Materialtechnik der

Rheinisch -Westfälischen Technischen Hochschule Aachen

zur Erlangung des akademischen Grades eines

Doktors der Naturwissenschaften

genehmigte Dissertation

vorgelegt von

M. Sc. Alexey Vlasov

aus Prokopyevsk, Region Kemerovo, Russland

Berichter: **Herr Univ.-Prof. Dr. Valentin Gordeliy**
Herr Prof. Dr. Norbert Dencher
Herr Prof. Dr. Ernst Bamberg
Herr Prof. Dr. Martin Engelhard

Tag der mündlichen Prüfung: 07.12.2020

Table of contents

List of Abbreviations

6AHA	amino hexanoic acid
AA	acrylamide
ACMA	9-Amino-6-Chloro-2-Methoxyacridine
ADP	adenosine diphosphate
AEX	anion exchange chromatography
AgBh	silver behenate
APS	ammonium persulfate
ATP	adenosine triphosphate
ATP synthase	adenosine triphosphate synthase (enzyme)
APS	ammonium persulfate
AS	ammonium sulphate
BDQ	bedaquiline
bF_OF_1	bacterial F_1F_O ATP synthase
BN PAGE	blue native polyacrylamide gel electrophoresis
CHES	2-(cyclohexylamino) ethanesulfonic acid
cF_OF_1	chloroplast F_1F_O ATP synthase
CM	culture medium
CMC	critical micelle concentration
CoQ_n	coenzyme-Q_n (ubiquinone-n)
CYMAL-4	4-cyclohexyl-1-butyl-β-D-maltoside
DAPIT	diabetes-associated protein in insulin-sensitive tissue
DCCD	N,N′-dicyclohexylcarbodiimid
DDM	n-dodecyl β-D-maltoside
DGDG	digalactosyl diacylglycerol
DLS	dynamic light scattering
DM	β-decyl-maltoside
DMSO	dimethyl sulfoxide
DNA	deoxyribonucleic acid
DTT	dithiothreitol
EDTA	ethylenediaminetetraacetic acid
FCCP	Carbonyl cyanide-p-trifluoromethoxyphenylhydrazone
FTIR	Fourier-transform infrared spectroscopy
IC_{50}	half-maximal inhibitory concentration
IMM	inner mitochondrial membrane
IMS	intermembrane space
IPTG	isopropyl β-D-1-thiogalactopyranoside
LCP	lipid cubic phase
LDAO	N, N-dimethyldodecylamine N-oxide
LSU	large subunit of Ribulose-1,5-bisphosphate carboxylase/oxygenase (RuBisCO)

MES	2-(N-morpholino) ethanesulfonic acid
MK-n	menaquinone-n
MO	monoolein, $C_{21}H_{40}O_4$, 2,3-Dihydroxypropyl oleate
MP	membrane protein
MR	molecular replacement
MPD	2-methyl-2,4-pentanediol
MPTP	mitochondrial permeability transition pore
mtDNA	mitochondrial DNA
mtF_OF_1	mitochondrial F_1F_O ATP synthase
mQ	Milli-Q® water
MSP	membrane scaffold protein
MSP1E3D1	membrane scaffold protein 1E3D1
Mw	molecular weight
NCBI	National Center for Biotechnology Information
ND	nanodisc
NLS	sodium lauroyl sarcosinate
OG	octyl β-D-glucopyranoside
ON	overnight
OSCP	oligomycin sensitivity conferral protein
OXPHOS	oxidative phosphorylation system
PA	phosphatidic acid
PC	phosphatidylcholine
PCM	preculture medium
PCR	polymerase chain reaction
PDB	protein data bank
PEG	polyethylene glycol
PMF	proton motif force
POPC	1-palmitoyl-2-oleoyl-sn-glycero-3-phosphocholine
PQ-n	(PQ_n) plastoquinone-n
PQ_nH_2	plastoquinol-n
PSQ-n	plastosemiquinone-n
RT	room temperature
RuBisCO	Ribulose-1,5-bisphosphate carboxylase/oxygenase
SAXS	small-angle X-ray scattering
SDS	sodium dodecyl sulphate
SDS PAGE	sodium dodecyl sulphate polyacrylamide gel electrophoresis
SEC	size-exclusion chromatography
Sod.Ch.	sodium cholate (3α,7α,12α-Trihydroxy-5β-cholan-24-oic acid sodium salt)
SSU	small subunit of Ribulose-1,5-bisphosphate carboxylase/oxygenase (RuBisCO)
TDM	n-tridecyl-β-D-maltopyranoside
TEMED	tetramethyl ethylenediamine

TMBQ	trimethyl benzoquinone
$TMBQH_2$	trimethyl benzoquinol
tPCC-α-M	4-trans-(4-trans-Propylcyclohexyl)-cyclohexyl α-maltoside
UDM	undecyl-β-d-maltoside
VD	vapor diffusion
VdW surface	Van-der-Waals surface
WB	Western blot
WT	wild-type
XFEL	X-ray free electron laser
XRD	X-ray diffraction

1. Introduction

ATP synthase is a unique molecular machine that produces the energy-rich molecule adenosine triphosphate (ATP), which is necessary for numerous biochemical reactions in almost all living organisms. ATP is synthesized during the oxidative and photo phosphorylation process and is involved into the processes of biosynthesis, transport, signaling, etc. ATP synthase uses an ion motif force created by transmembrane ion gradient to generate ATP from adenosine diphosphate (ADP).

Dysfunctions of ATP synthase lead to various diseases such as diabetes, metabolic disorders, mitochondrial diseases, dysfunctions of tissues and organs [1]. Some of them have a fatal outcome in the first days of life, which is not surprising because the deficiency of the key molecule in metabolism leads to various disorders in metabolic processes [2]. ATP synthase was shown to be a mediator in Parkinson's [3], Alzheimer's [4] diseases, and processes associated with aging [5]. Recent studies show that ATP synthase is involved in regulation of Ca^{2+} channel $Ca_v2.3$ in neutrophils which makes it a potential therapeutic target for treatment of neutrophil-related diseases [6].

ATP synthase consists of the membrane integral and the water-exposed parts F_O and F_1, respectively. F_O includes a c-ring – a rotary part with a various number of c_1 subunits (protomers) from 8 to 17 in different organisms [7], [8], which rotates with a frequency of several hundred Hz [9]. Subunits a and c form an interaction interface which establishes ion transfer through a lipid membrane. Subunit a has alpha helices which are oriented parallelly to the membrane plane and create two half-channels together with the c-ring allowing ions interact with active centers of c protomers. ATP is synthesized in a catalytic center of α/β interface with rotation of $\alpha_3\beta_3$ in F_1 part induced by rotation of a c-ring in F_O part via γ and ε subunits ("central stalk") connecting $\alpha_3\beta_3$ with a c-ring. A so called "peripheral stalk", which subunit composition depends on type of ATP synthase, additionally connects $\alpha_3\beta_3$ with F_O part and does not rotate during ATP synthesis (Figure 1.1).

ATP synthases were found in cellular and organellar membranes of almost all organisms. F-type ATP synthases are the most widespread in bacteria and eukaryotes. They can be incorporated into cellular membranes in Eubacteria, in thylakoid membranes inside chloroplasts, and into inner membranes of mitochondria of eukaryotes, where ATP synthases form dimers. Four types of mitochondrial ATP synthase (mtF_OF_1) dimers are known currently and each type determines a topology of mitochondria cristae resulting in different morphology of cristae observed in nature [10]. If a eukaryotic cell also has chloroplasts, ATP synthases are present both in chloroplasts and

mitochondria. They have different subunit composition and oligomeric state, although the major functions of the enzyme in monomeric and dimeric forms remain the same according to the current knowledge.

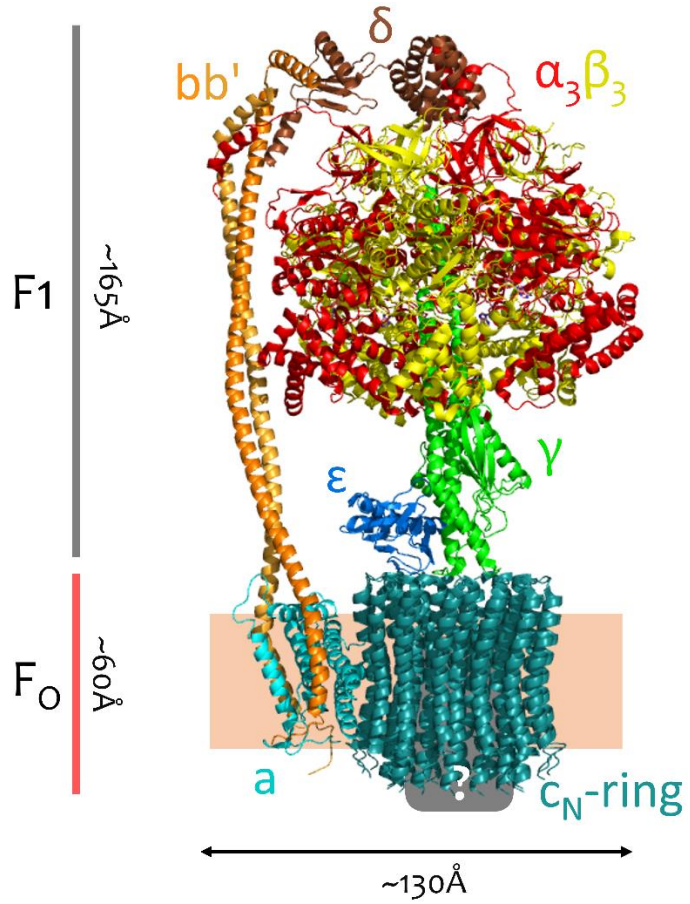

Figure 1.1. Overall view of ATP synthase from chloroplasts (bacterial ATP synthase has the same subunit composition). F_O part consists of abb'c_N subunits, F_1 part consists of $\alpha_3\beta_3\gamma\varepsilon\delta$ subunits, bb' subunits form a peripheral stalk, c_N-ring has c/a, c/γε interfaces and interface of interaction with a postulated "plug" inside its central pore (denoted with a question mark). PDB structure of ATP synthase (6FKF) was used for representation [11].

Crystallization and structural studies of ATP synthases remain a big challenge for structural biology, despite recent advances in X-ray diffraction (XRD), XFEL and cryo-EM techniques. Most of structural studies on ATP synthase revealed unique features about the enzyme, however, have left unclear details of intersubunit interfaces due to not sufficient resolution of protein structures. Molecular mechanisms of c/a and c_1/c_1 interfaces and their stabilization during rotation of a c-ring in a membrane are still not fully understood. Residues responsible for c/a interface contacts accurately preserve a distance from each other in order to provide an effective transmembrane ion transport. It requires additional stabilization of an ATP synthase besides a peripheral stalk which is formed by several subunits in almost all organisms except type II of mtF_OF_1 dimers [12].

Different organization of c-ring interface context was found in types I, III and IV of mtF_OF_1 dimers [13]–[15]. For example, an alpha-helix of 6.8PL subunit (the 6.8 kDa proteolipid) was found inside a c_8-ring of porcine mtF_OF_1 tetramer [13]; or an alpha helix of ATPEG-1 subunit was found to interact via sliding contacts with a β-barrel extension of a c_{10}-ring N-terminus alpha helices in *Euglena gracilis* [15]. In case of c-rings of monomeric bacterial or chloroplast ATP synthases (bF_OF_1 and cF_OF_1) no interfaces except c/a and c/γε were found. Thus, cγε subunits rotate as a rigid body transmitting ion motif force to rotation and conformational changes of $\alpha_3\beta_3$ catalytic center. The rotating subunits seem to be stabilized by a peripheral stalk that in case of bF_OF_1 and cF_OF_1 consists of *bb*' subunits – two long alpha helices which connect δ subunit on the top of $\alpha_3\beta_3$ with "a" subunit in F_O part.

Variability of interfaces additionally stabilizing a c-ring of mtF_OF_1 dimers in different organisms raised a question of similar mechanisms for a c-ring of bF_OF_1 and cF_OF_1 monomers. Interface context of a c-ring remains hidden and is a matter of different hypotheses. In dimers of type I and III additional stabilization of a c-ring is realized by different interfaces with a corresponding alpha helix attached to the F_O machinery, which is also responsible for dimerization of ATP synthases.

The functional importance of c-ring interface context occurs with its possible role in mitochondrial permeability transition pore (MPTP) *phenomenon* – the formation of a mega-channel in the mitochondrial inner membrane involved in cell death [16], [17]. There are still serious debates in literature about the mechanisms of MPTP formation and involvement of F_O machinery of ATP synthase in this process [17], [18].

Although a lot of structural information on ATP synthase was obtained in recent years, the molecular mechanisms of how a c-ring is stabilized inside the membrane are still missing due to the lack of the structural details. Thus, there were only a few high-resolution structures (better than 3 Å) of the c-rings from bacteria [19]–[21], and mitochondria [22] and was no high-resolution structure of the c-ring from plants. Other studies, although provided a general structural information about c-rings, almost did not show c_1/c_1 interfaces and omitted structural features in the inner pore of a c-ring due to low resolution.

An alpha helix attached to F_O machinery and interacting with a c-ring in corresponding mtF_OF_1 dimers is not the only way for its additional stabilization. In case of c-rings of monomeric bF_OF_1 and cF_OF_1 a so-called lipid "plug" inside a c-ring was discussed in literature [23]–[25]. However, the exact composition of this "plug", its interface with a c-ring and a role in mechanisms of stabilization of ATP synthase remain unclear.

In my thesis, it is shown that the "plug" might consist of isoprenoid quinones, such as plastoquinone-9 (PQ-9) [26] in the case of spinach cF_OF_1. This well correlates with our crystallographic high-resolution data (2.3 Å); UV-Vis differential spectroscopy experiments; calculated distances between polar/apolar interfaces in the inner pore of c-rings from different organisms, which are about 1.2 – 1.4 times bigger than outside of the c-rings; and the universality of isoprenoid quinones in cellular and organellar membranes among different species [26].

The "gap" in knowledge of molecular mechanisms of c_1/c_1 interface was for c-rings of cF_OF_1 due to low resolution structures of c-rings from plants [27]–[29]. Our high-resolution structure of a c-ring from spinach chloroplasts filled this gap and allowed comparison with available high-resolution structures of other c-rings from mitochondria and bacteria. In literature the three conserved interlacing motifs G(A,S)xxxG(A,S) in the middle of an N-terminus alpha helix of c-ring protomers were predicted to determine hydrogen bonds of c_1/c_1 interface and therefore, the stoichiometry of a c-ring [30].

In our work, the molecular mechanisms of a c_1/c_1 interface formation in the c_{14}-ring of cF_OF_1 from spinach were directly shown as a net of hydrogen bonds between residues of neighbor protomers, connected directly and via water molecules. Thus, in addition to the motifs S21xxxG25, G23xxxG27 and G25xxxG29, other hydrogen bonds were defined and the complete c_1/c_1 interface was shown. This is important since all these together determine the angle between neighbor protomers and, therefore, the stoichiometry of the c-ring.

The hypothesis of isoprenoid quinones as one of the "plug" compounds inside a c-ring was previously not discussed in the literature. In my thesis, experimental evidences are presented and arguments are given towards the hypothesis. This study sheds a new light on molecular mechanisms of stabilization of a c-ring in monomeric cF_OF_1 from plants and fills the gap in knowledge of its c_1/c_1 interface, which might help to understand deeply the role of one of the most important enzymes in biology – ATP synthase. Thus, the aim of this work was to investigate unusual structural features of a c-ring of ATP synthase from spinach chloroplasts.

2. Main Results

The most important result of my thesis is that for the first-time the attention was paid to the presence of additional characteristic circular electron densities inside the c-rings, found that they are universal for all ATP synthases among all domains of life and raised the question about their fundamental origin.

In this study, the high-resolution structure (2.3 Å) of the c_{14}-ring of the F-type ATP synthase from spinach chloroplasts (cF_OF_1) was obtained using X-ray diffraction on protein crystals. It is the first high-resolution structure (better than 3 Å) of the c-ring from plants and the first c-ring protein that was crystallized by using lipid meso phases (*in meso*) method. The structural data fill the gap in available high-resolution structures of c-rings from bacteria and mitochondria.

Additional electron densities, which are not associated with polypeptide chains of the protein, have been found inside the inner pore of the c_{14}-ring of the cF_OF_1. They have a circular shape and the circles are placed parallel to the membrane plane at the distance of 5.4 Å from each other. They are also placed between the residues of the hydrophobic amino acids Ala7, Ile11, Leu15, Leu19, exposed from the inner surface of the c-ring, which form the "grooves" of the Van-der-Waals surface of the protein. Similar densities were also found in almost all available high-resolution structure of c-rings in distant lineages of bacteria and eukaryotes. The presence and nature of the densities were previously not discussed in the literature.

In my thesis, we suggest the hypothesis that isoprenoid quinones may fit the electron densities inside the c-rings of the F-type ATP synthases (such as plastoquinone-9 (PQ-9) in the case of spinach chloroplasts, coenzyme-Q_{10} (CoQ_{10}) in the case of eukaryotic mitochondria, etc.), thus, being universal cofactors of the ATP synthases among all organisms which have ATP synthases. They may be necessary to stabilize the c-ring of the enzyme and prevent ion leakage through it. This hypothesis corresponds well with the experimentally observed additional densities inside the c_{14}-ring in almost all other high-resolution structures of c-rings available in literature. It may explain the distance between polar/apolar interfaces, which is about 1.2 – 1.4 times more inside c-rings than outside in the membrane bilayer. It also corresponds to the length of an isoprene subunit (~ 5.4 Å) that is the same as between the circles of the additional electron densities inside the c-ring; and a universality of CoQ molecules among different organisms.

The hypothesis was indirectly proved also by differential UV-Vis spectroscopy on qualitative reaction of reducing ketones (and, therefore, isoprenoid quinone polar heads) to aldehydes and alcohols, with the samples of the purified c_{14}-ring solved in EtOH. The difference between the UV-Vis spectra before and after addition of $NaBH_4$ (oxidized – reduced form) was similar to the

reference differential spectrum of trimethyl benzoquinone (TMBQ), which is a polar head of the PQ-9.

The presence of additional characteristic circular electron densities inside the c-rings and the universality of the *phenomenon* is very important, however, it is not excluded that other possible explanations of the nature of the densities and also shortly discuss them in our work.

The molecular mechanisms of c_1/c_1 interface of the c_{14}-ring of ATP synthase from spinach chloroplasts are directly evidenced in crystallographic high-resolution structure. A net of hydrogen bindings in addition to the three interlacing motifs S21xxxG25, G23xxxG27 and G25xxxG29 involve other residues connecting neighbor protomers via water molecules and stabilize the c_1/c_1 interface. Thus, the complete c_1/c_1 interface that determines the c-ring stoichiometry was shown in this work.

In addition, small-angle X-ray scattering (SAXS) of purified intact ATP synthase from spinach chloroplasts reconstituted into POPC/MSP1E3D1 nanodiscs was performed in this work and obtained *ab initio* 3D low-resolution structure was similar to that of V-shape dimers of mitochondrial ATP synthases. It raised questions of possible physiological role of such oligomers in chloroplasts.

3. Literature overview

This chapter describes the classical studies that significantly accounted for the formation of modern paradigm of ATP synthase role in biology, its functional and structural studies, comparison of purification and crystallization protocols, and unusual features discovered in the membrane (F_O) region of the enzyme. It begins with the historical perspective and ends with the most relevant works giving the whole picture of unrevealed questions and problems in the field. It might be useful to understand the main trends of this enzyme studies in order to see the gaps in knowledge and our attempts to answer these questions.

3.1. ATP synthase

3.1.1. Historical background

In 1929, the German biochemist Karl Lohmann discovered adenosine triphosphate (ATP) [31] – the major compound for biochemical reactions in almost all living organisms. Sixteen years later, in 1937, Herman Kalckar found the link between the cell respiration and the ATP synthase – an enzyme, that catalyzes the oxidative phosphorylation of adenosine diphosphate (ADP) and produces ATP [32]. Two years later the term "oxidative phosphorylation" was introduced [33]. Then after several studies of ATP [34], [35] the first scheme of oxidative phosphorylation with chemical intermediates was proposed in 1953 by E.C. Slater [36]. In the 1960s, the paradigm of energy transfer from respiratory chain complexes to ATP synthase with the help of proton translocation was established [37], and the key role of membrane proton gradient coupling with ATP synthesis, known as chemiosmotic hypothesis, was suggested by P. Mitchell [38] (contemporary scheme of oxidative phosphorylation is shown in Fig. 3.1), and experimentally proved by V. Skulachev [39]. L. Yaguzhinsky *et al.* showed that ATP synthesis takes place at the interphase boundary (authors used water-octane interface as a model system) [40].

The importance of oxidative phosphorylation for the vast majority of species prompted the study of ATP synthase and investigation of connections between ATP synthase and other respiratory chain protein complexes. The studies of Boyer *et al.* [41], [42] proposed that the mechanism of ATP catalysis proceeds through the conformational changes of the enzyme ATP synthase. In the 1980s the DNA sequence coding membrane (F_O) part of the ATP synthase was determined by J.E. Walker's group [43] and in 1994 they presented the first high-resolution crystal structure (2.8 Å) of the water-soluble part (F_1) of the ATP synthase from bovine mitochondria by X-ray diffraction method (XRD) [44].

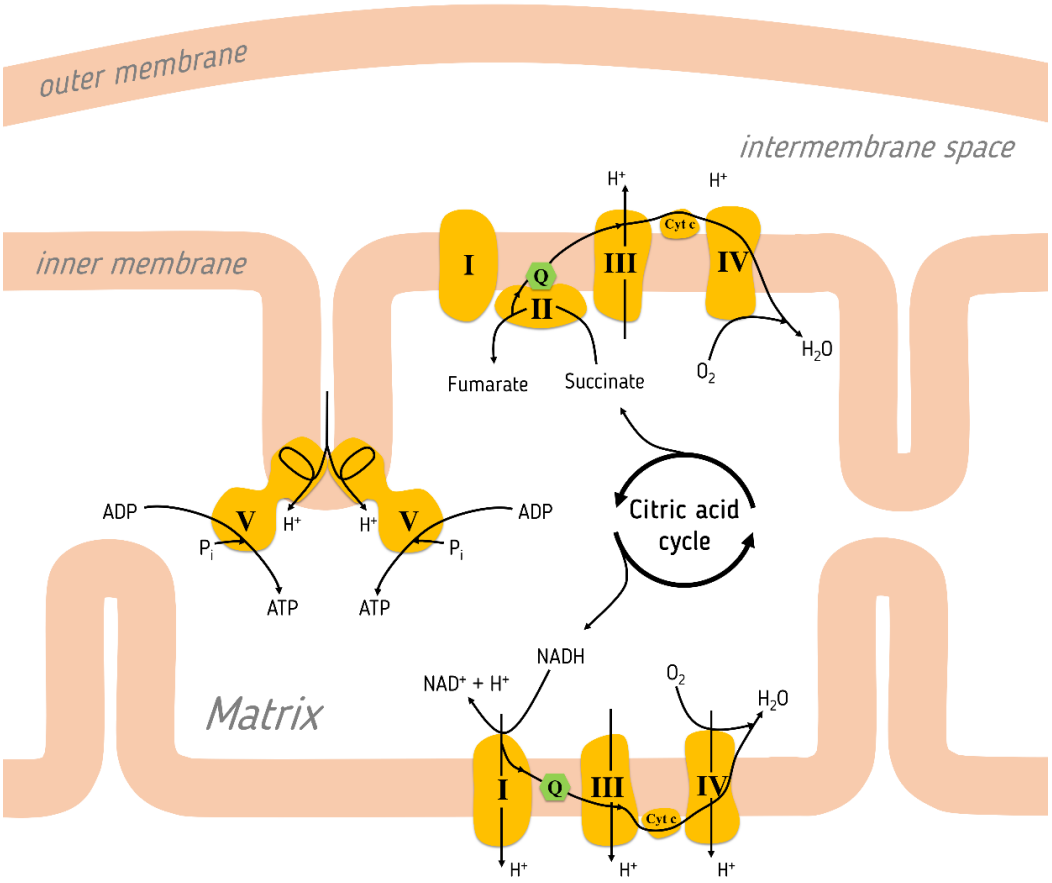

Figure 3.1. Contemporary scheme of oxidative phosphorylation mechanism. Respiratory chain proteins are colored yellow. ATP synthase is shown as the respiratory chain complex V. Coenzyme-Q is colored green.

The importance of the ATP synthase studies was so significant that the Nobel prize in chemistry 1997 was awarded to Paul D. Boyer and John E. Walker "for their elucidation of the enzymatic mechanism underlying the synthesis of adenosine triphosphate (ATP)" and to Jens C. Skou "for the first discovery of an ion-transporting enzyme, Na^+, K^+ -ATPase." [45].

Another significant work on understanding the mechanism of ATP catalysis was done by M. Yoshida's group in 1997 [46], where it was directly shown that the F_1 part of the ATP synthase rotates producing three molecules of ATP per one turn. The experiments [47], [48] demonstrated mechanically driven ATP synthesis by F_1-ATP synthases. The processes of ATPase activity and reversibility of ATP synthesis were studied by A. Vinogradov *et al.* [49].

Thus, the modern paradigm of how an ATP synthase functions was established by the end of the twentieth century. Then it seemed that further structural studies would only clarify the details of the enzyme functioning. However, since that time new structural information expanded our view on the role of ATP synthase.

3.1.2. Structural studies

In 1999, the c-ring and F_1 part of the ATP synthase from yeast mitochondria were resolved with 3.9 Å resolution using XRD method [50]. It was the first structure of the membrane segments (*c* subunit of F_O part) together with water-exposed ($\alpha_3\beta_3\gamma\delta\varepsilon$ subunits of F_1 part) segments of the complex. Since that time, during 11 years the structural studies of ATP synthase had resulted only in structures of separate parts (F_1 or F_O) or separate subunits from F_1 or F_O parts of the complex.

Only in 2010 two cF_1 structures of ATP synthases were obtained by XRD: from yeast mitochondria in Mg-ADP inhibited state (3.4 Å) [51] and from bovine mitochondria (3.5 Å) [52]. Also, based on the work [50] the structure of the ATP synthase from yeast mitochondria was refined to 3.0 Å resolution. In 2012 the structure of ATP synthase from yeast mitochondria inhibited by adenylyl-imidodiphosphate (AMP-PNP) and dicyclohexylcarbodiimid (DCCD) was obtained (6.5 Å, XRD) [53].

The study [54] firstly showed that ATP synthases form dimers in mitochondria cristae and therefore might determine their topology. The ATP synthase from yeast mitochondria was studied by electron cryotomography with further subtomogram averaging, which resulted in the structure of dimers of the complex with 37 Å resolution.

Further studies resulted in a number of monomeric and oligomeric structures of ATP synthases from different species (Table 3.1). The following structures were obtained by cryo-EM: a bovine mitochondrial ATP synthase structure (F_O and F_1 parts) in six different states (6.4 – 7.4 Å) [55], a dimer of mitochondrial ATP synthase from algae *Polytomella* (7.0 Å) [56], autoinhibited ATP synthase from *E. coli* in three states (6.9 – 7.8 Å) [57], mitochondrial ATP synthase from *Pichia angusta* (7.0 – 7.9 Å) [58], a dimer of ATP synthase from yeast mitochondria (3.6 Å in the F_O region) [59], and a monomer reconstituted into nanodiscs (3.6 Å) [60], chloroplast ATP synthase from *Spinacia oleracea* in three conformations reconstituted into nanodiscs (3.15 – 4.3 Å) [11], a number of structures of ATP synthase from algae *Polytomella* (2.9 – 3.2 Å) [12], a structure of ATP synthase from *Bacillus* PS3 in three states (3.0 – 3.2 Å) [61], a number of structures (monomer and dimer) of ATP synthase from *Euglena gracilis* (2.8 – 4.3 Å) [15], a tetramer (6.2 Å) and a monomer in two states (3.3 – 3.5 Å) of porcine ATP synthase [13]. The ATP synthase structure from *Paracoccus denitrificans* with 4 Å resolution [62] was obtained by XRD. The structure of a dimer of ATP synthase from *Yarrowia lipolytica* (7.7 Å) was obtained by cryo-EM and its cF_1 part was crystallized and obtained by XRD method (3.5 Å) [63].

Each study revealed new or clarified already known features of ATP synthase functioning for different species (see Tables 3.2, 3.3, and sections *Crystallization trials* and *Cryo-EM experiments*).

Table 3.1. The structures of ATP synthases with cF_1 or higher completeness from different origins. "Cn" column describes the number of protomers in the corresponding c-ring of the ATP synthase. All structures are H^+ F-type ATP synthases and sorted by a year of publishing. At the moment of writing, six studies reported XRD-solved structures, thirteen studies – cryo-EM. The resolution is shown as a range in case of more than one PDB structure is in a publication.

№	Cn	Origin	Type	Year	Method	Res. [Å]	PDB ID(s)
1	10	*S. cerevesiae*	H^+	1999	XRD	3.0 – 3.9	1QO1; 2XOK
2	10	*S. cerevesiae*	H^+	2010	XRD	3.4	2WPD
3	8	*Bos taurus*	H^+	2010	XRD	3.5	2XND
3	10	*S. cerevesiae*	H^+	2012	XRD	6.5	3ZRY
4	10	*S. cerevesiae*	H^+	2012	Cryo-EM	37.0	4B2Q
5	8	*Bos taurus*	H^+	2015	Cryo-EM	6.4 – 7.4	5FIL; 5ARI; 5ARH; 5FIK; 5FIJ; 5ARA; 5ARE
6	12	*Paracoccus denitrificans*	H^+	2015	XRD	4.0	5DN6
7	10	*Polytomella*	H^+	2015	Cryo-EM	7.0	wwPDB: EMD-2852
7	10	*E. coli*	H^+	2016	Cryo-EM	6.9 – 8.5	5T4P; 5T4O; 5T4Q
8	10	*Pichia angusta*	H^+	2016	Cryo-EM	7.0 – 7.9	5LQX; 5LQY; 5LQZ
9	10	*Yarrowia lipolytica*	H^+	2016	XRD/Cryo-EM	3.5 / 7.7	5FL7 / wwPDB: EMD-8151
10	10	*S. cerevesiae*	H^+	2017	Cryo-EM	3.6	6B8H; 6B2Z
11	10	*S. cerevesiae*	H^+	2018	Cryo-EM	3.6	6CP6
12	14	*Spinacia oleracea*	H^+	2018	Cryo-EM	3.15 – 4.3	6FKI; 6FKF; 6FKH
13	10	*Polytomella*	H^+	2019	Cryo-EM	2.9 – 3.2	6RDV; 6RDE; 6RE4; 6RE1; 6RE7; 6REU; 6RDP; 6REA; 6RDS; 6RDY; 6RED; 6RDJ; 6RDB; 6RDG; 6RDM; 6RER; 6RD9; 6RE2; 6RE3; 6RE5; 6RE6; 6RE0; 6RDX; 6RDW; 6RET; 6RES; 6REB; 6REC; 6RDC; 6RDI; 6RDH; 6REP; 6RDK; 6REF; 6REE; 6RDZ; 6RDR; 6RDL; 6RDU; 6RDT; 6RE9; 6RE8; 6RDO
14	10	*Bacillus PS3 (recombinant)*	H^+	2019	Cryo-EM	3.0 – 3.2	6N30; 6N2Z; 6N2Y
15	10	*Euglena gracilis*	H^+	2019	Cryo-EM	2.8 – 4.3	6TDU; 6TE0; 6TDY; 6TDZ
16	8	*Sus scrofa*	H^+	2019	Cryo-EM	3.3 – 6.2	6J5K; 6J5J; 6J5I

Among all six XRD-obtained structures of ATP synthases there is only one structure with almost full peripheral stalk (*bb'* subunits) and "a" subunit of the F_O part of the enzyme [62]. The other structures lack the peripheral stalk and "a" subunit, and have only the cF_1 part.

The cryo-EM structures of ATP synthases have better completeness. However, even the latest trials experienced limits of about 3 Å resolution that does not allow to figure out some structural details and molecular mechanisms, such as exact transmembrane proton transfer pathway, interactions between subunits inside the membrane (F_O) part, etc. Overcoming these limitations seems a big challenge for modern cryo-EM techniques. A way to better define the molecular mechanisms of protein functioning is a crystallographic structure with high-resolution better than 2.5 – 3 Å.

3.1.2.1. Crystallization

The crystallization of ATP synthase requires protein crystals. Due to the method limitations only six structures of almost full complexes since 1999 were obtained [50], [51], [53], [62], [63], and all of them lack several subunits or their parts. The resolution 3.0 – 6.5 Å was not sufficient to clarify the molecular mechanisms of proton transfer and inter-subunit interactions. The crystals of ATP synthases were obtained by vapor diffusion (VD) crystallization method (Table 3.2).

Table 3.2. Overview of the structures of ATP synthase complexes obtained by XRD, their completeness, and experiment details.

№	Origin, PDB ID(s)	Cryst. Method	Completeness	Crystallization conditions	New features
1	*S. cerevesiae* 1QO1; 2XOK	Microbatch	α_3, β_3, γ, δ, ε, c_{10}	0.1 M Tris/Cl pH 8.0, 12% PEG 6000, 150 mM NaCl, 1 mM AMP-PNP, 40 μM ADP, 1 mM DTT, 0.02% NaN_3, Mixed 1:1 with protein solution under paraffin oil in microbatch plate.	Showed 10 c subunits in yeast mitochondrial ATP synthase, close contacts between c-ring and γ, δ subunits. Suggested ensemble rotation of cγδ [50].
2	*S. cerevesiae* 2WPD	Vapor diffusion	α_3, β_3, γ, δ, ε, c_{10}	0.1 M HEPES/HCl pH 7.5, 12% PEG MME 5000, 100 mM NaCl mixed 1:1 with protein solution containing 0.64 mM DDM, 25 mM TRIS/HCl pH 8.0, 100 mM NaCl, 25 mM trehalose, 0.5 mM EDTA, 0.02% NaN_3, 2 mM $MgCl_2$, 0.66 mM ADP, 0.1 mM DCCD, 2.5 mM DTT, 0.5 mM PMSF.	Presented a model of a new Mg-ADP-inhibited state of the yeast ATP synthase. Showed that the contacts between c-ring and γ, δ subunits are due to electrostatics; Glu59 of the c-ring was not involved in hydrogen bonding [51].
3	*Bos taurus* 2XND	Microbatch	α_3, β_3, γ, δ, ε, c_8	Crystals were grown under oil by mixing 1:1 (v/v) protein (10 mg/mL	Showed 8 c subunits in bovine mitochondrial ATP synthase [52].

				in 20 mM Tris pH 8.0, 10% glycerol, 1 mM ADP, 1 mM AMP-PNP, 2 mM $MgSO_4$, 0.02% NaN_3, 5.7 mM TDM) and precipitant solution (50 mM HEPES pH 7.0, 14% PEG4600, 50 mM K_2HPO_4)	
4	*S. cerevesiae* 3ZRY	Vapor diffusion	α_3, β_3, γ, δ, ε, c_{10}	10% PEG 4000, 100 mM NaCl, 100 mM HEPES pH 6.5 mixed 1:1 with protein solution (10 mg/mL) containing 0.64 mM DDM, 25 mM TRIS/HCl pH 8.0, 100 mM NaCl, 25 mM trehalose, 0.5 mM EDTA, 3 mM NaN_3, 2 mM $MgCl_2$, 0.04 mM ADP, 1 mM AMP-PNP, 0.1 mM DCCD, 2.5 mM DTT, 0.5 mM PMSF.	Showed a tilt between the F_1 central stalk and the c-ring [53].
5	*Paracoccus denitrificans* 5DN6	Vapor diffusion	α_3, β_3, γ, δ, ε, a, b, b', c_{12}	Probably the initial protocol was [64]: Protein (15 mg/mL) in 50 mM Tris-HCl, pH 7.4, 1 mM $MgCl_2$, 10% glycerol, 0.5 mM ATP, 0.05% UDM and Complete EDTA-free protease inhibitor tablets (1 tablet : 100 mL) mixed with an equal volume of buffer, consisting of 50 mM Tris-HCl pH 8.0, 70-100 mM $MgCl_2$, 18-20% PEG 4000.	Showed 12 c subunits in ATP synthase from bacteria *Paracoccus denitrificans*, firstly showed a, b, b' subunits, close relation of a and c subunits and suggested a mechanism of protons pathway through the a, c subunits via two half-channels in the a-subunit [62].
6	*Yarrowia lipolytica* 5FL7	N/A, probably microbatch [65]	α_3, β_3, γ, δ, ε, c_{10}	100 mM Tris-HCl, PEG 400, pH 8.0 [63]. Probably, the initial protocol was [65]: Protein (6 mg/mL) in 20 mM Tris-HCl pH 8.0, 100 mM NaCl, 1 mM EDTA, and reservoir buffer: 1 M LiCl, 100 mM Tris-HCl pH 8.8, and 20% (w/v) PEG 6000 was mixed 1:1 to yield a final volume of 4 mL in 70 mL of dry paraffin oil.	ATP synthase was crystallized without additional nucleotides, however, Mg-ATP and Mg-ADP were found in α and β subunits, respectively. The structure is an addition to the dimeric one obtained by cryo-EM [63].

However, VD method is usually performed with water-soluble proteins [66] and has drawbacks when applied to membrane proteins. The major drawbacks are stabilization of membrane proteins into the far-from-native environment (solution instead of a membrane). It might explain a large number of trials used intact ATP synthases as a starting crystallization material, however, resulted only in structures of F_1 or F_O parts, or their subunits [29].

The crystallization in lipid meso phases (*in meso*) was proven to be efficient in the case of membrane proteins [67]. Lipid *meso* phases are a membrane-mimicking environment – lipid bilayers that form 3D infinite periodic lattice with two non-intersecting nets of water channels (Fig. 3.2A). Membrane proteins can easily diffuse laterally inside the lipid bilayers and form crystallographic contacts [68].

Comparing VD and *in meso*, in the first case six structures have been obtained with at least completeness cF_1, although it required significant effort, and in the second case no any structures of ATP synthases were published. In my thesis, the first *in meso* crystallization trials resulted in the high-resolution structure of the c-ring with using intact ATP synthase as a starting crystallization material is presented [26]. To our best knowledge, it is the first and the only structure of any subunit of ATP synthase obtained using *in meso* method.

In fact, *in meso* method works well for membrane proteins with not very large water-soluble part if using standard protocols with monoolein (MO) as a matrix lipid. The other subunits of ATP synthase were lost due to limitations of water channels diameters (d_w) of the LCP (Fig. 3.2B). A more complete ATP synthase complex could be obtained via *in meso* with d_w in the range of 115 – 160 Å. With an LCP with d_w > 160 Å, one could in principle crystallize a full complex of ATP synthase (Fig. 3.2C). However, the problem of swelling of LCP water channels is still a great challenge.

The problems of *in meso* crystallization of ATP synthase full complex are the following:

- Concentrating the protein for crystallization experiments may lead to the increase of the detergent concentration that implies instability of the complex and its partial dissociation;
- Small diameters of water channels in LCPs cannot fit the large water soluble (F_1) part of the protein;
- Protein complexity and large water-soluble part make the ATP synthase susceptible to proteolytic activity, especially at times of crystal growth. This problem relates to all methods of crystallization.

Dealing with the problems mentioned above might be the following:

- Concentrating membrane proteins directly in LCPs using the “cubicon” method [69];

- Swelling lipid meso phases using charged glycerophospholipids (1,2-Distearoyl-sn-glycero-3-phosphoglycerol) (DSPG) as supplements to matrix lipid monopalmitolein (1-(9Z-hexadecenoyl)-rac-glycerol) [70]; (however, the method should be carefully used when performing crystallization at high-salt concentrations of precipitants due to the charge shielding effect and the shrinking of LCP)
- Using proteases inhibitors in the crystallization trials;
- Using stabilizing agents interacting with ATP synthase (Mg-ADP, DCCD, Inhibitor factor (IF), oligomycin, etc).

All approaches mentioned above might help to develop the strategy of the whole enzyme crystallization, although the problem is extremely challenging. Currently none of the structures of full or almost full complex of ATP synthase had a resolution better than 2.5 – 3 Å required to reveal molecular mechanisms of proton transport, stabilization of the c-ring, or intersubunit interactions in F_O part. The crystallization of a dimer of ATP synthases seem to be even more difficult.

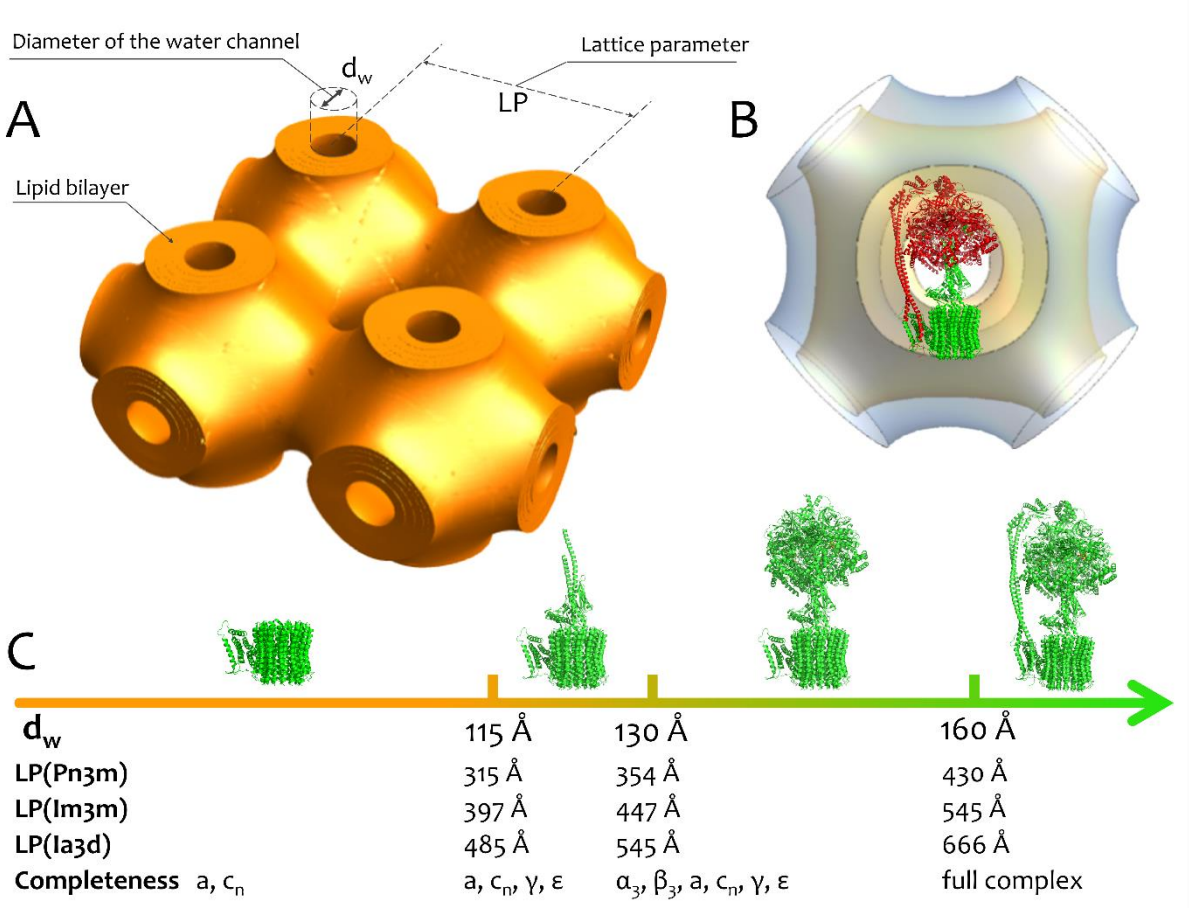

Figure 3.2. (A) A schematic representation of a lipid cubic phase (LCP) with an Im3m type of symmetry. The lattice parameter (LP) and the diameter of water channels (d_w) characterizing the LCP are shown. **(B)** A schematic reconstruction of an ATP synthase in the LCP. Several subunits (colored in red) did not fit in the unit cell of the LCP. This illustrates the limitations of large

membrane protein complexes crystallization. **(C)** Required diameters of water channels and corresponding lattice parameters of LCPs of different types and completeness of the ATP synthase complex that in principle can be reconstituted into different LCPs. The PDB model 6FKF of ATP synthase from spinach chloroplasts was used for illustration [11].

3.1.2.2. Cryo-EM studies

Fortunately, due to recent advances in cryo-EM techniques, the method allowed the structural investigations of large proteins and protein complexes much more than 100 kDa with relatively high resolution ~ 3 – 6 Å without growing crystals. Several cryo-EM studies on ATP synthases shed light on its structural properties at new level of completeness of the complex. Starting from the study in 2012 [54], showing a dimeric structure of the ATP synthase in yeast mitochondria, cryo-EM studies revealed a number of unique features of an ATP synthase structure, discovered new subunits involved into dimeric molecular machinery in the membrane (F_O) part of the complex (Table 3.3).

Table 3.3. Overview of the structures of ATP synthase complexes obtained by cryo-EM, their completeness, experiment details and new features they revealed.

№	**Origin, PDB ID(s)**	**Completeness**	**Experiment details**	**New features**
1	*S. cerevesiae* 4B2Q	α_3, β_3, γ, δ, ε, OSCP, 4, 6, 8, c_{10} (9_{10}), d, f, h, e, g, i, k	Mitochondria samples were washed with trehalose buffer (250 mM trehalose, 10 mM Tris-HCl pH 7.4) and mixed 1:1 with fiducial gold markers (6 nm gold particles conjugated to protein A, Aurion) immediately before plunge-freezing in liquid ethane.	Showed that ATP synthase forms dimers and determines the topology of the cristae in mammals, plants, and fungi [54].
2	*Bos taurus* 5FIL; 5ARI; 5ARH; 5FIK; 5FIJ; 5ARA; 5ARE	α_3, β_3, γ, δ, ε, a, e, f, g, A6L, DAPIT, 6.8, b, c_8, OSCP, d, F_6	N/A, purification protocols are described in [71].	Determined the fold of the a subunit; suggested a proton translocation path through the F_O region that involves a and b subunits; revealed seven distinct states of the ATP synthase [55].
3	*Polytomella* wwPDB: EMD-2852	α_3, β_3, γ, δ, ε, a, b, d, c_{10}	A 3 µl aliquot of a 0.5 mg/mL ATP synthase dimer solution in 0.05% (w/v) DDM showing oligomycin and DCCD-sensitive ATPase activity was applied to R2/2 Quantifoil grids without carbon backing, and plunge-frozen in a Vitrobot (FEI) at 75% humidity, 10 °C with 9 s blotting time.	Revealed that 4 alpha-helices of the a subunit are parallel to a membrane plane and wrap the c-ring, create the cavities in the membrane for proton transport via a and c subunits [56].

4	*E. coli* 5T4P; 5T4O; 5T4Q	α_3, β_3, γ, δ, ε, a, b, b', c_{10}	Aliquots of 4 µL of purified F-ATPase at a concentration of 3.58 µM were placed on glow-discharged holey carbon grids (Quantifoils Copper R2/2, 200 Mesh). Grids were blotted for 2 s and flash-frozen in liquid ethane using a Vitrobot (FEI).	Observed three different states that relate to rotation of the enzyme [57].
5	*Pichia angusta* 5LQX; 5LQY; 5LQZ	α_3, β_3, γ, δ, ε, OSCP, c_{10}, a, f, j, ATP8, b, d, h,	Portions of the purified F-ATPase (3 µl, 3-3.5 mg/mL) in CYMAL-7 were applied to glow-discharged holey-carbon Quantifoil® R 0.6/1 grids and blotted for 12-14 s. Grids were plunged into liquid ethane using a Vitrobot (FEI).	Showed that ATP8 subunit provides an additional brace between the peripheral stalk and subunit a; b, d, h subunits allow the stator to bend to accommodate lateral movements during the activity of F_1 [58].
6	*Yarrowia lipolytica* wwPDB: EMD-8151 (5FL7 – corresponding XRD structure)	α_3, β_3, γ, δ, ε, c_{10}, a, b, d, h, OSCP, e, g, f, i, 8	3 µl of a 2-3 mg/mL dimer or monomer of ATP synthase solution in 0.05% (w/v) digitonin (or 0.1% (w/v) DDM) was applied to R2/2 holey carbon grids (Quantifoil, DE) and plunge-frozen in liquid ethane using a Vitrobot (FEI) at 100% humidity after blotting for 7 to 9 s.	Showed that horizontal helices of subunit a wrap around the c-ring, six alpha-helices assigned to subunits a, b, f, i, 8 are vertically placed in the membrane; subunit f establishes direct contact between the two monomers; subunits e and g do from contacts for dimer formation but enable it by curving the membrane at ~100° [63].
7	*S. cerevesiae* 6B8H; 6B2Z	α_3, β_3, γ, δ, ε, a, b, e, f, g, i/j, k, l, 8, c_{10}, OSCP, d, h	Purified F_O dimers (2.5 µL) were applied to homemade nanofabricated EM grids consisting of a holey layer of gold on carbon that had been glow-discharged in air for 2 min. EM grids were then blotted in a FEI Vitrobot for 26 s with ~100% RH at 4 °C before freezing in a liquid ethane/propane mixture.	Clarified arrangement of subunits in F_O part of the ATP synthase dimer. Showed that subunits 8, f, and b contribute to the base of the peripheral stalk, with subunit d acting as a clip; subunits a, i/j contribute to dimerization, subunit k contacts with subunit e in the IMS; b, e, g, and k bend lipid membrane [59].
8	*S. cerevesiae* 6CP6	OSCP, b, α_3, β_3, d, f, a, c_{10}, δ, ε, γ, i/j, 8	F_1F_O in nanodiscs 1 mg/mL (2.5 µL) was applied to a glow-discharged Quantifoil holey carbon grid (1.2/1.3, 400 mesh), and blotted for 3 s with ~91% humidity before plunge-freezing in	Showed detailed structure of subunits of F_O part. Suggested that oligomycin binds the c-ring inside lipid surrounding [60].

			liquid ethane using a Cryoplunge 3 System (CP3, Gatan).	
9	*Spinacia oleracea* 6FKI; 6FKF; 6FKH	α_3, β_3, γ, δ, ε, a, b, b', c_{14}	3 µL of cF_1F_O at a concentration of 2 mg/mL was applied to freshly glow-discharged Quantifoil R1.2/1.3 grids and plunge-frozen in liquid ethane using a Vitrobot (Thermo Fisher/FEI).	Showed details of intersubunit contacts (a/c_{14} interface) and redox control switch in the central stalk, which is responsible to the adaptation of chloroplast ATP synthase redox potential to day-night cycle [11].
10	*Polytomella* 6RDV; 6RDE; 6RE4; 6RE1; 6RE7; 6REU; 6RDP; 6REA; 6RDS; 6RDY; 6RED; 6RDJ; 6RDB; 6RDG; 6RDM; 6RER; 6RD9; 6RE2; 6RE3; 6RE5; 6RE6; 6RE0; 6RDX; 6RDW; 6RET; 6RES; 6REB; 6REC; 6RDC; 6RDI; 6RDH; 6REP; 6RDK; 6REF; 6REE; 6RDZ; 6RDR; 6RDL; 6RDU; 6RDT; 6RE9; 6RE8; 6RDO	α_3, β_3, γ, δ, ε, c_{10}, a, OSCP, ASA(1-10)	A solution of 3-4 mg/mL purified complex was applied to C-flat 1/1 or 2/1 holey carbon grids (Science Services GmbH) glow-discharged for 45 s at 0.15 mA. Grids were blotted for 4-5 s at blotforce 20 using a Vitrobot, and vitrified in liquid ethane.	Demonstrated flexibility of the enzyme during discrete ATP synthesis; found 10 new subunits forming a rigid peripheral stalk in *Polytomella* (ASA), that connect two ATP synthase monomers in the luminal side of the membrane; discovered a metal ion (presumably Zn^{2+}) in a subunit, which possibly synchronizes c-ring rotation and protonation; found ordered water in half-channels [12].
11	*Bacillus PS3 (recombinant)* 6N30; 6N2Z; 6N2Y	α_3, β_3, γ, δ, ε, c_{10}, a, b, b'	Purified ATP synthase (2.5 µL) was applied to homemade nanofabricated EM grids consisting of a holey layer of gold that had been glow-discharged in air for 2 min. Grids were then blotted on both sides in a FEI Vitrobot mark III for 26 s at 4°C and ~100% RH before freezing in a liquid ethane/propane mixture.	Provided the structure of recombinant ATP synthase. Clarified the mechanism of ATP synthesis inhibition by ε subunit in bacterial ATP synthase and the path of transmembrane proton transfer [61].
12	*Euglena gracilis* 6TDU; 6TE0; 6TDY; 6TDZ	α_3, β_3, γ, δ, ε, c_{10}, a, OSCP, d, f, i/j, k, 8, ATPEG(1-8), ATPTB(1, 3, 4, 6, 12)	3 µL sample (~5 mg/mL) were applied to glow-discharged Quantifoil R1.2/1.3 Cu grids and vitrified by plunge-freezing into liquid ethane after blotting for 3 s.	Discovered a new type of ATP synthase dimers (type IV), that belongs to *Euglena* and trypanosomes [10]; showed a number of additional subunits, associated phospholipids and cardiolipins; showed that the c-ring is stabilized by additional β-barrel contacting with ATPEG1 subunit [15].

13	*Sus scrofa* 6J5K; 6J5J; 6J5I	α_3, β_3, γ, δ, ε, c_8, a, b, d, OSCP, e, g, f, k, 6.8PL, DAPIT, A6L, F6,	Cryo-EM samples were prepared using Quantifoil R1.2/1.3 400 mesh Au grids (Quantifoil, Micro Tools GmbH, Germany). The grids were coated with a home-made continuous 3-5 nm thick layer of carbon. Aliquots of 4 μL of tetrameric ATP synthase protein sample at a concentration of 0.3 mg/mL were applied to the grids which were pre-glow discharged by Plasma cleaner (PDC-32G, Harrick plasma) for 30 seconds at medium power setting. The grids were blotted for 1.5 s by the blotting filter paper (Ted pella) and plunged into liquid ethane cooled by liquid nitrogen using Mark IV Vitrobot (Thermo Fisher) operated at 8 °C and 100% humidity.	Showed the structure of a tetramer of ATP synthases from mammalian mitochondria; showed that subunits b, k, g and inhibitory factor 1 (IF1) link two V-shaped ATP synthase dimers and form H-shaped tetramer; showed that 6.8PL subunit is inside the c-ring pore; suggested three different mechanisms of ATP synthase inhibition: by using IF1, by using Mg-ADP and by inhibition of e subunit connected with 6.8PL that is inside the c-ring central pore [13].

Cryo-EM studies, although seemed more perspective (about ten publications since 2015 and about 70 structures with the resolution 2.8 – 8.5 Å), they experienced difficulties with obtaining high-resolution structures better than 2.5 Å. Especially there were problems with cryo-EM of the membrane protein complexes in their membrane part, where lipidic surrounding distorts the order and unity of investigated objects and consequently lowers the resolution. The latter occurred to be a challenge. Though some authors reported 2.8 – 2.9 Å resolution in the F_O part of an ATP synthase, this is still not sufficient for recovering important part of molecular mechanisms.

3.1.2.3. Complementarity of XRD & Cryo-EM

XRD studies of proteins require crystals. Growing crystals is a common procedure for water-soluble proteins. However, it becomes a real challenge for membrane proteins and especially for large protein complexes. Membrane proteins without or with small water-soluble segments can be crystallized *in meso* [67]. ATP synthase is a membrane protein complex with a large water-soluble part of about 160 Å, which implied difficulties on the way of its crystallization due to the mentioned limitations of VD and *in meso* methods.

Cryo-EM method is very sensitive to surrounding disordered objects such as detergent micelles or lipids, although it easily recovers protein structures at megadalton scale. The working resolution

of about 3 Å allows obtaining a general structure of a protein complex with recovering the details of the secondary structure. However, the resolution lacks the molecular mechanisms of protein functioning, allowing only suggestions and hypotheses about them.

Mentioned before was one of the reasons why cryo-EM studies could be, and sometimes were, complementarily used with XRD technique. Such approach provided on the one hand – a completeness of a structure unachievable for modern crystallography (~1.2 MDa for an ATP synthase dimer), and on the other hand – an accuracy in places hidden for cryo-EM such as membrane parts of protein complexes that are surrounded with lipids or in active centers of proteins. The key subunits of the complexes could be crystallized separately in order to reveal specific intersubunit interactions and molecular mechanisms of functioning of enzymes with high resolution using XRD, while cryo-EM could provide a structure of the whole protein complex. Thus, integrating these results, one could build a mosaic atomic model of a protein complex with necessary resolution in necessary places.

3.1.3. Similarity and divergence

A composition of monomeric ATP synthases is very similar among different species (in bacteria (bF_OF_1) and chloroplasts (cF_OF_1) it is $\alpha_3\beta_3\gamma\delta\varepsilon c_n bb'$). A different picture is for mitochondrial ATP synthases (mtF_OF_1), which, though preserve a general commonality (F_1 and F_O parts, c-ring, peripheral stalk), significantly vary in subunit composition. There are four types of mtF_OF_1 dimers among different species known to date (Fig. 3.3) [10].

Despite the differences, their functionality remains the same: ATP synthesis/hydrolysis and transmembrane proton transport with the extension that mtF_OF_1 dimers influence the cristae topology. The dimerization of mtF_OF_1 and their ability to create arrays were observed in all investigated eukaryotes; however, the mechanisms of these processes are remaining unclear. V-shaped mtF_OF_1 dimers that were found in animals and fungi (type I, Fig. 3.3A,E) provide a significant membrane curvature (~86°) as do V-shaped mtF_OF_1 dimers of type II and IV (~55 – 56°) (Fig. 3.3B, F and D, H), and U-shaped mtF_OF_1 dimers from ciliates (type III, Fig. 3.3C,G) almost do not bend a membrane (~0°), however also create arrays forming helical mitochondrial cristae (Fig. 3.3G) [14].

A topology of mitochondrial cristae seems to be conditioned by general bioenergetic needs of the exact species. It is defined by mtF_OF_1 dimerization and its tendency of self-assembly into arrays – the very conserved properties of mtF_OF_1 in different lineages despite the diversity of their subunit composition. The morphology of the cristae defines the efficiency of ATP synthesis (ATP/proton ratio) and cellular bioenergetics. Whatsoever mechanisms control the dimerization of the complex,

they seem to be strongly conserved, even more than subunits responsible for dimerization of mtF_OF_1 [10].

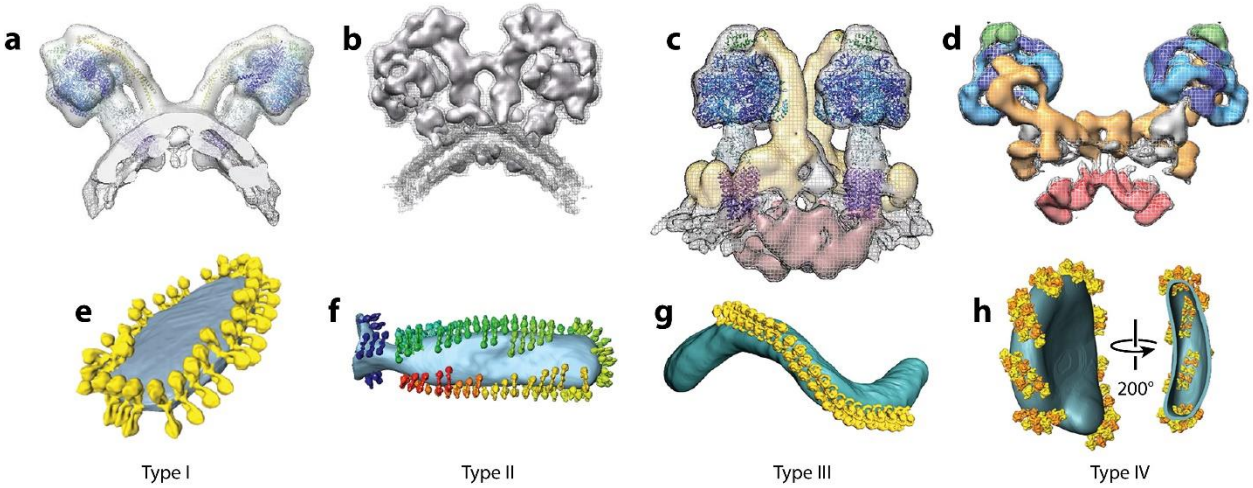

Figure 3.3. Four types of mtF_OF_1 dimers. A - D show subtomogram averaging of mtF_OF_1 and E - F – their arrangement in 3D volume cristae vesicles. **(A)**, **(E)** – the dimers of mtF_OF_1 from animals & fungi (type I). **(B)**, **(F) –** the dimers of mtF_OF_1 from unicellular green algae (type II). **(C)**, **(G)** – the dimers of mtF_OF_1 from ciliates. **(D)**, **(H)** – the dimers of mtF_OF_1 from *Euglena* and trypanosomes. The figure is reprinted from [10] with a permission from Annual Reviews, Inc.

It is believed that mitochondria originated from alphaproteobacteria, which intercellular membranes have similar functionality as mitochondria cristae [72]. It is also known that different phylogenetic groups have different morphology of mitochondria cristae [10] and the morphology is determined by proteins of mitochondrial inner membrane complex (MICOS) and mtF_OF_1 [73]. The phylogenetic taxonomy database NCBI [74] shows that Eukaryota superkingdom contains 18 groups of different rank [75]. According to available structural data, representatives from four of the groups are described in terms of cristae morphology and have specific types of mtF_OF_1 (Fig. 3.4). According to what is known, the organisms belonging to Viridiplantae kingdom, Opisthokonta, Sar, and Discoba supergroups differ cristae morphology and type of mtF_OF_1.

The completeness of structures of mtF_OF_1 dimers from different species is striking (Table 3.4). The full complex machinery was deciphered for yeast [58], [59], [63] and porcine [13] mitochondria (type I) from Opisthokonta supergroup, for mitochondria of unicellular green algae *Polytomella* [12] (type II) from Viridiplantae kingdom, and unicellular flagellate eukaryotes *Euglena* [15] (type IV) from Discoba supergroup, for bacteria [57], [61] and chloroplasts [11] (monomers). Low-resolution structural data of full mtF_OF_1 were obtained for ciliates *Paramecium tetraurelia* from Sar supergroup – this specie has a mtF_OF_1 dimer of type III [14]. That was the only work on this

class of dimers. It provided the cryo-EM structure with 26 Å resolution, that is not enough to decipher an amino acid sequence or a protein secondary structure (Table 3.4).

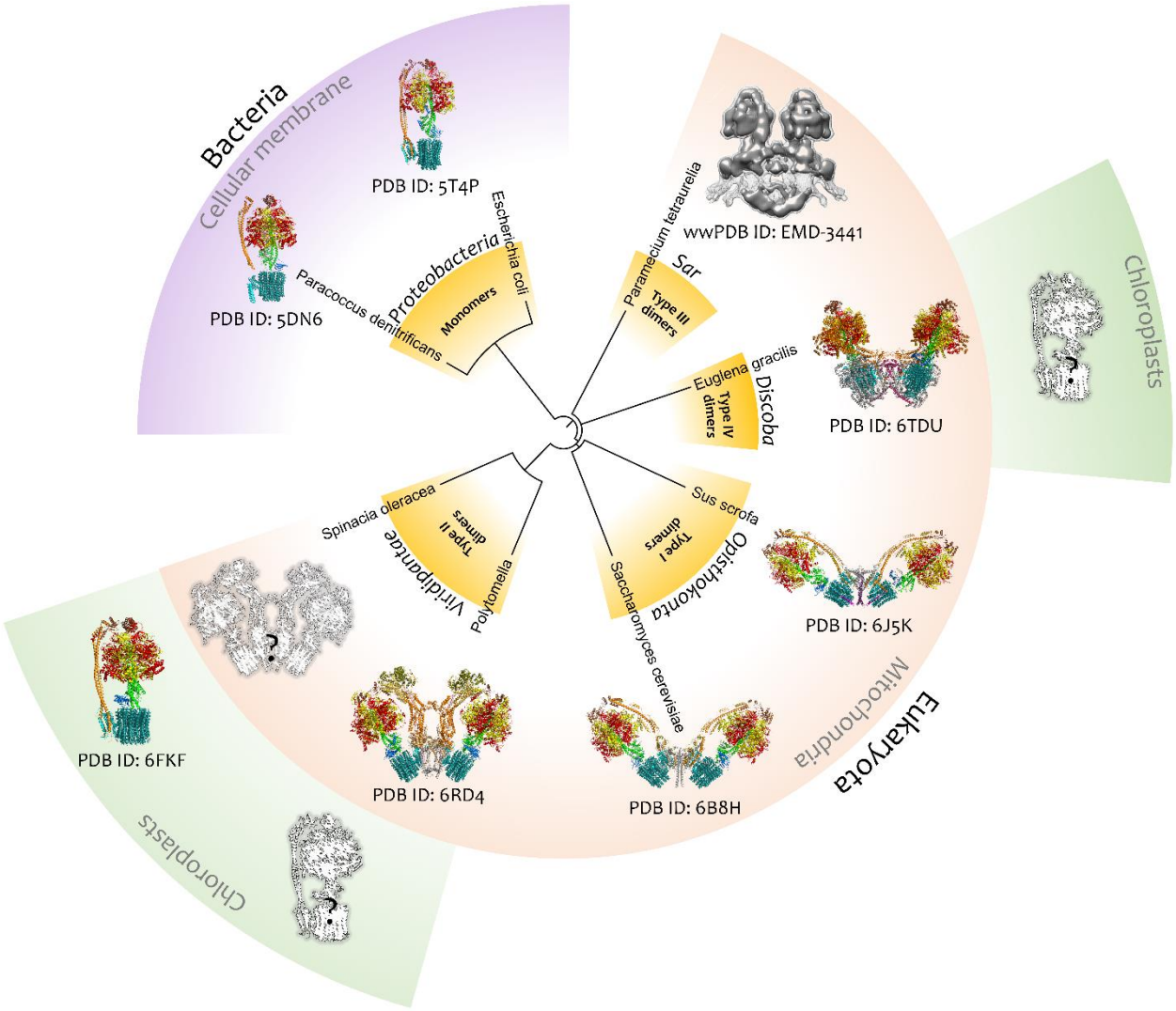

Figure 3.4. Phylogenetic tree of species with available structural data on ATP synthases. In the center the phylogenetic tree shows the species from two superkingdoms (Bacteria and Eukaryota), and eukaryotes from Viridiplantae kingdom, Opisthokonta, Sar, and Discoba supergroups. The type of ATP synthase oligomeric state is shown for cellular membrane bF_OF_1 in the case of bacteria and for mitochondrial mtF_OF_1 in the case of eukaryotes. Some eukaryotes which have chloroplasts, and consequently cF_OF_1, are shown with segments of additional ring. Structures of ATP synthases are shown with corresponding (ww)PDB IDs. Unknown structures of ATP synthases are shown as a sketch of a faded gray color with a question mark. The representation of the structure wwPDB ID: EMD-3441 was adapted from [14].

Table 3.4. Subunit composition of F-type ATP synthases from different groups according to the available structural data. The ellipsis in the “dimers” column “Type III” subcolumn means the lack

of the high-resolution structural data to decipher amino acid sequence or protein secondary structure.

Superkingdom	***Bacteria***	***Eukaryota***			
		Opisthokonta	*Viridiplantae*	*Sar*	*Discoba*
Organelle	cellular membrane	mitochondria			
Oligomeric state of F_OF_1	monomers	dimers			
		Type I	Type II	Type III	Type IV
Subunit composition of F_OF_1	α_3, β_3, γ, δ, ε, a, b, b', c_n	α_3, β_3, γ, δ, ε, a, b, c_n, d, e, f, g, h, i (i/j or 6.8PL), k (DAPIT), l, 8, OSCP, F6	α_3, β_3, γ, δ, ε, c_n, a, OSCP, ASA(1-10)	α_3, β_3, γ, δ, ε, c_n, OSCP, …	α_3, β_3, γ, δ, ε, a, c_n, d, f, i/j, k, 8, OSCP, ATPEG(1-8), ATPTB(1, 3, 4, 6, 12)

Mentioned above implies the paradoxical features of ATP synthases. Firstly, mtF_OF_1 are similar in their tendency to form dimers and are at the same time diverged in their subunit composition resulting in completely different forms of mitochondria cristae determined by at least four types of mtF_OF_1 dimers. Secondly, all known bF_OF_1 and cF_OF_1 are monomers and their subunit composition is very conserved in distant lineages. In other words, the variability of comparatively simple bF_OF_1 and cF_OF_1 monomers is much lower than of more complex mtF_OF_1 dimers between lineages. Moreover, if comparing mtF_OF_1, bF_OF_1 and cF_OF_1 – the commonality between them is only F_1 and partially a and c subunits in F_O part. Even the stabilization mechanisms of c-rings significantly differ between mtF_OF_1, not to mention the peripheral stalks that can be completely unlike from each other in different phylogenetic groups of eukaryotes, at the same time being almost identical in bF_OF_1 and cF_OF_1.

Occasionally, some eukaryotes have mitochondria and chloroplasts, thus could possess different ATP synthases (mtF_OF_1 dimer and cF_OF_1 monomer). The coexistence of different types of F_OF_1 in one organism rises a plenty of questions. One of them is about gene regulations of mtF_OF_1 and cF_OF_1 subunits, especially when considering that some subunits are totally different and some of them can be almost homologous. Unfortunately, no structural data was obtained for mtF_OF_1 and cF_OF_1 for one specie. Thus, the structural data allowed suggesting the hypothesis that every organism belonging to *Viridiplantae* kingdom inherits the same morphology of mitochondria cristae with mtF_OF_1 dimers of type II and chloroplasts with cF_OF_1 monomers.

Interestingly there is evidence that cF_OF_1 from *Chlamydomonas reinhardtii* form dimers and the dimerization process undergoes cellular metabolic control [76], [77]. Also, the evidence of formation of cF_OF_1 dimers from *Spinacia oleracea* after reconstitution into lipid nanodiscs was obtained by SAXS during this work [78]. However, due to the absence of high-resolution atomic structure it is still unclear whether these structures are biologically relevant. The work [79] shows electron microscopy data of solubilized cF_OF_1, which form oligomers in different ways. As it was shown by tomography of the thylakoid membranes, cF_OF_1 in plants form oligomers with the following distribution: approximately 85% of monomers, ~12% – pairs of cF_OF_1, ~3% – groups of three cF_OF_1 and less than 1% of groups of 4-6 cF_OF_1 [80]. The study of cF_OF_1 from *Spinacia oleracea*, reconstituted into nanodiscs consisting of native lipids from spinach thylakoid membranes, that resulted in 3 Å resolution structure obtained by cryo-EM [11], suggests towards monomeric state of ATP synthases in chloroplasts. Considering mentioned above data one could hypothesize that although commonly cF_OF_1 might have a monomeric state, it is not excluded a native oligomerization of cF_OF_1 in thylakoid membranes under different conditions and metabolic processes.

3.1.4. Functional studies

Structural investigations that were performed with different ATP synthases raised a very important question of the data validity. It was necessary to check whether the enzyme used for structural studies was functional, thus, preserved its' intact properties and native conformation. This was important for understanding the molecular mechanisms of enzyme functioning based on the obtained structural information.

There are two common functional tests of F_OF_1 ATP synthase: measuring ATP synthesis activity, and proton pumping. These tests, though do not guarantee the full completeness of the complex, nevertheless show whether and how efficient the purified ATP synthase performs its major function.

The protocols of functional characterization were published in the work [57] showing the full-size bF_OF_1 structure from *E.coli*. The authors studied proton pumping with the help of 9-Amino-6-Chloro-2-Methoxyacridine (ACMA) – a pH sensitive fluorescent probe, and measured ATPase activity by N,N-dimethyldodecylamine N-oxide (LDAO) as described in [81]. They calculated ATP synthesis rate of 0.75 μM ATP/min/mg protein, that corresponds to ~ 6 ATP/sec/enzyme and discovered LDAO stimulation of ATPase activity by bF_OF_1 *E. coli* increasing it about 13 times (Table 3.5).

Table 3.5. Selected protocols and results of functional studies of ATP synthases. Different functional tests are enumerated. The rate of ATP synthesis is converted to ATP/sec/enzyme for convenient comparison.

№	Origin, PDB ID(s)	Protocols	Results
1	*E. coli* 5T4P; 5T4O; 5T4Q	1) Proton pumping by proteoliposomes was studied with ACMA. The reaction was started with 0.25 mM ATP and stopped by 2 mM of the uncoupler FCCP [81]. 2) ATPase activity and its stimulation by LDAO was measured with ATP regenerating system using 5 mg of the protein with 1 mM ATP [81]. 3) DCCD inhibition of proteoliposomes was performed [81]. 4) DCCD inhibition of pure F_1F_O was performed [82] with the modifications: 10ug of the protein was incubated in 1 mL buffer A (50 mM MES, pH 6.4, 100 mM KCl, 1 mM $MgCl_2$) with 50 mM DCCD for 30 min at RT. Control sample contained 1% ethanol instead of DCCD. Reaction was started by mixing the inhibited protein with 1 mL of buffer A containing all the components of ATP regenerating system.	Prior to addition of LDAO, the hydrolysis rate was 0.75 μM ATP/min/mg protein or 6 ATP/sec/enzyme; in presence of 0.4% LDAO it increased ~13 times (78 ATP/sec/enzyme) [57].
2	*Spinacia oleracea* 4MJN	ATP synthase was reconstituted into liposomes (PC/PA = 9:1, w/w) [83]. 1) As a control, ATP synthase was inhibited by adding DCCD 50 μM before reconstitution into liposomes and incubated 30 min at RT [84]. 2) ATP synthesis activity was measured [85], [86] with the modifications: 240 μL buffer L2 (200 mM Tricin, 5 mM NaH_2PO_4, 2.5 mM $MgCl_2$, 120 mM KCl, 0.2 mM ADP, pH 8.3) was added into a cuvette and mixed with 12.5 μL Luciferin–Luciferase-reagent (ATP-Monitoring Kit; Thermo Labsystems). The cuvette was placed into a Luminometer (BioOrbit 1250) and the baseline was recorded. ~43 μL of proteoliposomes were equilibrated with 217 μL buffer L1 (20 mM sodium succinate, 5 mM NaH_2PO_4, 2.5 mM $MgCl_2$, 0.6 mM KCl, 1 μM Valinomycin, pH 4.7). After 100 s, the mixture was injected via a cannula into the cuvette containing L2. ATP synthesis, driven by the electrochemical gradient (ΔpH and ΔK^+), was monitored as luminescence using the Luciferin–Luciferase-Assay. As a standard, 20 μL of 10 μM ATP was added.	ATP synthesis activity of 41 ± 4 ATP/sec/enzyme was determined [29].
3	*Myco-bacterium phlei* 4V1F, 4V1G	1) BDQ inhibition of inverted micelles of *Mycolicibacterium phlei* was performed. To determine IC_{50}, the BDQ concentrations were screened in range of 0.0 – 1.0 mM.	IC_{50} value of 20 - 25 nM shows the highly effective inhibition of bF_OF_1 by BDQ; 0.1 mM BDQ completely inhibited the synthesis activity [87].
4	*Spinacia oleracea* w/o PDB	1) ATP synthesis was measured. ATP synthase was inserted into the liposomal membranes (PC/PA = 19:1) using a method [88]. The liposome aliquots were thawed at room temperature before being combined with 5–20 μL enzyme-micelle solution (2–5	ATP synthesis activity of ~ 200 ATP/sec/enzyme was determined [25].

		mg/mL), 125 µL buffer (20 mM Tricine, 20 mM succinate, 0.6 mM KOH, 80 mM NaCl, 5 mM $MgCl_2$, pH 8.0 with NaOH), and 20 µL of Triton X-100 (10% w/v). Biobeads (80 mg) were added and the solution was stirred at room temperature for 1 h before the solution was decanted off. The proteoliposomes (10 µL) were incubated with 50 µL acidic buffer (20 mM succinate, 0.6 mM KOH, 2.5 mM $MgCl_2$, 20 µM valinomycin, 10 mM NaH_2PO_4, pH 4.5) for 2 min. ATP synthesis was triggered in a $\Delta pH/\Delta\psi$ jump by the addition of 200 µL of basic buffer (200 mM Tricine,130 mM KCl, 10 mM NaH_2PO_4, 2.5 mM $MgCl_2$, 0.1 mM ADP, pH 8.8) and halted by the addition of 250 µL trichloroacetic acid (6% w/v) at discrete time intervals (0.5, 1.0, 2.0, 3.0, 5.0, 10.0 s). Basic buffer without ADP (500 µL) was added to adjust the pH of the solution towards neutral for the ATP-determination assay. The ATP quantity was determined by the luciferin–luciferase assay.	
5	*Bacillus* w/o PDB	1) ATP synthesis/ase rate *vs.* PMF was measured. 2) ATP synthesis/ase rate *vs.* concentrations of ATP, ADP, and P_i were measured. Proteoliposomes were acidified: 30 µL of the PLs (40 mg lipid/mL) was mixed with 70 µL buffer (40 mM buffer containing 0.147 mM to 14.7 mM NaH_2PO_4, 6 mM $MgCl_2$, 5 mM KCl, 4 mM NaCl, 0.5 M sucrose, 0.03 - 0.9 mM ADP, 0.04 - 3 µM ATP, 0.3 µM valinomycin), pH was adjusted with NaOH. The mixture was incubated for 10 - 20 h at 23 - 27 °C. Base medium was prepared by mixing 25 µL of the luciferin/luciferase mixture (2x concentration of CLSII solution in ATP bioluminescence assay kit; Roche) supplemented with 5 mM luciferin, 800 µL of base buffer (350 mM HEPES, 11.3, 1.13, or 0.113 mM NaH_2PO_4, 5.6 mM $MgCl_2$, 5.6 mM KCl, 11.25 mM NaCl, 272 mM mixture of KOH + NaOH to keep total concentration of Na+ plus K+ in the solution), 18 µL of 1 - 32 mM ADP, and 57 µL of water. The catalytic reaction, ATP synthesis/hydrolysis, was triggered by injecting 100 µL of the acidified proteoliposomes suspension into the base medium.	H^+/ATP ratio of 3.3 ± 0.1 was determined [89].
6	*Ilyobacter tartaricus* and *E.coli* w/o PDB	1) ATP hydrolysis activity was determined by the pH indicator phenol red. Liposomes were prepared by passing the total *E. coli* lipid extract (20 mg/mL) in the buffer containing 15 mM Tris-HCl, 1 mM KH_2PO_4, 5 mM $MgSO_4$, 100 mM NaCl, and 50 mM KCl, pH 7.5. ATP synthase was mixed with the liposomes (lipid/protein = 10/1) (w/w) and in the presence of 1% DDM. For measuring the ATP synthesis the proteoliposomes were resuspended at 40 mg/mL. 2) ATP synthesis was monitored by a continuous luciferin/ luciferase assay. Luciferase (1.5 µg) and 10 nmol of D-luciferin were added to 300 µL of the reaction mixture 15 mM Tris-HCl (pH 7.5), 1 mM KH_2PO_4, 5 mM $MgSO_4$, 50–200 mM KCl, 0–100 mM NaCl, 75 nM valinomycin, 50 µM ADP. The reaction was triggered by injection of 3 µL proteoliposomes into the reaction mixture.	The ATP synthesis activity was 1.3–1.8 µM ATP/min/mg protein that is equal to ~11–15 ATP/sec/enzyme [30].

7	*Spinacia oleracea* w/o PDB	1) ATP synthesis was monitored by a continuous luciferin/ luciferase assay. 2) ATP hydrolysis activity was measured. Proteoliposomes (10 µL) were added to 50 µL of acidic buffer (20 mM sodium succinate, pH 4.9, 5 mM NaH_2PO_4, 2.5 mM $MgCl_2$, 0.6 mM KOH, 5 µM valinomycin). After 2 min, ATP synthesis was started by addition of 60 µL (200 mM Tricine, 5 mM NaH_2PO_4, 2.5 mM $MgCl_2$, 120 mM KOH, 200 µM ADP, pH 8.7).	The maximum synthesis ratio in reverse phase liposomes was 80±3 ATP/sec/enzyme, and 110±5 ATP/sec/enzyme in dialysis liposomes [90].

Other experimental data on functional characterization were published in the work [29] showing the structure of separate c-ring of cF_OF_1 from *Spinacia oleracea* with 6 Å resolution (see detailed description in the section *H^+ c-rings*). The intact cF_OF_1 was used as a starting crystallization material and therefore was functionally characterized. Unlike the previously mentioned study, the authors tested ATP synthesis activity using proteoliposomes and Luciferin–Luciferase-Assay as described in [85], [86] (Fig. 3.5).

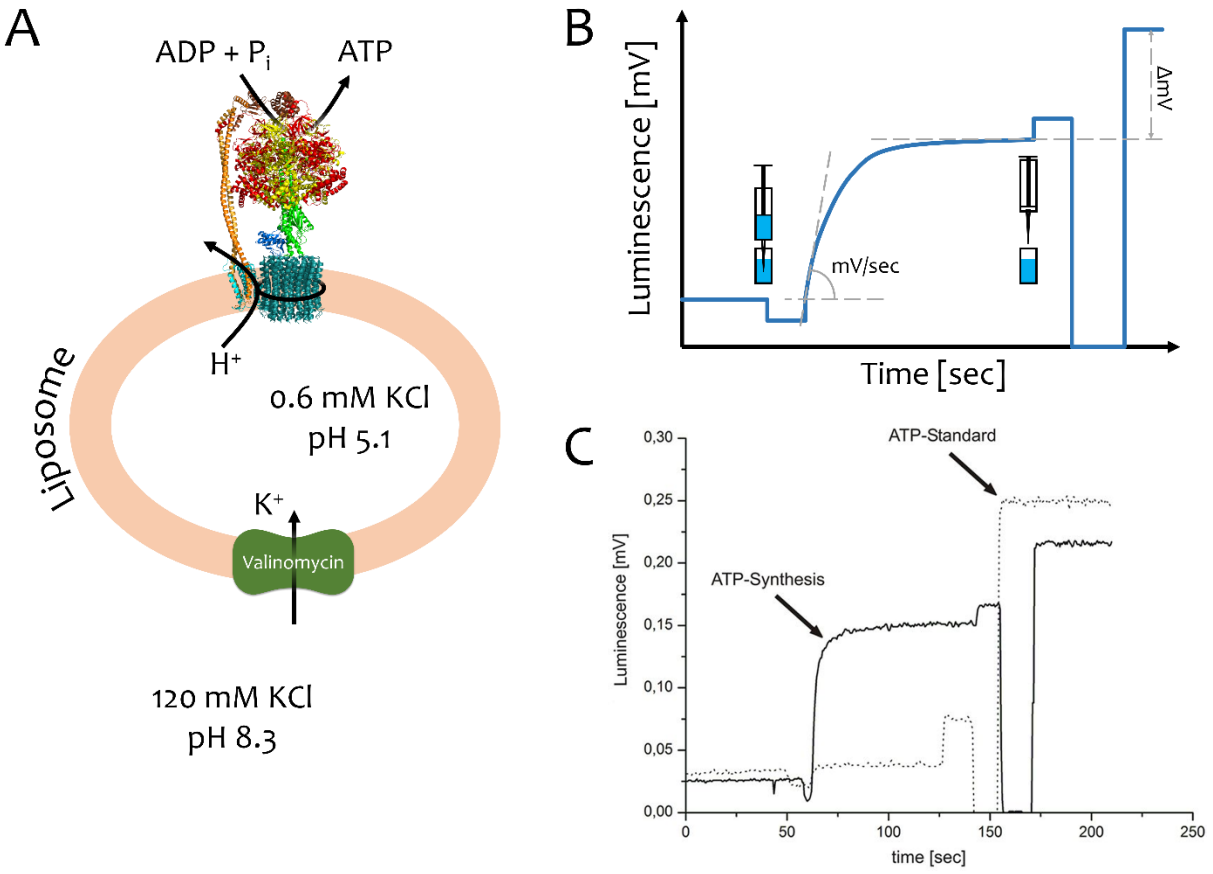

Figure 3.5. ATP synthesis functional test of H^+ F-type ATP synthase. **(A)** A schematic model of the functional test. A liposome with reconstituted ATP synthase and valinomycin (proteoliposome) is shown. **(B)** A schematic and **(C)** experimental plots of luminescence signal *vs.* time are shown. Firstly, background signal is measured; then proteoliposomes are inserted in a cuvette via a cannula, that causes a slight signal decrease; after that there is an exponential growth of the signal due to ATP synthesis until the plateau is reached. When removing the cannula, there is a slight

increase of the signal; then – the ATP standard is added. The slope at the beginning of the exponential growth (mV/sec) and the difference between the plateau value and when adding the ATP standard (ΔmV) are required to calculate the rate of the ATP synthesis (ATP/sec/enzyme) (see Appendix). ATP synthase PDB ID: 6FKF in panel A is shown. The plot in the panel C was reprinted from [29].

Another branch of studies where the functional tests of ATP synthases are required is a design of drugs targeting ATP synthases of different pathogens, for example, the study [87], which also shows two high-resolution structures of separate c-ring of bF_OF_1 from *Mycolicibacterium phlei* with a resolution of 1.55 and 1.7 Å respectively (XRD) (see detailed description in the section *H^+ c-rings*). The functional tests demonstrated ATP synthesis inhibition by bedaquiline (BDQ) (anti-tuberculosis drug), which binds to the active center of the mycobacterial bF_OF_1 c-ring. In case of drug design, the major parameter to measure is a half-maximal inhibitory concentration IC_{50}, which shows the efficiency of a drug. The authors performed BDQ inhibition of inverted micelles of *Mycolicibacterium phlei* and calculated IC_{50} was 20-25 nM indicating highly efficient inhibition of ATP synthesis activity and consequently highly efficient binding of the drug (BDQ) to its target protein (bF_OF_1 c-ring).

The other publications of functional studies of ATP synthases did not contain high-resolution structural information, however, they shed light on several intriguing questions of ATP synthase functioning. B. Varco-Merth *et al.* [25] in 2008 performed structural and functional studies of the cF_OF_1 c-ring from spinach thylakoid membranes. The functional studies of the intact cF_OF_1, that was used as a starting crystallization material, reported the ATP synthesis rate of approximately 200 ATP/sec/enzyme, which is five times more than in the work [29] (A.M. Balakrishna *et al.*) in 2014 for the same cF_OF_1 c-ring from spinach thylakoid membranes. Although such a large discrepancy was not discussed in the paper [29], detailed comparison of the protocols used for sample preparations revealed several minor differences (ΔpH 4.3 *vs.* 3.6; slightly different salt and ADP concentrations) that presumably could not significantly influence the ATP synthesis, a difference in liposomes preparation – PC/PA in case of B. Varco-Merth *et al.* was 19:1 *vs.* 9:1 in case of A.M. Balakrishna *et al*, and in reconstitution procedures; and one major difference – the concentration of valinomycin in the case of B. Varco-Merth *et al.* was 20 μM *vs.* 1 μM in the case of A.M. Balakrishna *et al*. Different reconstitution procedures could influence the ATP synthesis as it was shown [90] (80 – 110 ATP/sec/enzyme depending on the reconstitution procedures) and twenty times increase of valinomycin concentration could also possibly impact the ATP synthesis rate, however, exact experiments are required to quantitatively estimate these effects.

ATP synthase has a perfect chemomechanical coupling between F_1 and F_O parts and the H^+/ATP ratio is defined very accurately [89], it is equal to n/3, where n means the number of protomers in the c-ring; and proton motif force (PMF) depends linearly on ATP synthesis rate with the slope of n/3, thus the ATP synthesis rate can be calculated when the PMF is known (depends on accurate control during samples preparation) and the c-ring stoichiometry.

The c-ring stoichiometry itself could be engineered and assemble with the other subunits of an ATP synthase into a functional complex [30] (see detailed description in the section *Intersubunit contacts and c-ring stoichiometry*). The functional activity of such modified ATP synthases with the c-ring from *Ilyobacter tartaricus* and other subunits from *E. coli* showed the ATP synthesis activity of 11–15 ATP/sec/enzyme – 2-2.5 times more than bF_OF_1 from *E. coli* [57].

The problem of data comparison of different ATP synthases activity is due to the absence of unified protocols and preparation-conditioned results. However, even now it can be noticed that results of measuring of ATP synthesis rate can be significantly different, for example, for *E. coli* bF_OF_1 and spinach cF_OF_1, that are unlikely to be explained only by different sample preparation conditions. One of the possible explanations might be the difference in c-rings. All these questions require additional studies in the framework of standard kits and protocols in order to make functional studies of ATP synthases not in a qualitative but quantitative way.

3.1.5. Recent discoveries

ATP synthase though having been intensively studied for last decades, still brings surprises. Recent works show that the biological functions of ATP synthase seem to be much wider than being supposed earlier and its role in organisms has possibly only started to be understood. The molecular mechanisms of symmetry mismatch accommodation are at one of the focuses of interest. For the first time it was experimentally shown for c_{14}-ring from spinach chloroplasts [91] (14 protomers indicated that the synthesis of one ATP molecule corresponds to the fractional number of a c-ring rotation quanta 14/3) and the remarkable work on bF_OF_1 from *E.coli* shows torsional flexing of the entire complex to establish c_{10}/β_3 flexible coupling [92] (four structures with 3.1 – 3.4 Å resolution, cryo-EM, PDB IDs: 6OQR-U). Other focuses of interest are: the ATP synthase as a part of respiratory chain supercomplexes [93]–[95]; the possibility that ATP synthase acts as a Ca^{2+} channel [96], and the role of ATP synthase in mitochondrial permeability transition pore (MPTP) *phenomenon* [17], [97] – the question that has sparked intensive debates [17], [18], [98].

3.1.5.1. ATP synthase as a part of respiratory chain supercomplexes

Respiratory chain complexes I-V constitute the OXPHOS in mitochondria (Fig. 3.1). ATP synthase is so-called V complex provides the final functional step of mitochondria – ATP synthesis. As it

was shown, I-IV respiratory chain complexes form different types of supercomplexes in mammals, for example, $I_1III_2IV_1$ or even a megacomplex $I_2III_2IV_2$ [99]. The formation of megacomplexes in plant mitochondria goes weaker as well as dimerization of ATP synthases (V_2), however some supercomplexes such as III_2IV_{1-2} and $I_1III_2IV_{1-4}$ have been reported for plants in a number of works [100], [101]. The formation of V_2 was reported for plant mitochondria and detected by BN PAGE method [102], [103]. It was also shown that the OXPHOS complexes (Fig 3.6A) are not only associated as supercomplexes (Fig. 3.6B), but also can coexist in monomeric and supercomplex forms (Fig. 3.6C) showing a dynamic behavior of supercomplexes which are exchanging separate OXPHOS complexes.

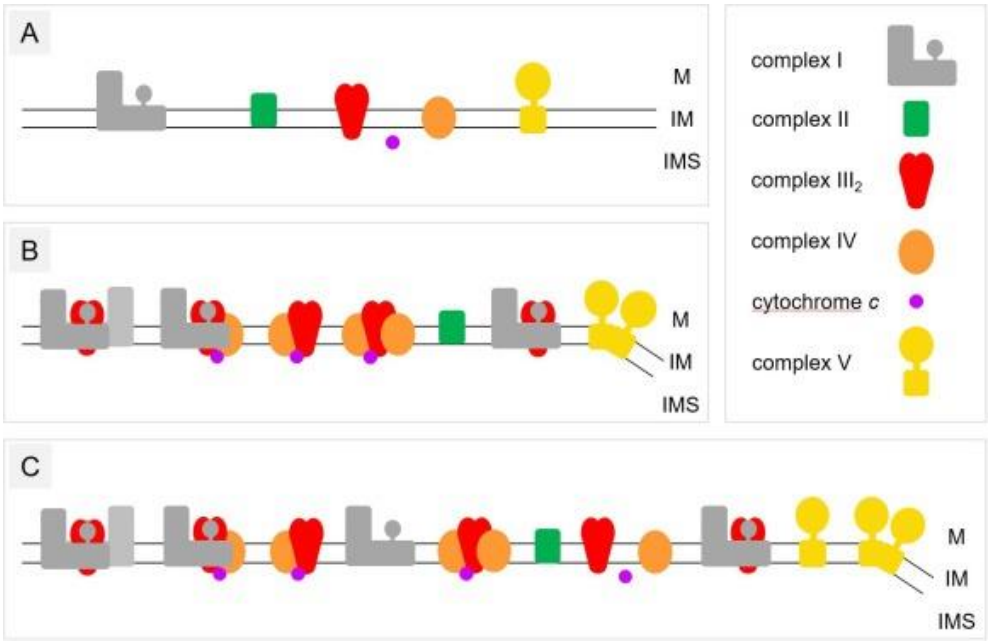

Figure 3.6. (A) Separate OXPHOS complexes, **(B)** different types of supercomplexes, and **(C)** coexistence of separate complexes and supercomplexes are shown. OXPHOS complexes are denoted as on the legend. The figure is reprinted from [93].

3.1.5.2. ATP synthase role in mitochondrial permeability transition pore (MPTP)

One of the unclear questions in biology is a so-called mitochondrial permeability transition pore (MPTP) – a *phenomenon* of opening of a non-selective mega-channel in the inner mitochondrial membrane (IMM) at sufficient Ca^{2+} concentrations leading to the IMM disruption, PMF dissipation and therefore to cell death. This *phenomenon* seems to be one of the most intriguing in mitochondria world and hypothetically may be very attractive for designing drugs targeting MPTP [104]–[107].

According to some of the works, a dimer of mtF_OF_1 appeared to have an ability of becoming a Ca^{2+}-dependent channel itself matching the PMTP parameters [96]. However, other authors show

that MPTP is independent on the mtF_OF_1 assembly [98]. The role of ATP synthase in formation of MPTP is discussed in literature at the moment of this writing [17], [18]. It is proposed that mtF_OF_1 in different ways might be involved in MPTP formation and suggestions that even c-ring itself might act as a leakage channel (Fig. 3.7) [16], [17], [97], [108]. However, until the structural information is not obtained all evidences are indirect and the question remains a matter of hypotheses and debates.

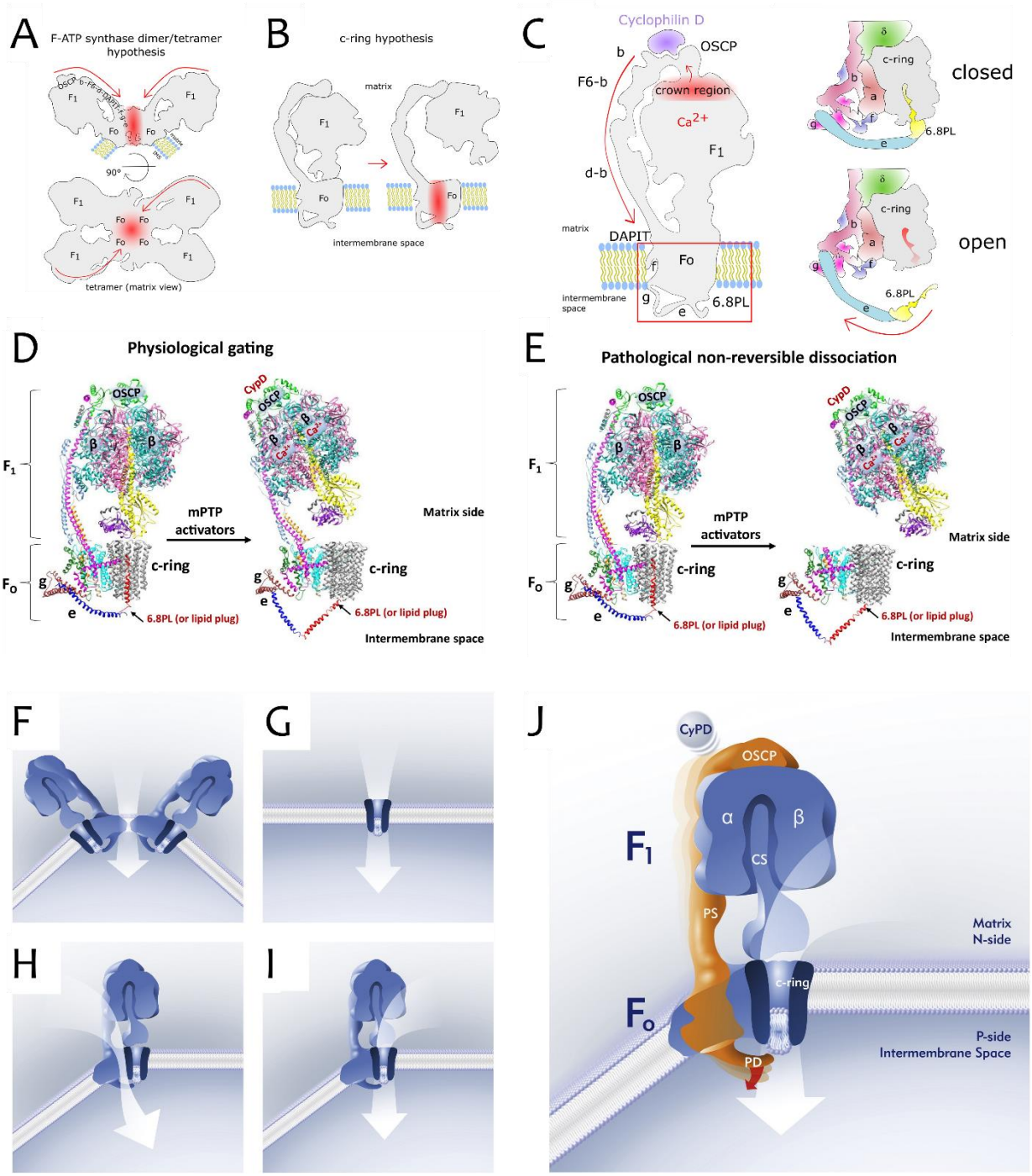

Figure 3.7. Different hypotheses of ATP synthase role in MPTP. **(A)** F-ATPase dimer/tetramer hypothesis suggests that MPTP is in the middle of F_O parts of mtF_OF_1 dimer or tetramer with

conformational changes of ATP synthases induced by Ca^{2+}; **(B)** C-ring hypothesis suggests the absence of c/γ interface with preserving only c/a interface and a c-ring acting as a pore induced by Ca^{2+}; **(C)** "Death finger" hypothesis suggests conformational changes induced by Ca^{2+} and amplified by cyclophilin D, displacement of 6.8PL and e subunits and dislocation of a lipid "plug" inside the c-ring and formation of a pore. A hypothesis of "bent-pull" model of mtF_OF_1 gating in **(D)** physiological and **(E)** pathological conditions suggest dislocation of c/γ interface and a lipid "plug" inside the c-ring with preservation of the assembled complex under physiological and dislocation of F_1 part in pathological conditions. Interfaces of potential formation of MPTP might be the following: **(F)** the F_O-F_O interface of mtF_OF_1 dimer; **(G)** a separate c-ring if removing a lipid "plug" inside it; **(H)** a half-channel near the c/a interface; **(I)** a c-ring in assembled mtF_OF_1 if removing a lipid "plug" inside it; **(J)** Another representation of a "death finger" hypothesis. Cyclophilin D and Ca^{2+} might induce conformational changes of the protein density near the lipid plug inside the c-ring. In this hypothesis c/γ interface is preserved and no significant conformational changes of F_1 part occur. Panels A-C were adapted from [17]; panels D, E were adapted from [97]; panels F-J were adapted from [16].

3.1.5.3. Towards the structure of human ATP synthase

The lack of the structural studies of human mtF_OF_1 might be due to difficult expression and purification procedures. The relevant protocols of obtaining human mtF_OF_1 are described by J. He *et al.* [109]. The work shows the steps of assembling of human mtF_OF_1 by manipulations with the genes encoding its subunits. The key intermediate c_8F_1,IF,OSCP,bdF_6 consisting of the subunits encoded in nuclear genome was shown to provide a template for ATP6 (a), ATP8 (8) subunits encoded in mitochondrial genome. Their association with mtF_OF_1 is additionally stabilized by 6.8PL subunit and at this point the mtF_OF_1 starts ATP synthesis. Finally, a dimerization process is initiated by the subunit DAPIT (k) (Fig. 3.8) [109].

However, the quantity of the protein purified with immuno-capture resin was not enough for structural studies, though it shed light on the mtF_OF_1 assembly processes. The large-scale expression and purification of human mtF_OF_1 are a cornerstone on the way of obtaining the high-resolution structure of human ATP synthase. One of the possible ways of purification might be obtaining ATP synthase assembled with another protein complex. The study [6] shows that the mtF_OF_1 in human neutrophils binds to a voltage-gated Ca^{2+} channel $Ca_v2.3$ and regulates its activity. Interestingly that a $Ca_v2.3$ was found in dopaminergic neurons and its disfunctions are connected with Parkinson's disease [110]. Also interesting fact that $Ca_v2.3$ is not so large membrane protein (~160kDa) in comparison with human mtF_OF_1 (~590kDa), which makes it

theoretically possible to recombinantly express $Ca_v2.3$ with, for example, a His-tag and try to purify it in a complex with the mtF_OF_1.

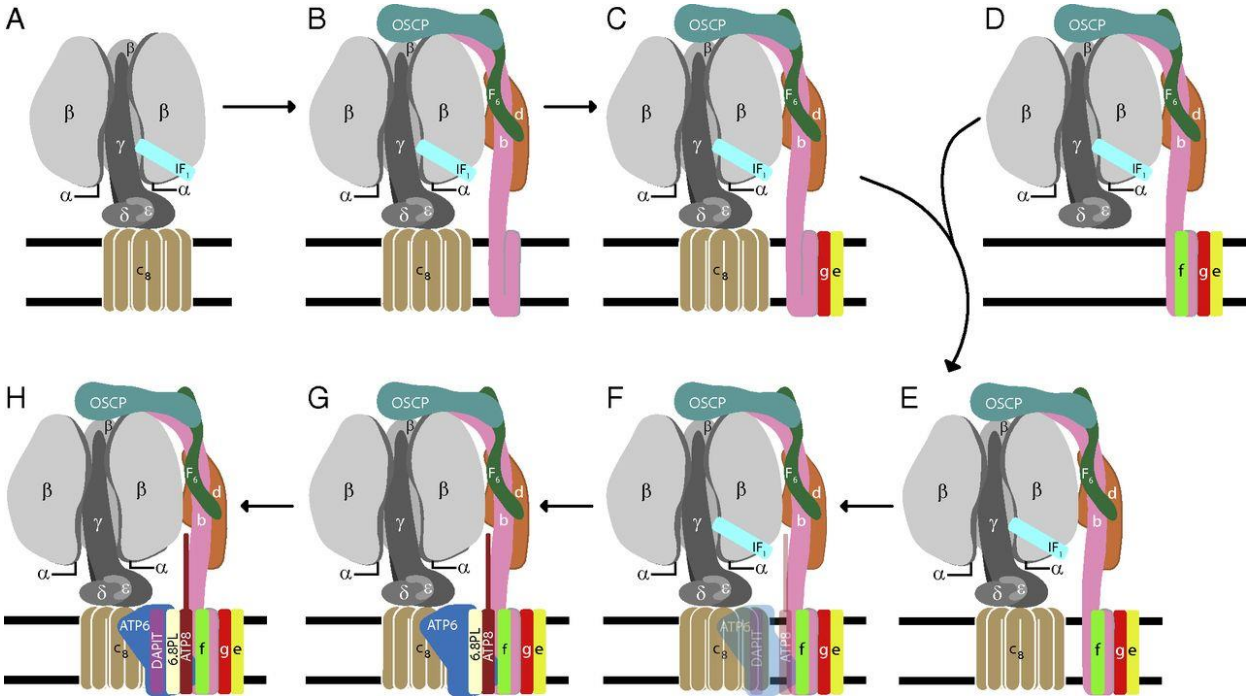

Figure 3.8. Steps of the assembly of human mtF_OF_1. ATP synthases with blocked genes encoding different subunits are shown. **(A)** w/o b or OSCP, **(B)** w/o e or g, **(C)** w/o f, **(D)** w/o c, **(E)** mtF_OF_1 from ρ^0 cells (without mtDNA), **(F)** w/o 6.8PL, **(G)** w/o DAPIT, **(H)** full mtF_OF_1 from WT cells. The figure is reprinted from [109].

Structural studies of ATP synthase will be not completed until the high-resolution structure of human mtF_OF_1 is resolved. This is one of the major future issues addressed to ATP synthase studies [10].

3.2. C-ring

One of the key parts of ATP synthase is a rotary part (c-ring). The c-ring is an assembly of protomers (c-subunits) from 8 to 17 copies [10]. Each protomer is a two-alpha helices hairpin with an inner and an outer alpha helix so that N and C termini are on the one side of the membrane. Two alpha helices of the protomer on the other side of the membrane are connected by a loop which also serves as a c-ring / γ subunit interface. An active center of a c-ring is in the middle of the outer alpha helix of each protomer. It also serves as a c-ring / a subunit interface. Amino acids of the active center as well as the loop of a protomer are strongly conserved. However, different species have a different number of protomers, therefore, H^+/ATP ratio and ATP synthesis rate – parameters that seem to be defined by bioenergetic needs of different organisms (see the section

Intersubunit contacts and c-ring stoichiometry). Recent structural studies of c-rings (as a separate protein or in context of assembled ATP synthases) revealed intriguing features about their role in the enzyme functionality, intersubunit interfaces and molecular mechanisms of transmembrane ion transport.

3.2.1. Available structural data

C-rings as well as ATP synthases have been studied by atomic-force microscopy, XRD and cryo-EM methods. There are much more structures of the c-rings than the full complexes, first, due to investigations where the full enzyme was used as a starting crystallization material but only c-ring crystals were obtained, second, due to the studies of separate c-rings, and third, obtained structures of full ATP synthases have also provided information about their c-rings. However, a c-ring is a membrane protein oligomer and its crystallization is challenging as well as obtaining a high-resolution structure (better than 3 Å) using cryo-EM method due to the limitations mentioned in the section *Cryo-EM experiments*. Therefore, the structural details of the neighborhood of protomer polypeptide chains remained vague, especially when concerning additional positive electron densities that were not associated with amino acids of the c-subunits, and were found in almost every available high-resolution structure of a c-ring from different species. In literature these densities were usually either associated with a lipid "plug" [23], [24], [111], or briefly discussed without paying attention to their nature due to the low resolution structures, or just omitted.

Fortunately, there are high-resolution structures which might shed light on these unusual features of the c-rings. High-resolution structures of different types of the c-rings are also required to understand deeply the nature of additional densities inside them.

3.2.1.1. H^+ c-rings

Proton type of the c-rings is the most investigated one at the moment. Thirteen studies resulted in more than 70 structures of high or near-high resolution (~3 – 3.5 Å or better) (Table 3.6). There are even more studies of c-rings, however, the structures do not have necessary resolution for the analysis of the additional densities.

Table 3.6. The structures of H^+ c-rings (separately or in context of ATP synthase) from different origins. "Cn" column describes the number of protomers in the corresponding c-rings. All structures are H^+ F-type c-rings and sorted by a year of publishing. The resolution is shown as a range in case of more than one PDB structure is in a publication. According to the context of this work, only high-resolution structures of the c-rings are considered.

№	Cn	Origin	Year	Method	Res.[Å]	PDB ID(s)
1	10	*Polytomella*	2019	Cryo-EM	2.9 – 3.2	6RDV; 6RDE; 6RE4; 6RE1; 6RE7; 6REU; 6RDP; 6REA; 6RDS; 6RDY; 6RED; 6RDJ; 6RDB; 6RDG; 6RDM; 6RER; 6RD9; 6RE2; 6RE3; 6RE5; 6RE6; 6RE0; 6RDX; 6RDW; 6RET; 6RES; 6REB; 6REC; 6RDC; 6RDI; 6RDH; 6REP; 6RDK; 6REF; 6REE; 6RDZ; 6RDR; 6RDL; 6RDU; 6RDT; 6RE9; 6RE8; 6RDO
2	10	*Bacillus PS3 (recombinant)*	2019	Cryo-EM	3.0 – 3.2	6N30; 6N2Z; 6N2Y
3	10	*Euglena gracilis*	2019	Cryo-EM	2.8 – 4.3	6TDU; 6TE0; 6TDY; 6TDZ
4	8	*Sus scrofa*	2019	Cryo-EM	3.3 – 6.2	6J5K; 6J5J; 6J5I
5	9	*Mycolicibacterium phlei*	2016	XRD	1.55 – 1.8	4V1F, 4V1G, 4V1H
6	10	*Saccharomyces cerevisiae*	2015	XRD	2.1 – 2.3	5BPS, 5BQ6, 5BQA, 5BQJ
7	13	*Bacillus pseudofirmus OF4*	2014	XRD	2.42 – 2.8	4CBJ, 4CBK
8	10	*Saccharomyces cerevisiae*	2012	XRD	1.9	4F4S
9	10	*Saccharomyces cerevisiae*	2012	XRD	2.0 – 2.5	3UD0, 3U2F, 3U2Y, 3U32
10	15	*Arthrospira platensis*	2010	XRD	1.84 – 3.0	2XQS, 2XQT, 2XQU
11	13	*Bacillus pseudofirmus OF4*	2010	XRD	2.5	2X2V
12	15	*Arthrospira platensis*	2009	XRD	2.13	2WIE

Except four recent studies in 2019 which showed the structures of complete mtF_OF_1 or bF_OF_1 and, therefore, their c-rings, other high-resolution structures have been obtained by XRD on protein crystals.

Every study revealed novel features of the c-rings. The structures of complete mtF_OF_1 dimers from *Polytomella* [56], *Euglena gracilis* [15], and *Sus scrofa* [13] discovered subunit arrangement and composition of novel types of H^+ mtF_OF_1 dimers and therefore, organization of interfaces between the c-ring and other subunits of mtF_OF_1 (see detailed description in sections *a/c interface*, *A secret inside* and *Diversity of stabilization mechanisms*).

The studies, which resulted in high-resolution structures of isolated c-rings, allowed one to determine molecular mechanisms of the ion-coordination active center and its inhibition with small-molecule ligands, and to analyze the nature of the contacts between neighbor protomers in different c-rings of bF_OF_1 and mtF_OF_1. The high-resolution structure of the c-ring of bF_OF_1 from *Mycolicibacterium phlei* showed molecular mechanisms of anti-tuberculosis drug BDQ binding to the c-ring active center Glu65 [87]; the structures of the yeast mtF_OF_1 c-ring with oligomycin A binding to its active center explained the effect of ATP synthesis inhibition [112] and (Mueller,

D.M., to be published) (PDB IDs: 5BPS, 5BQ6, 5BQA, 5BQJ); the structure of the c-ring of bF_OF_1 from *Bacillus pseudofirmus OF4* helped to understand the link between hidden structural adaptations and alkaliphile cell physiology [21]; the structures of the yeast mtF_OF_1 c-ring firstly showed "opened" state of the active center Glu59 [22]; the structures of the bF_OF_1 c-ring from *Arthrospira platensis* presented evidence supported a suggestion that rotation of the c-ring depends on the interplay between its ion-binding active centres and the nonhomogeneous environment in their neighbourhood [19], [113]; and the structure of the c-ring of bF_OF_1 from *Bacillus pseudofirmus OF4* reported a novel type of ion coordination in its active center [20].

3.2.1.2. Na+ c-rings

Besides a proton type of F-ATP synthases, several species among bacteria have a sodium type of bF_OF_1 (Fig. 3.9) [111], [114]–[117]. The mechanisms of transmembrane ion transfer remain the same with only remark that their c-ring active centers bind Na^+ instead of H^+, since they utilize Na^+ ion motif force $\Delta\mu(Na^+)$ instead of the PMF.

Structural studies revealed intriguing examples of c-rings. The first structure of the hybrid Na^+ F/V-type c-ring of ATP synthase from *Acetobacterium woodii* was obtained (2.1 Å) [116]. It showed a functional Na^+ heteromeric c-ring with nine protomers of F-type and one c-subunit of V-type. The stoichiometry $9_F/1_V$ is near to 11_F because a V-type c-subunit consists of five alpha helices, four of which form two hairpins with a pair of inner and outer alpha helices, and one alpha helix at the extension of the N terminus goes across the c-ring inner pore. It is also considered to be an evolutionary link between F- and V-type ATP synthases [116].

Other high-resolution structures were obtained for Na^+ c-rings of bF_OF_1 by XRD method (Table 3.7). The structures of the Na^+ bF_OF_1 c_{11}-ring from *Fusobacterium nucleatum* were obtained (2.2 – 2.6 Å) and revealed a new mode of ion coupling in ATP synthases [115]. Two studies obtained structures of the Na^+ bF_OF_1 c_{11}-ring from *Ilyobacter tartaricus* (2.35 and 2.4 Å, respectively) and showed a buried structural water molecule coordinated by Thr67 which is the only amino acid involved in ion coordination that distinguishes Na^+ from H^+ F-ATP synthases [111], [118].

Table 3.7. The high-resolution structures of Na^+ c-rings from different origins. "Cn" column describes the number of protomers in the corresponding c-rings. All structures are Na^+ F-type c-rings and sorted by a year of publishing. The resolution is shown as a range in case of more than one PDB structure is in a publication.

№	Cn	Origin	Year	Method	Resolution[Å]	PDB ID(s)
1	$9_F/1_V$	*Acetobacterium woodii* (F/V-type hybrid)	2014	XRD	2.1	4BEM
2	11	*Fusobacterium nucleatum*	2013	XRD	2.2 – 2.6	3ZK1; 3ZK2

3	11	*Ilyobacter tartaricus*	2009	XRD	2.35	2WGM
4	11	*Ilyobacter tartaricus*	2005	XRD	2.4	1YCE

All available structures show that the Na^+ c-rings have eleven protomers or similar geometry (11 inner and 11 outer alpha helices) with different stoichiometry, such as a hybrid $9_F/1_V$ c-rings. The difference between H^+ and Na^+ c-rings was found only in ion coordination for one amino acid Thr67. Therefore, a suggestion, that H^+ c-rings could evolve to Na^+ c-rings and sodium bioenergetics – to proton bioenergetics, was discussed in literature [111].

3.2.1.3. Crystallization

Experiments for obtaining high-resolution structures of c-rings using XRD method required growing crystals. According to the context of this work, crystallization experiments which resulted only in high-resolution structures (better than 3 Å) have been considered (Table 3.8). Comparison of protein purification protocols showed that either a c-ring was purified with 1-1.5% NLS at 45-68°C, or intact ATP synthase was used as a starting crystallization material. In case of recombinant expression of a c-ring in *E.coli*, a His-tag was added at the N terminus of a c-subunit with followed purification by Ni-NTA [115].

Table 3.8. Overview of the high-resolution (better than 3 Å) structures of separate c-rings obtained by XRD, their stoichiometry, experiment details and whether the complete ATP synthase was used as a starting crystallization material.

№	Origin, PDB ID(s)	Type	Cn	Cryst. Method	Starting cryst. material	Crystallization conditions
1	*Mycolicibacterium phlei* 4V1F, 4V1G, 4V1H	H^+	9	Vapor diffusion (hanging drops)	C-ring was purified with 1.5%NLS, 60°C	The protein was diluted 1:1 with 20 mM tris-HCl (pH 8.0) and 4% (w/v) OG. For cocrystallization, 0.35 mM BDQ was added to the protein solution; 1µL of the protein solution was then mixed with 0.5 mL of 28-30% PEG600 [87].
2	*S. cerevisiae* 5BPS, 5BQ6, 5BQA, 5BQJ	H^+	10	Vapor diffusion (sitting drop)	Intact ATP synthase	pH 7.5; 68% MPD, 8% propylene glycol, 0.3M NaCl, 2 mM $MgSO_4$, 50 mM MES, pH 5.5; 298K (Mueller, D.M., to be published)
3	*S. cerevisiae* 4F4S	H^+	10	Vapor diffusion (sitting drop)	Intact ATP synthase	pH 5.5; 68% MPD, 8% propylene glycol, 0.3 M NaCl, 2 mM $MgSO_4$, 50 mM MES, pH 5.5; 298K [112].
4	*S. cerevisiae* 3UD0, 3U2F, 3U2Y, 3U32	H^+	10	Vapor diffusion (sitting drop)	Intact ATP synthase	68% MPD, 8% propylene glycol, 0.3M NaCl, 0.1M malonate pH 7.0, 2 mM $MgSO_4$, 50 mM MES pH 5.5; 294K. Soaking: 68% MPD, 8% 8% propylene glycol, 0.4M NaCl, 2 mM $MgCl_2$, 50 mM MES pH 5.5, 12 h at 294K [22].

5	*Bacillus pseudo-firmus OF4* 4CBJ, 4CBK	H^+	13	Vapor diffusion (hanging drops)	C-ring was purified with 1%NLS, 45°C	0.5µL of c_{13} ring (2.5 mg/mL) was supplied with 0.5% TDM and mixed with 0.25µL of 0.1 M Tris/HCl pH 9.0, 20% (v/v) PEG 400 [21].
6	*Bacillus pseudo-firmus OF4* 2X2V	H^+	13	Vapor diffusion (hanging drops)	C-ring was purified with 1%NLS, 65°C	The c-ring sample was supplied with 1% (w/v) of UDM and mixed with 0.1 M sodium acetate, pH 4.3 and 20% PEG 400 (v/v). Before flash-freezing in liquid nitrogen, the rod-shaped clear crystals were transferred for 2 min into 30% PEG 400 (v/v), 0.1 M sodium acetate pH 4.5, and 0.05% DM (w/v) [20].
7	*Arthro-spira platensis* 2XQS, 2XQT, 2XQU	H^+	15	Vapor diffusion (hanging drops)	C-ring was purified with 1%NLS, 65°C	The c-ring 1 mg/mL was mixed with DGDG from wheat at a lipid-to-protein ratio of 0.4 (w/w) to yield OG concentration of 0.6%. Bipyramidal crystals with dimensions 100 × 50 × 50 µm^3 grew within 3–5 d upon mixing the protein sample (1.8 mg/mL) in 2.5% (w/v) CYMAL-4– containing solution (in water) with crystallization buffer (10% (v/v) PEG 600, 350 mM Li_2SO_4, in 0.1 M sodium acetate buffer, pH 4.3). Before flash-freezing in liquid nitrogen, the crystals were transferred for 1 min into the same buffer but containing 35% (v/v) PEG 600 [19].
8	*Arthro-spira platensis* 2WIE	H^+	15	Vapor diffusion (hanging drops)	C-ring was purified with 1%NLS, 65°C [119]	Bipyramidal crystals with dimensions 100 × 50 × 50 µm^3 grew within 3–5 d, upon mixing the protein sample (1.8 mg/mL) in 2.5% (w/v) CYMAL-4– containing solution (in water) with crystallization buffer (10% (v/v) PEG 600, 350 mM Li_2SO_4, in 0.1 M sodium acetate buffer, pH 4.3). Before flash-freezing in liquid nitrogen, the crystals were transferred for 1 min into the same buffer but containing 35% (v/v) PEG 600 [113].
9	*Aceto-bacterium woodii* (F/V-type hybrid) 4BEM	Na^+	9_F/ 1_V	Vapor diffusion (hanging drops)	C-ring was purified with 1%NLS 1 hat RT, then 10 min at 68°C	Before crystallization, 3% (w/v) n-heptyl-β-D-thioglucopyranoside was added to the c-ring (4 mg/mL) and incubated ON at RT, followed by a 10-min incubation at 60 °C and 1 hat RT. The protein was mixed 1:1 with 100 mM sodium acetate, pH 4.5; 9% (v/v) PEG 400; 20 mM $MnCl_2$ and crystallization was done in a 24-well plate with 500 µL reservoir (100 mM sodium acetate, pH 4.5; 9% (v/v) PEG 400) at 12 °C in 4 days. After the crystals reached their final size, the PEG 400 concentration was gradually increased from 9 to 40% (v/v) within 48 h and the crystals were flash frozen in liquid nitrogen [116].
10	*Fuso-bacterium nucleatum* 3ZK1, 3ZK2	Na^+	11	Vapor diffusion (hanging drops)	Recom-binant c-ring from *E.coli* with a His-tag at	2 mg/mL of c-ring and 2% (w/v) DM was mixed with either crystallization buffer 1 (0.1M NaAc pH 4.5, 28% (v/v) PEG 300), or buffer 2 (0.1 M CHES pH 9.6 (NaOH), 27.5% (v/v) PEG 300, 5 mM $MgCl_2$). Crystals grew within one week to a size of ~100×40×40 µm^3. After three (buffer

					the N-terminus	1) or four months (buffer 2) of incubation at 18°C, crystals were fished and flash-frozen in liquid nitrogen [115].
11	*Ilyobacter tartaricus* 1YCE	Na^+	11	Vapor diffusion (hanging drops)	C-ring was purified with NLS	The purified c-ring was dialyzed against 10 mM Tris/HCl (pH 8.0) to precipitate the protein by removal of the detergent. The material was collected by centrifugation and dissolved at 10 mg protein/mL in dialysis buffer containing 0.02% (w/v) NaN_3 and 0.78% (w/v) Zwittergent 3-12. Crystals were grown within 2-3 days at 17°C to a size of approximately 400 x 100 x 100 μm^3. A drop consisted of 1 µL protein solution (passed through a 0.22 µm sterile filter) and 1 µL 15% (v/v) PEG 400 in 0.1 M sodium acetate, pH 4.5. The crystals were flash-frozen in liquid nitrogen after an equilibration for 24 h with 30% (v/v) PEG 400 as cryo-protectant in the reservoir buffer at 17°C [118].
12	*Ilyobacter tartaricus* 2WGM	Na^+	11	N/A	N/A	Reanalyzed data [111] of PDB ID:1YCE [118].

Crystallization of proteins significantly depends on the pre-history of sample preparation. The stability of the c-ring allowed mixing of purified protein (1-4 mg/mL) with 0.5 – 3% (w/v) detergents, such as DM, UDM, DDM, TDM, Zwittergent 3-12, CYMAL-4, OG and n-heptyl-β-D-thioglucopyranoside; and its thermostability allowed heating up to 45-68 °C. Similar concentrations of detergents are usually used for solubilization of membrane proteins from cellular or organellar membranes where the ratio of detergent molecules to target membrane proteins is significantly lower, and heating to high temperatures with such detergent concentrations lays far beyond the stability region of most other membrane or water soluble proteins. However, considering investigations of interfaces between a c-ring and other ATP synthase subunits, and additional electron densities inside the c-ring, this is crucial to purify c-rings with as mild as possible temperature and detergents. The problem of unsatisfied resolution of the c-ring inside might be in overpurification of samples and substitution of intact molecules inside the c-ring with detergents.

3.2.2 Intersubunit contacts

3.2.2.1 a/c interface

Most of the high-resolution structures of c-rings proposed molecular mechanisms of transmembrane proton transfer via the a/c interface. The structures of near-high resolution of F_O part of ATP synthases showed two half-channels formed by invagination of the lipid membrane caused by alpha helices of a-subunit, which lie parallel to the membrane plane (Fig. 3.9A, E) [11], [13].

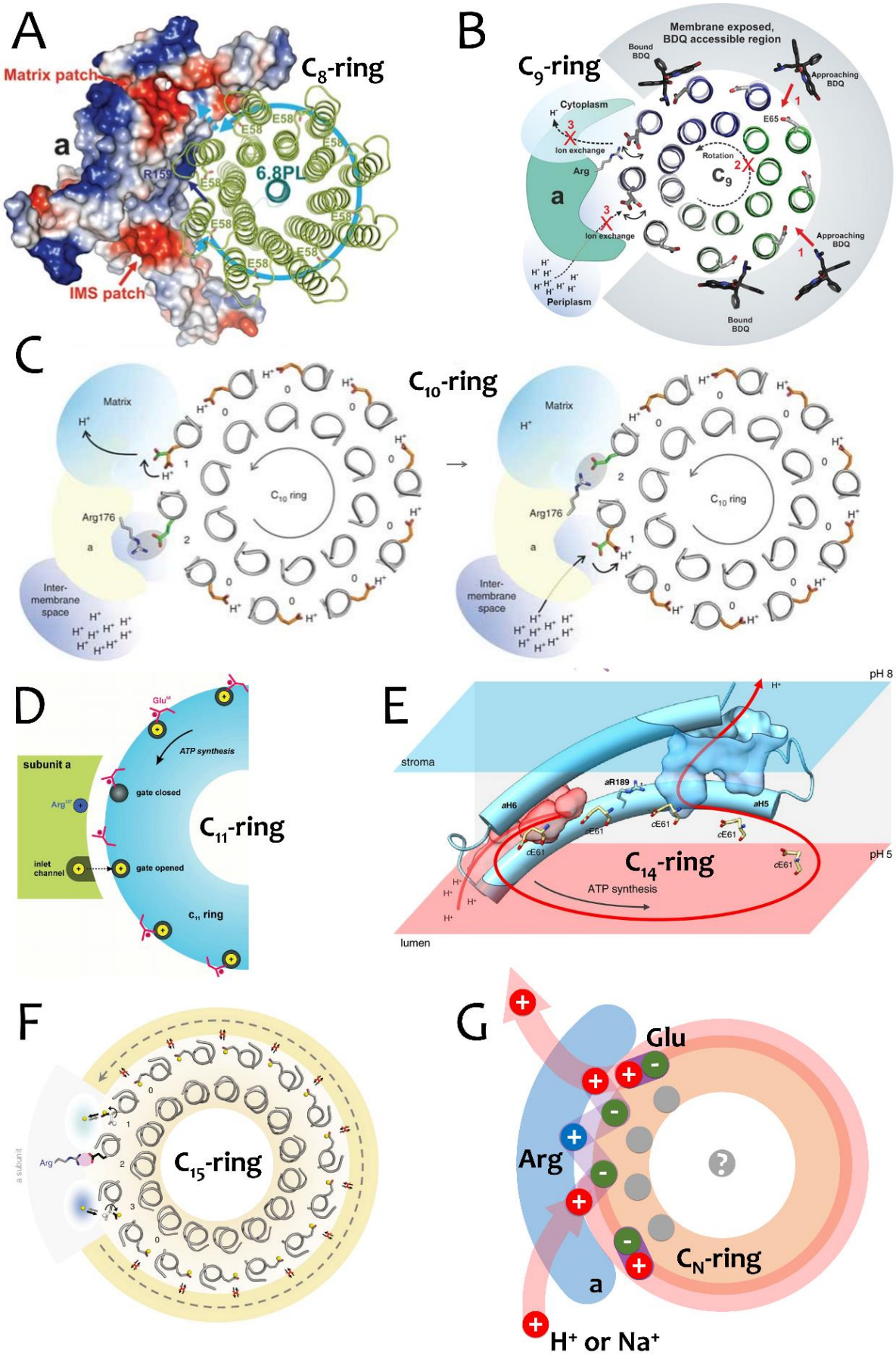

Figure 3.9. Schematic representations of a/c interfaces. **(A)** a/c_8 interface of H^+ mtF_OF_1 tetramer from *Sus scrofa*; **(B)** a/c_9 interface of H^+ bF_OF_1 from *Mycolicibacterium phlei*; **(C)** a/c_{10} interface

of H^+ mtF_OF_1 from *Saccharomyces cerevisiae*; **(D)** a/c_{11} interface of Na^+ bF_OF_1 from *Ilyobacter tartaricus*; **(E)** a/c_{14} interface of H^+ cF_OF_1 from *Spinacia oleracea*; **(F)** a/c_{15} interface of H^+ bF_OF_1 from *Arthrospira platensis*; and **(G)** a general representation of a/c_N interface of H^+ or Na^+ ATP synthase (Glu of the c-ring active center are colored green, Arg of the subunit a is colored blue, H^+ or Na^+ ions are colored red, other amino acids are colored gray showing the inner alpha helices of the c-ring, in the middle of the c-ring a "plug" of unidentified nature is colored gray with the question mark, electrostatic interactions and ions pathway are shown in shades of semitransparent purple and pink, respectively). Panels A-F were adapted from [11], [13], [22], [87], [113], [118], respectively.

Thus, cations (H^+ or Na^+) access a/c interface via the first half-channel and interact with the negatively charged amino acid Glu – an active center of protomers ("opened" state), making it neutrally charged ("closed" state). Then, ion carrying protomer turns until the other half-channel is reached. The a-subunit has a positively charged Arg in between of the half-channels. It acts as an uncoupler of Glu^- and ion^+ and release the cation via the second half-channel. At the next quantum of rotation (1/N of a turnover, where N – the number of protomers in a c-ring) the Glu^- is again in the first half-channel where another cation interacts with it, and further along the cycle (Fig 3.9G). This mechanism was found to be the same in different types of c-rings with different stoichiometry and might be ubiquitous among all species which have ATP synthases (Fig. 3.9).

3.2.2.2. c_1/c_1 interface

Another open question about c-rings is about the contacts between neighbor protomers (c_1/c_1 interface) and how they determine a c-ring stoichiometry. The possibility of engineering of c-ring stoichiometry was demonstrated for Na^+ c_{11}-ring from *Ilyobacter tartaricus* [30]. It was suggested that the number of c_1 copies depends on contacts between neighbor protomers, which are determined by specific motifs in c_1-subunit amino acid sequence. In particular, three interlaced conserved G(A,S)xxxG(A,S) motifs in the middle of an inner alpha helix allow close packing of two alpha helices (Fig. 3.10). C-rings with mutations G→A in these motifs demonstrated different stoichiometry with assembled c-rings with 12,13 and 14 protomers in context of ATP synthase and persisted its functionality, although correspondingly changed Na^+/ATP ratio.

Unfortunately, due to the lack of resolution, the molecular details of c_1/c_1 interface were not shown. Molecular dynamics was used to predict a net of hydrogen bindings coordinated by residues of the G(A,S)xxxG(A,S) motifs, however, it was not fully complete. These bindings are defined directly by an amino acid sequence of c_1 and form N c_1/c_1 interfaces which determine the stoichiometry of a c_N-ring [30].

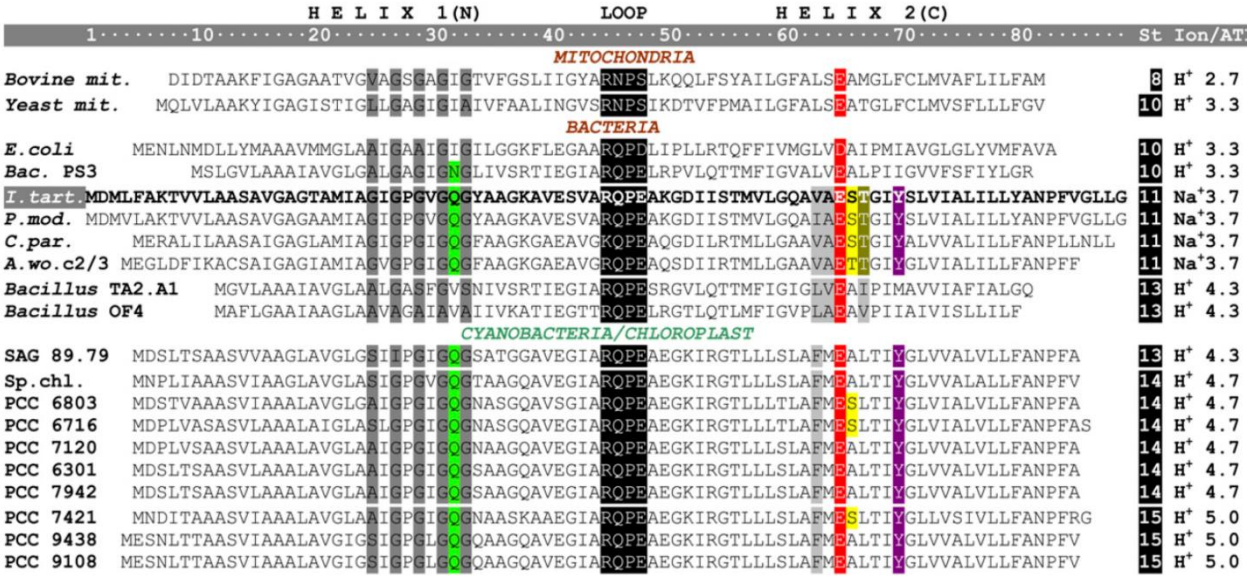

Figure 3.10. Phylogenetic analysis of c-subunit sequences of mtF_OF_1, bF_OF_1 and cF_OF_1 from different species. Numbering of amino acids is according to *Ilyobacter tartaricus* (highlighted). Alignment was done on the highly conserved loop connecting two alpha helices of a c_1-subunit (colored black). The active centers of c-rings Glu (E) are colored red. Conserved motifs G(A,S)xxxG(A,S) are colored dark gray and the Na^+ coordinating motif (Gln32, Val63, Glu65, Ser66, Thr67, Tyr70) is colored (green, light gray, red, yellow, brown, magenta) according to [50]. C-ring stoichiometry, a type of c-ring (H^+ or Na^+) and Ion^+/ATP ratio are shown on the right. The figure is reprinted from [30].

3.2.3. C-ring stoichiometry

The literature shows that a number of c-subunits and even a type of c-ring (H^+ or Na^+) in bacteria is not so conserved as a monomeric state of bF_OF_1, in contrary to eukaryotes, where only H^+ F-ATP synthases were found, the c-ring stoichiometry seems to be even more conserved than a type of mtF_OF_1 dimers. Interestingly, all available Na^+ c-rings of bF_OF_1 found in distinct bacteria lineages (Firmicutes phylum of Terrabacteria group and Fusobacteria phylum) have 11 protomers. According to available data a phylogenetic tree shows a variability of c-ring stoichiometries at different levels, groups and subgroups (Fig. 3.11). Considering what is known, in Eukaryota superkingdom species have 8 or 10 protomers of corresponding c-rings of mtF_OF_1, and 14 protomers of c-rings of cF_OF_1 if they have chloroplasts. Actually, all representatives of eukaryotes with available information on c-ring stoichiometry were found to have 10 protomers of mtF_OF_1 c-rings except the species from Metazoa kingdom: *Sus scrofa* and *Bos taurus*, which have 8 protomers. However, there are only two species with the available information for such a large group, as well as in the other groups in Eukaryota and Bacteria superkingdoms (only one or several representatives per group are investigated) and there are fourteen groups in Eukaryota and eighteen

groups in Bacteria superkingdoms with no available data on c-ring stoichiometry of their representatives at all.

Despite the variability in different species, the c-ring stoichiometry was found to be independent of different surrounding factors: the carbon source, pH of medium, host protein expression or its membrane composition, or ATP synthesis rate [120]–[123]. The c-rings experimentally obtained without one or several protomers did not form c-rings with other stoichiometries, but remained as unclosed circles [124]. Thus, a variability of c-ring stoichiometry in terms of phylogenetic analysis does not mean a variability for intact c-rings in exact specie, though it was shown that functional ATP synthases could be produced with different c-ring stoichiometries and even with a c-ring from different species (hybrid ATP synthases) [30], [125].

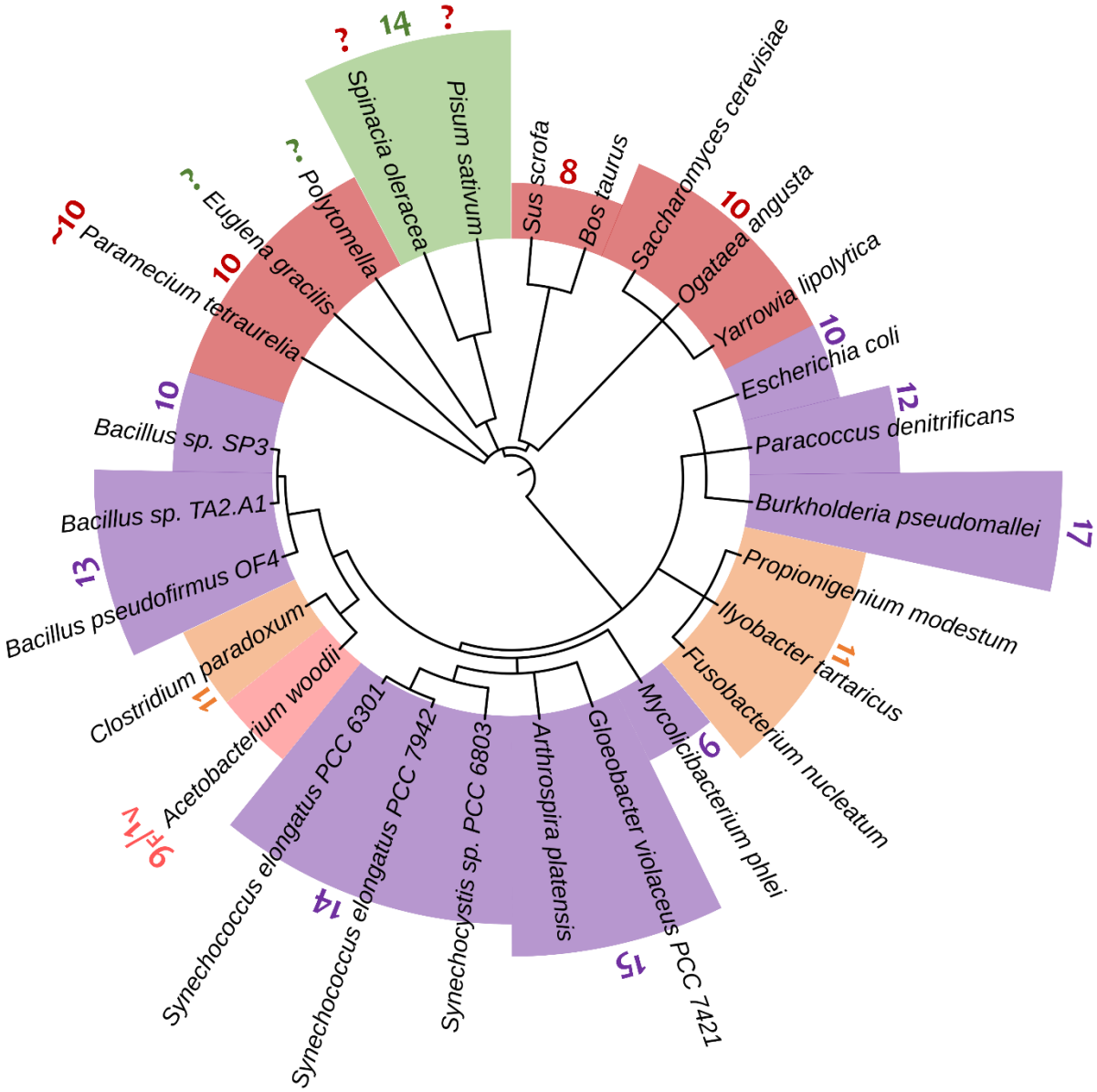

Figure 3.11. A phylogenetic tree of different species with available number of c-subunit copies in corresponding ATP synthases. A circled histogram shows the numbers of the copies. Eukaryotes

with available data of corresponding H^+ mtF_OF_1 are colored red, and H^+ cF_OF_1 – green; bacteria with corresponding H^+ bF_OF_1 are colored purple, and Na^+ bF_OF_1 – orange. *Acetobacterium woodii* is colored pink because it has a Na^+ c-ring of a hybrid F/V type with a stoichiometry of $9_F/1_V$, though the form factor of this c-ring is similar to a c-ring with 11_F protomers [116]. The c-ring stoichiometry of mtF_OF_1 from *Paramecium tetraurelia* was suggested based on the schematic picture showing the possible fit of the cryo-EM data with the PDB structure of the yeast c_{10}-ring [14] and marked correspondingly as "~10". Red and green question marks indicate unknown stoichiometry of mtF_OF_1 and cF_OF_1 c-rings for corresponding species, respectively. Information about the stoichiometries of *Bacillus SP3* and *TA2.1*, *Clostrudium paradoxum*, *Synechococcus elongatus PCC 6301* and *7942*, *Synechocystis PCC 6803*, *Gloeobacter violaceus PCC 7421*, *Fusobacterium nucleatum* and *Propionigenium modestum* was taken from [126]; for other species – from corresponding available PDB structures.

The lack of the structural information makes it difficult to more deeply understand some important details and the role of ATP synthases and, in particular, c-rings in bioenergetics of cellular organisms. The authors of structural studies were focused on tackling the enigma about a/c interface and molecular mechanisms of the transmembrane ion transfer; c_1/c_1 interface was partially investigated with biochemical methods and molecular modeling. What was even more hidden and less investigated is an inner pore of a c-ring. Though there was almost no structural works discussing the problem, available data revealed several unusual features that might be universal among all species that have ATP synthases.

3.2.4. A mystery inside

An enigmatic question of what is inside of a c-ring central pore was not sufficiently investigated due to low resolution of c-ring structures. Though it was shortly discussed in literature, there were hypotheses suggested the lipidic [23], [24], [111] or protein [127] nature of a "plug" inside the c-ring.

However, the first inconsistency occurred when investigating c-rings of cF_OF_1 from spinach chloroplasts. Structural studies reported additional electron densities inside the c-ring (Fig. 3.12A, B) [27], however, did not pay attention to the *phenomenon*. Yellow or green color of the protein crystals was associated with pigments naturally included into the thylakoid membranes (chlorophyll *a* and beta-carotene) [25], [29] (Fig. 3.12C-F).

Pigment analysis of the crystals, made by B. Varco-Merth *et al*. [25], showed that chlorophyll *a* and beta-carotene are clearly observed by UV-Vis spectroscopy and reverse-phase HPLC analysis (Fig. 3.12H, I). Unfortunately, due to the absence of the structure the question of the exact place

of the pigments remained open. The purification trials that were performed by the authors showed that the pigmentation occurred even after the treatment of purified ATP synthase at harsh detergent and temperature conditions (1%NLS, 65°C). SDS PAGE showed that only dissociation of the c_{14}-ring to separate protomers (c_1) led to discoloration of the sample. This was an indirect biochemical evidence that pigment molecules are tightly binding to the c_{14}-ring of spinach chloroplasts and, possibly, they might be inside the c-ring.

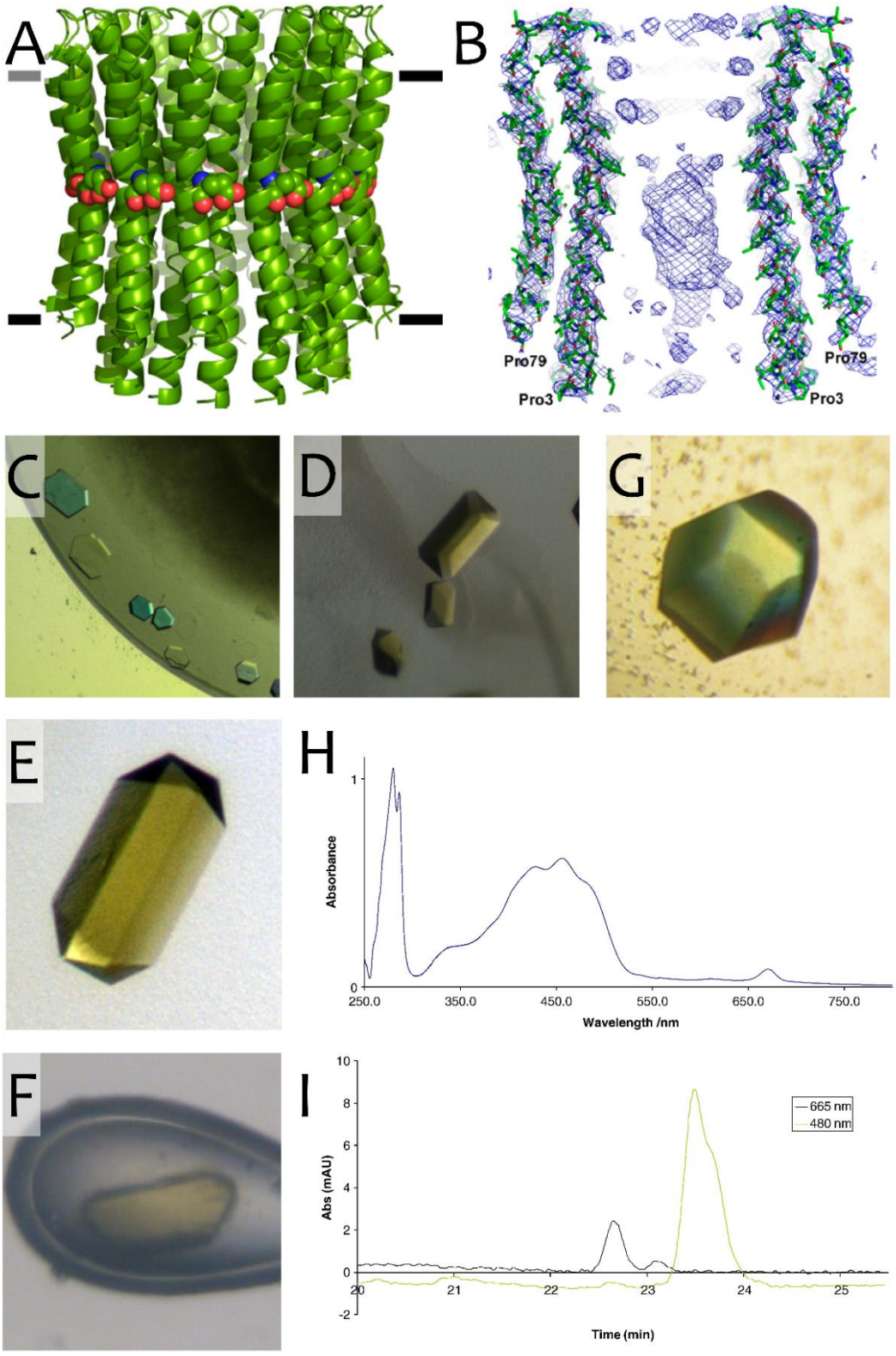

Figure 3.12. (A) The profile of the c_{14}-ring from spinach chloroplasts and **(B)** additional electron densities in the inner pore. A gallery of c_{14}-ring crystals, obtained by **(C - F)** B. Varco-Merth *et al*. [25] and **(G)** Balakrishna *et al.* [29]. **(H)** UV-Vis spectra of dissolved c_{14}-ring crystals and **(I)** reversed-phase HPLC diagram at 480 nm (beta-carotene) and 665 nm (chlorophyll *a*). Panels A, B were adapted from [27]; panels C – F and H, I were adapted from [25] with permission from Elsevier; panel G was adapted from [29].

Pigment molecules such as chlorophyll *a* and beta-carotene are very specific due to their commonality only in plants and cyanobacteria. However, other structural studies with bacterial and mitochondrial c-rings and ATP synthases from different organisms also revealed either additional electron densities in the inside of c-rings or even additional structural details of c-rings themselves [12], [13]. Pigments were not as much ubiquitous as to describe the presence of them in membranes of so distinct species.

Thus, the question of what stabilizes the c-ring of cF_OF_1 in plants was only partially answered with indirect experimental biochemical evidence. No structures with high resolution (better than 3 Å) was available for cF_OF_1 from spinach or other plants, therefore, without structural evidence one could not determine what type of interactions is between pigments and the c-ring.

Another important question was the composition of small molecules inside the cF_OF_1 c-ring. The presence of chlorophyll *a* and beta-carotene did not exclude other compounds that are also natural in thylakoid membranes. The possibility that chlorophyll *a* and beta-carotene might be cofactors of ATP synthase was attracting, however, was not ubiquitous for other species but those with chloroplasts or cyanobacteria. One more possibility is a protein “plug” inside the c-ring [127], however, a-subunit is unlikely to act as a plug in active functional state of the cF_OF_1 due to its role in maintaining membrane invaginations that create half-channels necessary for transmembrane ion transport.

3.2.5. Diversity of interface context

Considering different arrangement of mtF_OF_1 dimers (four types) that were discovered recently, one could notice that c-rings in these mtF_OF_1 have significantly different context of interfaces with other subunits (Fig. 3.13). For each type of mtF_OF_1 dimer there is one or several representatives with available structural data directly showing or prompting the context of these interfaces.

The mtF_OF_1 dimers of type I (Opisthokonta supergroup) were found to have a 6.8PL subunit inside their c-rings [13]. The 6.8PL subunit interacts with a subunit e in F_O part forming an anchor-like or a hook-like structure. The c/6.8PL interface remained hidden, however, the fact that alpha helices could be inside a c-ring is unusual because it rotates in the membrane with a frequency of

~350 Hz, thus its interactions with an alpha helix attached to stable non-rotating F_O part via an e-subunit arise a lot of questions. The first is about function of 6.8PL, either it leads to inhibition of c-ring rotation, or, *vice versa*, stabilizes a c-ring. The second is about c/6.8PL interface for the both cases because there should be compounds in between of an alpha helix and a c-ring and it hardly coincides with usual lipids.

The mtF_OF_1 dimers of type II (Viridiplantae kingdom) were found to have a large peripheral stalk for each monomer consisting of 10 subunits ASA(1-10) which form a dimerization interface in F_O and in F_1 parts [12]. A c-ring has interfaces with a and γ subunits, but the question of what is inside a c-ring is still open.

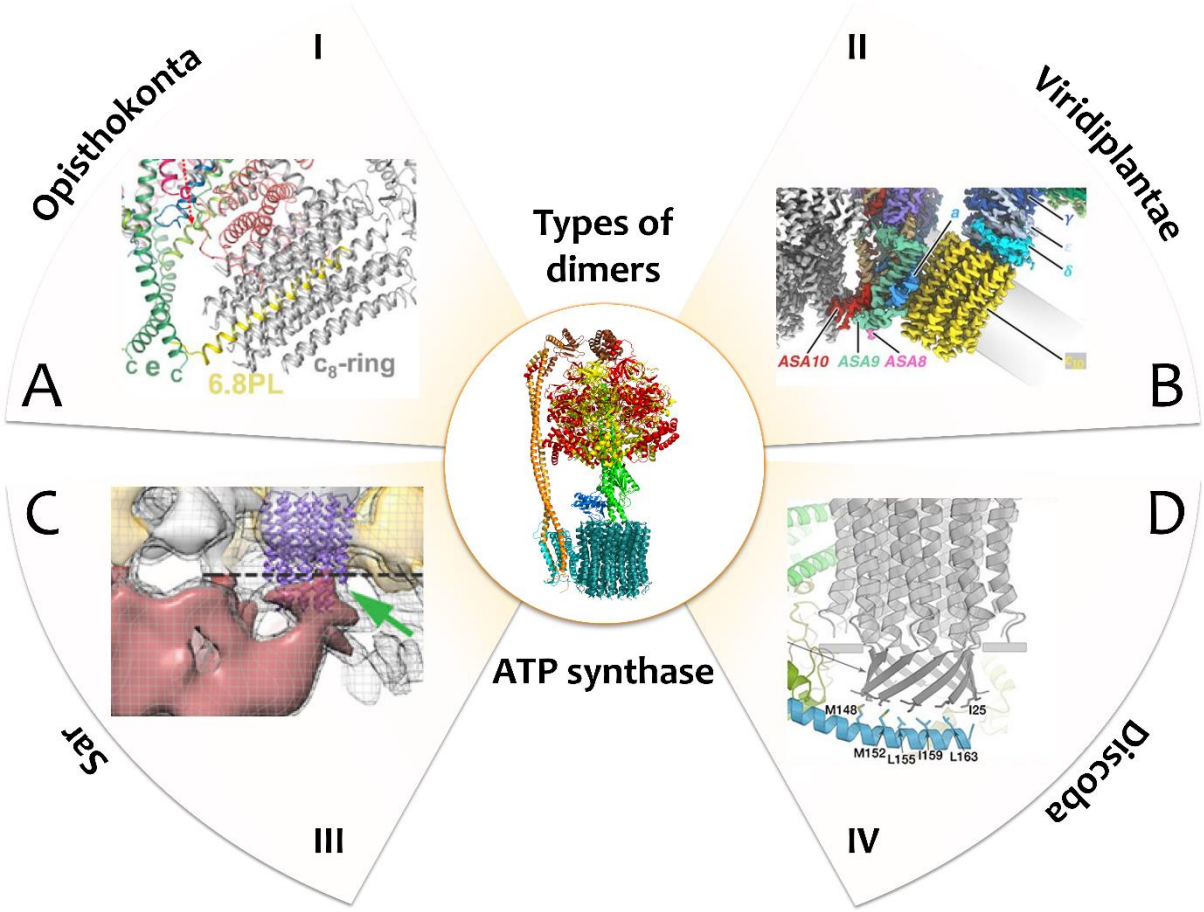

Figure 3.13. Four types of mtF_OF_1 dimers with a corresponding c-ring interface context. **(A)** Type I of mtF_OF_1 dimer has a c/PL6.8 interface, PL6.8 is attached to e-subunit, also there are c/a and c/γ interfaces. **(B)** Type II of mtF_OF_1 dimer has a large peripheral stalk forming F_O/F_O and F_1/F_1 dimerization interfaces, for a c-ring there are only c/a and c/γ interfaces. **(C)** Type III of mtF_OF_1 dimer has an unusually large U-shaped anchor-like density near a c-ring, a c-ring interface context remains unclear due to low resolution. **(D)** Type IV of mtF_OF_1 dimer has a β-barrel as an N-terminus extension of a c-ring. An c/ATPEG-1 interface is sliding contacts between the β-barrel and ATPEG-1 subunit [15]. A structure of an ATP synthase in the middle is taken from PDB (6FKF)

[11]. Panel A was adapted from [13]; panel B was adapted from [12]; panel C was adapted from [14]; panel D was adapted from [15].

The mtF_OF_1 dimers of type III (Sar supergroup) are less investigated, however, were found to have an anchor-like U-shaped density in F_O part that comes to c-ring similarly to that in type I dimers, but is significantly larger [14]. The context of interfaces between a c-ring and other ATP synthase subunits as well as the inner side of a c-ring remain hidden due to low structure resolution.

The mtF_OF_1 dimers of type IV (Discoba supergroup) were found to have a β-barrel as an N-terminus extension of a c-ring [15]. ATPEG-1 subunit comes close to a c-ring and forms an interface with sliding contacts between the β-barrel of a c-ring and ATPEG-1 subunit. Besides, there are c/a and c/γ interfaces. The question of what is inside a c-ring is unclear also due to the fact that there should be molecules with much longer tails to fit the length of a hydrophobic c-ring inner part. Typical lipids do not fit the length; therefore, a specific composition of a "plug" cannot be excluded.

3.3. Summary of knowledge

In the context of the relevant studies, it became possible to understand the importance of stabilization mechanisms of such a complex molecular machine as ATP synthase. Being widely spread in different species, it occurred to be unexpectedly variable in subunit composition, type of dimers and realization of c-ring interfaces context; at the same time, it remained highly conserved in particular details such as a loop connecting two alpha helices of a c-ring protomer, active centers of c and α/β subunits, amino acids of a-subunit responsible for transmembrane ion transfer, etc.

The mechanisms of transmembrane ion transfer are still open questions; why a cation goes such a difficult pathway through half-channels and rotates a c-ring, which is itself a large protein complex (~100 kDa). What is inside a c-ring that blocks an ion transfer through a huge pore (~20-30 Å)? In case of type I mtF_OF_1 dimers an alpha helix was found to be inside a c-ring, however, what is in between of this alpha helix and the Van-der-Waals inner surface of a c-ring? What is the interface of intersubunit interaction?

One more question of special cofactors stabilizing a c-ring is also open. The evidences, that were proposed before, suggested pigments (chlorophyll *a* and beta-carotene) as small molecule cofactors of spinach cF_OF_1. However, pigments are not universal among all other species but those with chloroplasts or cyanobacteria. Available structural data of high resolution (better than 3 Å) were only for bacterial and mitochondrial c-rings. Another "gap" in the knowledge was the c_1/c_1 interface. The role of G(A,S)xxxG(A,S) interlacing motifs in determination of the stoichiometry

of c-rings was theoretically predicted, however there was no direct experimental evidence for the c-ring from spinach chloroplasts.

Another question of oligomeric state of the ATP synthase in chloroplasts is also debated in literature. Do oligomers of ATP synthase that can occur in the thylakoid membranes have a physiological meaning and how they change (if they do) their functional role? Are there additional subunits responsible for oligomers formation and how the structure of ATP synthase changes during aggregation processes? All these questions are issues of future studies.

4. Materials and Methods

4.1. Materials

4.1.1. Organisms

In this work *E. coli* cells of TOP10, BL21, C41 strains (described in Table 4.1) were used for recombinant expression of c_1-subunit from spinach chloroplasts.

Table 4.1. Organisms that were used in this work.

№	**Origin, strain**	**Genotype**	**Source**
1	Escherichia coli TOP10	F- mcrA Δ(mrr-hsdRMS-mcrBC) φ80lacZΔM15 ΔlacX74 nupG recA1 araD139 Δ(ara-leu)7697 galE15 galK16 rpsL(StrR) endA1 λ-	Invitrogen
2	Escherichia coli BL21 (DE3)	fhuA2 [lon] ompT gal (λ DE3) [dcm] ΔhsdS λ DE3 = λ sBamHIo ΔEcoRI-B int::(lacI::PlacUV5::T7 gene1) i21 Δnin5	New England BioLabs
3	Escherichia coli C41 (DE3)	F - ompT gal dcm hsdSB (rB- mB-) (DE3)	Lucigen

4.1.2. Vectors

Vectors pBKT7 and pEKT7R were used in this work (Fig. 4.1). The vectors contain Kan/neoR gene and among main features pEKT7R has a repressor lacI for preventing promotor leakage.

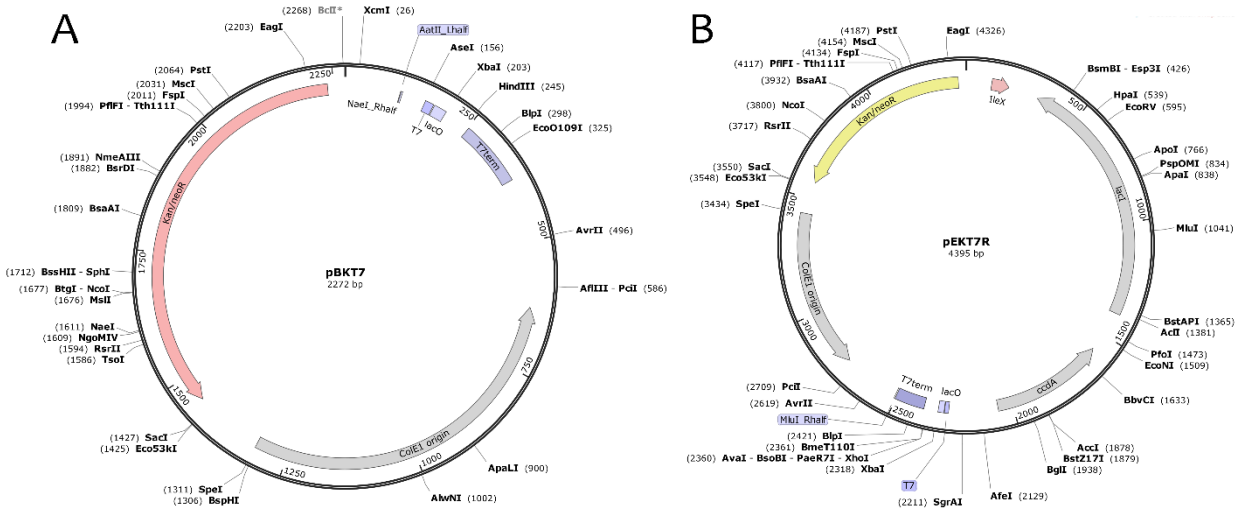

Figure 4.1. Maps of vectors **(A)** pBKT7 and **(B)** pEKT7R used in this work. The maps are generated by SnapGene® program.

4.1.3. Genes and oligonucleotides

The construct for recombinant expression was based on the gene AtpH, which encodes a c_1-subunit from spinach chloroplasts. A construct H8_Tr_AtpH* contains a His8-tag for purification with Ni-NTA and thrombin cleavage site (Fig. 4.2).

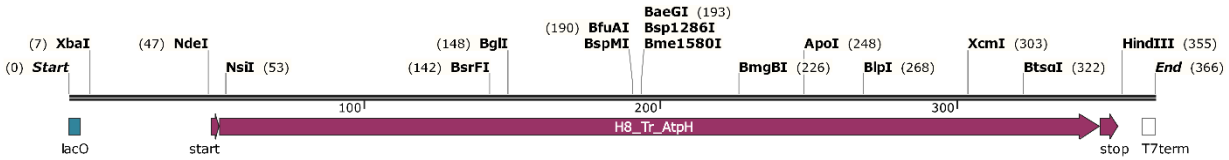

Figure 4.2. The map of the construct H8_Tr_AtpH* (generated by SnapGene® program).

All genes were optimized for expression in *E.coli* cells by using GeneArt® service from Thermo. The sequences of AtpH and H8_Tr_AtpH* are the following:

AtpH amino acid sequence

NPLIAAASVIAAGLAVGLASIGPGVGQGTAAGQAVEGIARQPEAEGKIRGTLLLS
LAFMEALTIYGLVVALALLFANPFV

H8_Tr_AtpH* amino acid sequence

HHHHHHHHSSGLVPRGSGSNPLIAAASVIAAGLAVGLASIGPGVGQGTA
AGQAVEGIARQPEAEGKIRGTLLLSLAFMEALTIYGLVVALALLFANPFV

H8_Tr_AtpH* nucleotide sequence

5'TTCCCCTCTAGAAATAATTTTGTTTAACTTTAAGAAGGAGATATACATATGCATCATC
ACCACCATCACCATCATAGCAGCGGTCTGGTTCCGCGTGGTAGCGGTAGCAATCCGCT
GATTGCAGCAGCAAGCGTTATTGCAGCCGGTCTGGCAGTTGGTCTGGCAAGCATTGG
TCCTGGTGTTGGTCAGGGCACCGCAGCAGGTCAGGCCGTTGAAGGTATTGCACGTCA
GCCGGAAGCCGAAGGTAAAATTCGTGGCACCCTGCTGCTGAGCCTGGCATTTATGGA
AGCACTGACCATTTATGGTCTGGTTGTTGCACTGGCACTGCTGTTTGCAAATCCGTTT
GTTTAATGAAAGCTTGGCTGC3'

The following oligonucleotides were used for PCR amplification of H8_Tr_AtpH*:

i_f_Xba_Nde

5'CCCCTCTAGAAATAATTTTGTTTAACTTTAAGAAGGAGATATACATATG3'

Length: 49mer GC: 28.6% Tm: 67.7°C CMW: 15075.8[g/mol]

i_r_Hind_SS

5'GCAGCCAAGCTTTCATTAAACAAACGGATTTGCAAACAG3'

Length: 39mer GC: 41% Tm: 69.5°C CMW: 11976.8[g/mol]

4.1.4. Biological materials

Fresh spinach leaves (*Spinacia oleracea*) of different spinach varieties were used for isolation and purification of intact ATP synthase and c-ring from spinach chloroplasts.

4.1.5. Chemicals

Non-organic salts and acids were purchased from Merck and Applichem; lipids and detergents – from Merck, Avanti Polar Lipids, GLYCON Biochemicals GmbH; enzymes for working with DNA – from Thermo; thrombin protease – from Merck.

4.2. Methods

4.2.1. Isolation and purification of intact proteins from spinach chloroplasts

4.2.1.1. Preparation of thylakoid membranes

Isolation of chloroplasts (*Spinacia oleracea*) was adapted from protocol [128] based on the work [129]. Fresh spinach leaves (m ~ 5 kg) were washed under cold distilled water. The roots under the leaves were cut using a scalpel and discarded, leaves were incubated ON, +4°C, without light. Then the main veins of the leaves were also cut and discarded, and leaves without veins were used to isolation of chloroplasts.

Two buffers B1 and B2 were prepared as described in Table 4.2A, B.

Table 4.2. (A) Compounds of buffer B1.

Buffer B1 for spinach homogenization

Volume[mL]	2000					
Compound	**Mw [g/mol]**	**conc [mM]**	**conc [%]**	**m [g]**	**Vstock [M]**	**V [mL]**
Sucrose	342.3	400	13.69	273.84	0	0
Tricine	179.17	20	0.36	7.17	0	0
$MgCl_2$	203.3	5	0.1	2.03	2	5
PMSF	174.19	on the tip of spatula				

pH 8.0 (NaOH)

(B) Compounds of buffer B2.

Buffer B2 for spinach cells lysis

Volume[mL]	1000					
Compound	**Mw [g/mol]**	**conc [mM]**	**conc [%]**	**m [g]**	**Vstock [M]**	**V [mL]**

Tricine	179.17	10	0.18	1.8	0	0
$MgCl_2$	203.3	2.5	0.05	0.5	4	1.25
PMSF	174.19	on the tip of spatula				

pH 8.0 (NaOH)

The spinach leaves with B1 (V ~ 1.8 – 1.9 L) were homogenized with a blender. A homogeneous mixture was filtered by using a 2-layer cloth "Nylongaze" with a pore sizes of 80 μm - the 1st layer and 20 μm - the 2nd layer. The filtered mixture was centrifuged for 20 min at 10,800 g (a rotor jl-8.1, + 4°C) and SN was discarded. The precipitate was resuspended in 500 mL B2. Since the buffer does not contain sucrose, the cells are disrupted due to the osmotic shock. The mixture was centrifuged for 20 min at 10,800 g (a rotor Ti-45, + 4°C) and SN was discarded. The thylakoid membranes in precipitate were resuspended in ~100 mL B1.

4.2.1.2. Calculation of chlorophyll concentration

Chlorophyll concentration in solutions of thylakoid membranes is a marker of concentration of proteins participating in photosynthesis and, in particular, ATP synthase [130]. A small ammount of chloroplast solution (V = 40 μL) was dissolved in 10 mL of 80% acetone in mQ (v/v). The concentration of chlorophyll *a* and *b* can be calculated by the formula

$$Clorophyll\ a+b = \left(19.54(A_{646.6nm} - A_{750nm}) + 8.29(A_{663.6nm} - A_{750nm})\right) \times k \left[\frac{umol}{L}\right]$$

according to [131], where A means absorption at corresponding wavelength, k – dilution factor, for example, in our case k = 40 μL/ 10 mL = 250. UV-vis absorption spectrum was measured using a spectrophotometer NanoDrop™ 2000. The final concentration chlorophyll *a* and *b* was adjusted to 5 – 6 mM with B1 buffer, then aliquoted, frozen with a liquid nitrogen and stored at –80 °C.

4.2.1.3. Solubilization of membrane proteins from thylakoid membranes

For solubilization of thylakoid membranes the buffer B3 was prepared as described in Table 4.3.

Table 4.3. Compounds of buffer B3.

Buffer B3 for thylakoid membranes solubilization

Volume[mL]	100					
Compound	**Mw [g/mol]**	**conc [mM]**	**conc [%]**	**m [g]**	**Vstock [M]**	**V [mL]**
Sucrose	342.3	400	13.69	13.69	0	0
Tricine	179.17	20	0.36	0.36	0	0

$MgCl_2$	203.3	5	0.1	0.1	2	0.25
$(NH_4)_2SO_4$	132.14	400	5.29	5.29	0	0
Na_2-ATP (pg II)	551.14	0.2	0.01	0.011	0	0
Sodium cholate	430.55	25	1.08	1.076	0	0
OG	292.37	60	1.75	1.75	0	0
DTT	154.25	50	0.77	0.77	0	0
PMSF	174.19	on the tip of spatula				

pH 8.0 (NaOH)

Thylakoid membranes (V = 100 mL) were unfrozen on ice and DTT was slowly added up to 50 mM at constant stirring with following incubation at + 4°C, 30 min. Then, B3 (V = 100 mL) was slowly added to the solution of thylakoid membranes at constant stirring and then incubated 30 min at + 4 °C in the dark. Important, that DTT was added to B3 just before mixing it with the solution of thylakoid membranes. The solution was centrifuged 60 min at 208,000 g (a rotor Ti 70, +4°C) and pellet was discarded. The volume of SN was ~182 mL.

4.2.1.4. Precipitation with ammonium sulfate

The SN after solubilization underwent AS precipitation. The saturated solution of AS (~4.1 M at RT), pH 8 (NH_4OH), was slowly added to the SN so that to adjust the AS concentration up to 1.2 M. It is worth to point out that initial SN solution already contained 0.2 M AS. The calculation of a volume of AS saturated solution required to adjust the necessary concentration was done by formula

$$4.1x + c_i v = c_f(x + v)$$

where x – the volume of AS saturated solution that has to be added in a volume v to adjust the AS concentration from c_i to c_f.

First, the AS concentration was slowly (~ 10 min) and at constant stirring at +4°C adjusted to 1.2 M of AS and incubated for 20 minutes at + 4°C, then centrifuged for 10 min at 12 000 g (+4°C) and pellet was discarded. The volume of SN was ~ 234 mL. Second, the AS concentration, as in the first step, was gently adjusted to 1.8 M AS, incubated for 20 minutes at + 4 °C, then centrifuged for 10 min at 12 000 g (+4°C) and SN was discarded. The centrifuge tubes were turned upside down and put on the clean paper until all SN was completely removed. At this stage, the precipitate can be stored at + 4°C for 24 h.

4.2.1.5. Anion exchange chromatography

The precipitant after AS 1.8 M was resuspended in a buffer RSB (a total volume 100 mL) that was prepared as described in Table 4.4. The solution was centrifuged at 45 000 g, 30min, +4°C, the SN was 0.2 µm filtered and used for AEX chromatography.

Table 4.4. Compounds of buffer RSB.

Buffer RSB for AS precipitate resuspension

Volume[mL]	100					
Compound	**Mw [g/mol]**	**conc [mM]**	**conc [%]**	**m [g]**	**Vstock [M]**	**V [mL]**
HEPES	238.3	30	0.71	0.71	0	0
$MgCl_2$	203.3	2	0.04	0.04	2	0.1
EDTA	292.2	0.5	0.01	0.01	0.5	0.1
tPCC-α-M	547.67	1.9	0.1	0.1	0	0

pH 8.0 (NaOH)

AEX chromatography was performed using the protocol based on the work [11] with modifications. Poros HQ-20 resin was used CV = 8 mL pre-equilibrated in the buffer A1 (Table 4.5A). The sample was loaded onto the column directly in Akta Purifier system at a flow of 1mL/min. Then ATP synthase was eluted in gradient of NaCl concentration by mixing A1 with the buffer B (Table 4.5B) in the range of ~ 200 – 400 mM NaCl. The peak fractions were merged and used for structural and functional studies and further purification of the separate c-ring.

Table 4.5. (A) Compounds of buffer A1.

Buffer A1 for AEX chromatography

Volume[mL]	100					
Compound	**Mw [g/mol]**	**conc [mM]**	**conc [%]**	**m [g]**	**Vstock [M]**	**V [mL]**
HEPES	238.3	30	0.71	0.71	0	0
$MgCl_2$	203.3	2	0.04	0.04	2	0.1
NaCl	58.44	50	0.29	0.29	2	2.5
tPCC-α-M	547.67	0.8	0.04	0.04	0	0

pH 8.0 (NaOH)

(B) Compounds of buffer B.

Buffer B for AEX chromatography

Volume[mL]	100					
Compound	**Mw [g/mol]**	**conc [mM]**	**conc [%]**	**m [g]**	**Vstock [M]**	**V [mL]**
HEPES	238.3	30	0.71	0.71	0	0
$MgCl_2$	203.3	2	0.04	0.04	2	0.1
NaCl	58.44	1000	5.84	5.84	2	50
tPCC-α-M	547.67	0.8	0.04	0.04	0	0

pH 8.0 (NaOH)

After AEX purification, the column was cleaned by 2M NaCl solution.

4.2.1.6. Rate-zonal centrifugation

The Buffer B4 was prepared (Table 4.6).

Table 4.6. Compounds of buffer B4 (2x stock).

Buffer B4 for sucrose gradient centrifugation (2x)

Volume[mL]	100					
Compound	**Mw [g/mol]**	**conc [mM]**	**conc [%]**	**m [g]**	**Vstock [M]**	**V [mL]**
Tris	121.14	60	0.73	0.73	0	0
Succinic acid	118.09	60	0.71	0.71	0	0
$MgCl_2$	203.3	10	0.2	0.2	0	0
DDM	510.6	16	0.82	0.82	0	0

pH 8.0 (NaOH)

The sucrose/asolectin centrifuge tube with a steps of sucrose gradient was prepared. Asolectin 40 mg/mL was dissolved in mQ by sonification. The buffer B4(1x) with of 2mg/mL asolectin (Buf S0) and the buffer B4(1x) with 50% (w/v) sucrose and 2mg/mL asolectin (Buf S50) were mixed in corresponding proportions to create steps of sucrose concentration from 15 – 50% (w/v) (Table 4.7). Then the syringe with a long needle was used to prepare the centrifuge tube by loading the buffers starting from 15% to 50% (w/v) sucrose on the bottom of the cup (Fig. 4.3A). The precipitant after AS 1.8 M was resuspended in 10 mL of buffer B4 (1x) (Fig. 4.3B) and loaded

onto the centrifuge tube (Fig. 4.3C). After centrifugation at 125 500 g, 16 h, +4°C the ATP synthase was in the fractions at level of about 29 – 36% (w/v) sucrose.

Table 4.7. Preparation of buffers with sucrose concentration gradient.

Sucrose, % (w/v)	**Buf S0 [mL]**	**Buf S50 [mL]**
15	21	9
22	14.6	11.4
29	10.9	15.1
36	7.3	18.7
43	3.6	22.4
50	0	30

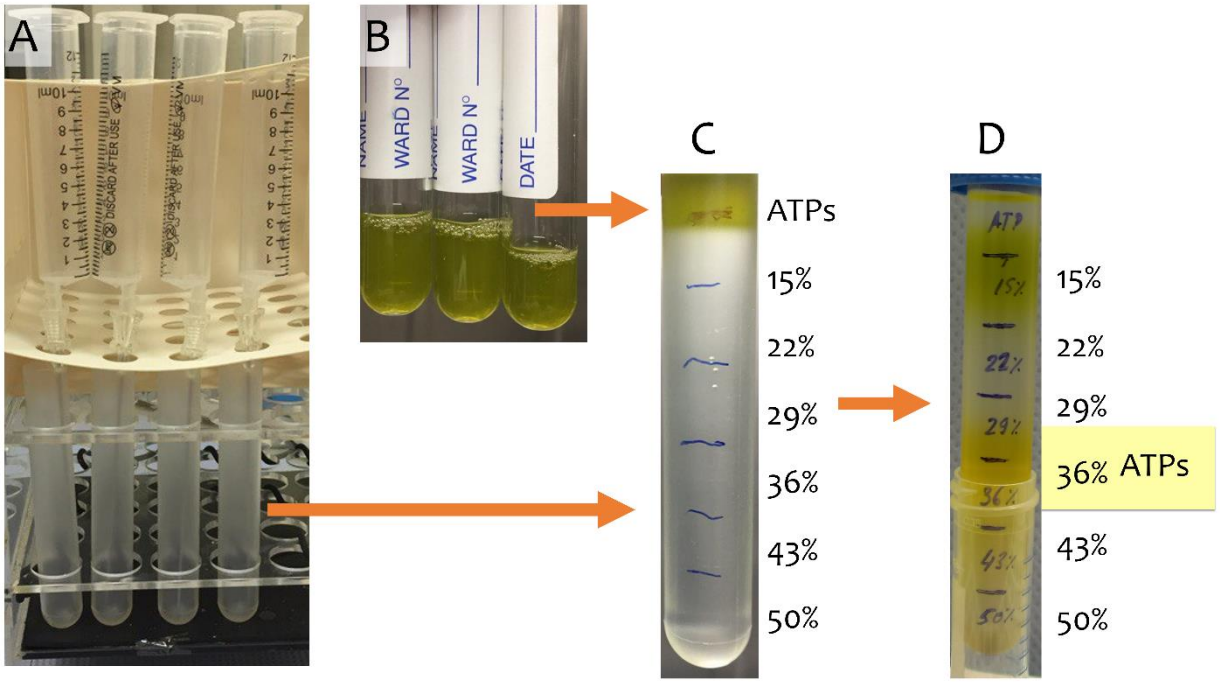

Figure 4.3. A scheme of preparation of the centrifuge tubes. **(A)** The syringes with long needles for loading buffers with different sucrose concentrations. **(B)** Resuspended AS precipitant in buffer B4. **(C)** Prepared centrifuge tube before centrifugation. **(D)** The centrifuge tube after centrifugation. ATP synthase was in the fractions at ~ 29 – 36% (v/w) sucrose.

4.2.1.7. Dye-ligand chromatography

The buffers CA, CB (Table 4.8A, B) were prepared.

Table 4.5. (A) Compounds of buffer CA.

Buffer CA for Red-120 chromatography

Volume[mL]	1000					
Compound	**Mw [g/mol]**	**conc [mM]**	**conc [%]**	**m [g]**	**Vstock [M]**	**V [mL]**
Tris	121.14	20	0.24	2.42	0	0
$MgSO_4$	120.366	5	0.06	0.6	0	0
Glycerol	92.1	2172	20	200	0	0
DDM	510.6	4	0.2	2.04	0	0
NaN_3	65	3	0.02	0.2	0	0

pH 8.0 (HCl)

(B) Compounds of buffer CB.

Buffer CB for Red-120 chromatography

Volume[mL]	500					
Compound	**Mw [g/mol]**	**conc [mM]**	**conc [%]**	**m [g]**	**Vstock [M]**	**V [mL]**
Tris	121.14	20	0.24	2.42	0	0
$MgSO_4$	120.366	5	0.06	0.6	0	0
NaCl	58.4	1000	5.84	29.2	0	0
Glycerol	92.1	2172	20	200	0	0
DDM	510.6	4	0.2	2.04	0	0
NaN_3	65	3	0.02	0.2	0	0

pH 8.0 (HCl)

The fractions of ~ 29 – 36% after sucrose gradient centrifugation were mixed with a buffer CA 1/1 (v/v) and loaded onto HiPrep 26/10 Desalting column pre-equilibrated with a buffer CA. After desalting the samples were loaded onto a column with Red-120 dye (pre-equilibrated with a buffer CA), that was received from Prof. Dr. Norbert Dencher. Red-120 is used in textile industry and occurred to bind active centers of globular proteins, thus acts as a ligand. The goal of dye-ligand chromatography was to purify the samples of ATP synthase from RuBisCO – a water-soluble protein, which has a similar properties with cF_OF_1. Being a globular protein, RuBisCO binds with Red-120 and ATP synthase is freely eluted from the column. After that a buffer CB is used to elute RuBisCO. A_{280} was monitored. The experiment was done using Akta Purifier system.

The samples of ATP synthase after dye-ligand chromatography were concentrated (100kDa cutoff) and used for further structural and functional studies.

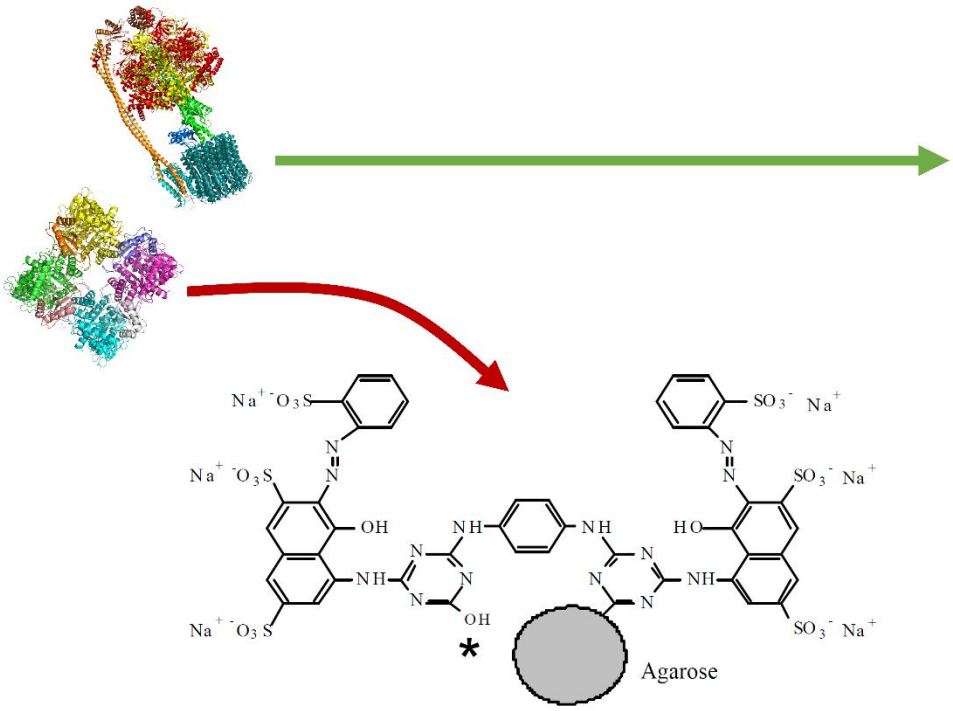

Figure 4.4. A formula of Red-120 agarose resin and a sheme of ATP synthase purification from a RuBisCO protein (6FKF [11] and 1AUS PDB [132] models are shown).

4.2.2. Expression and purification of recombinant proteins

4.2.2.1. E. coli culture and overexpression

Hereinafter Y_1 and T_1 denote yeast extract and tryptone 1% (w/v), respectively; OD = OD_{600} (absorbance at 600 nm).

Cells transformation protocol: 1µL of DNA was added to cells on ice, 30 min ice, heatshock +42°C 70 sec, 5 min on ice, add SOC 800µL, +37°C 30 min shaker 130 rpm, 3 krpm 3 min, delete 750 µL SN, resusp. cells infect petri dish, +37°C overnight.

Plasmid seeding: LB 10 mL Kan50 5 clones +37°C 130 rpm shaker overnight.

Plasmid isolation: cells 3.5 krpm 10 min, delete SN, resusp. buf. 500 µL, lys. buf. 500 µL, neutraliz. buf. 600 µL, 14 krpm 5 min, take SN onto spin columns on vacuum pump, wash buf. AW 500 µL x2, wash buf. A4 800 µL x2, empty columns 11 krpm 2 min, elution buf. 70µL 2min, 4 krpm 1 min, 11 krpm 1 min).

Analytical expression:

Preculture medium (PCM): Y_1T_1, Glycerin 0.5%, autoclaved, NPS 1x, Mg^{2+} 2 mM, Glucose 0.5%, Succinic acid 10 mM, Kan50, (20 mL) at +37°C 130rpm shaker 4 h.

Culture medium (CM): Y_1T_1, Glycerin 0.5%, autoclaved, NPS 1x, Mg^{2+} 2 mM, Glucose 0.05% 20 mL Kan50 $OD_{initial}$= 0.03, +37°C 130 rpm shaker.

Overexpression of pBKT7_H8Tr_AtpH in *E.coli* C41:

PCM (Y_1T_1, Glycerin 0.5%, autoclaved, NPS 1x, Mg^{2+} 2 mM, Glucose 0.5%, Succinic acid 10 mM) 400 mL Kan50, +37°C 130 rpm shaker 4 h, OD = 4.8.

CM (Y_1T_1, Glycerin 0.5%, autoclaved, NPS 1x, Mg^{2+} 2 mM, Glucose 0.05%) 5L Kan50 $OD_{initial}$=0.15, +37°C 130 rpm shaker:

Add 1 mM IPTG at OD = 0.9, +20°C, 130 rpm shaker overnight.

Final OD = 7.28.

Overexpression of pBKT7R_H8Tr_AtpH in *E.coli* BL21:

PCM (Y_1T_1, Glycerin 0.5%, autoclaved, NPS 1x, Mg^{2+} 2 mM, Glucose 0.5%, Succinic acid 10 mM) 400 mL Kan100, +37°C 130 rpm shaker 4 h.

CM (Y_1T_1, Glycerin 0.5%, autoclaved, NPS 1x, Mg^{2+} 2 mM, Glucose 0.05%) 5 L, Kan100, $OD_{initial}$ = 0.05, +37°C 130 rpm shaker:

Add Lactose 0.2% at OD = 0.5, add 1 mM IPTG at OD = 1.0, +20°C 130 rpm shaker overnight.

Final OD = 2.2.

4.2.2.2. Cells disruption

Cells were centrifuged at 4.2 krpm, 20 min, +4°C, pellet (m = 15 g) was resuspended with a buffer B: (NaPi 20 mM, NaCl 100 mM, proteases inhibitor 6AHA 2 mM, pH 7.5, lysozyme 7.5 mg, deoxyribonuclease I from bovine pancreas 0.75 mg). The solution (V_{final} = 150 mL) was homogenized in «loose» mode and loaded in microfluidizer P = 1000 bar (x5).

4.2.2.3. Solubilization of membrane proteins from E.coli membranes

Cell lysate was centrifuged at 28 krpm, 2 h, +4°C, pellet was resuspended in buffer B up to 75 mL and homogenized in «tight» mode. The solution was solubilized in 1% DDM, overnight, +4°C, with magnetic stirrer 300 rpm and then was centrifuged 25 krpm, 30 min, +4°C. SN was taken for further purification.

4.2.2.4. Ni-NTA purification

20 mM imidazole was added to the solution after solubilization and pH was adjusted to 7.8 (Tris/Tris-HCl). The solution was batched with Ni-NTA resin and incubated overnight at +4°C with magnetic stirrer 300 rpm. Ni-NTA was preliminary equilibrated with buf «0»:(NaPi 20 mM, NaCl 100 mM, 6AHA 2 mM, 0.1% DDM, pH 7.8). The system was equilibrated by buf H:(buf «0» + Imidazole 200 mM + Histidine 200 mM), buf. «200»: (buf «0» + Imidazole 200 mM) and buf «0». Ni-NTA was then put onto the column; it was then attached to the system and followed the program with steps of imidazole concentration of 30, 200 mM, and addition of histidine 200 mM (Fig. 4.5A) or gradient imidazole concentration from 20 – 200 mM and addition of histidine 200 mM (Fig. 4.5B).

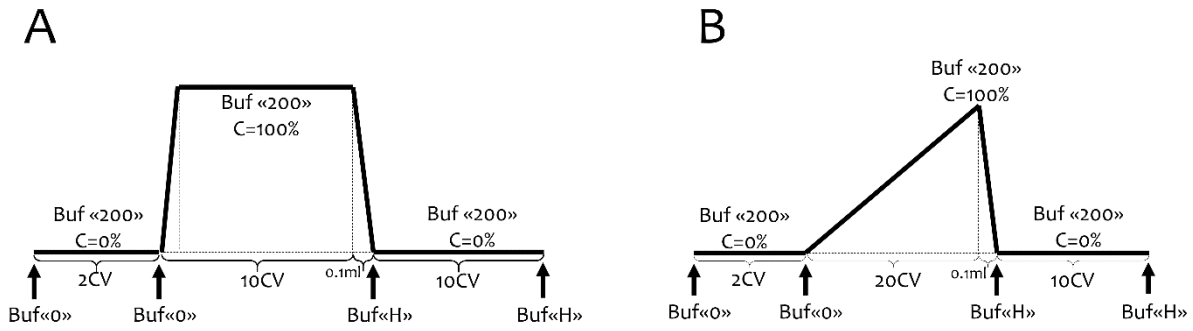

Figure 4.5. Schemes of programs of Ni-NTA purification with (A) steps of concentration (30 mM, 200 mM) and (B) gradient of concentration (30 – 200 mM) of imidazole with following purification by a buffer containing imidazole 200 mM and histidine 200 mM.

4.2.2.5. Size exclusion chromatography

The samples after Ni-NTA purification were loaded onto Superdex G-200 column pre-equilibrated with a buffer (NaPi 20 mM, NaCl 100 mM, 6AHA 2 mM, 0.1% DDM, pH 7.8). A_{280} was monitored. The experiment was done using Akta Purifier system.

4.2.3. Samples quality control

4.2.3.1. UV-Vis spectrometry

For UV-Vis spectrometry of thylakoid membranes in acetone solution, or to measure OD_{600} of E.coli cells a spectrophotometer Nanodrop^{TM} 2000 was used.

4.2.3.2. SDS PAGE

For analysis of analytical expression in *E.coli*, the cells were prepared by following protocol:

Preparation of *E.coli* cells for SDS PAGE: Cells (OD_{final}=2) 11krpm, 1min, delete SN, resuspend in mQ 160µL, add a stain (5x) 40µL, sonification at 10% power, 30 sec.

Preparation of polyacrylamide gels:

For analysing of ATP synthase and c-ring 13% acrylamide (AA) separating gel was used (Table 4.6A). For analysing of c_1-subunit (~8 kDa), up to 16% AA separating gel was used (Table 4.6B).

Table 4.6. (A) Compounds of 13% AA separating gel.

№		**Stacking**	**Separating**
	Gel percentage [%]	5.25	13
1	30%AA [mL]	0.7	4.334
2	mQ [mL]	2.707	2.936
3	1T7.5/1.5T8.8 [mL]	0.5	2.5
4	BrPhBlue(sat) [µL]	1	0
	Degase 5 min		
5	10%SDS [µL] (0.2%)	80	200
6	TEMED [µL]	4	10
7	20%APS [µL]	8	20
	Σ Volume [mL]	**4**	**10**

(B) Compounds of 16% AA separating gel.

№		**Stacking**	**Separating**
	Gel percentage [%]	5.25	16
1	30%AA [mL]	0.7	5.334
2	mQ [mL]	2.707	1.936
3	1T7.5/1.5T8.8 [mL]	0.5	2.5
4	BrPhBlue(sat) [µL]	1	0
	Degase 5 min		
5	10%SDS [µL] (0.2%)	80	200
6	TEMED [µL]	4	10
7	20%APS [µL]	8	20
	Σ Volume [mL]	**4**	**10**

Gel electrophoresis parameters: 150 V 40 mA (2 gels) 1 h 20 min.

After SDS PAGE, gels were washed in mQ for 5 min to eliminate SDS and then were stained with coomassie blue 2-4 h and destained using 10% acetic acid.

4.2.3.3. Silver staining

For silver staining a kit Silver Stain Plus^{TM} from Bio-Rad was used. The staining protocol was the following:

Reactive preparation:
Dissolve 1.25 g of development accelerator reagent in 25 mL of mQ to make Development accelerator solution.

Fixation – 20 min:
incubate a gel with 200 mL fixation solution – 20 min (RT).
Fixation solution:
100 mL methanol
20 mL acetic acid
20 mL fixation enhancing solution
60 mL mQ

Rinsing – 20 min:
Rinse a gel with 200 mL of mQ, repeat this procedure

Staining – up to 20 min:
Place 17.5 ml of mQ into beaker. Add reagents in the following order:
2.5 mL Silver Complex Solution
2.5 mL Reduction Moderator Solution
2.5 mL Image Development Reagent
Before use add 25 mL of Development accelerator solution. Swirl well.
Stain a gel approx. 10 min (up to 20 min) with monitoring staining intensity.

Stop - 20 min:
Incubate a gel with 5% acetic acid for minimum 15 min. Then rinse gel with mQ for 5 min.

4.2.3.4. Western Blot

Transfer to a nitrocellulose membrane: The transfer was performed with Bio-Rad equipment. The polyacrylamide gel after SDS PAGE was loaded into a stack between a nitrocellulose membrane and filters (Fig. 4.6) and then immersed into a transfer buffer: (50 mM Tris-base, 40 mM Glycine, 0.04% (w/v) SDS, 20% methanol). The transfer parameters: 90V 400mA 1h, with the refrigerant and at constant stirring.

After transferring the nitrocellulose membrane was washed in mQ for 5 min and then in a buffer TBST-milk: (10 mM Tis-HCl pH 8, 100 mM NaCl, glycerin 5% (v/w), NaN_3 0.02% (w/v), Tween-20 0.05% (w/v), dry milk 5% (w/v)) 10 min x3. After that for recombinant proteins containing a His-tag antibodies (AB) PentaHis (mouse) dissolved 1:2000 (v/v) in TBST-milk were used (10 mL

per 1 membrane) and incubated at +4°C overnight. Then they were washed in TBST-milk 10 min x3 and incubated with goat anti-mouse AB with alkaline phosphatase dissolved 1:1500 in TBST-milk (10 mL per 1 membrane) 1 hat RT. Then the membrane was washed in TBST-milk 10 min x2, TBST (without milk) 10 min x2, and was stained in 3-5 min with 50 µL 5%NBT 50g/L in 70%DMFA and 50 µL 2%BCIP 50g/L in 100%DMFA dissolved in AP buffer (100 mM TrisHCl, 100 mM NaCl, 1 mM $MgCl_2$, pH 9.0) (7.5 mL per 1 membrane).

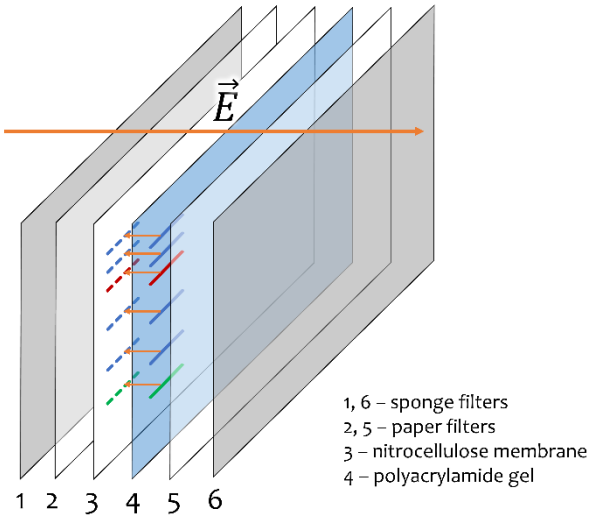

Figure 4.6. A scheme of a stack for transfer of proteins from a polyacrylamide gel to a nitrocellulose membrane. $\vec{E}$ shows electric field during the experiment.

For intact ATP synthase AB (ATP synthase, whole enzyme; Host: rabbit; Reactivity: *C. reinhardtii*, *E. opiuroides*, *S. oleracea*, *P. sativum*, *P. vaginatum*) from Agrisera and AB (Goat Anti-Rabbit IgG) with alkaline phosphatase from Merck were used. The other part of the protocol was the same as for recombinant proteins.

4.2.3.5. Dynamic light scattering

DLS was performed on SpectroSize 300 from Xtal Concepts (a cuvette based DLS instrument) with the samples of recombinantly expressed c-ring. mQ was used for calibration and a buffer was used as a referecnce. The data was treated with the help of SpectroSize 300 software. The results were merged from 20 measurements for better statstics. Mean autocorrelation function and mean radius distribution were obtained. All measurements were done at +20°C.

4.2.3.6. Functional tests

ATP synthase purified by Red-120 dye-ligand chromatography was reconstituted into liposomes (phosphatidylcholine/ phosphatidic acid = 9/1, (w/w)) and the functional studies were performed by using the following protocol, described in [29]: buffer L2 (200 mM Tricin, 5 mM NaH_2PO_4, 120 mM KCl, 2.5 mM $MgCl_2$, 0.2 mM ADP) (V=240 µL) was added into a clinicon-cuvette and

mixed with 12.5 µL Luciferin-Luciferase reagent. The cuvette was placed into a Luminometer "BioOrbit 1250" and the baseline was recorded, 43 µL of proteoliposomes were equilibrated with 217 µL buffer L1 (20 mM sodium succinate, 5 mM NaH_2PO_4, 2.5 mM $MgCl_2$, 0.6 mM KCl, 1 µM Valinomycin, pH 4.7). After 100 seconds the mixture was injected via a cannula into the cuvette containing L2. ATP-synthesis driven by ΔpH and $\Delta\mu(K^+)$ was monitored by a luminescence when using the Luciferin-Luciferase-Assay. The slope at the beginning of the measured signal was calculated to determine the ATP synthesis rate. The luminescence signal was calibrated by addition of 20 µL 10 µM ATP.

ATP synthase purified by AEX chromatography was analysed by reconstitution in azolectin liposomes prepared by the following protocol: azolectin was dissolved in chloroform 1% (w/v) which was evaporated using rotary evaporator and then exicator minimum at 1h. Then a buffer containing 2% Sod.Ch. was used to resuspend the lipids and the solution was sonicated 5min. The solution was centrifuged at maximum speed and a pellet was discarded. SN was sonicated for 1min. After that the concentrated ATP synthase was added up to a final concentration of 0.5 mg/mL. Amberlite XAD-2 were incubated with the solution to absorb a detergent. ATP synthase reconstituted into liposomes was tested and qualitatively showed ATP hydrolysis activity measured by the Luciferin-Luciferase-Assay.

4.2.4. Reconstitution into nanodiscs

Purified cF_OF_1 was mixed with POPC and MSP1E3D1 and then lipid-detergent micelles (48 mM POPC/96 mM Sod Ch.) were added. Membrane scaffold protein MSP1E3D1 in 10 mM Sod.Ch and Sod. Ch. were adjusted to final Sod.Ch concentration of 20 – 40 mM. The solution was incubated in the neighborhood of the phase transition of the POPC (+ 4°C) minimum 1 hor ON. Amberlite XAD-2 (assuming that 1 g can absorb ~70 mg Triton X-100) was added using the same calculation for Sod. Ch. and changed 3 times. Size exclusion chromatography was performed using Superose 6 Increase 10/300 GL column, then peak fractions were concentrated (100kDa cutoff) and used for further structural studies.

4.2.5. Small angle X-ray scattering (SAXS)

4.2.5.1. Samples preparation for SAXS measurements

Samples of purified ATP synthase for SAXS measurements were prepared by concentrating (30 or 100kDa cutoff) and following centrifugation at 10 000 g, 10min, +4°C to eliminate aggregates. They were put into capillaries, which then were sealed by wax or using a gas-burner, placed on a holder and measured at vacuum.

4.2.5.2. SAXS facilities

SAXS measurements were performed using BM-29 BioSAXS beamline, European Synchrotron Radiation Facility (ESRF), Grenoble, France, equipped with a detector Pilatus3 2M in-vac, tunable energy range (7.0 - 15.0 keV), a beam size ((H x V) : 50.0 x 50.0 μm² - 2.0 x 1.0 mm²) and the flux is about 10^{12} photons/s, (Fig. 4.7A, B).

In addition, SAXS experiments were done using Rigaku, Moscow Institute of Physics and Technology, Dolgoprudny, Russia, with a portable X-ray source MicroMax^{TM} 007 HF and a position sensitive detector ASM, DTR Triton 200, a beam size (H x V) : 400 x 400 μm² and the flux is about 10^{9} photons/s (Fig. 4.7C, D).

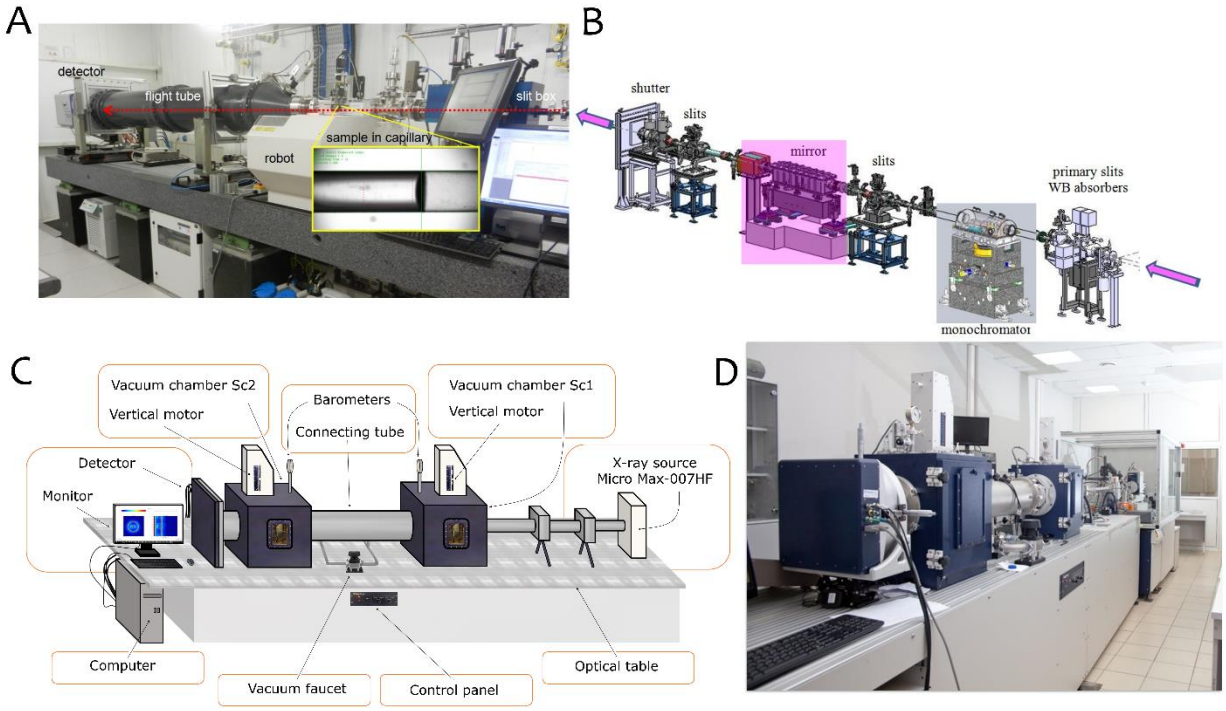

Figure 4.7. (A) The photograph of BM-29 BioSAXS beamline experimental hutch (B) The scheme of main elements in BM29 optics hutch. (C) The scheme of Rigaku instrument with a portable X-ray source (D) The photograph of Rigaku instrument. Panels A, B were adapted from ESRF official web-site: https://www.esrf.eu/home/UsersAndScience/Experiments/MX/About_our_beamlines/bm29.html.

4.2.5.3. SAXS data treatment and low-resolution structure determination

The SAXS method provides 2D images of scattering intensity vs. transmitted impulse $Q = \frac{4\pi}{\lambda}\sin(\theta)$, λ – X-ray wavelength, 2θ – scattering angle. 2D images of proteins in solution have a central symmetry due to mean distribution of angles for particles, therefore the rings were observed on the 2D I(Q) images (Fig 4.8A). The images then were radially integrated using BSXCube software for BM-29 beamline and SAXSGui for Rigaku instrument (Fig. 4.8B), thus 1D profiles of I(Q) were obtained (Fig. 4.8C). A calibration of a Q value was done by measuring of silver

behenate (AgBh). Regularized model fit of I(Q) profiles was used for calculation of a pair-distance distribution function P(R) (Fig 4.8D) by GNOM from program suite ATSAS [133]. Then P(R) and I(Q) were used to obtain *ab initio* 3D models – low-resolution structures of measured objects (shown in the section *Low-resolution structure of the ATP synthase from spinach chloroplasts*, Results and discussion). These models, in contrary to those obtained by XRD, consist of dummy atoms or "pseudo atoms" with given scattering properties. The models were obtained by DAMMIN, DAMMIF or GASBOR programs from ATSAS online web-platform [133].

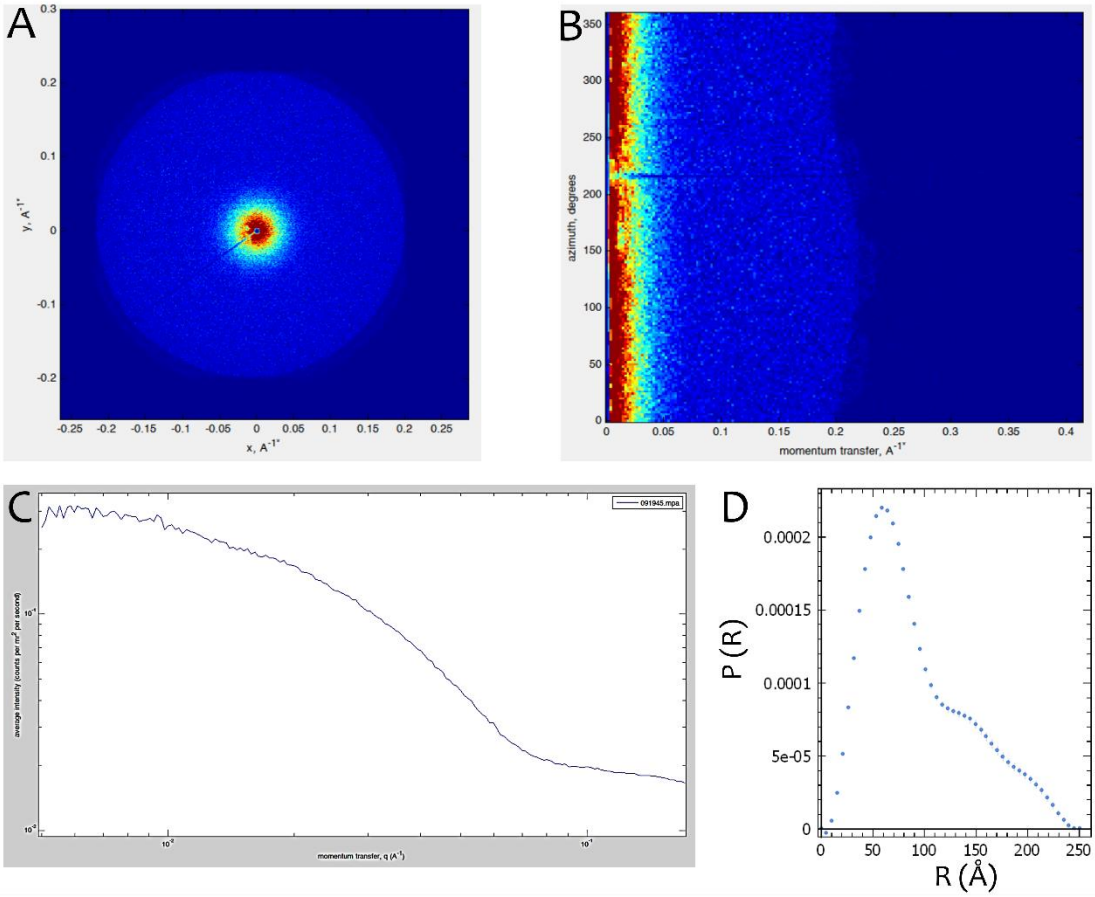

Figure 4.8. Examples of data treatment for ATP synthase in detergent micelles after AEX purification. **(A)** Raw 2D image from a position-sensitive detector. **(B)** Polar transformation of 2D image and Q-calibration with AgBh. **(C)** 1D scattering profile I(Q). **(D)** Calculated pair-distance distribution function P(R).

Taking into account a dimerization of ATP synthase, in case of samples with the protein reconstituted into nanodiscs, that significantly affected the I(Q) profiles, was done by the same algorithms as described in our publication [134] and was connected with choosing the correct Q-range, making a series of dilutions and measuring I(Q) profiles for different concentrations.

4.2.6. Protein crystallization

4.2.6.1. Vapor diffusion crystallization

VD crystallization was performed with the help of HTX Lab, EMBL, Grenoble, France. The experiments were done by sitting drop VD method in 96-well COC protein crystallization microplate with three 1 µL conical flat bottom crystal cup wells from Corning. The intact ATP synthase was concentrated (100kDa cutoff) up to ~80 mg/mL and the drops of the samples were set into the wells and mixed with corresponding precipitants in ratios 3/1, 1/1, 1/3 (v/v) (150 nL/50 nL, 100nL/ 100nL, 50nL/150nL) by using a Drop Setter for Protein Crystallization - NT8® from Formulatrix and imaged at 1d, 3d, 7d, 15d of the experiment (Fig. 4.9).

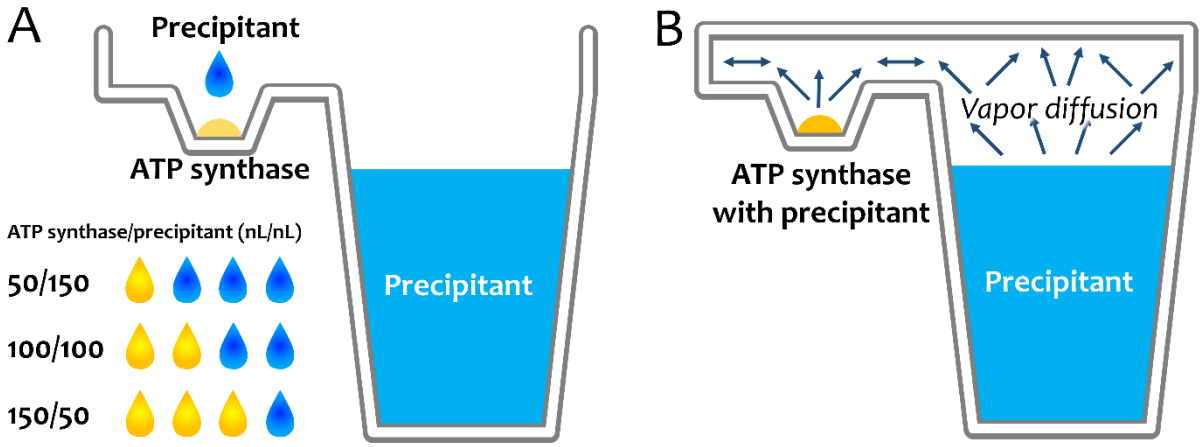

Figure 4.9. The scheme of VD crystallization experiment. **(A)** Preparation of a VD crystallization plate with conical flat bottom crystal cup wells. ATP synthase is mixed with a precipitant in three different ratios 3/1, 1/1, 1/3 (v/v) (150 nL/50 nL, 100nL/ 100nL, 50nL/150nL) and then the plate is sealed. **(B)** Three wells are connected with the precipitant reservoir through the vapor diffusion processes.

4.2.6.2. In meso crystallization

The intact ATP synthase was concentrated (100 kDa cutoff) and different final concentrations were checked (27.4, 26.4, 43.1, 50.9, and 80 mg/mL). *In meso* crystallization was performed using LCP crystallization plates from MiTeGen. The MO lipid cubic phase (LCP) was prepared as described in the work [67] with modifications. Thus, the ratio of MO to a liquid solution was varied (1/2, 2/3, 1/5). The MO-protein phase was incubated for 12 h before preparation of a crystallization plate. The plate was prepared with different ratios of the protein in MO/ precipitant (Fig. 4.10).

Crystallization plates were prepared using a Drop Setter for Protein Crystallization - NT8® from Formulatrix and imaged at a RockImager® (Formulatrix). All crystallization experiments were done at +22°C.

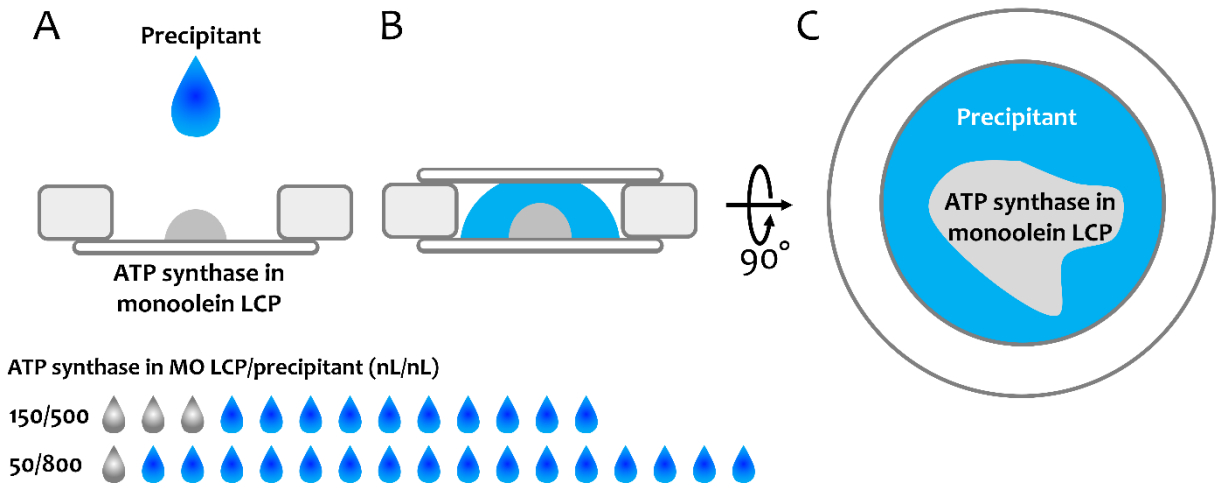

Figure 4.10. The scheme of *in meso* crystallization experiment. **(A)** A precipitant is added to a drop of ATP synthase in MO LCP. Different ratios (150nL/500nL and 50nL/800nL) were tested. **(B)** A cover glass seals the volume of crystallisation probe **(C)** Another view on a schematic crystallization probe. It consists of a lipid-protein phase surrounded by a precipitant.

4.2.7. X-ray diffraction (XRD) experiments

4.2.7.1. Samples preparation for XRD measurements

The cover glass was removed with a glass cutter and a corresponding buffer with 20% glycerol was added to a crystallization probe. Protein crystals were harvested with a loop and flash-frozen in a liquid nitrogen.

4.2.7.2. XRD facilities

X-ray diffraction data were collected using the beamline ID23-1, European Synchrotron Radiation Facility (ESRF), Grenoble, France, equipped with a PILATUS 6M-F detector with an active area of 424 x 435 mm^2, which can collect 25 images per second with a readout time of 3ms. The measurements are available in range of 5 – 20 keV energy with the flux of about 10^{12} photons/s. During the measurements, crystals are cooled by a cryostream at 100K.

4.2.7.3. XRD data treatment and high-resolution structure determination

Diffraction patterns were integrated using XDS [135]. The space group was determined to be I121. The intensities of the reflexes were scaled and merged using the AIMLESS from the CCP4 program suite [136]. Molecular replacement (MR) was performed by MOLREP [137] using 3V3C [28] as an initial model. The further refinement was done by REFMAC5 [138] and Coot [139].

4.2.8. Differential UV-Vis spectroscopy

Differential UV-Vis spectroscopy was performed using the spectrophotometer Shimadzu UV-2450. The samples were dissolved in pure EtOH with a high dilution factor of about ~1/30 (v/v) to eliminate the influence of a protein buffer. The UV-Vis measurements were done before and after addition of $NaBH_4$ (several grains on the tip of a spatula; samples were incubated 2-5min) and then the latter spectrum was subtracted from the first one. The addition of $NaBH_4$ triggers the qualitative reaction reducing ketones and aldehydes to alcohols, therefore it can change UV-Vis absorption spectra, for example, in case of compounds with quinone groups. Quinones or semiquinones are reduced to quinols with two OH^- groups instead of oxygens. In our case, PQ-9 and PSQ-9 are reduced to PQH_2. As a reference, a differential spectrum of TMBQ dissolved in pure EtOH (a polar moiety of PQ-9) before and after addition of $NaBH_4$ was measured. TMBQ changes its' UV-Vis absorption spectrum after addition of $NaBH_4$ similarly to PQ-9. As a control experiment, a differential spectrum of pure EtOH before and after addition of $NaBH_4$ was measured. All measurements were done at RT in the wavelength range from 230 to 750 nm.

5. Results and discussion

This chapter contains detailed description of main obtained results; their comparison with reanalyzed and systematized available information in literature; suggested hypotheses and experimental evidences arguing towards them; and discussion of questions and problems related to structural organization of c-rings and ATP synthases, and their possible implications. The major part of the results connected with the high-resolution structure of the c-ring is published in [26], SAXS studies of ATP synthase and development of protocols for ATP synthase purification were presented on international conferences and abstracts were published in [78] and [140], respectively. Development of SAXS method was published in [134], [141] and further was applied for SAXS studies of ATP synthase, e.g. SAXS data treatment of protein dimers.

5.1. Sample preparation

5.1.1. Purification of intact ATP synthase from spinach chloroplasts

Preparation of thylakoid membranes from spinach chloroplasts was performed as described in Materials and Methods in the section *Preparation of thylakoid membranes* and adapted from protocol [128] based on the work [129]. Concentration of chlorophyll *a* and *b* was used as a marker of ATP synthase concentration in the samples and was measured by UV-Vis spectroscopy of thylakoid membranes dissolved in 80% (v/v) actetone in mQ (Fig. 5.1). The concentration of chlorophyll *a* and *b* was always adjusted to 5 mM.

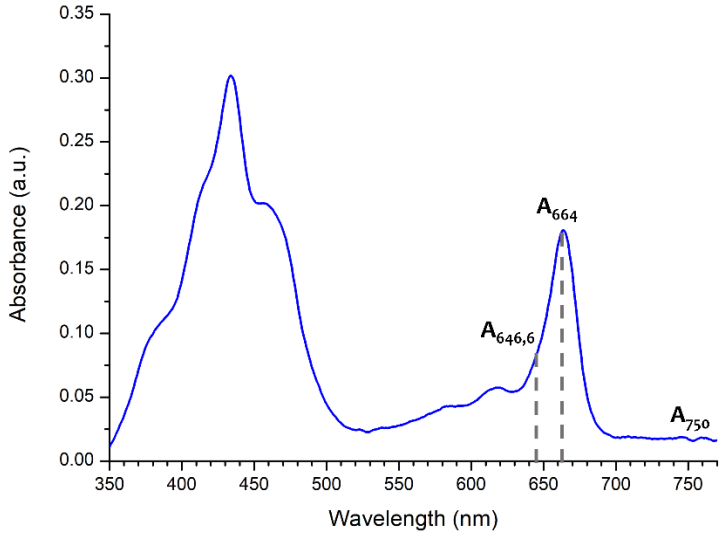

Figure 5.1. UV-Vis absorbance spectrum of spinach thylakoid membranes dissolved in 80% acetone in mQ. Absorbance values at 646.6, 664 and 750 nm ($A_{646.6}$, A_{664} and A_{750}) are used to calculate the concentration of chlorophyll *a* and *b* [130].

5.1.1.1. AEX chromatography purification of ATP synthase

This protocol is based on that described in [11] with some modifications. ATP synthase was solibilized from thylakoid membranes as described in the corresponding section of the chapter Materials and Methods: *Solubilization of membrane proteins from thylakoid membranes*. During solubilization the solution contained 0.2 M of ammonium sulfate (AS) and after centrifugation it was dark green (Fig. 5.2A) with a significant ammount of precipitate (Fig. 5.2B). The supernatant was used to perform AS precipitation and a precipitant in range of 1.2 – 1.8 M AS was taken for further purification (Fig. 5.2C-F). The color of the solution became lighter in shades of green with increasing AS concentration (Fig. 5.2A, C, E) and the color of precipitant became more yellow (Fig. 5.2B, D, F).

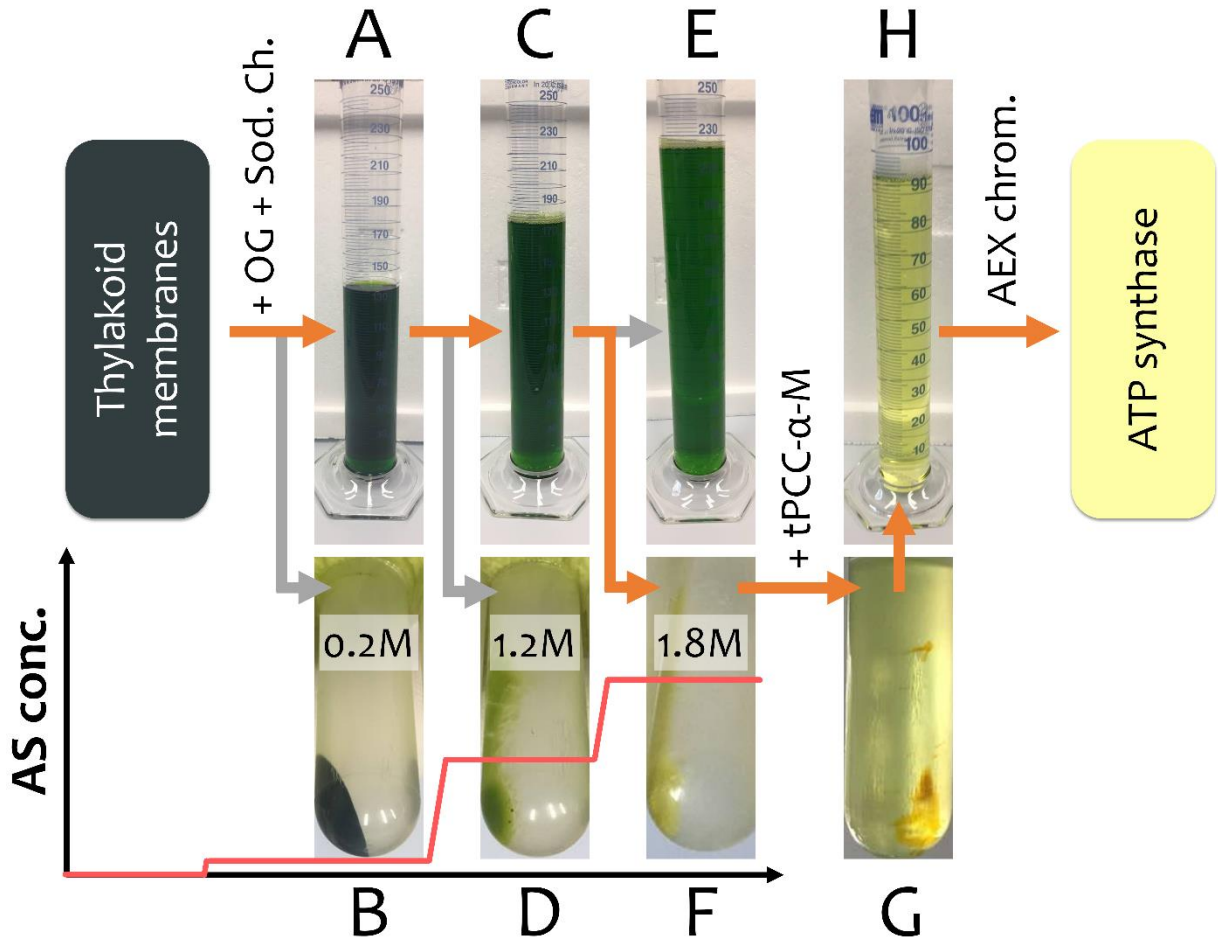

Figure 5.2. ATP synthase purification pipeline. Thylakoid membranes underwent solubilization by OG and Sod.Ch. detergents in presence of 0.2 M AS and centrifugation (corresponding **(A)** supernatant and **(B)** precipitant). The supernatant was used for the further AS precipitation at 1.2 M AS (corresponding **(C)** supernatant and **(D)** precipitant) and then at 1.8 M AS (corresponding **(E)** supernatant and **(F)** precipitant). Then the precipitant at 1.8 M AS was resuspended in a buffer containing tPCC-α-M and centrifuged (**(G)** deep yellow supernatant and small ammount of brown

precipitant). **(H)** The supernatant was filtered at 0.2 µm and was used for AEX chromatography and following obtaining of purified ATP synthase.

The precipitant that was obtained after centrifugation at 1.8 M AS was resuspended in a buffer solution containing 0.1% (w/v) of 4-trans-(4-trans-Propylcyclohexyl)-cyclohexyl α-maltoside (tPCC-α-M) – a non ionic detergent for mild solubilization of membrane proteins. After centrifugation a small amount of brown precipitant occurred (Fig. 5.2G). The supernatant after filtering at 0.2 µm (Fig. 5.2H) was used for purification by anion exhange (AEX) chromatography (Fig. 5.3A).

SDS PAGE analysis of fractions after AEX chromatography showed the best completeness of ATP synthase in peak factions (Fig. 5.3B, C) with clearly visible bands corresponding to α, β, γ, δ, ε, a, b, b' and c_{14} subunits. These fractions corresponded to ~ 320 – 360 mM NaCl, the whole range of concentrations with protein compound was ~ 200 – 400 mM NaCl.

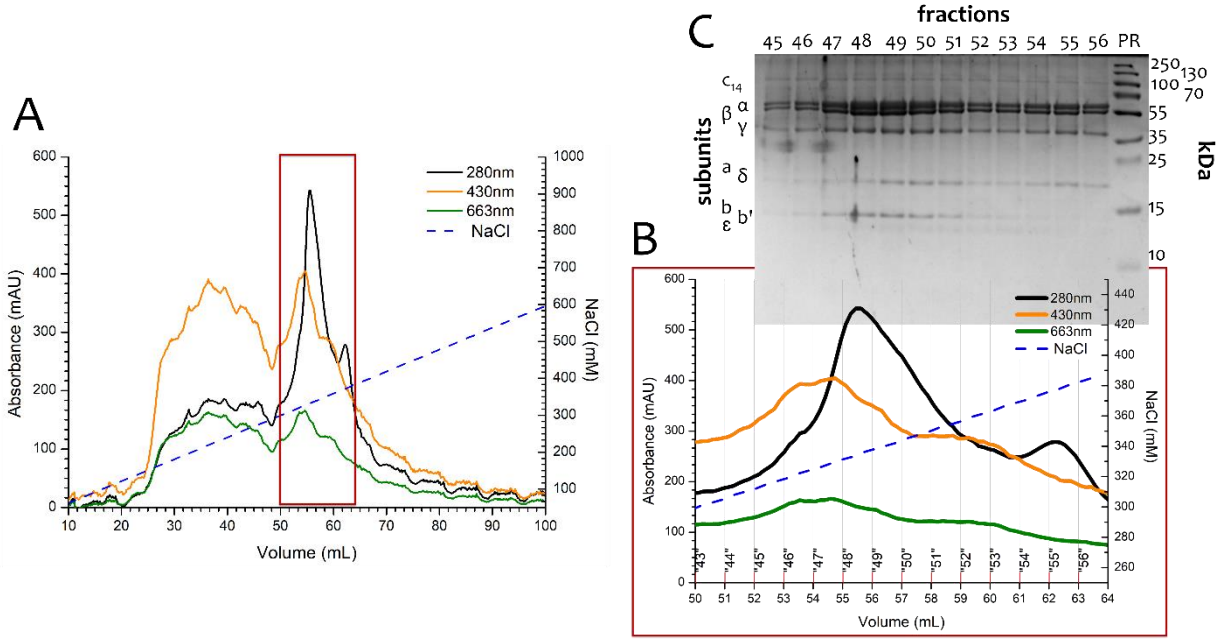

Figure 5.3. (A) AEX chromatogram (Absorbance *vs.* eluted volume) of ATP synthase samples after resuspension in a buffer containing tPCC-α-M, centrifugation and filtering of a supernatant. POROS™ 20 HQ resin was used. A range of NaCl concentrations was 50 – 1000 mM. **(B)** Major peak fractions containing ATP synthase at ~320 – 360 mM NaCl and **(C)** 16% SDS PAGE of corresponding fractions. Absorbance at 280, 430 and 663nm were recorded (black, orange and green lines, respectively). NaCl concentration is shown as blue dashed line.

The samples of purified ATP synthase that were used for further structural studies were in a buffer containing HEPES 30 mM, $MgCl_2$ 2 mM, NaCl ~300 mM, ~0.04% tPCC-α-M, pH 8.0.

5.1.1.2. Rate zonal centrifugation & dye-ligand chromatography purification of ATP synthase

Intact ATP synthase was also purified by alternative protocol in this work (Fig. 5.4). This protocol was optimized based on that described in [29], [128] with some modifications. After solubilization of thylakoid membranes and centrifugation (Fig. 5.4A, B), and AS precipitation (Fig. 5.4C-F) procedures (the same as described in the section *AEX chromatography purification of ATP synthase*), a rate-zonal centrifugation in a sucrose density gradient (15 – 50% (w/v) with a 7% step) was performed (Fig. 5.4G) (see the section *Rate-zonal centrifugation* in the chapter Materials and Methods).

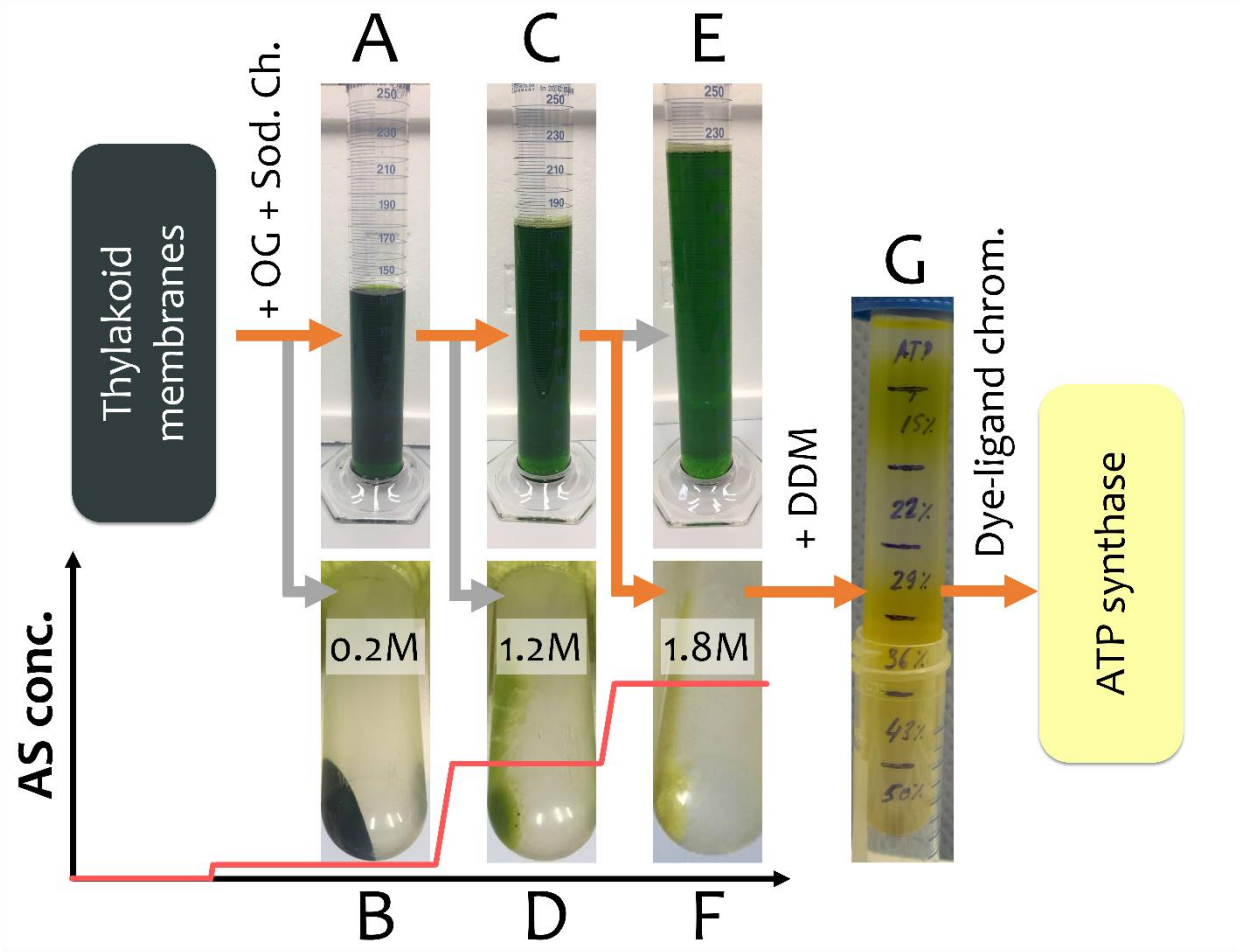

Figure 5.4. ATP synthase purification pipeline. Thylakoid membranes underwent solubilization by OG and Sod.Ch. detergents in presence of 0.2 M AS and centrifugation (corresponding **(A)** supernatant and **(B)** precipitant). The supernatant was used for the further AS precipitation at 1.2 M AS (corresponding **(C)** supernatant and **(D)** precipitant) and then at 1.8 M AS (corresponding **(E)** supernatant and **(F)** precipitant). Steps A – F are the same as in Fig. 5.2. Then the precipitant at 1.8 M AS was resuspended in a buffer containing DDM and loaded onto sucrose gradient column. After centrifugation **(G)** a deep yellow stripe in range of ~29 – 36% sucrose (w/v) was

used for further purification by dye-ligand chromatography and following obtaining of purified ATP synthase.

The fractions in range of ~29 – 36% sucrose (w/v) (a deep yellow stripe) were used for further desalting and dye-ligand chromatography to discard Ribulose-1,5-bisphosphate carboxylase/oxygenase (RuBisCO) protein complex (see the section *Dye-ligand chromatography* in the chapter Materials and Methods). RuBisCO has similar physico-chemical properties and molecuar weight as in the monomer of ATP synthase from spinach chloroplasts. RuBisCO consists of eight large (~55 kDa) and eight small (~13 kDa) subunits (LSU and SSU, respectively) and the whole complex is about 540 kDa. It is also one of the most abundant enzymes in biology [142] and discarding RuBisCO during purification of ATP synthase was a real challenge several decades ago. Dye-ligand chromatography is one of possible solutions for this problem. In this work Red-120 reactive dye resin was used to capture RuBisCO and purify ATP synthase samples as it is shown in Figure 5.5A, lane #11.

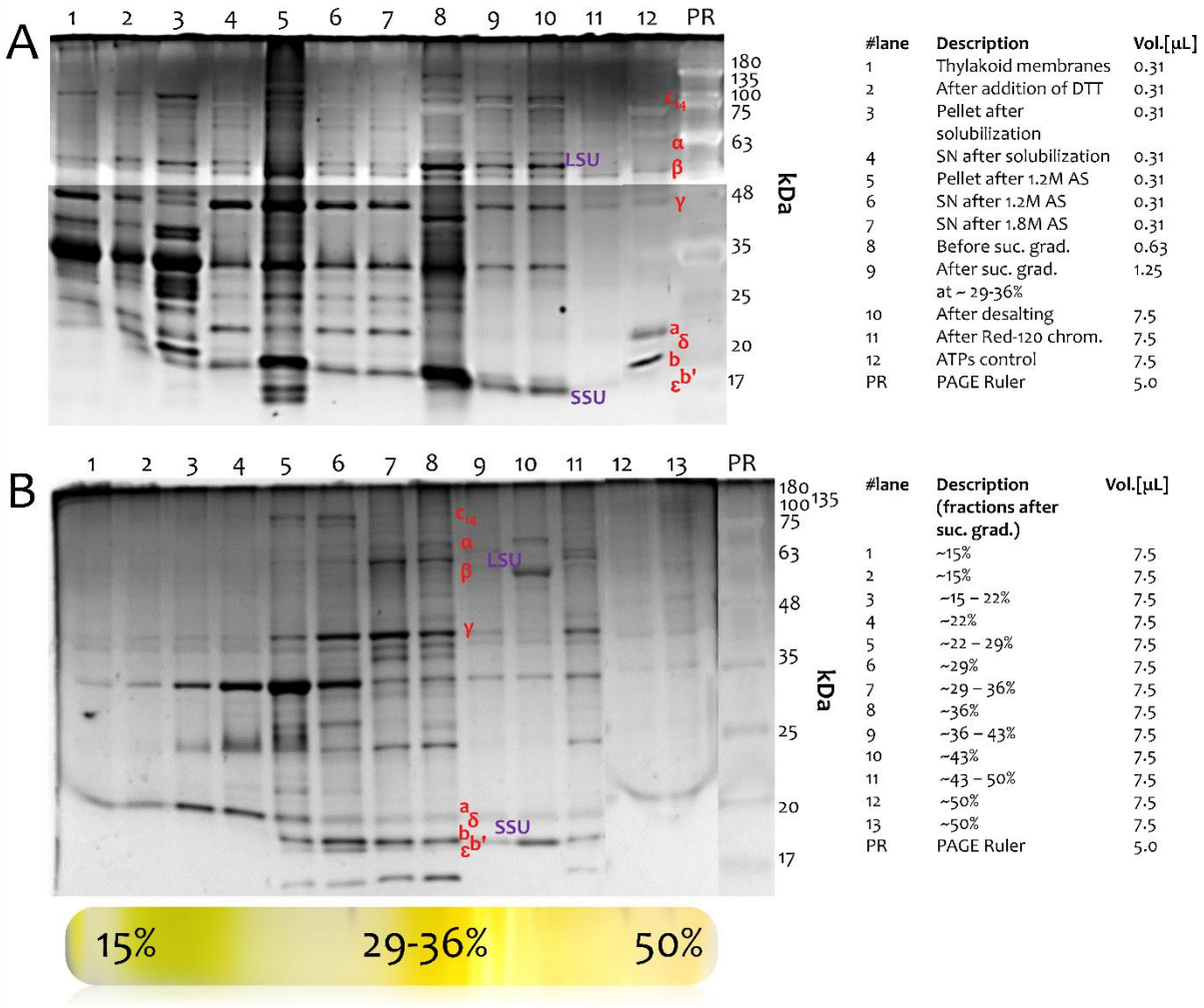

Figure 5.5. Silver stained 12% SDS PAGEs for **(A)** purification pipeline and **(B)** fractions after centrifugation in sucrose gradient. Description of lane numbers is shown on the right. ATP synthase

subunits associated with corresponding bands are shown in red color, RuBisCO subunits are shown in purple. In the panel A two different image filters were used for convenient visualization of a polyacrilamide gel (below and above ~50kDa Mw according to page ruler line). Below the panel B the column after centrifugation in sucrose gradient depicts the color of fractions analyzed by SDS PAGE.

RuBisCO subunits LSU and SSU can be observed by SDS PAGE as two bands at ~55 and ~13kDa. LSU is typically observed very close to subunit β of ATP synthase and presents in all lanes of ATP synthase purification pipeline (Fig. 5.5A, lanes #1, 2, 4, 6-10) until Red-120 dye-ligand chromatography (Fig. 5.5A, lane #11). SSU that is observed in proximity to ε subunit of ATP synthase also presents until the final step of purification.

Rate-zonal centrifugation in sucrose density gradient does not discard RuBisCO due to its similar physico-chemical properties to ATP synthase, so its' LSU and SSU subunits are clearly visible by SDS PAGE in the fractions containing ATP synthase at ~29 – 36% (w/v) of sucrose (Fig. 5.5B, lanes# 6-8).

Finally, ATP synthase (~4 mg/mL) in a buffer containing 20 mM Tris, 5 mM $MgCl_2$, 0.2% (w/v) DDM, 0.02% (w/v) NaN_3, pH 7.5 was also used for structural studies and for crystallization trials as a starting crystallization material. In particular, crystals that resulted in the high-resolution structure of the c-ring were obtained from ATP synthase samples prepared by this protocol.

5.1.2. Purification of the c-ring from ATP synthase

This protocol is based on that described in [25] with modifications. The sample of purified ATP synthase underwent heating at 65°C, 10 min in presence of 1% (w/v) NLS. Then, the AS concentration was adjusted to 2.5M, incubated 20 min and the solution was centrifuged (Fig. 5.6A). After centrifugation a white protein film (according to SDS PAGE, results not shown) occurred on the top and almost transparent solution was on the bottom. The protein film was discarded and the solution on the bottom was used for further purification by desalting or dialysis against a buffer 50 mM NaCl, 10 mM HEPES, 2 mM 6AHA, 0.5 mM EDTA, 0.03% (w/v) DDM, pH 7.0.

SEC was performed with samples in the same buffer using Superdex G-200 column (Fig. 5.6B). The chromatogram showed absorbance peaks at ~ 11.5 and ~14.0 mL. SDS PAGE of the peak fraction at 11.5 mL showed the band corresponding to c_{14}-ring, while the fraction at 14.0 mL, presumably, c_1 subunit did not show any bands on Coomassie SDS PAGE (Fig. 5.6C).

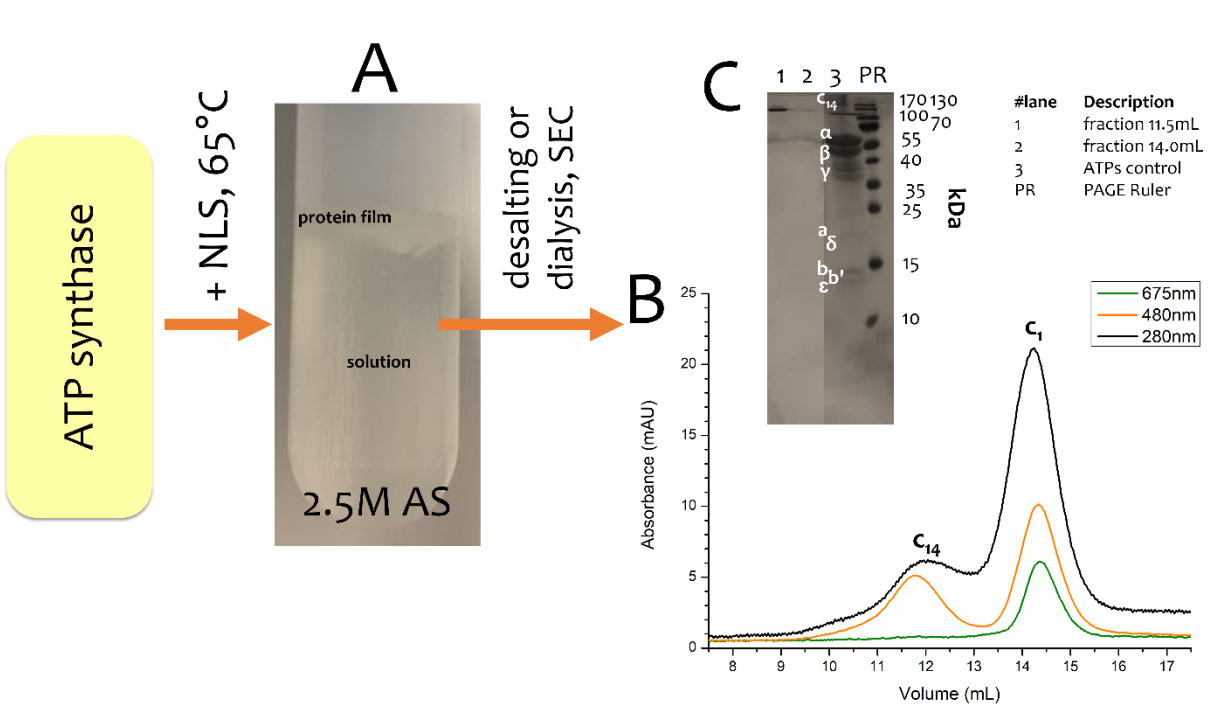

Figure 5.6. C-ring purification pipeline. The sample of ATP synthase after addition of 1% (w/v) NLS and heating at 65°C, 10 min underwent AS precipitation at 2.5M AS. **(A)** A protein film that occurred after centrifugation on the top of the solution and was discarded. The almost transparent solution was used for further purification by desalting or dialysis, and after that SEC was performed using Superdex G-200 column. **(B)** The chromatogram shows two A_{280} peaks at ~11.5 and ~14.0 mL of eluted volume that presumably correspond to c_{14}-ring and c_1-subunit, respectively. **(C)** 16% SDS PAGE of fractions and lanes description are shown.

Interestingly, that absorbance at 480 nm (A_{480}) showed two peaks at ~ 11.5 and ~14.0 mL, which were at the same positions as those at 280 nm; and A_{675} showed only one peak at ~14.0 mL (Fig. 5.6B). UV-Vis spectra of the fractions in range of 250 – 750 nm at ~ 11.5 and ~14.0 mL showed difference at 675nm and in range of 375 – 525 nm (Fig. 5.7). The fraction with, presumably, c_1 subunit (c_1-fraction) showed signal from both chlorophyll *a* and beta carotene, whereas the fraction corresponding to c_{14}-ring (c_{14}-fraction) showed only beta carotene signal.

The form of the three-peaks in range of 375 – 525 nm corresponding to beta carotene signal was also different for these fractions. In particular, the c_{14}-fraction showed the highest second peak at ~450 nm in contrary to the c_1-fraction, which highest peak was the first one at ~425 nm (Fig. 5.7A). It could be due to different isomers of beta carotene or its derivatives, however, UV-Vis spectra are not able to clarify the exact structure of measured compounds. Detailed pigment analysis is described in the section *Analysis of pigment compound*.

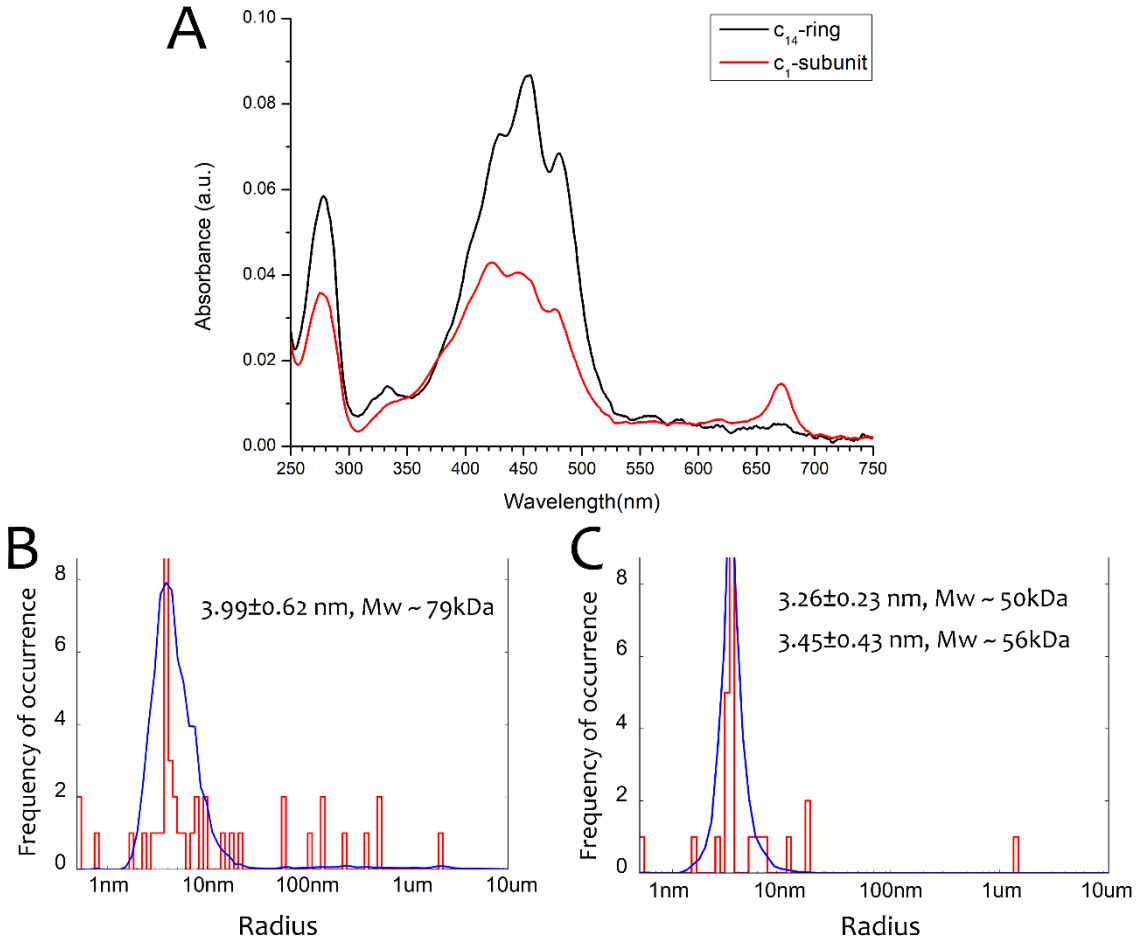

Figure 5.7. (A) UV-Vis spectra of the fractions at ~ 11.5 and ~14.0 mL (c_1- and c_{14}-fractions) (red and black lines, respectively). Histograms of DLS measurements for **(B)** c_1- and **(C)** c_{14}-fractions. Mean diameters and approximate molecular mass of particles are shown.

Dynamic light scattering (DLS) with the c_1- and c_{14}-fractions showed different mean diameters of ~ 3.3 – 3.4 nm and ~ 4 nm, respectively (Fig. 5.7B, C). This, in general, is consistent with SEC chromatogram, however, the accurate assessment of Mw of particles was not possible due to limitations of the method.

5.1.3. Expression and purification of a recombinant c_1-subunit

A pre-history of sample preparation can significantly affect crystallization processes and small-molecule composition that is especially important in case of the c-ring. In order to check whether the pigment compound of the c-ring is necessary for stabilization of the protein and species-conditioned the new protocol of recombinant expression and purification of the spinach chloroplast c_1-subunit in *E. coli* was developed.

5.1.3.1. Constructs design

A gene AtpH encoding c_1-subunit of cF_OF_1 from *Spinacia oleracea* with N-terminus His8-tag (H8) and a thrombin cleavage site LVPR||GS (|| – cleavage site) (Tr), (H8_Tr_AtpH*) was amplified by PCR as it is shown in Figure 5.8A. For PCR forward and reverse primers i_f_Xba_Nde and i_r_Hind_SS were used (see detailed description in the section *Genes and oligonucleotides*, Materials and Methods).

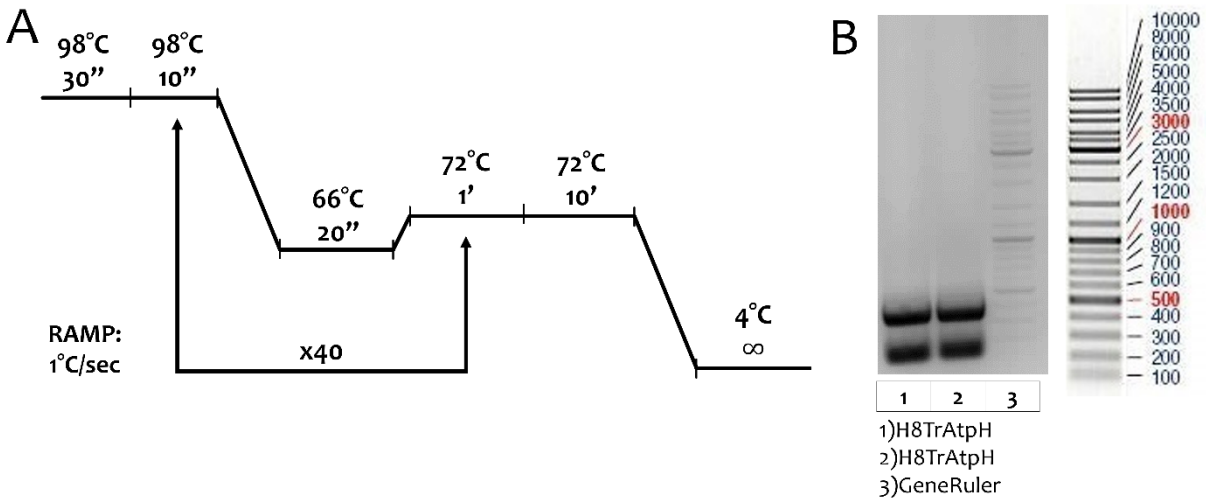

Figure 5.8. (A) PCR scheme of H8_Tr_AtpH* amplification. A temperature per each step with corresponding time (1' denotes 1 min, 1'' – 1 sec) are shown. Temperature ramp was 1°C/sec. **(B)** Results of agarose gel electrophoresis of amplified H8_Tr_AtpH* construct. Gene ruler is shown on the right.

The top band at ~350 b.p. (Fig. 5.8B) was taken for further DNA manipulations. A vector pBKT7 and amplified H8_Tr_AtpH* were taken for digestion at HindIII and XbaI sites, and ligation by T4 DNA Ligase (Fig. 5.9A). The plasmid pBKT7_ H8_Tr_AtpH* and a vector pEKT7R were used to obtain the plasmid pBKT7R_ H8_Tr_AtpH* with additional repressor for decreasing possible promotor leakage (digestion was done at EagI and XbaI sites with following ligation by T4 DNA Ligase) (Fig. 5.9C). Thus, the construct H8_Tr_AtpH* was inserted into pBKT7 and pBKT7R vectors which were transformed to *E. coli* TOP 10 cells with following clone selection checked by digestion and sequence analyses. Digestion analysis was done at XbaI and HindIII sites for pBKT7_ H8_Tr_AtpH*, and at EcoRV and HindIII sites for pBKT7R_ H8_Tr_AtpH* (Fig. 5.9B, D).

Appropriate clones were taken to sequence analysis which proved the success of insertions. The plasmids that were used for further transformation, overexpression and purification of the protein are shown in Figure 5.10.

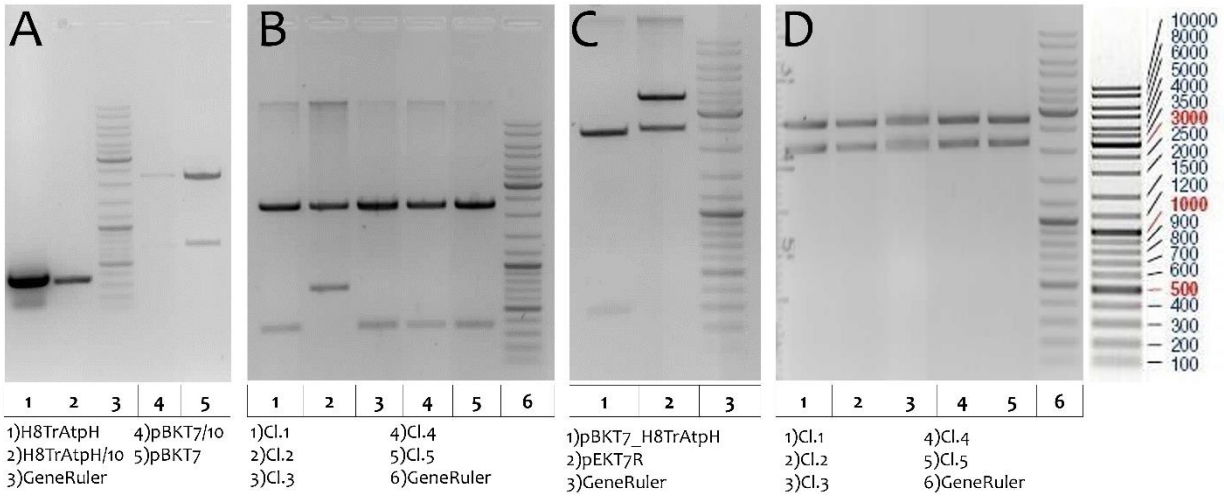

Figure 5.9. Agarose gels showing results of digestion for **(A)** pBKT7 and H8_Tr_AtpH* construct; and for **(C)** pBKT7_H8_Tr_AtpH* and pEKT7R. Digestion analysis of clones *E. coli* TOP 10 transformed with **(B)** pBKT7_H8_Tr_AtpH* (at XbaI and HindIII sites) and **(D)** pBKT7R_H8_Tr_AtpH* (at EcoRV and HindIII sites) plasmids. Gene ruler is shown on the right.

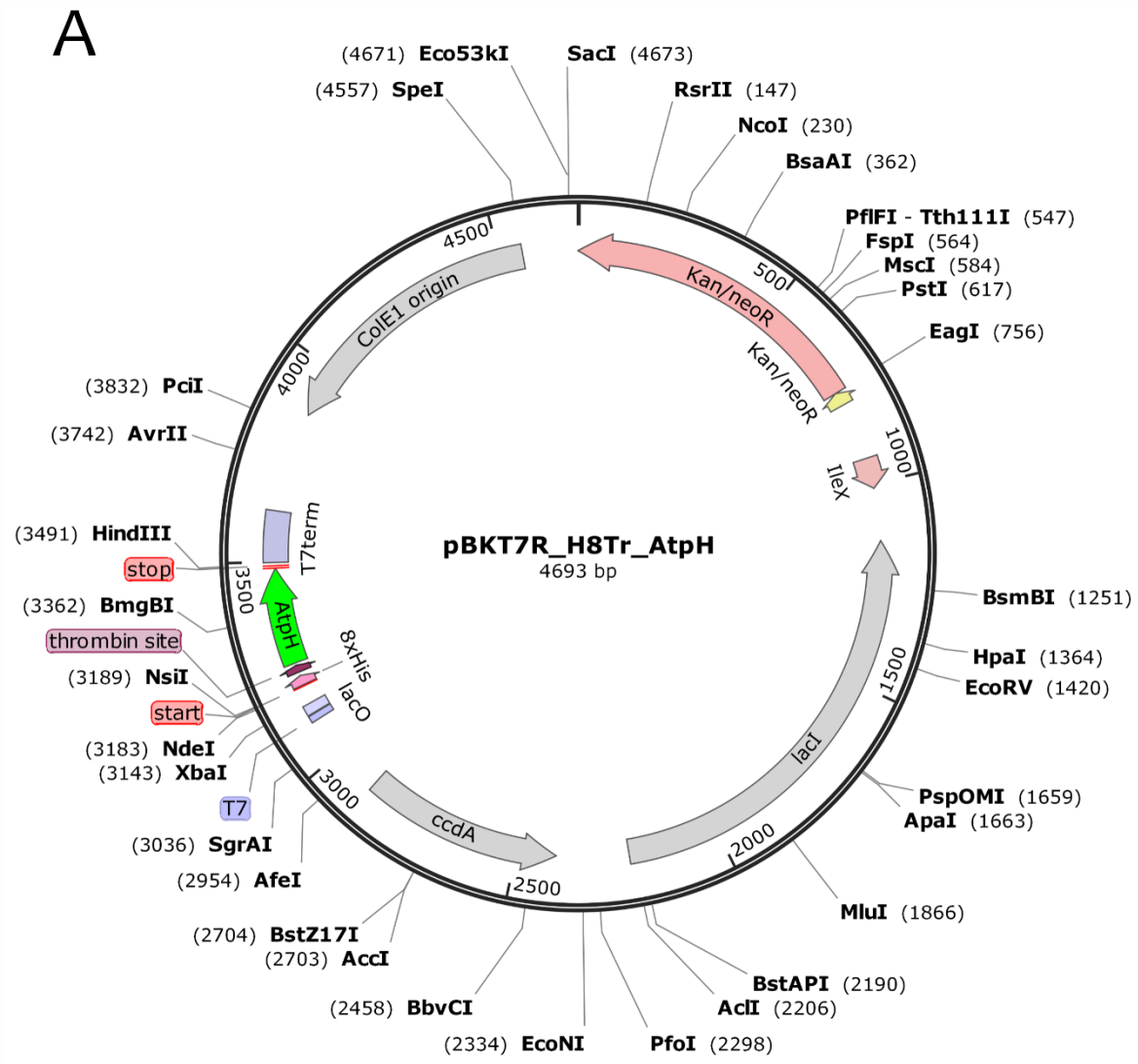

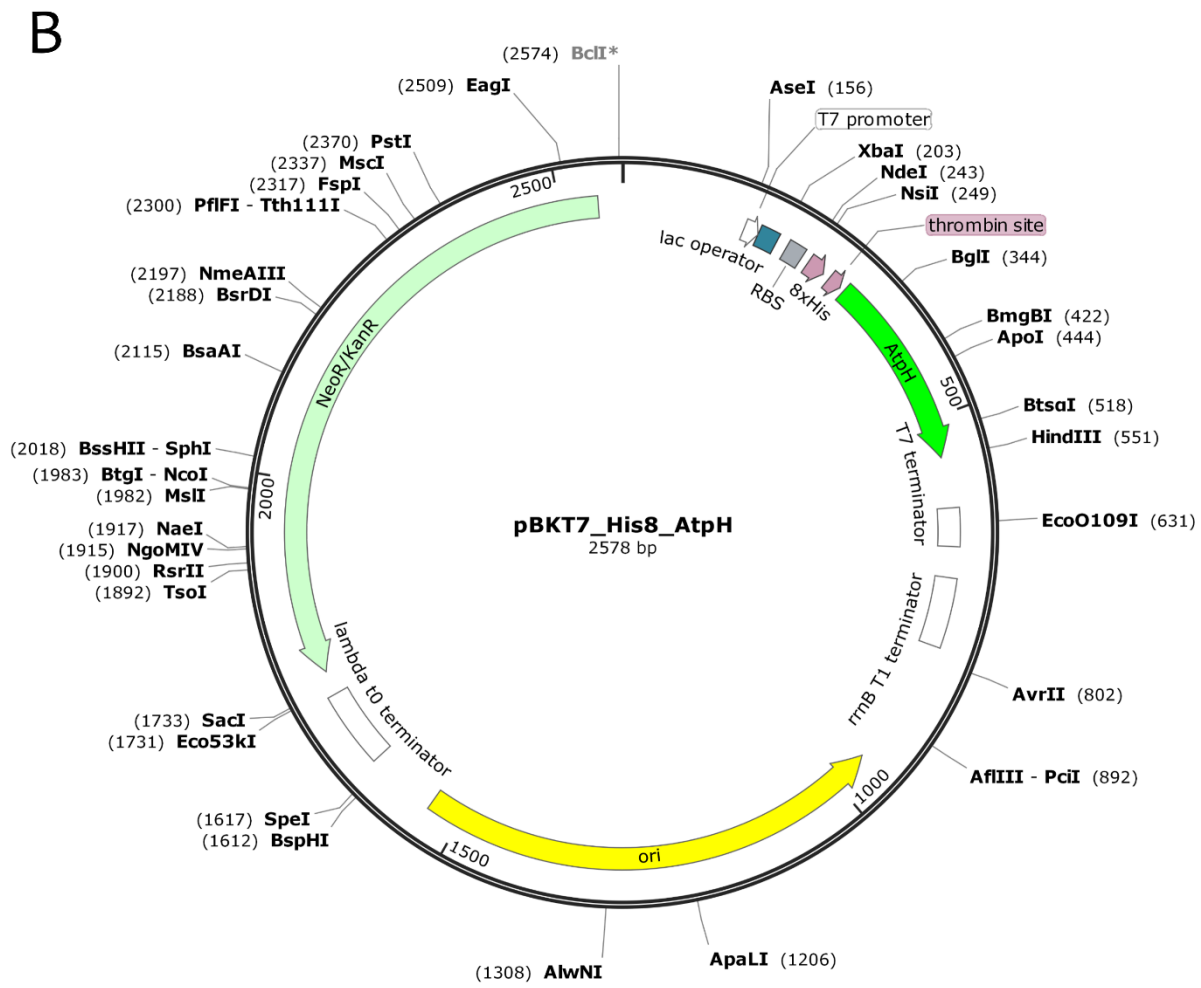

Figure 5.10. Plasmid maps of **(A)** pBKT7R_ H8_Tr_AtpH* and **(B)** pBKT7_ H8_Tr_AtpH*. The maps are generated by SnapGene® program.

5.1.3.2. Overexpression optimization

C41 and BL21 *E. coli* cells have been transformed with the plasmids pBKT7_ H8_Tr_AtpH* and pBKT7R_ H8_Tr_AtpH* as described in the section *E. coli culture and overexpression*, Materials and Methods. The cells were grown in glucose-rich PCM overnight and then transferred to CM at different conditions: induction by 1 mM IPTG at OD_{600} = 1.8 or autoinduction by 0.2% (w/v) lactose, or both by 0.2% (w/v) lactose and 1 mM IPTG (Table 5.1).

Table 5.1. Different cell growth conditions for protein expression from plasmids pBKT7_H8_Tr_AtpH* and pBKT7R_H8_Tr_AtpH* in C41 and BL21 *E.coli* cells. "CM" highlights the common compounds of culture medium.

№	Name	Yeast extract	Tryptone	Mg^{2+}	Glycerol	Glucose	Lactose	IPTG	Comments
1	C41_L	1%	1%	2 mM	0.5%	0.05%	0.2%	-	-
2	C41_I	1%	1%	2 mM	0.5%	0.05%	-	1 mM	IPTG added at OD=1.8
3	C41_LI	1%	1%	2 mM	0.5%	0.05%	0.2%	1 mM	
4	BL21_L	1%	1%	2 mM	0.5%	0.05%	0.2%	-	-

5	BL21_I	1%	1%	2 mM	0.5%	0.05%	-	1 mM	IPTG added at OD=1.8
6	BL21_LI	1%	1%	2 mM	0.5%	0.05%	0.2%	1 mM	
		CM							

The cell growth was monitored by monitoring OD_{600}. Final OD_{600} values after expression ON showed a slight better growth in C41 cells with the plasmid with repressor (pBKT7R) at induction by 1 mM IPTG as well as for autoinduction by 0.2% (w/v) lactose, than in BL21 cells (Table 5.2, "C41_L" and "C41_I" samples). *Vice versa* was for BL21 cells, which showed 1.5 times better growth with the plasmid without repressor (pBKT7) at autoinduction by 0.2% (w/v) lactose and at presence of 1 mM IPTG with or without lactose 4 times better cell growth was observed (Table 5.2, "BL21" samples).

Table 5.2. Final OD_{600} value for the c_1-subunit overexpression for plasmids pBKT7_H8_Tr_AtpH* and pBKT7R_H8_Tr_AtpH* in BL21 and C41 *E.coli* cells at different conditions of induction.

№	**Name**	**OD_{600}**	
		pBKT7_H8_Tr_AtpH*	pBKT7R_H8_Tr_AtpH*
1	C41_L	10.6	11.7
2	C41_I	7.2	11.44
3	C41_LI	9.82	9.08
4	BL21_L	10.58	7.9
5	BL21_I	12.9	3.24
6	BL21_LI	12.2	3.26

However, the efficiency of c_1-subunit expression did not correlate with the cell growth. In contrary, the most efficient expression was observed at conditions which resulted in the least OD_{600} value. The reasons might be the toxicity of c_1-subunits and possible c_{14}-rings in cellular membranes of *E.coli*. The protein overexpression was observed by WB (Fig. 5.11). Sample preparation for WB for test expressions and WB procedure are described in the sections *SDS PAGE* and *Western Blot*, Materials and Methods, respectively.

According to the WB, the maximum efficiency was shown for BL21 with pBKT7R_H8_Tr_AtpH* autoinduced by 0.2% (w/v) lactose and 1 mM IPTG, and for C41 with pBKT7_H8_Tr_AtpH* induced by 1 mM IPTG at OD_{600} = 1.8. These conditions were tested for large-scale expression of the c_1-subunit.

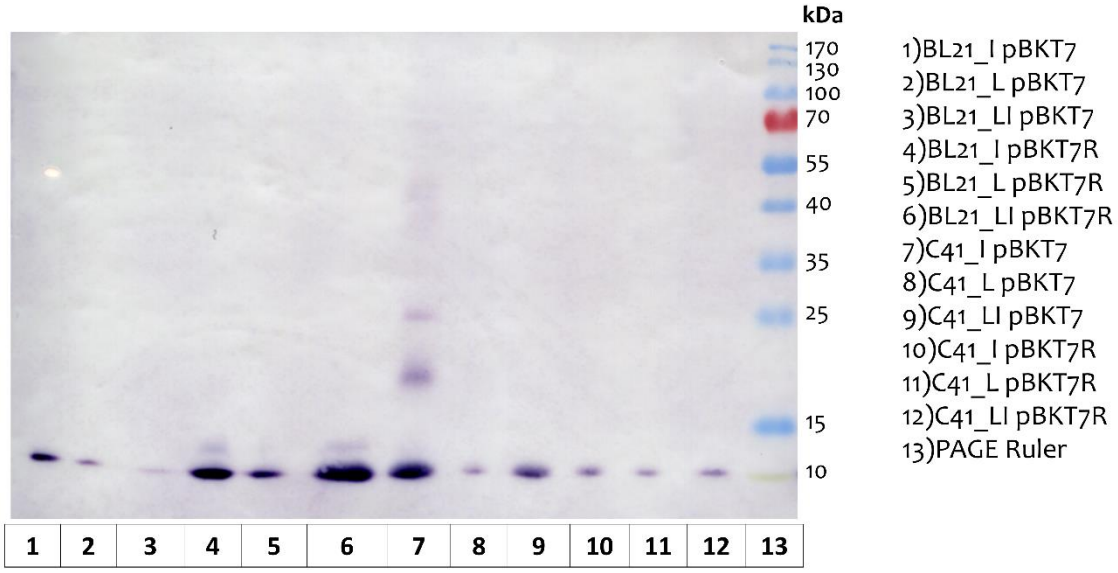

Figure 5.11. WB of normalized amount of BL21 and C41 *E.coli* cells with plasmids pBKT7_H8_Tr_AtpH* and pBKT7R_H8_Tr_AtpH* grown at different conditions of H8_Tr_AtpH expression. Lanes description is shown on the right.

5.1.3.3. C_1-subunit expression and purification

The large-scale expression was obtained using C41 *E.coli* cells with pBKT7_H8_Tr_AtpH* plasmid induced by 1 mM IPTG at OD_{600} = 0.9; and BL21 *E.coli* cells with pBKT7R_H8_Tr_AtpH* plasmid induced by lactose 0.2% (v/v) at OD_{600} = 0.5 and 1 mM IPTG at OD_{600} = 1.0. Cells were grown as described in the section *E. coli culture and overexpression*, Materials and Methods, and final OD_{600} was 7.28 and 2.2 for the C41 and BL21 cells, respectively.

Further, the cells were disrupted and c_1-subunit was purified as described in the sections *Cells disruption*, *Solubilization of membrane proteins from E.coli membranes*, *Ni-NTA purification* and *Size exclusion chromatography*, Materials and Methods. For C41 *E.coli* cells, after cells disruption several steps of membranes purification were tested (with DDM 0.1% (w/v), 1% (w/v) and NLS 1% (w/v)) (Fig. 5.12). The solubilisates were purified by Ni-NTA chromatography (Fig. 5.13A, B) and the samples were analysed by WB method (Fig. 5.13C). As it was shown, the pure band corresponding to c_1-subunit could be obtained using DDM detergent for solubilization of the protein (Fig. 5.13C, lane #11). It also leads to a clear visible peak on the Ni-NTA chromatogram, however, only ~50 mAU height (Fig. 5.13A, blue curve). If using NLS the WB showed a "ladder" of bands which can correspond to oligomers of the c_1-subunit, however, the peak on the Ni-NTA chromatogram almost disappeared (Fig. 5.13A, orange curve). Using this protocol, the quantity of the purified protein in general was not enough for further structural studies, therefore another purification protocol was established with BL21 *E. coli* cells.

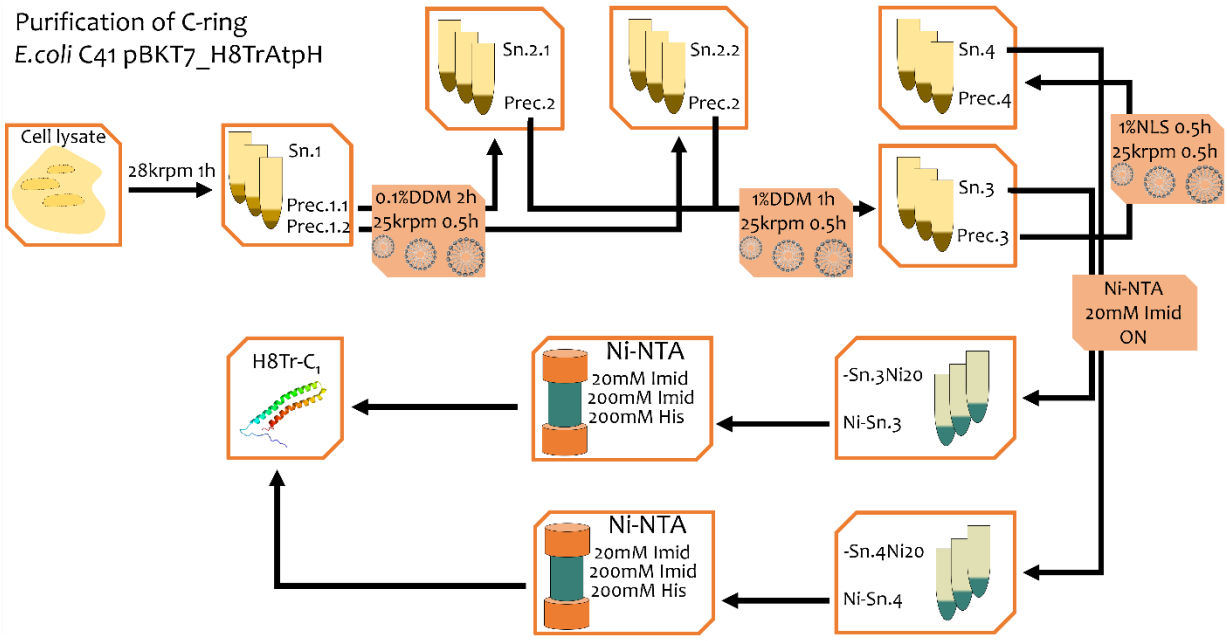

Figure 5.12. A scheme of purification protocol for recombinant c_1-subunit of cF_OF_1 from C41 *E.coli* cells with pBKT7_H8_Tr_AtpH* plasmid. "Sn." – supernatant, "Prec." – precipitant. "Imid" – imidazole, "-Sn.(3 or 4)Ni20" – discarded supernatant after batching the sample with Ni-NTA resin and 20 mM imidazole overnight, "Ni-Sn(3 or 4)" – Ni-NTA resin after batching the sample with 20 mM imidazole overnight. During Ni-NTA chromatography several steps were used. The column "20 mM Imid", "200 mM Imid", "200 mM His" denotes that three buffers containing imidazole 20 mM, imidazole 200 mM, and imidazole 200 mM with histidine 200 mM, respectively, were used to elute the sample.

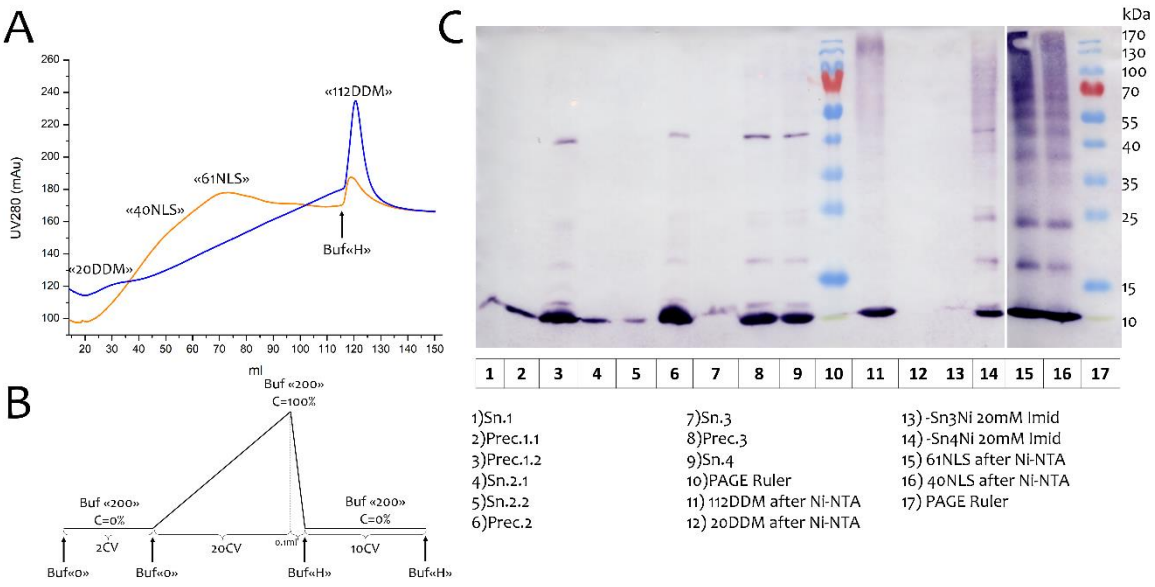

Figure 5.13. (A) Ni-NTA chromatogram of the samples solubilized in DDM 1% (w/v) (blue curve), and in NLS 1% (w/v) (orange curve) (names "20DDM", "112DDM", "40NLS", "61NLS"

denote a number of fraction and a detergent used for solubilization) and **(B)** corresponding scheme of experiment. "Buf 0" – a buffer: NaPi 20 mM, NaCl 100 mM, 6AHA 2 mM, 0.1%DDM, pH 7.8; "Buf 200" – a "Buf 0" with imidazole 200 mM, "Buf H" – "Buf 200" with histidine 200 mM. **(C)** WB of samples from all purification steps (Fig. 3.12).

For BL21 *E.coli* cells, after cells disruption the protein was solubilized with DDM 1% (w/v) (Fig. 5.14) and batched with a Ni-NTA resin in the presence of 20 mM imidazole overnight. Then, Ni-NTA and SEC chromatography were done to purify the sample and evaluate its molecular weight (Fig. 5.15A-C). Ni-NTA chromatogram showed a peak of ~ 1500 mAU height (30 times more than in case of the C41 *E.coli* cells) (Fig. 5.15A) and it was enough for the SEC evaluation of the protein (Fig. 5.15C). SEC was performed using Superdex G-200 (the working range: 60 – 600 kDa) and showed a number of peaks in range of 8.5 – 14 mL of eluted volume. Five of them at ~ (8.5, 10.5, 11.5, 13, 14) mL were analysed by SDS PAGE and WB (Fig. 5.15D, E). The peak at ~10.5 mL corresponds the literature to be associated with a complete c_{14}-ring from spinach chloroplasts [25], and SDS PAGE of this fraction showed a strong band at ~100 kDa (Fig. 5.15D, lane #7), however, WB showed only one weak band at ~10 kDa which corresponds to the c_1-subunit. The strong band on WB at ~10 kDa could be observed only for a SEC peak at ~8.5 mL, which corresponds large molecular mass (~ 400 – 500 kDa) and unlikely to be explained by c_{14}-ring. SDS PAGE also did not show a band at ~100 kDa region for this fraction. Therefore, aggregates of c_1-subunit were suggested to explain the SEC, SDS PAGE and WB experimental data due to their presence in all SEC fractions, however, there is no direct proof that complete c_{14}-ring was assembled.

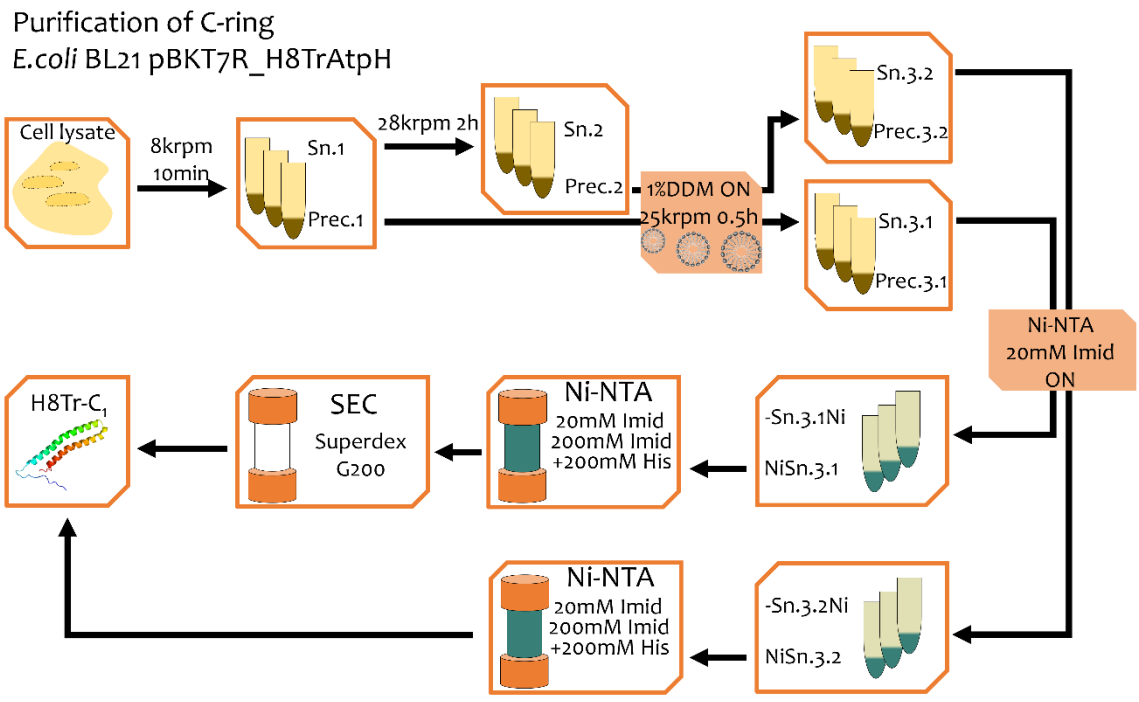

Figure 5.14. A scheme of purification protocol for recombinant c_1-subunit of cF_OF_1 from BL21 *E.coli* cells with pBKT7R_H8_Tr_AtpH* plasmid. "Sn." – supernatant, "Prec." – precipitant. "Imid" – imidazole, "-Sn.(3.1 or 3.2)Ni" – discarded supernatant after batching the sample with Ni-NTA resin and 20 mM imidazole overnight. "NiSn(3.1 or 3.2)" – Ni-NTA resin after batching the sample with 20 mM imidazole overnight. During Ni-NTA chromatography several steps were used. The column "20 mM Imid", "200 mM Imid", "200 mM His" denotes that three buffers containing imidazole 20 mM, imidazole 200 mM, and imidazole 200 mM with histidine 200 mM, respectively, were used to elute the sample.

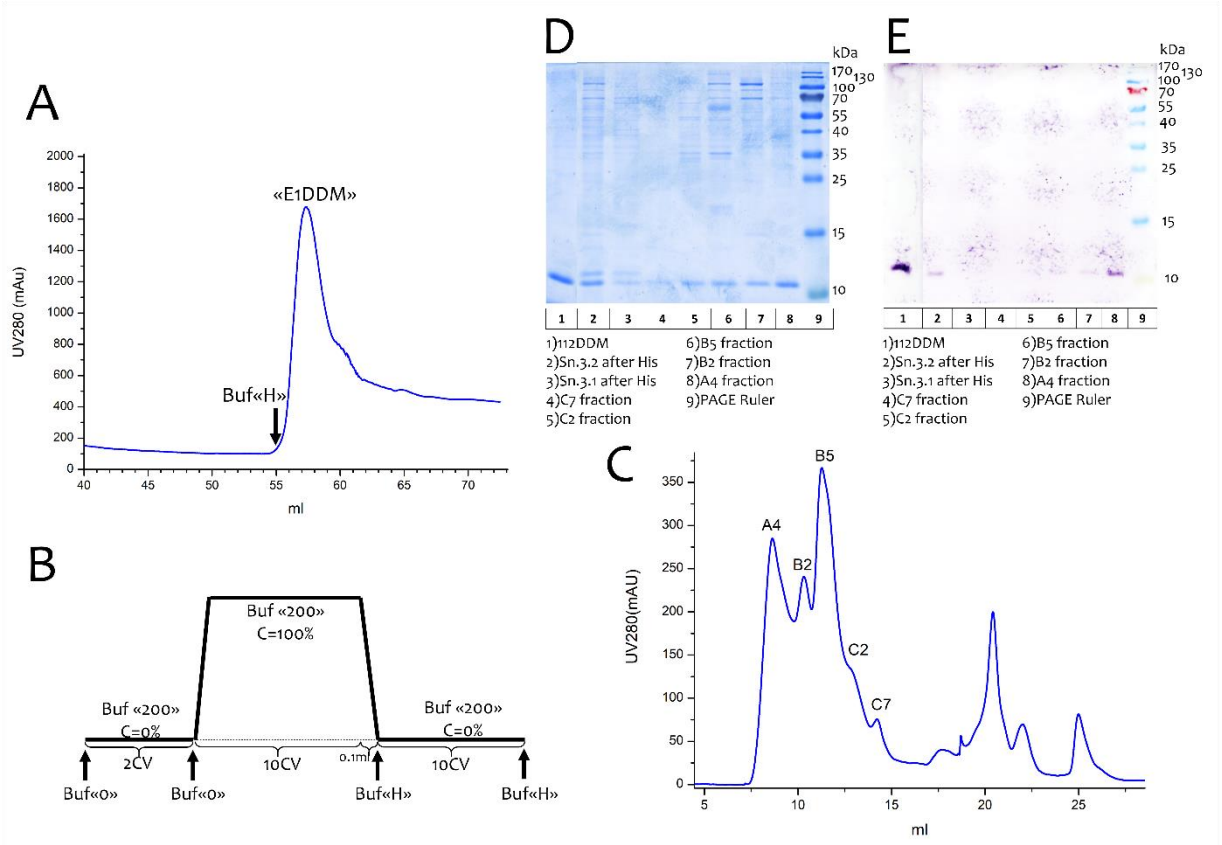

Figure 5.15. (A) Ni-NTA chromatogram of the samples solubilized in DDM 1% (w/v) (blue curve), name "E1DDM", denote a number of fraction and a detergent used for solubilization; and **(B)** corresponding scheme of experiment. "Buf 0" – a buffer: NaPi 20 mM, NaCl 100 mM, 6AHA 2 mM, 0.1%DDM, pH 7.8; "Buf 200" – a "Buf 0" with imidazole 200 mM, "Buf H" – "Buf 200" with histidine 200 mM. **(C)** SEC chromatogram of the fraction "E1DDM". **(D)** 15% SDS PAGE and **(E)** WB of samples after Ni-NTA and SEC chromatography described in Figure 5.14, and a comparison with the peak fraction after Ni-NTA chromatography of the C41 *E.coli* cells (Figs. 5.12, 5.13).

Thus, the trials showed a possibility of obtaining recombinant c_1-subunit of cF_OF_1 expressed in *E.coli*. In my thesis it is shown that *E.coli* cells are able to overexpress the spinach chloroplast c_1-

subunit of ATP synthase, however, the following purification did not resulted in the protein assembly into c_{14}-ring. This might have been that His-tags at N-terminus alpha helices did not allow the assembly of the circle from H8_Tr_AtpH protomers due to electrostatic reasons. However, the usage of Thrombin protease in order to cleave His-tags also did not improve the assembly even at high concentrations (Tr 0.1U per 5 ug of H8_Tr_AtpH). Thus, the protocol showed in principle the possibility of recombinant expression of c_1-subunits in *E.coli* cells, however, the assembly of the c_{14}-ring from c_1-subunits is still to be done.

The problems of assembly might be due to possible tight regulation of intact c-rings by the "plug". The literature and experimental data suggest unusually high stability of intact c-rings at harsh temperature and detergent conditions (~1% NLS, 65°C). Also these data show persistence of color of c-ring samples purified in such way and discoloration of samples only when dissociating the c-rings into protomers [25], [26]. All this implies that being once assembled into a membrane the c-ring remains a highly stable protein complex. Then the plug can be changed to phospholipids or proteins, or even removed at all [23] – the c-ring is still stable, but the very initial process of its self-assembly into a membrane seems to strongly depend on surrounding molecules that compose the inner "plug" of the c-ring.

5.2. Low resolution structure of intact ATP synthase from spinach chloroplasts

Checking the completeness of the cF_OF_1 was done by small-angle X-ray scattering (SAXS) method. The cF_OF_1 was in detergent micelles as well as reconstituted into nanodiscs.

5.2.1. Reconstituion of the ATP synthase into nanodiscs

The samples of cF_OF_1 purified by AEX or Red-120 chromatography were reconstituted into POPC/MSP1E3D1 nanodiscs (NDs) (detailed description in the section *Reconstitution into nanodiscs*, Materials and Methods). Briefly, at first, purified cF_OF_1 was mixed with POPC and MSP1E3D1, and then Sod. Ch. was added to final concentration of 1-2 CMC and incubated at near the phase transition of POPC (+4°C) for minimum 1 hor ON. Biobeads or Amberlite XAD-2 resin were used to absorb the excess of Sod. Ch., and SEC was performed for the final sample purification. The SEC of the samples with cF_OF_1/POPC/MSPE3D1 = 1/130/1 molar ratio showed two peaks at ~ 8 mL and ~ 14.5 – 15 mL elution volume (Fig. 5.16, black curve) and the samples in excess of NDs with cF_OF_1/POPC/MSPE3D1 = 1/2600/20 molar ratio showed several wide peaks with the major two peaks at ~ 11 – 11.5 mL and ~ 14.5 – 15 mL (Fig. 5.16, dashed magenta curve). The second peak of the samples in excess of NDs ~ 14.5 – 15 mL was associated with empty NDs. The fractions that showed peaks of A_{280} were analysed by SAXS.

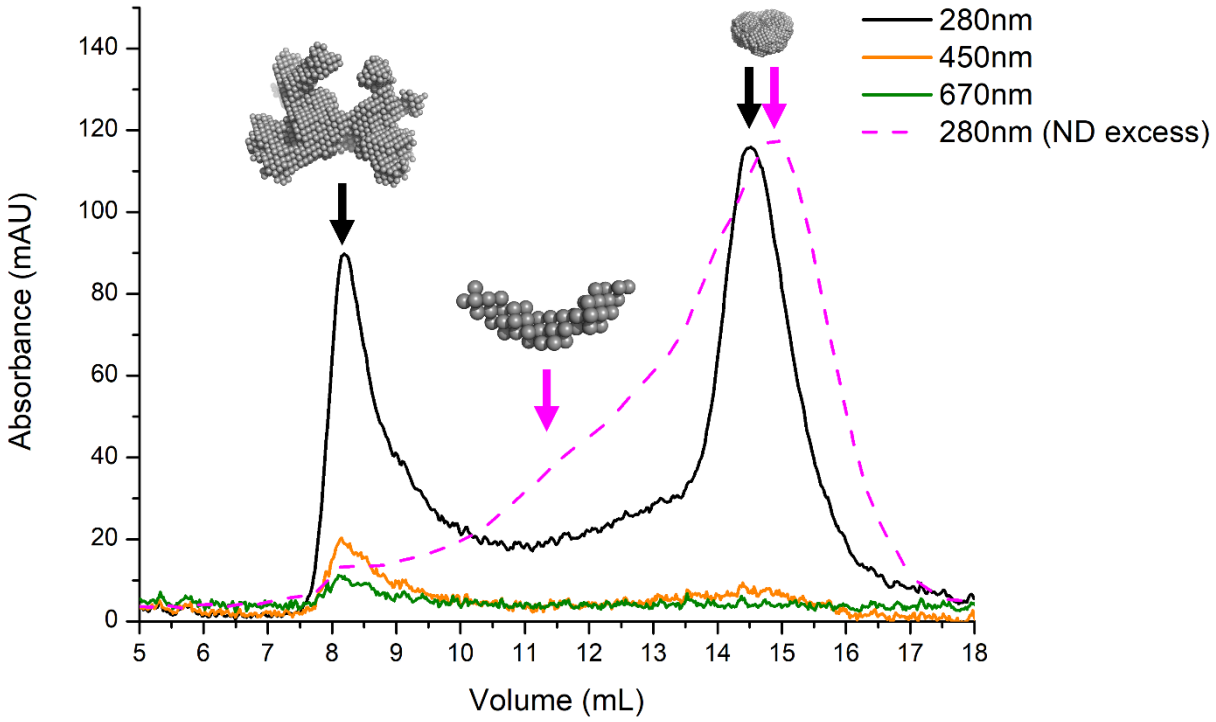

Figure 5.16. Size exclusion chromatography of ATP synthase reconstituted into POPC/MSP1E3D1 nanodiscs. Absorbances at 280, 450 and 670 nm are shown as black, orange and green lines, respectively. A dashed magenta line shows absorbance at 280 nm of the samples in excess of nanodiscs. Low-resolution structures obtained by SAXS are shown for corresponding peak fractions for both experiments (black and magenta arrows, respectively).

5.2.2. SAXS studies of the ATP synthase from spinach chloroplasts

Small-angle X-ray scattering (SAXS) was performed with the samples of cF_OF_1 reconstituted into nanodiscs in ratio cF_OF_1/POPC/MSPE3D1 = 1/130/1 and 1/2600/20 (excess of NDs) and purified by SEC. The samples that showed peaks of A_{280} were concentrated (30kDa cutoff) and thereafter were loaded into quartz capillaries which then were sealed and used for SAXS measurements (detailed description in the section *Samples preparation for SAXS measurements*, Materials and Methods).

SAXS measurements of the fractions from the peak of A_{280} at ~11 – 11.5 mL (cF_OF_1 in excess of NDs) showed objects with a radius of gyration R_g = 138.7 ± 5.9 Å (Fig. 5.17A) and a characteristic size D_{max} of ~ 440 Å according to corresponding pair-distance distribution function P(R) (Fig. 5.17B). Recovered 3D *ab initio* model showed a dimer-like structure that has a V-shape in one projection (V-projection) (Fig. 5.17C) and N-shape in another projection (N-projection) (Fig. 5.17D), so called V-N-shaped structure.

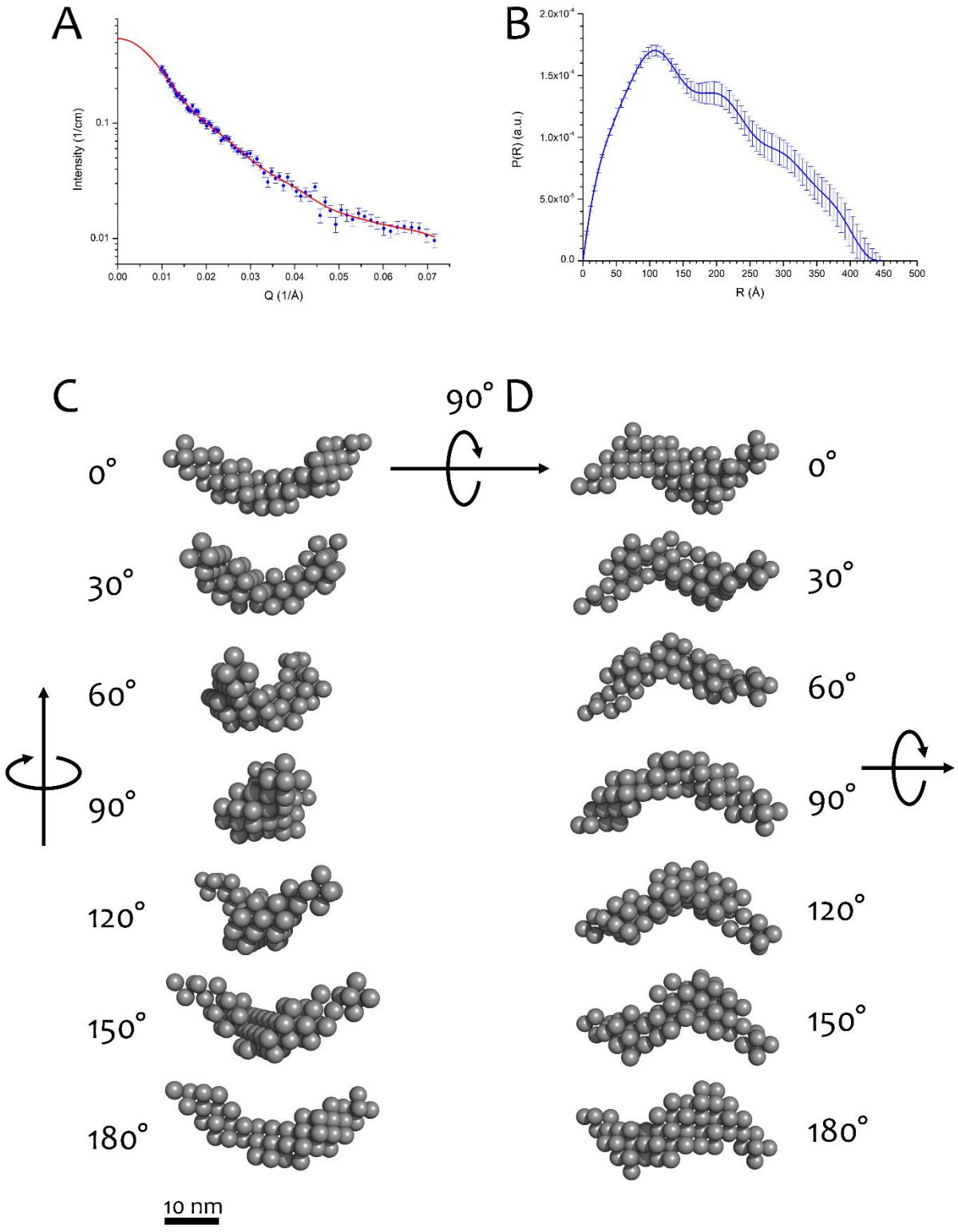

Figure 5.17. SAXS studies of cF_OF_1 in excess of NDs after SEC (fractions from the peak of A_{280} at ~11 – 11.5 mL). **(A)** A radially integrated 1D SAXS profile of intensity (I) *vs.* modulus of scattered vector (Q) (blue dots) and regularized model fit (red line); and **(B)** a pair-distance distribution function P(R) are shown. **(C)** Different projections of a 3D dummy atom *ab initio* low-resolution structure with a rotation around the vertical axis and **(D)** horizontal axis are shown with corresponding angles of rotation relatively to the structures in the first line (0°).

Superimposition of two cF_OF_1 PDB structures (6FKF) (*Spinacia oleracea*) (Fig. 5.18A-C), preliminary aligned with mtF_OF_1 dimer (6B8H) (*Saccharomyces cerevesiae*) (Fig. 5.18D), with the SAXS low-resolution structure showed a slight inconsistency that actually distinguishes between form-factors of V-N-shape and V-shape objects and results in ~30° mismatch in the projection where the structure has an "N" shape (Fig. 5.18B).

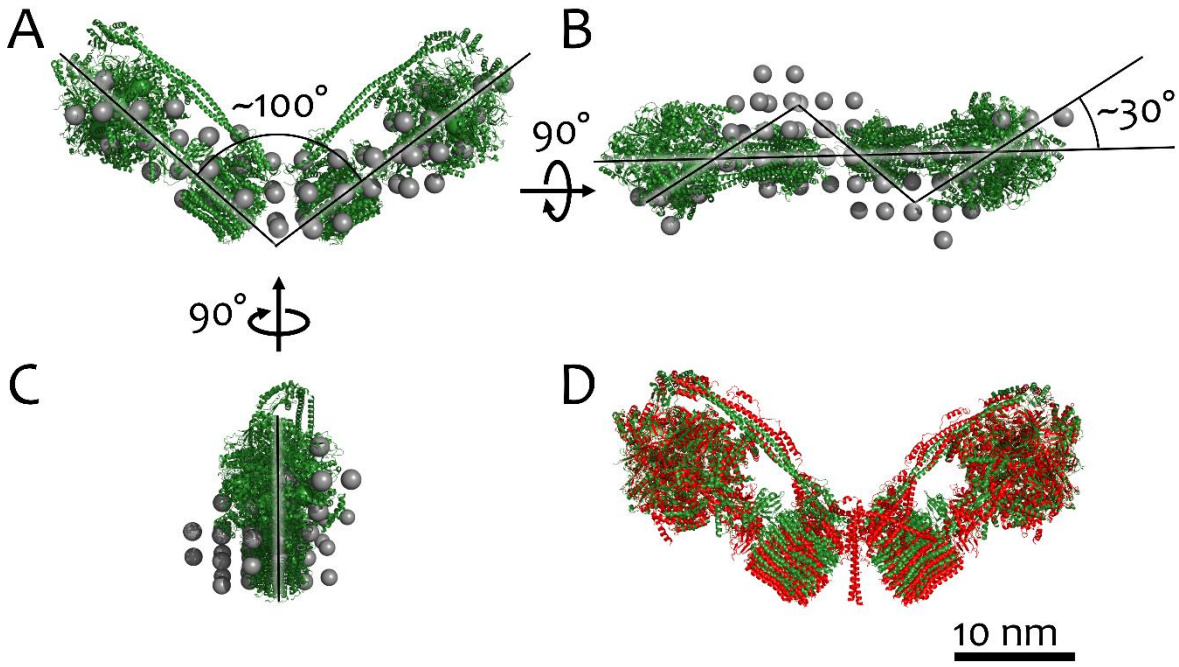

Figure 5.18. Superimposition of two cF_OF_1 PDB structures (6FKF [11]) with the SAXS low-resolution structure of cF_OF_1 in excess of NDs after SEC (fractions from the peak of A_{280} at ~11 – 11.5 mL). **(A)** The projection shows a V-shaped structure with the angle of about 100°. **(B)** The projection shows a ~30° mismatch between the V-shaped PDB structure (2x 6FKF) and the V-N-shaped low-resolution structure. **(C)** Another projection of the 2x 6FKF and the low-resolution structures. **(D)** Alignment of the 2x 6FKF and the structure of a mtF_OF_1 dimer from *Saccharomyces cerevesiae* (6B8H [59]) structures. 6FKF is shown in green and 6B8H – in red color. Low-resolution structure is shown as gray spheres.

The V-N-shape form-factor of the low-resolution structures persisted at a number of experiments with different protein/lipid/MSP molar ratio. The SAXS experiments with the samples that have a molar ratio cF_OF_1/POPC/MSP1E3D1 = 1/80/0.8 and were collected with a good statistic on the synchrotron X-ray source (I(Q) and P(R) are displayed in Fig. 5.19A, B). The data showed a similar V-N-shaped *ab initio* low-resolution structure, which has even less mismatch between form-factors of V-N-shape and V-shape (~10°) (Fig. 5.19C-E). The low-resolution structure was superimposed with two PDB structures of cF_OF_1 (6FKF) that were aligned with mtF_OF_1 dimer (6B8H) (Fig. 5.19F).

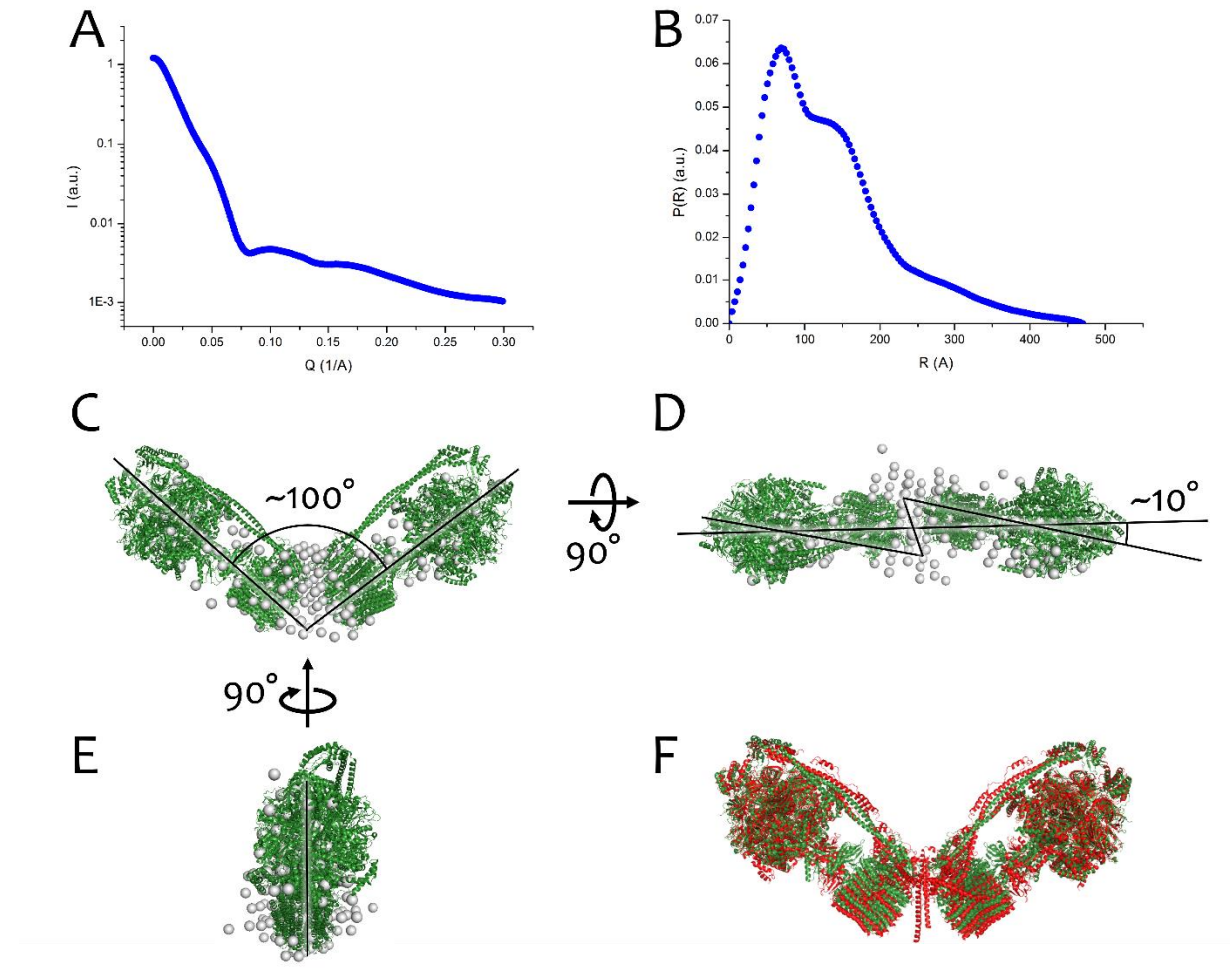

Figure 5.19. SAXS studies of the samples with a molar ratio cF_OF_1/POPC/MSP1E3D1 = 1/80/0.8 after SEC (fractions from the peak of A_{280} at ~12.5 mL). **(A)** A radially integrated 1D SAXS profile of intensity (I) *vs.* modulus of scattered vector (Q) (blue dots) and **(B)** a pair-distance distribution function P(R) are shown. Superimposition of two cF_OF_1 PDB structures (6FKF [11]) with the SAXS low-resolution structure of cF_OF_1 (gray spheres) is shown in three projections: the **(C)** projection displays a V-shaped structure with the angle of about 100°, **(D)** is another projection of the 2x 6FKF and the low-resolution structures, and the **(E)** projection displays a ~10° mismatch between the V-shaped PDB structure (2x 6FKF) and the V-N-shaped low-resolution structure. **(F)** Alignment of the 2x 6FKF and the structure of a mtF_OF_1 dimer from *Saccharomyces cerevesiae* (6B8H [59]) structures. 6FKF is shown in green and 6B8H – in red color.

The samples with a molar ratio cF_OF_1/POPC/MSPE3D1 = 1/130/1 showed peaks of absorbance corresponding to aggregates and empty NDs (Fig. 5.16). As a control experiment, SAXS was done to study the fractions from the peaks at ~ 8 mL and ~ 14.5 – 15 mL. Aggregates have been observed in case of the peak at ~ 8 mL with a D_{max} > 800 Å (Fig. 5.20A, B) and a low-resolution structure showed a characteristic form-factor corresponding to disordered aggregates (Fig. 5.20C).

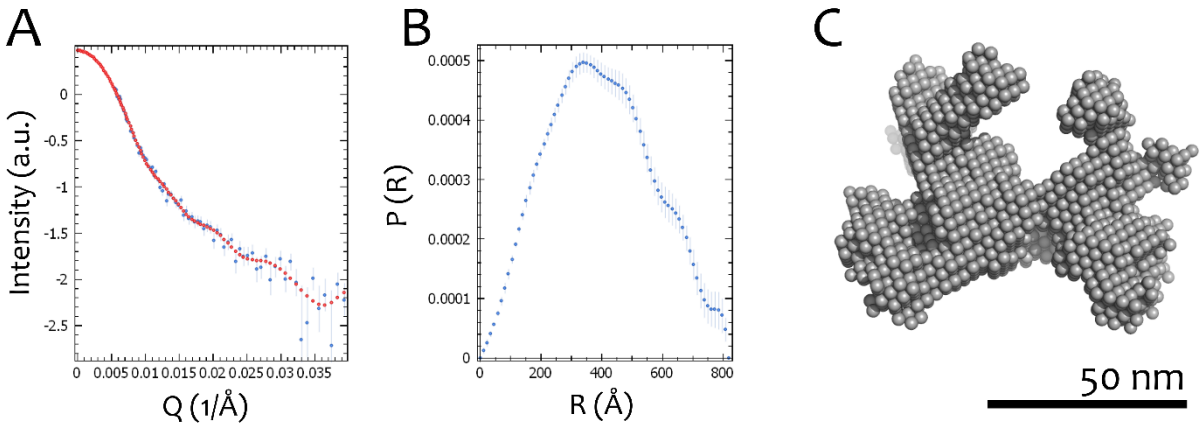

Figure 5.20. SAXS studies of the samples with a molar ratio cF_OF_1/POPC/MSP1E3D1 = 1/130/1 after SEC (fractions from the peak of A_{280} at ~8 mL). **(A)** A radially integrated 1D SAXS profile of intensity (I) *vs.* modulus of scattered vector (Q) (blue dots) and regularized model fit (red dots); **(B)** a pair-distance distribution function P(R); and **(C)** a low-resolution *ab initio* structure are shown (gray spheres).

Empty NDs have been observed at the ~ 14.5 – 15 mL by SAXS. It showed a D_{max} = 150 Å (Fig. 5.21A, B), and a low-resolution structure was well-fitted by a PDB model of MSP1E3D1 lipid ND (Fig. 5.21C, D).

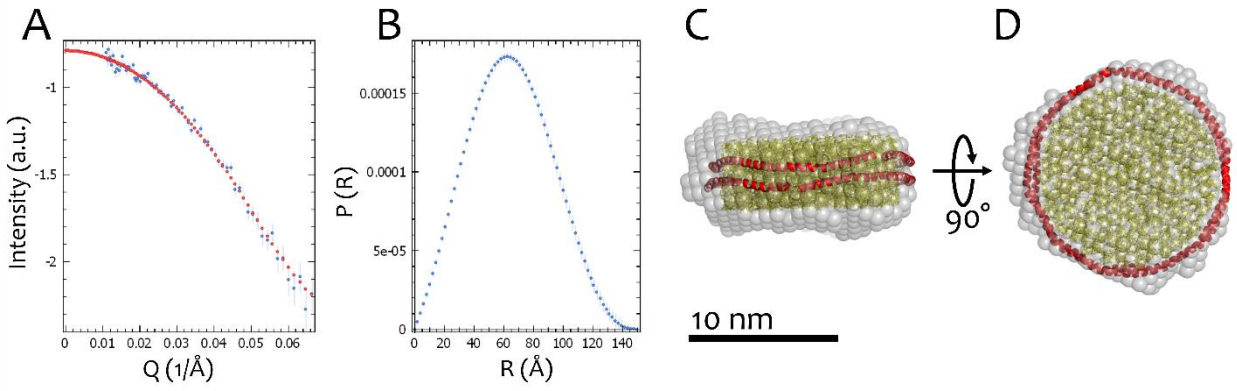

Figure 5.21. SAXS studies of the samples with a molar ratio cF_OF_1/POPC/MSP1E3D1 = 1/130/1 after SEC (fractions from the peak of A_{280} at ~14.5 – 15 mL). **(A)** A radially integrated 1D SAXS profile of intensity (I) *vs.* modulus of scattered vector (Q) (blue dots) and regularized model fit (red dots); **(B)** a pair-distance distribution function P(R) are shown. Superimposition of a PDB model of MSP1E3D1 lipid ND with the SAXS low-resolution structure (gray spheres) is shown in two projections: **(C)** from the inside of the membrane and **(D)** from the outside of the membrane. MSP1E3D1 is shown in red and lipids inside the ND are shown in yellow color.

For a control, SAXS was done with the samples of cF_OF_1 in detergent micelles (tPCC-α-M) after purification by AEX chromatography – this samples were used for reconstitution into nanodiscs. It showed a D_{max} = 250 Å (Fig. 5.22 A, B), and a low-resolution structure was well-fitted by a PDB model of cF_OF_1 (Fig. 5.22C).

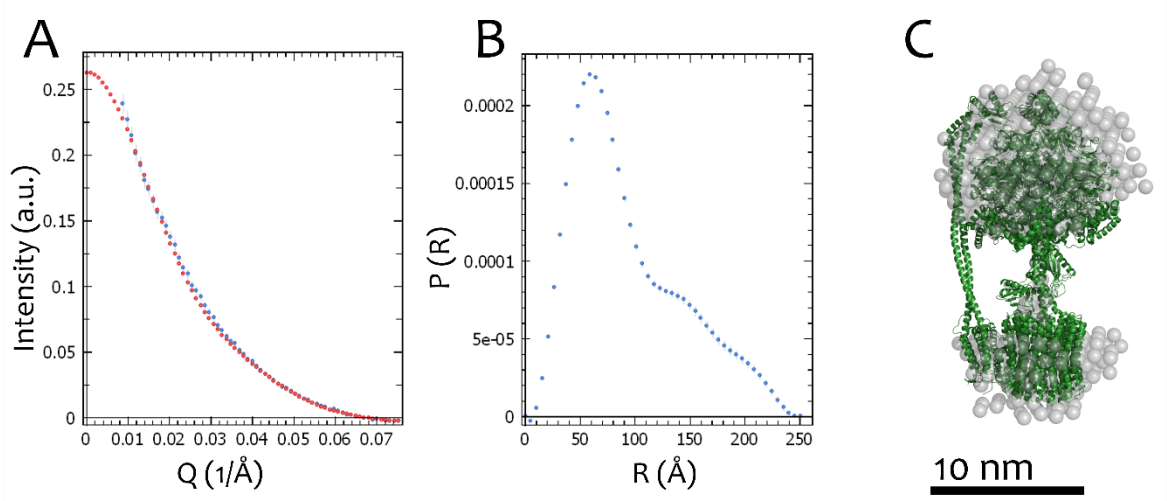

Figure 5.22. SAXS studies of cF_OF_1 in detergent micelles (tPCC-α-M). **(A)** A radially integrated 1D SAXS profile of intensity (I) *vs.* modulus of scattered vector (Q) (blue dots) and regularized model fit (red dots); **(B)** a pair-distance distribution function P(R) are shown. **(C)** Superimposition of cF_OF_1 PDB structure (6FKF [11]) with the SAXS low-resolution structure is shown.

Thus, in my thesis it is demonstrated that spinach cF_OF_1 may form V-N-shape dimer-like objects. The V-N-shape dimer-like objects might assemble in thylakoid membranes and act as non-functional dimers of ATP synthases during regulation processes. Although additional structural studies are required to check our suggestion the fact that cF_OF_1 may form dimeric structures is intriguing and this phenomenon should be investigated in further research.

5.3. High-resolution structure of a c-ring from spinach chloroplasts

5.3.1. Crystallization and structure determination of the c-ring from intact ATP synthase

In this part of my thesis, intact ATP synthase from spinach chloroplasts (cF_OF_1) was used for crystallization by *in meso* and vapor diffusion (VD) methods as a starting crystallization material.

The cF_OF_1 (~4 mg/mL) in a buffer HEPES 30 mM, $MgCl_2$ 2 mM, NaCl ~300 mM, ~0.04% (w/v) tPCC-α-M, pH 8.0 (after purification by AEX chromatography) was concentrated with 100kDa cutoff reaching the final concentration of ~80 mg/mL. Then the concentration of tPCC-α-M was measured by Fourier-transform infrared spectroscopy (FTIR) and was about ~2.5% (w/v) in the samples that were used for crystallization trials.

Crystallization was performed by VD and *in meso* methods with a wide screening of different conditions. For VD crystallization five commercially available kits were used: Classics Suite and PEGs I (Qiagen), JCSG + MD and PACT MD (Molecular Dimensions), and Wizard I & II (Rigaku) (Rigaku Reagents). After two weeks transparent needle-shape crystals ~100 – 300 µm length appeared predominantly in Classics Suite, PEGs I, PACT (MD) and Wizard I & II (Rigaku) (Fig. 5.23).

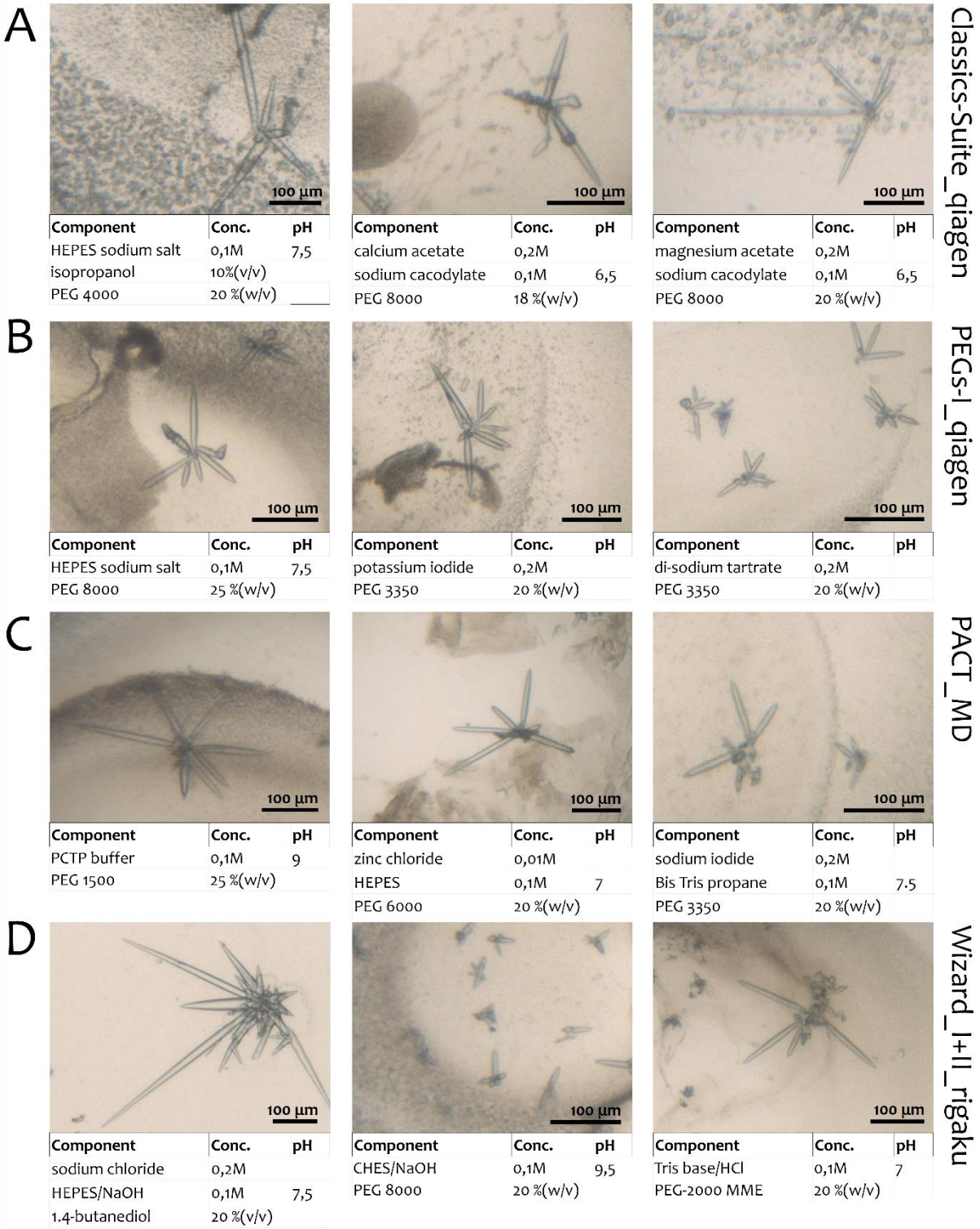

Figure 5.23. A gallery of crystals obtained by VD method using the cF_OF_1 (~80 mg/mL) in ~ 2.5% (w/v) tPCC-α-M as a starting crystallization material. Selected images from **(A)** Classics Suite and **(B)** PEGs I (Qiagen) kits, **(C)** PACT (MD) (Molecular Dimensions), and **(D)** Wizard I & II (Rigaku) (Rigaku Reagents) kits are shown.

Some of the crystals were checked by XRD and showed spots corresponded to protein diffraction, however, with cell dimensions of ~30 x 50 x 50 Å and resolution ~ 8 Å. The cell dimensions were not enough to fit even a c-ring of cF_OF_1 and low resolution did not allow to solve the structure. In addition, some of the crystals showed circles or circular arcs, but not spots on a diffraction pattern, which indicated the low quality of the crystals. Thus, although VD method seems very attractive for crystallization of the full-length cF_OF_1, there is still a challenge to find optimal conditions of crystallization. Other VD crystallization trials with different conditions did not improve these results. The problems might be in stabilization of cF_OF_1 in solution and proteolytic activity that in spite of the presence of different protease inhibitors accounted significantly during long-term experiments. Concerning protein stabilization, rapid clustering of proteins in a crystallization probe could lead to poor quality protein crystals due to the fast growth of the latter. Thus, *in meso* crystallization was used to solve the possible problems of protein stabilization.

For *in meso* crystallization the intact cF_OF_1 (~4 mg/mL) in a buffer HEPES 30 mM, $MgCl_2$ 2 mM, NaCl ~300 mM, ~0.04% (w/v) tPCC-α-M, pH 8.0 (after purification by AEX chromatography) or in a buffer 20 mM Tris, 5 mM $MgCl_2$, 0.02% (w/v) NaN_3, 0.2% (w/v) DDM, pH 7.5 (after purification by Red-120 chromatography) was concentrated (100kDa) and used as a starting crystallization material. Different conditions were screened using the kits Qiagen cubic phase I and II (QCPI and QCPII, respectively) (Table 5.3).

Table 5.3. Crystallization trials (*in meso* method) for the cF_OF_1. 0.1QCPI and 0.1QCPII – 10 times diluted (in mQ) QCPI and QCPII kits, respectively. Monoolein (MO) was used as a matrix lipid in different MO/buffer (v/v) ratios, where "buffer" means a protein in a corresponding buffer. Phase/prec. (v/v) ratio shows the ratio between the volume of a lipid mesophase mixed with a protein in a corresponding buffer and the volume of precipitant in a corresponding kit.

№	Final conc. ATPs [mg/mL]	Phase/prec. (v/v) (nL/nL)	Kit	MO/buffer (v/v)	Purification protocol
1	43.3	150/500	0.1QCPI	1:2	AS precipitation (1.2 – 1.8 M); resuspension in a buffer containing tPCC-α-M; AEX chromatography. The sample of ~4 mg/mL cF_OF_1 in a buffer HEPES 30 mM, $MgCl_2$ 2 mM,
2	43.3	150/500	0.1QCPII		
3	43.3	150/500	QCPI		
4	43.3	150/500	QCPII		
5	80	150/500	0.1QCPI		
6	80	150/500	0.1QCPII		

7	80	150/500	QCPI		NaCl ~300 mM, ~0.04% (w/v) tPCC-α-M, pH 8.0 was concentrated (100kDa) to ~80 mg/mL cF_OF_1 (~2.5% tPCC-α-M) and used for crystallization.
8	80	150/500	QCPII		
9	36.4	150/500	0.1QCPI	1:5	
10	36.4	150/500	0.1QCPII		
11	36.4	150/500	QCPI		
12	36.4	150/500	QCPII		
13	50.9	150/500	0.1QCPI		
14	50.9	150/500	0.1QCPII		
15	50.9	150/500	QCPI		
16	50.9	150/500	QCPII		
17	27.4	50/800	QCPI	1:2	AS precipitation (1.2 – 1.8 M); resuspension in a buffer containing DDM; Rate-zonal centrifugation in sucrose gradient (collected fractions at 29-36%); desalting and Red-120 chromatography. The sample of ~4 mg/mL cF_OF_1 in a buffer 20 mM Tris, 5 mM $MgCl_2$, 0.02% (w/v) NaN_3, 0.2% (w/v) DDM, pH 7.5 was concentrated (100kDa) to ~27.4 mg/mL cF_OF_1 and used for crystallization.
18	27.4	50/800	QCPI	2:3	

Yellow cubic-shape crystals of ~20x20x20 μm size appeared in two months in crystallization plates #17 and 18 from Table 5.3. The example of the crystals is shown in Figure 5.24.

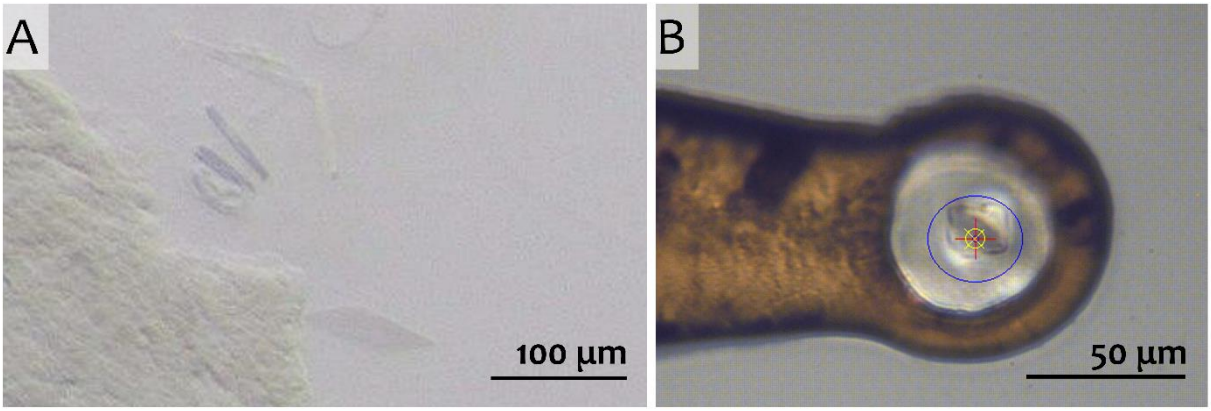

Figure 5.24. (A) A photograph of crystals of the c-ring obtained by *in meso* method using the cF_OF_1 (~27.4 mg/mL) in DDM as a starting crystallization material. **(B)** The crystal of the c-ring in a loop, which was used for dataset collection. All crystals have a strong yellow color.

In contrary to that obtained by VD method, these crystals resulted in ~2.5 – 3.0 Å protein diffraction and appeared to be a c-ring of cF_OF_1. The best crystals were obtained under conditions ~27.4 mg/mL cF_OF_1 and 0.1M MES pH 5.8, 1.4 M AS precipitate solution from QCPI kit. They were used to collect dataset with the resolution of 2.3 Å, the cell dimensions 93.14, 96.34, 158.68 Å, and I121 space group according to molecular replacement (MR) method. The data statistics is

shown in Table 5.4 and in our publication [26]. Crystal packing is presented in Figure 5.25. Structure determination and refinement were performed as described in the section *XRD data treatment and high-resolution structure determination* in Materials and Methods.

Table 5.4. The data collection and refinement statistics of a c-ring of cF_OF_1 from *Spinacia oleracea*. The table was adapted from [26].

Data collection	
Space group	I 1 2 1
Cell dimensions	
a, *b*, *c* (Å)	93.14, 96.34, 158.68
α, *β*, *γ* (°)	90, 106.72, 90
Wavelength (Å)	0.979
Resolution (Å)	48.17-2.30 (2.36-2.30)
R_{merge} (%)	19.2 (116.9)
R_{pim} (%)	15.7 (92.6)
$I/\sigma I$	4.9 (1.2)
CC1/2 (%)	99.3 (42.1)
Multiplicity	3.7 (3.5)
Completeness (%)	96.7 (75.6)
Unique reflections	57,691 (3484)
Refinement	
Resolution (Å)	20-2.30
No. reflections	54,827
R_{work}/ R_{free} (%)	21.0/24.5
No. atoms	
Protein	7935
Water	15
Lipid fragments	132
B-factors (Å^2)	
Protein	30
Water	34
Lipid fragments	48
R.m.s deviations	
Protein bond lengths (Å)	0.0056
Protein bond angles (°)	0.8712
Ramachandran analysis	
Favored (%)	97.5
Outliers (%)	0

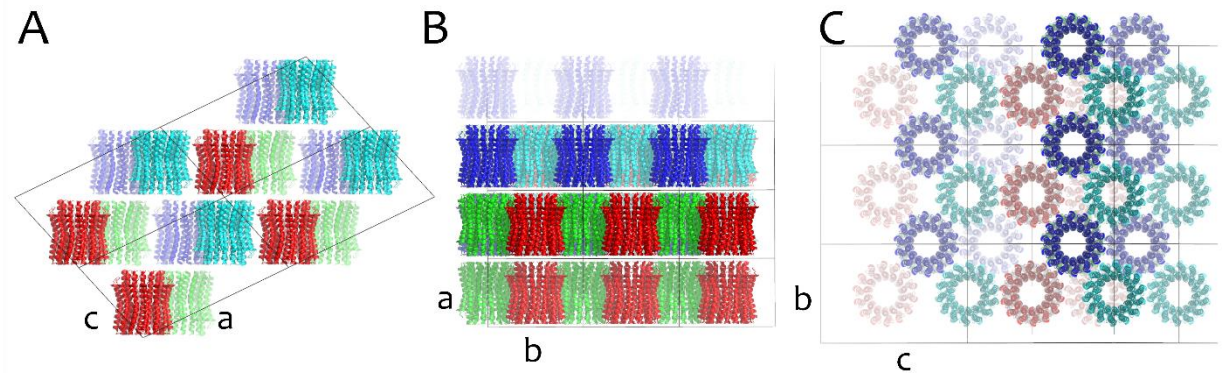

Figure 5.25. Crystal packing of the c-ring of cF_OF_1 has I121 space group of symmetry. The angles (α, β, γ) = (90.0°, 106.72°, 90.0°) and the cell dimensions (a, b, c) = (93.14 Å, 96.34 Å, 158.68 Å). The projections on **(A),** a/c **(B),** a/b **(C),** b/c planes are shown.

The full-length cF_OF_1 did not assemble into crystals due to possible limitations of *in meso* method mentioned in the corresponding section *Crystallization trials* in Literature Overview. The probability of reconstitution of the full-length cF_OF_1 into MO mesophases with diameters of water channels ~ 40 – 50 Å is negligible. Nevertheless, the c-ring well fits the conditions and was assembled in the crystals in lipid mesophases. Thus, during this work the subunits of ATP synthase were obtained by *in meso* crystallization in the first time.

5.3.2. Overview of the c-ring structure

The high-resolution structure (2.3 Å) showed a c-ring of cF_OF_1 from *Spinacia oleracea* that consists of 14 c_1-subunits (protomers). Each protomer consists of two alpha helices and has a "hairpin" shape. The alpha helices are connected by a loop in the stroma part of the chloroplast (Fig. 5.26A). The protomers are assembled in circles so that each protomer has one inner and one outer alpha helix (Fig. 5.26B, C).

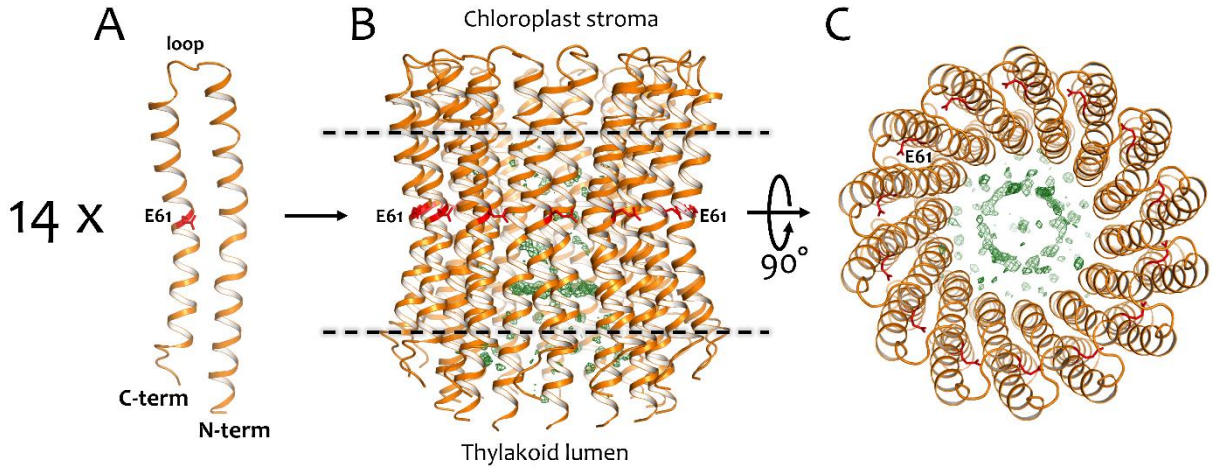

Figure 5.26. Overall structure of the c_{14}-ring of cF_OF_1 from *Spinacia oleracea* that consits of 14 protomers. **(A)** A protomer of the c_{14}-ring. **(B)** Assembled c_{14}-ring (a lateral view). **(C)** Assembled c_{14}-ring (a view from chloroplast stroma). Active center E61 is shown red. Polar/apolar interfaces outside the c_{14}-ring are shown as dashed black lines.

The overall structure (Fig 5.27A) shows the main features of the c-ring of cF_OF_1 such as complete c_1/c_1 interface that is organized by the net of hydrogen bondings forming direct and water-mediated intersubuint interactions (Fig 5.27B – D); the active center of the c-ring – E61 in the protonated ("closed") state and also takes part into c_1/c_1 interactions (Fig 5.27D); and additional positive

electron densities in the central pore of the c-ring which form circles parallely to the membrane plane. One more feature of the c-ring structure is a large hydrophobic region in its central pore, that is significantly thicker than the membrane lipid bilayer in which the c-ring is incorporated.

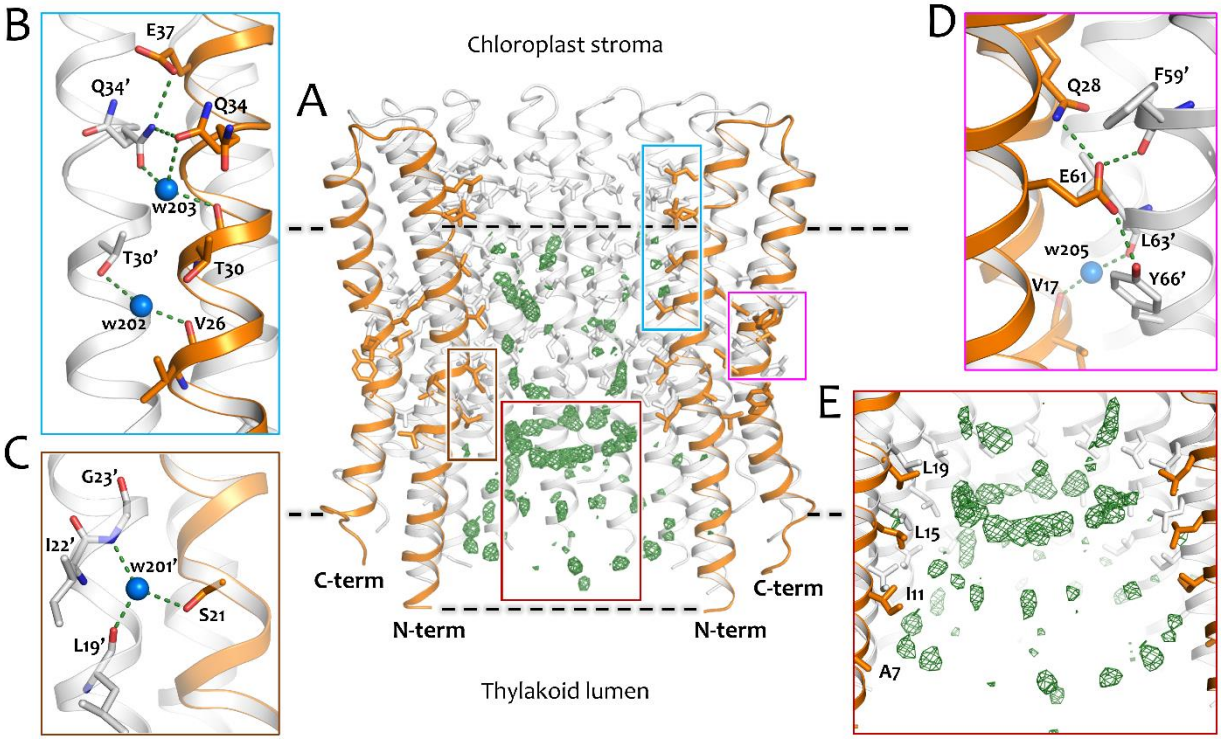

Figure 5.27. (A) Overall structure of the c_{14}-ring of cF_OF_1 from *Spinacia oleracea*. **(B)** c_1/c_1 contacts between inner alpha helices near the stromal part of membrane. **(C)** c_1/c_1 contacts between inner alpha helices near the lumenal part of membrane. **(D)** Active center (E61) of the c-ring and c_1/c_1 contacts in this region. **(E)** Additional electron densities in the central pore of the c-ring. A green mesh shows $F_O - F_C$ map at 3σ. Hydrogen bindings are shown as dark-green dashed lines. Amino acids of neighbor protomers are marked with apostrophe sign. Polar/apolar interfaces are shown as dashed black lines. Five c_1-subunits were hidden for convenient view on the central pore.

5.3.3. The structure of the active center (surrounding of Glu61)

The active center of the c_{14}-ring is an amino acid Glu61 (E61) in the middle of the outer alpha helix of the protomer (Fig. 5.27A). The structure of the c_{14}-ring was obtained in protonated (closed) conformation of the active center. Glu61 residue is coordinated by hydrogen bondings directly with Gln28 residue of the same protomer on its inner alpha helix, Tyr66' residue and oxygen of Phe59' of the neighbor protomer (Fig. 5.27D). This type of coordination is characteristic for the c_{14}-ring. In c-rings with smaller stoichiometries (actually less than 14 protomers) there is a water-mediated coordination of the active centers. However, all available high-resolution structures of c-rings are also in a closed state, except one – a c_{10}-ring from yeast mtF_OF_1, 3U2F, [22].

I compared closed and opened states of the active centers (E59) of c_{10}-ring from yeast mtF_OF_1 (Fig. 5.28A). It was shown that the E59 (Glu59) residue rotates through the $CH_2 - CH_2$ bond at the angle ~95° (Fig. 5.28B). Comparison of active centers of the c_{14}-ring from spinach cF_OF_1 and c_{10}-ring from yeast mtF_OF_1 allowed suggesting a molecular mechanism of conformational changes during protonation/deprotonation processes in a c-ring from spinach chloroplasts (Fig. 5.28C).

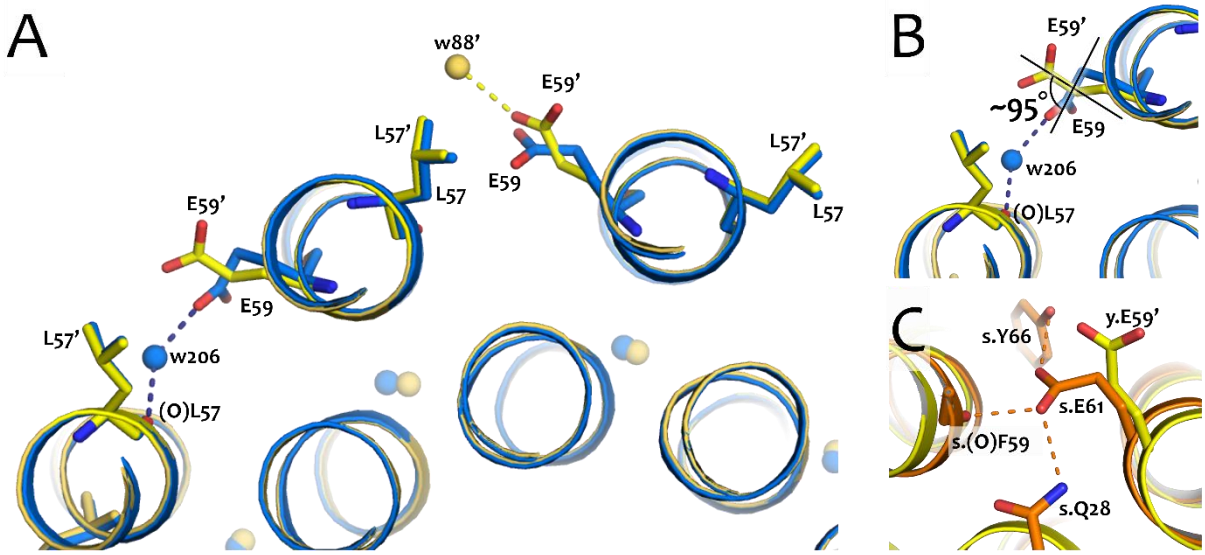

Fig. 5.28. Comparison of active centers of different c-rings in opened and closed states. **(A)** Alignment of structures of opened (3U2F, [22]) and closed (4F4S, [112]) states of a c_{10}-ring from yeast mtF_OF_1 (blue and yellow colors, respectively). **(B)** Alignment of the active centers E59 of c_{10}-ring from yeast mtF_OF_1. The angle between $CH_2 - CH_2$ bonds is ~95°. **(C)** Alignment of the active centers E59 of a c_{10}-ring from yeast mtF_OF_1 in opened state (3U2F) and the E61 of a c_{14}-ring from spinach cF_OF_1 in closed state (6TQJ, [26]) (yellow and orange colors, respectively). The view is from F_1 part of ATP synthase and hydrogen bindings are shown as dashed lines. The figure was adapted from [26].

Comparison of active centers between c-rings from different organisms showed interesting feature that c-rings with 14 or more protomers (according to what is known) have their active centers coordinated directly by amino acids of the same or neighbor protomers. Two oxygens of E61 are coordinated by Q28, F59', Y66' in case of c_{14}-ring from spinach chloroplast (6TQJ) (Fig. 5.29A) [26]; and two oxygens of E62 are coordinated by Q29, F60', Y67' in case of c_{15}-ring from bacteria *Arthrospira platensis* (2XQU) (Fig. 5.29D) [19]. Those c-rings with less than 14 protomers have a water hydrogen bond mediated coordination of their active centers. One oxygen of E59 is coordinated by L57' via W201 in case of c_{10}-ring from yeast mitochondria (5BPS) (Fig. 5.29B) (Mueller, D.M., to be published); and one oxygen of E54 is coordinated by A53' and V56' via W2006 in case of c_{13}-ring from bacteria *Bacillus pseudofirmus* (4CBK) (Fig. 5.29C) [21].

Thus, different organisms have different coordination of the active centers of their c-rings with a variability of amino acids involved into coordination depending on the c-ring stoichiometry. This might be due to the necessity of accurate positioning of protomers in order to form required angles between them. In our work, the coordination of the active center of the c_{14}-ring from chloroplasts was shown.

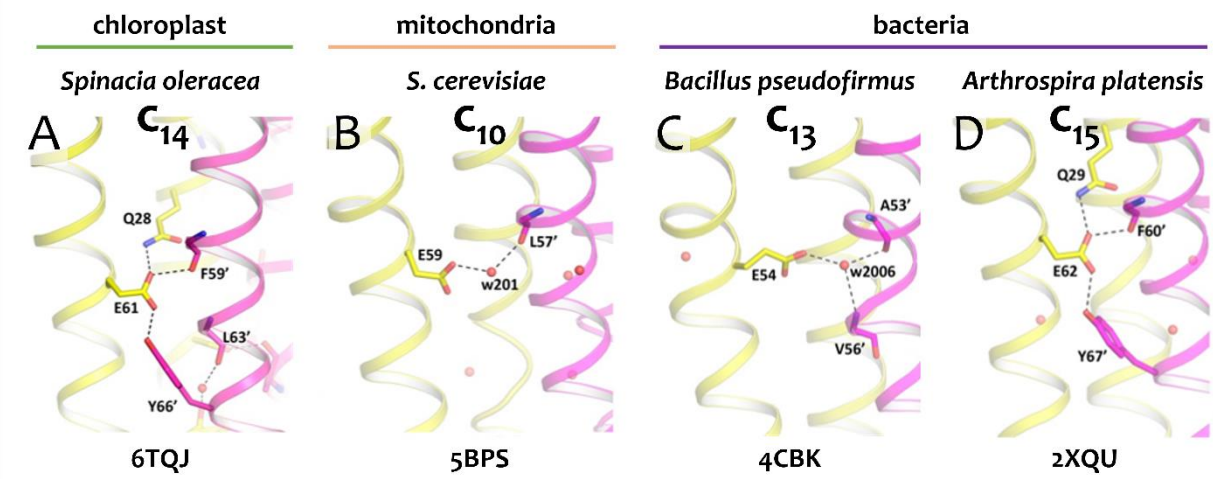

Figure 5.29. Comparison of active centers of c-rings from different organisms: **(A)** a c_{14}-ring of cF_OF_1 from *Spinacia oleracea* (6TQJ) [26], **(B)** a c_{10}-ring of mtF_OF_1 from *Saccharomyces cerevisiae* (5BPS) (Mueller, D.M., to be published), **(C)** a c_{13}-ring of bF_OF_1 from *Bacillus pseudofirmus* (4CBK) [21], and **(D)** a c_{15}-ring of bF_OF_1 from *Arthrospira platensis* (2XQU) [19]. The structures are shown without ligands. Neighbor protomers are shown in yellow and magenta, respectively. The figure was adapted from [26].

5.3.4. Complete c_1/c_1 interface

Analogous to coordination in the region of the active center, the protomers are connected by hydrogen bindings in the other regions. A net of hydrogen bindings form a c_1/c_1 interface that determines angles between protomers and, therefore, the stoichiometry of the c-ring. In my thesis, the complete c_1/c_1 interface of the c_{14}-ring from spinach chloroplasts is experimentally shown as well as the role of interlacing motifs G(A,S)xxxG(A,S) in the intersubunit interactions, that was theoretically predicted in the study [30] (Fig. 5.30). Missing details were added to the previous picture.

The hydrogen bindings between outer alpha helices of neighbor protomers are only in the region of the active center E61, so that it is also involved in the c_1/c_1 interface (Fig. 5.30A, C). As it was mentioned before, E61 is coordinated directly by Q28, F59' and Y66' that is characteristic for c-rings with large stoichiometries (more than 14 protomers, according to what is known). In addition, the contact between L63' and V17 via water molecule w205 connects the outer alpha helix with

the inner one of the neibour protomer (Fig. 5.30C). The hydrogen bindings between inner alpha helices of neighbor protomers encompass a wide region about half of the protomer length (Fig. 5.30B, D). Double conformations of Q34 are connected directly and via the water molecule w203, also there is a connection between Q34 and E37 directly, and between Q34 and T30 via the water molecule w203. T30' is connected with V26 via water w202 and S21 is connected with L19' and a backbone of G23' via water molecule w201' (Fig. 5.30D).

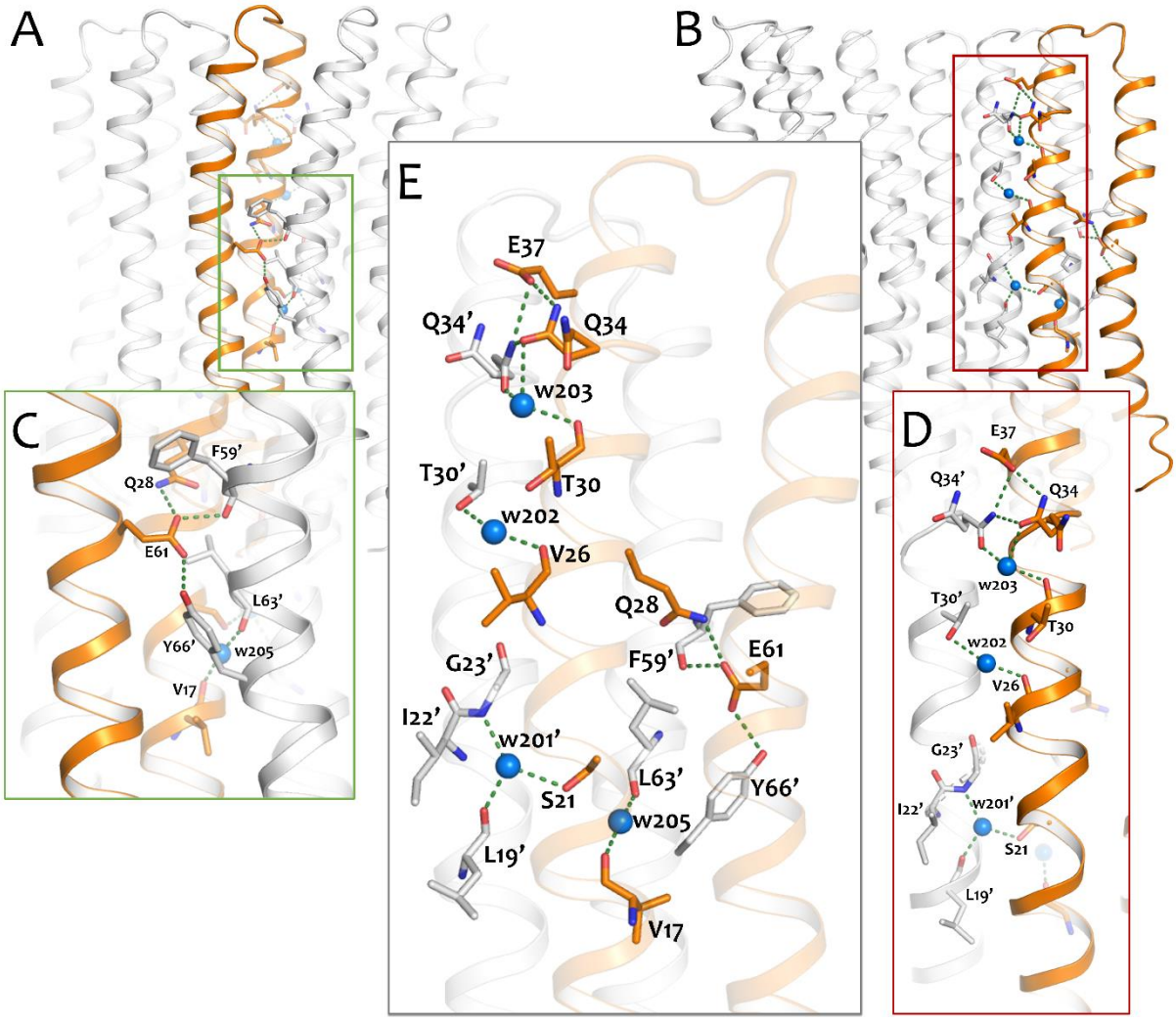

Figure. 5.30. A map of hydrogen bindings forming c_1/c_1 interface. **(A)** A lateral view from the outside of the c-ring. **(B)** A lateral view on the inner pore of the c-ring. **(C)** A map of hydrogen bindings between outer alpha helices of neighbor protomers. **(D)** A map of hydrogen bindings between inner alpha helices of neighbor protomers. **(E)** A complete map of c_1/c_1 interface hydrogen bindings. Neighbor protomers in panels C – E are colored orange and light gray, respectively.

Comparison with the c_1/c_1 interfaces of c-rings of different organisms showed that hydrogen bindings can differ in order to adjust the required angle between neighbour protomers. The c-rings with 9 or 10 subunits have more distant outer alpha helices than ones with 14 or 15 subunits (Fig.

5.31). This explains the absence of conserved amino acids in this region, except those in the neighbourhood of the active center. Inner alpha helices of neighbour protomers interact in two regions: one is close to the F_1 part of corresponding ATP synthase and occurs due to a number of polar amino acids that compose this part of a c-ring, – this region is usually mediated by several water molecules and has a wide net of hydrogen bonds; and another one is in front of the active center between the inner alpha-helices, – here the interactions are mediated by one water molecule, but in the case of c-rings with 9 or 10 subunits the connection is tighter due to direct interaction of this water molecule with oxygens and nitrogens of the backbone of the neighbor protomer. The latter mentioned region (Fig. 5.31, marked with dashed red ellipse) is only one of key determinants of the c-ring stoichiometry and is connected with the motifs G(A,S)xxxG(A,S) described in [30] that were predicted to play a role in determining the c-ring stoichiometry.

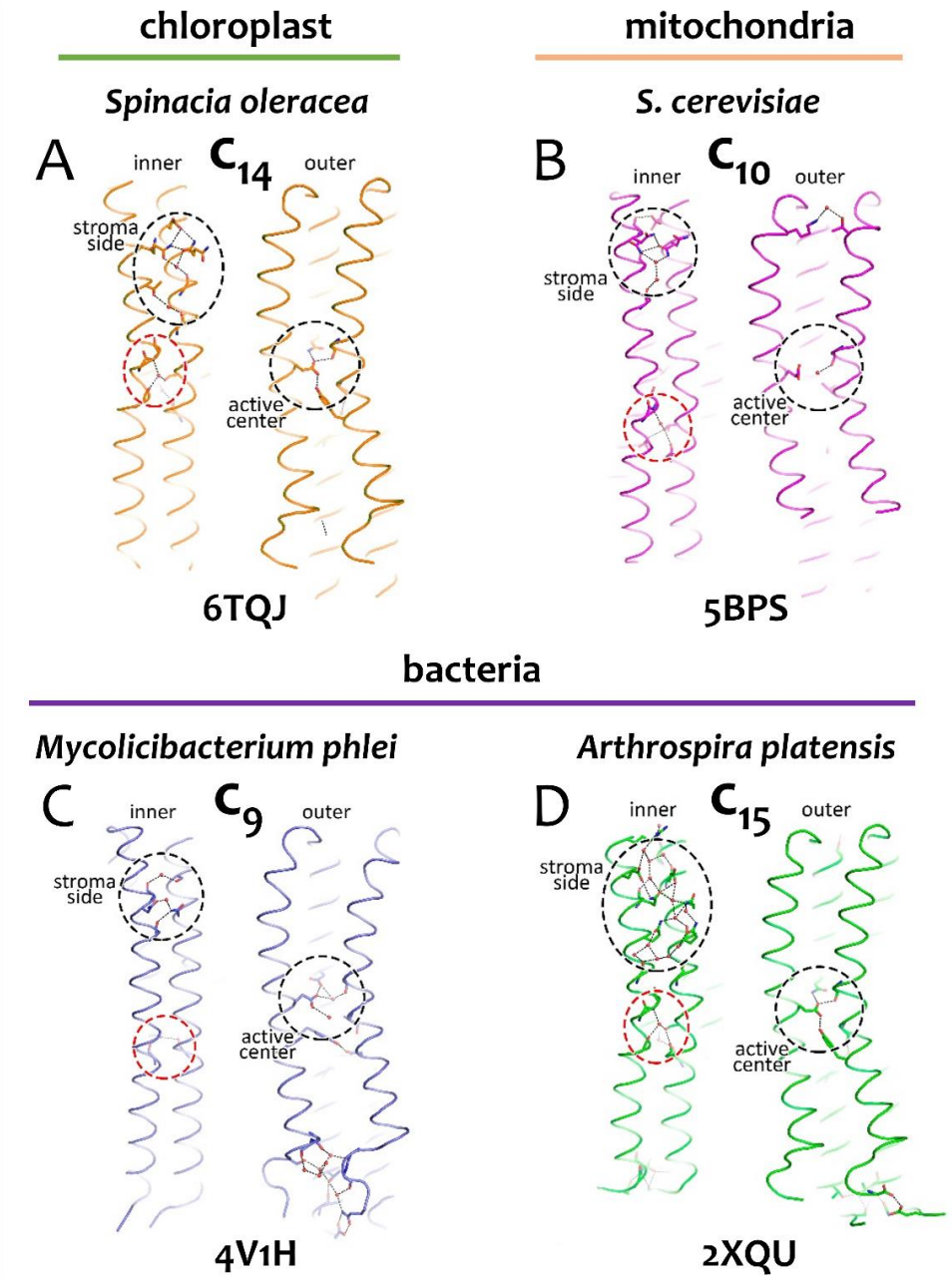

Figure 5.31. Comparison of c_1/c_1 interfaces in c-rings from different organisms: **(A)** a c_{14}-ring of cF_OF_1 from *Spinacia oleracea* (6TQJ) [26], **(B)** a c_{10}-ring of mtF_OF_1 from *Saccharomyces cerevisiae* (5BPS) (Mueller, D.M., to be published), **(C)** a c_9-ring of bF_OF_1 from *Mycolicibacterium phlei* (4V1H) [21], and **(D)** a c_{15}-ring of bF_OF_1 from *Arthrospira platensis* (2XQU) [19]. Inner and outer alpha helices of neighbor protomers are shown. The regions with hydrogen bindings are marked with dashed balck ellipses. The region with hydrogen bindings between the inner alpha helices near to the active center on the other side of the c-ring are marked with dashed red ellipses. The figure was adapted from [26].

Thus, the role of the motifs G(A,S)xxxG(A,S) in determination of the spinach chloroplast c-ring stoichiometry is that the motif S21x G23 x G25 x G27 x G29 is involved into interactions between inner alpha helices of neighbour protomers (Fig. 5.30E). It might determine one region of interactions (via w201') directly through S21 and G23 amino acids and one region (via w202) indirectly influencing the conformation of V26 and T30 amino acids. Another region of interactions (via w203) also involves T30 amino acid which can be indirectly influenced by the motif, however, more dense hydrogen binding is observed at the region of Q34 and E37 – amino acids that are distant from the motif, although they are also a part of the c_1/c_1 interface. Other interactions of the inner alpha helix of one protomer and outer alpha helix of the neighbour protomer via water molecule w205 additionally stabilize the c-ring and are an essential part of the c_1/c_1 interface. These parts were missing in the study [30], and in this work the full and complete c_1/c_1 interface were shown, and key determinants of the c-ring stoichiometry were defined.

5.3.5. Additional electron densities inside the c-ring

Inside the c-ring from spinach chloroplast there were additional positive electron densities that are not associated with the c-subunits. These densities have a circular shape and are placed as a stack of circles parallely to the membrane plane inside the central pore of the c-ring. The densities are strong enough on the map Fo – Fc at the level 3σ and are unlikely an artefact of the data treatment. In the c_{14}-ring from spinach chloroplasts there was a stack of three circles of the densities that are ~5.4 Å apart (Fig. 5.32A, B). The circles are placed in between of hydrophobic amino acids A7, I11, L15 and L19 of the inner alpha helices of the c-ring. These amino acids form "grooves" of Van-der-Waals (VdW) surface so that the circular densities are placed accurately inside them. The circles of the densities are formed by separate blobs (14 for each circle) so that one blob is placed near to the corresponding protomer. The first circle of the densities is placed between L15 and L19 residues, closer to L15 (Fig. 5.32C). The blobs are ~3.5 Å apart and are partially merged, however, each of the 14 blobs can still be identified. The distance between the blob and the nearest L15 residue is in range of ~ 6 – 7 Å and the angle between the line connecting two neighbour blobs

and the line connecting the blob and the nearest L15 residue is ~ 120° (let us denote it "b1-b2-R" angle). Also at the same level (~1 – 1.5 Å lower) there is a blob in the center of the circle of the densities. It is ~7.5 Å apart from the other blobs on the perimeter of the circle and the angle between lines from the central blob to the two neighbour ones on the perimeter of the circle equals ~26°, which conisides ~14 blobs in the circle. The second circle is at the level between I11 and L15 residues, closer to I11 (Fig. 5.32D). The densities are less prominent than in the top circle, however, still can be indentified. The distance between neighbour blobs is ~4.5 Å and between the blob and the nearest residue I11 – in range of ~ 4 – 5 Å. The angle b1-b2-R is ~100°. The third circle is at the level between A7 and I11 residues, closer to A7 (Fig. 5.32E). The densities here are even more prominent than in the middle circle and can be easily observed. The distance between neighbour blobs is ~6 Å and between the blob and the nearest residue A7 – ~4.5 Å. The angle b1-b2-R is ~120°.

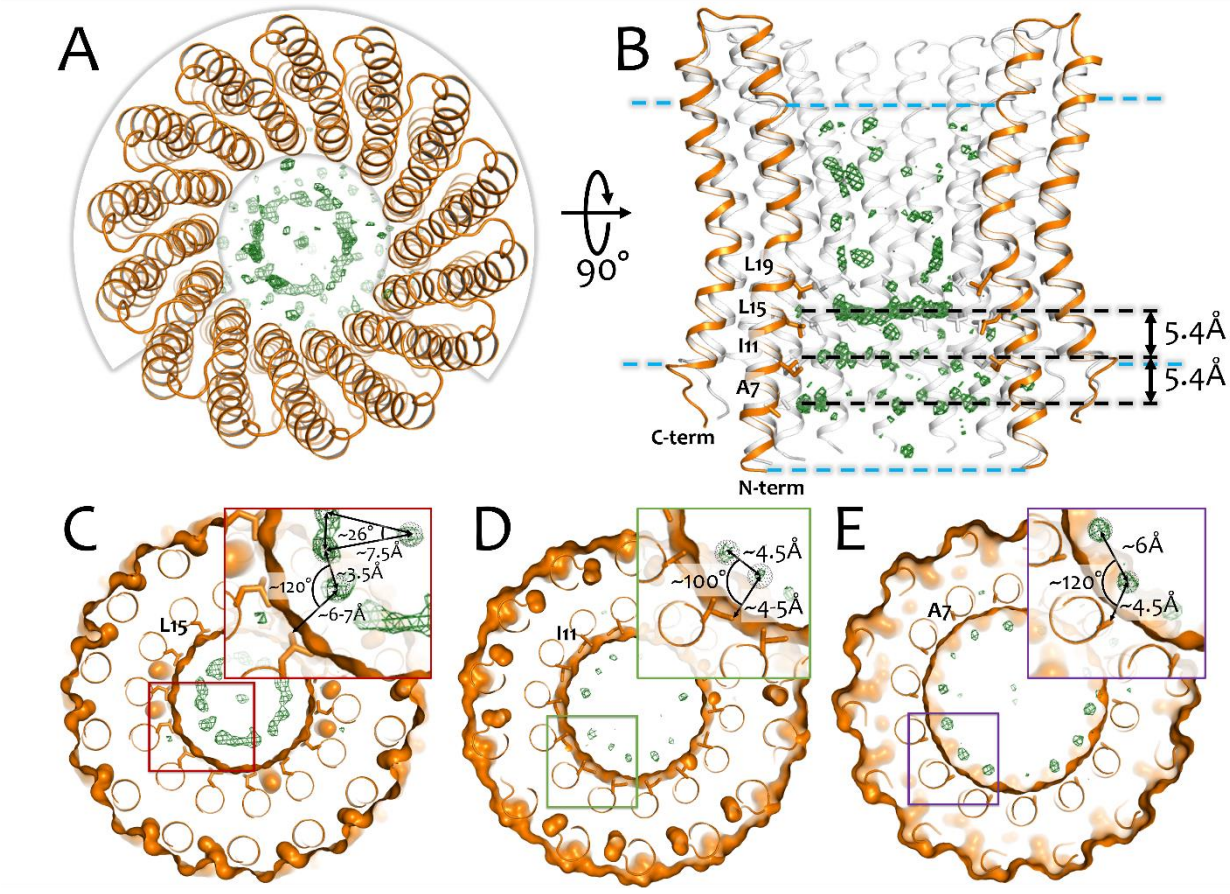

Figure 5.32. (A) Overall structure of the c_{14}-ring of cF_OF_1 from *Spinacia oleracea* (a view from the F_1 part of ATP synthase. **(B)** A lateral view on the clip of the c_{14}-ring so that the inner pore can be clearly seen. A view from the F_1 part of ATP synthase on the c_{14}-ring clip at the level of **(C)** L15, **(D)** I11, and **(E)** A7 residues. The distances between circles of the densities (panel B), between blobs and residues (panels C – E), and b1-b2-R angles (panels C – E) are shown.

Polar/apolar interfaces are shown with light blue dashed lines in panel B. The densities are shown as a green mesh that corresponds to the Fo – Fc map at 3σ. Panel B was adapted from [26].

I found similar additional densities in almost all available high-resolution structures of c-rings from different organisms (Fig. 5.33). They were previously not discussed in the literature. The densities share a common feature to form circles and "sit" in the proximity of the "grooves" of WdV surface. The number of circles was found to be variable in different organisms and in some cases the lipid-shape blobs are clearly visible. Here it is necessary to mention that I did not have original structure factors, therefore the Fo-Fc maps were rebuilt by using "REDO" protocol in Coot [139].

The densities were found in a wide range of pH (4.3 – 9.0), although there is an influence of pH if comparing the structures from the same organisms, for example *Saccharomyces cerevisiae* (Fig. 5.33B, C) or *Bacillus pseudofirmus* (Fig. 5.33F, G).

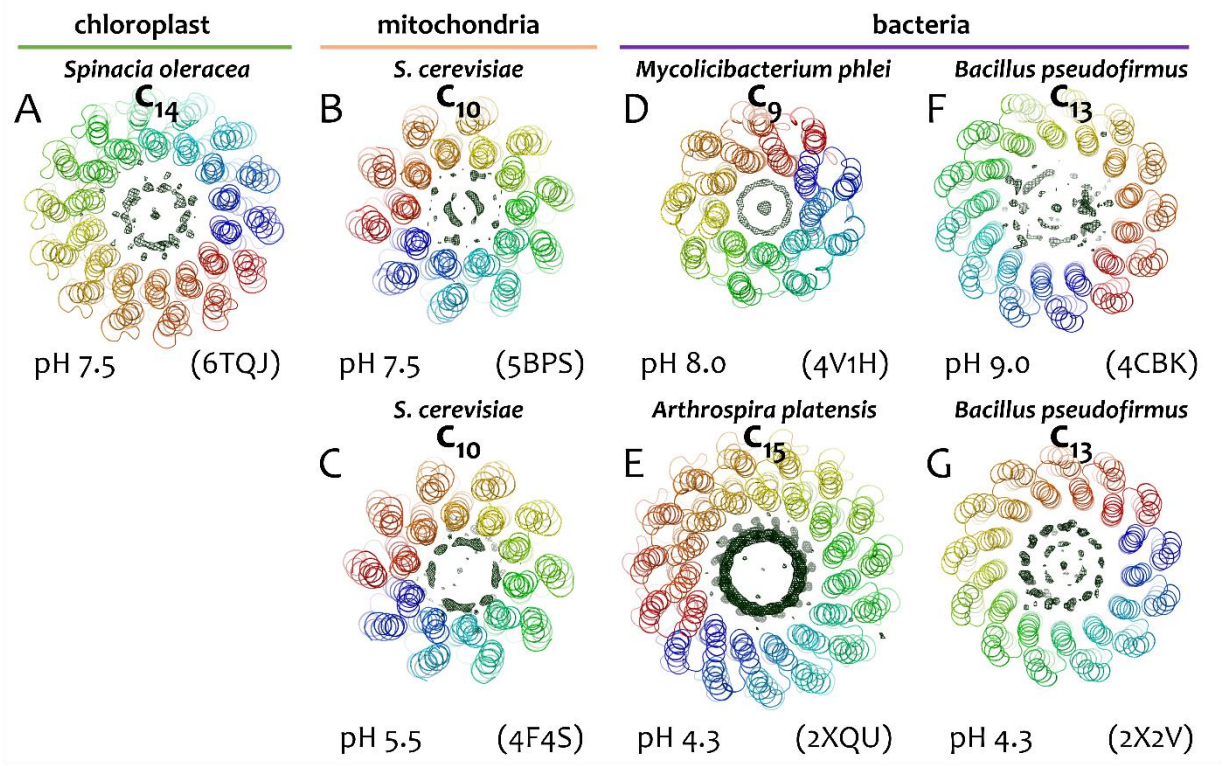

Figure 5.33. Comparison of additional positive electron densities inside c-rings from different organisms: **(A)** a c_{14}-ring of cF_OF_1 from *Spinacia oleracea* (6TQJ) [26], a c_{10}-ring of mtF_OF_1 from *Saccharomyces cerevisiae* **(B)** at pH 7.5 (5BPS) (Mueller, D.M., to be published) and **(C)** at pH 5.5 (4F4S) [22], **(D)** a c_9-ring of bF_OF_1 from *Mycolicibacterium phlei* (4V1H) [21], **(E)** a c_{15}-ring of bF_OF_1 from *Arthrospira platensis* (2XQU) [19], a c_{13}-ring of bF_OF_1 from *Bacillus pseudofirmus* **(F)** at pH 9.0 (4CBK) [21] and **(G)** at pH 4.3 (2X2V) [20]. The view in panels A, D – G is from F_1 part of corresponding ATP synthases, in panels B, C – from the other part of the membrane. The

densities are shown as a green mesh that corresponds to the Fo – Fc map at 3σ. The figure was adapted from [26].

Thus, it became clear that the *phenomenon* of the presence of unusual additional electron densities inside c-rings of different organisms is ubiquitous according to available structural information.

5.3.6. Distances between polar/apolar interfaces

Another intriguing feature of the c_{14}-ring is the unusually large distance between polar/apolar interfaces in the inner pore of the c-ring. The c-ring structure shows that the distance inside the inner pore is about ~1.2 – 1.4 times more than that outside the c-ring. However, exact calculation of polar/apolar interfaces in the inner pore of the c-ring turned out to be a real challenge.

Let us denote "outer p/a interface" as a polar/apolar interface on the outer surface of a c-ring, and "inner p/a interface" as a polar/apolar interface in its inner pore. In order to calculate p/a interfaces for membrane proteins a PPM server can be used [143]. It well calculates the exact rotational and translational positioning of transmembrane or peripheral proteins using their PDB structures and it was used to calculate the outer p/a interfaces of the c_{14}-ring. The distance between outer p/a interfaces equals 32.6 Å and was easily calculated by the PPM server. However, the PPM server does not take into account a topology of membrane proteins, thus it was impossible to calculate directly the inner p/a interfaces of the c-ring. In order to, on the one hand, presicely calculate the inner p/a interfaces, and, on the other hand, to use the smart algorithms of the PPM server that have proven their efficiency for this kind of tasks, I artificially modified the c-ring structure with the help of PyMOL [144] and used it as an input PDB structure for the PPM server.

The first step was to delete outer alpha helices of protomers and then change the opposite inner helices with each other using only translation of the helices without rotating them (Fig. 5.34A). The next step was to adjust the distance between the helices so that create a "contact" on the top part of the loop (Fig. 5.34B). Repeating the procedure for other protomers the "column" of inner alpha helices that are actually turned inside out (Fig. 5.34C) became an input PDB file for the PPM server, which calculated p/a interfaces that were actually almost equivalent to inner p/a interfaces of the c-ring (Fig. 5.34D). Although the validity of this method for calculating inner p/a interfaces of c-rings should be checked more carefully, it fits well with amino acid composition from the both sides of the calculated p/a interfaces in terms of their hydrophobicity, so even if there is an error of the calculation, it is small and near the same value as that provided by the PPM server.

Using the same procedure I calculated inner p/a interfaces of c-rings from different organisms with available high resolution structures (Table 5.5). The parameters of the PPM server output showed the precise calculation of inner p/a interfaces of c-rings and were used for further data analysis.

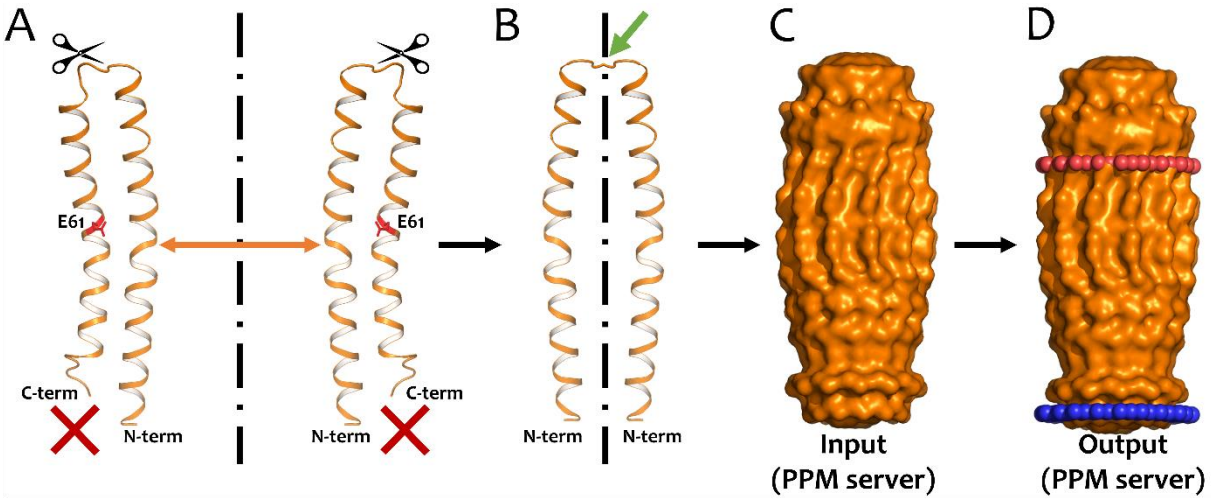

Figure 5.34. Artificial modifications of the c_{14}-ring structure for calculating inner p/a interfaces by the PPM server. **(A)** Deletion of outer alpha helices and translation (without rotation) of inner alpha helices to the opposite side of the inner pore of the c-ring. **(B)** Adjusting the distance between inner alpha helices until the "contact" of a part of the loop occurs. **(C)** Repeating the procedure for all protomers and creating a "column" of inner alpha helices. This structure is an input PDB file for the PPM server. **(D)** Output file of the PPM server. Calculated p/a interfaces are shown with red and blue spheres. All manipulations were done using PyMOL [144].

Table 5.5. Parameters of calculation of distances between p/a interfaces of different c-rigns using the PPM server. D_{out} and D_{in} denote distances between outer and inner p/a interfaces, respectively.

№	PDB ID, Origin	Cn	Outer p/a interfaces			Inner p/a interfaces			D_{in}/D_{out}
			Distance D_{out}, Å	ΔG, kcal/mol	Tilt angle	Distance, D_{in}, Å	ΔG, kcal/mol	Tilt angle	
1	6TQJ, *Spinacia oleracea*	14	32.6 ± 0.8	-109.2	0 ± 0°	45.8 ± 0.3	-156.4	0 ± 1°	1.40
3	5BPS, *Saccharomyces cerevisiae*	10	38.0 ± 0.8	-93.8	0 ± 0°	47.8 ± 0.3	-138.8	1 ± 1°	1.26
5	4F4S, *Saccharomyces cerevisiae*	10	38.0 ± 0.8	-93.6	0 ± 0°	47.8 ± 0.3	-138.6	0 ± 3°	1.26
2	4V1H, *Mycolici-bacterium phlei*	9	36.0 ± 2.2	-61.4	0 ± 0°	47.8 ± 0.7	-104.7	0 ± 4°	1.33
6	2XQU, *Arthrospira platensis*	15	31.4 ± 0.7	-110.9	0 ± 0°	38.2 ± 1.5	-168.5	0 ± 1°	1.22
4	4CBK, *Bacillus pseudofirmus*	13	35.9 ± 1.1	-144.3	1 ± 1°	35.4 ± 1.6	-140.5	0 ± 1°	0.99
7	2X2V, *Bacillus pseudofirmus*	13	35.9 ± 1.1	-149.3	0 ± 0°	35.4 ± 1.6	-136.6	0 ± 1°	0.99

Table 5.5 shows that c-rings of most organisms have an unusually large distance between inner p/a interfaces in comparison with outer p/a interfaces, D_{in}/D_{out} ratio is in range of 1.22 – 1.40, except *Bacillus pseudofirmus* where D_{in}/D_{out} ratio is ~ 1.0.

Interesting feature is that inner and outer p/a interfaces in different organisms are placed at different levels relatively either to each other or to the top or the bottom of corresponding c-rings (Fig. 5.35). Thus, in c-rings from yeast mitochondria and spinach chloroplasts the top inner p/a interface is at nearly the same level as the top outer p/a interface, and the bottom inner p/a interfaces are placed much below than the bottom outer p/a interfaces (Fig. 5.35A – C). In contrary, some bacteria have c-rings for which the top inner p/a interface is placed much below than the top outer p/a interface (Fig. 5.35D, E); and for some bacteria both inner and outer top p/a interfaces, and both inner and outer bottom p/a interfaces are at nearly the same levels (Fig. 5.35F, G).

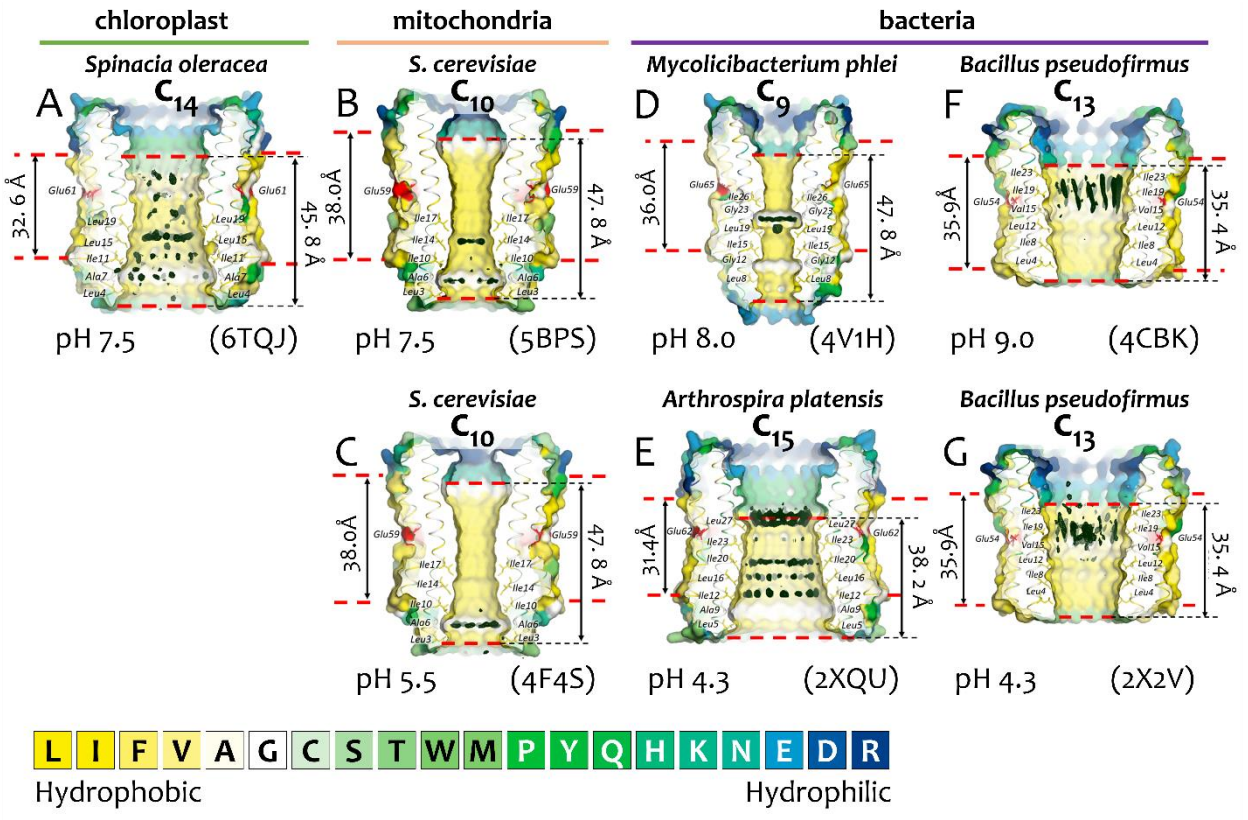

Figure 5.35. Comparison of inner and outer p/a interfaces of c-rings from different organisms: **(A)** a c_{14}-ring of cF_OF_1 from *Spinacia oleracea* (6TQJ) [26], a c_{10}-ring of mtF_OF_1 from *Saccharomyces cerevisiae* **(B)** at pH 7.5 (5BPS) (Mueller, D.M., to be published) and **(C)** at pH 5.5 (4F4S) [22], **(D)** a c_9-ring of bF_OF_1 from *Mycolicibacterium phlei* (4V1H) [21], **(E)** a c_{15}-ring of bF_OF_1 from *Arthrospira platensis* (2XQU) [19], a c_{13}-ring of bF_OF_1 from *Bacillus pseudofirmus* **(F)** at pH 9.0 (4CBK) [21] and **(G)** at pH 4.3 (2X2V) [20]. A lateral view on the clips of the c-rings so that their inner pores can be clearly seen. The c-rings oriented so that F_1 part of corresponding ATP synthases

is on the top and C and N termini are on the bottom. Amino acids are colored according to their hydrophobicity (the legend is on the bottom). The additional electron densities are shown as a green mesh that corresponds to the Fo – Fc map at 3σ, and the p/a interfaces are shown with red dahsed lines. The figure was adapted from [26].

The difference between D_{in} and D_{out} and the levels of inner and outer p/a interfaces indicates that the lipid composition of inner pore of a c-ring and outer membrane, which includes the c-ring, is different, and that arrangement of p/a interfaces is tightly adjusted to the compounds that naturally comprise lipid membranes of different organisms.

5.3.7. Additional electron densities outside the c-ring

Besides the additional electron densities that were found inside the inner pore of the c_{14}-ring, also additional densities were found between crystallographic contacts of the c-ring at b/c plane (Fig. 5.36A). Two strips of densities are placed accurately at the level of the active center E61 of two adjacent c-rings that are oriented in opposite directions (Fig. 5.36B). The strip at the level of the active center is more likely to belong to the corresponding c-ring, however another option is also not excluded (Fig. 5.36B, C).

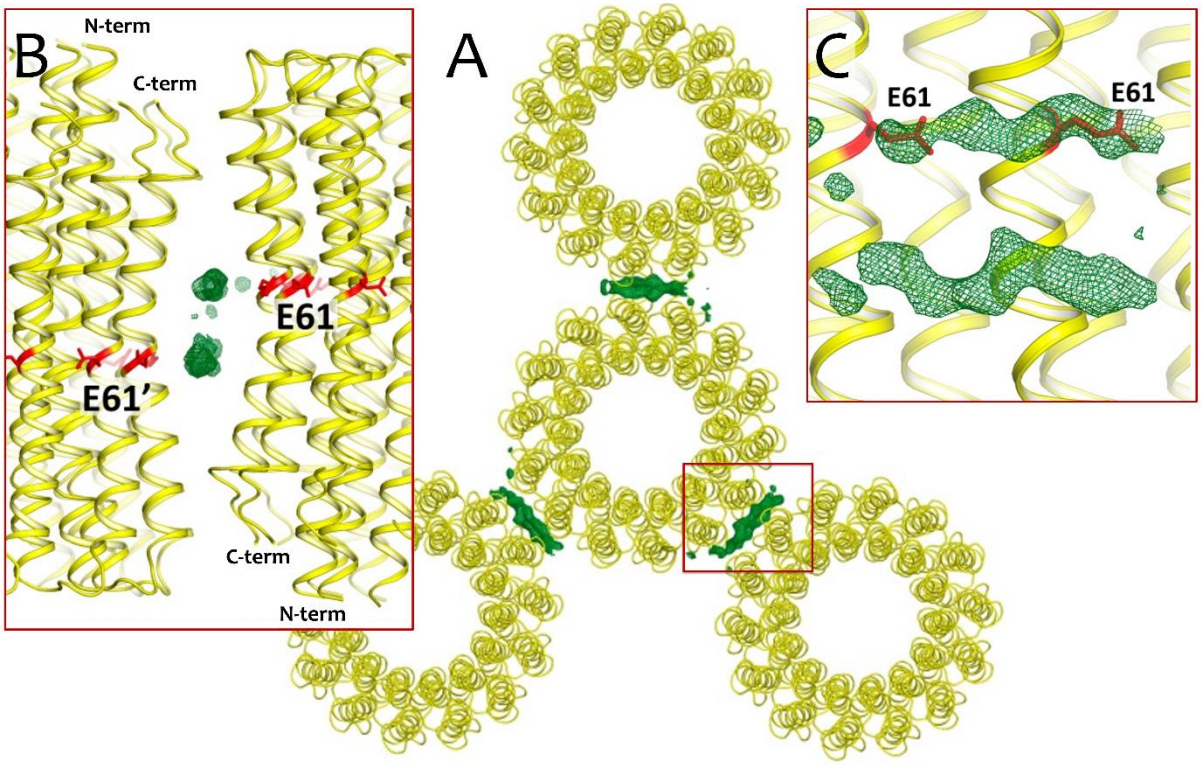

Figure 5.36. (A) Crystallographic contacts in b/c plane between adjacent c-rings. **(B)** Detailed view showing the level where contacts are placed. **(C)** Detailed view of the additional electron densities in the place of the contacts. In panels B, C active centers of c-rings are colored red. The

additional electron densities are shown as a green mesh that corresponds to the Fo – Fc map at 3σ. The figure was adapted from [26].

The densities at the level of the active center might be a part of subunit a of cF_OF_1, in particular – parts of its 5-th or 6-th alpha helices (aH5 and aH6, respectively) that are lying parallel to the membrane plane. The alignment of the PDB structure 6FKF [11] (cF_OF_1, *Spinacia oleracea*) with the structure of c_{14}-ring obtained in this work showed that the densities are at the level of aH5 (Fig. 5.37C,D) and aH6 (Fig. 5.37A,B) of corresponding subunit a of the cF_OF_1, and it is possible that a part of the alpha helix in different conformation could stack between two adjacent c-rings and form crystallographic contacts. In other high-resolution structures of separate c-rings there are no densities outside the c-ring surface, which might be due to the differences in crystallization methods. *In meso* crystallization might be milder than by VD method because it provides more native conditions for membrane proteins due to the matrix lipid surrounding, therefore a part of subunit a could present in crystals.

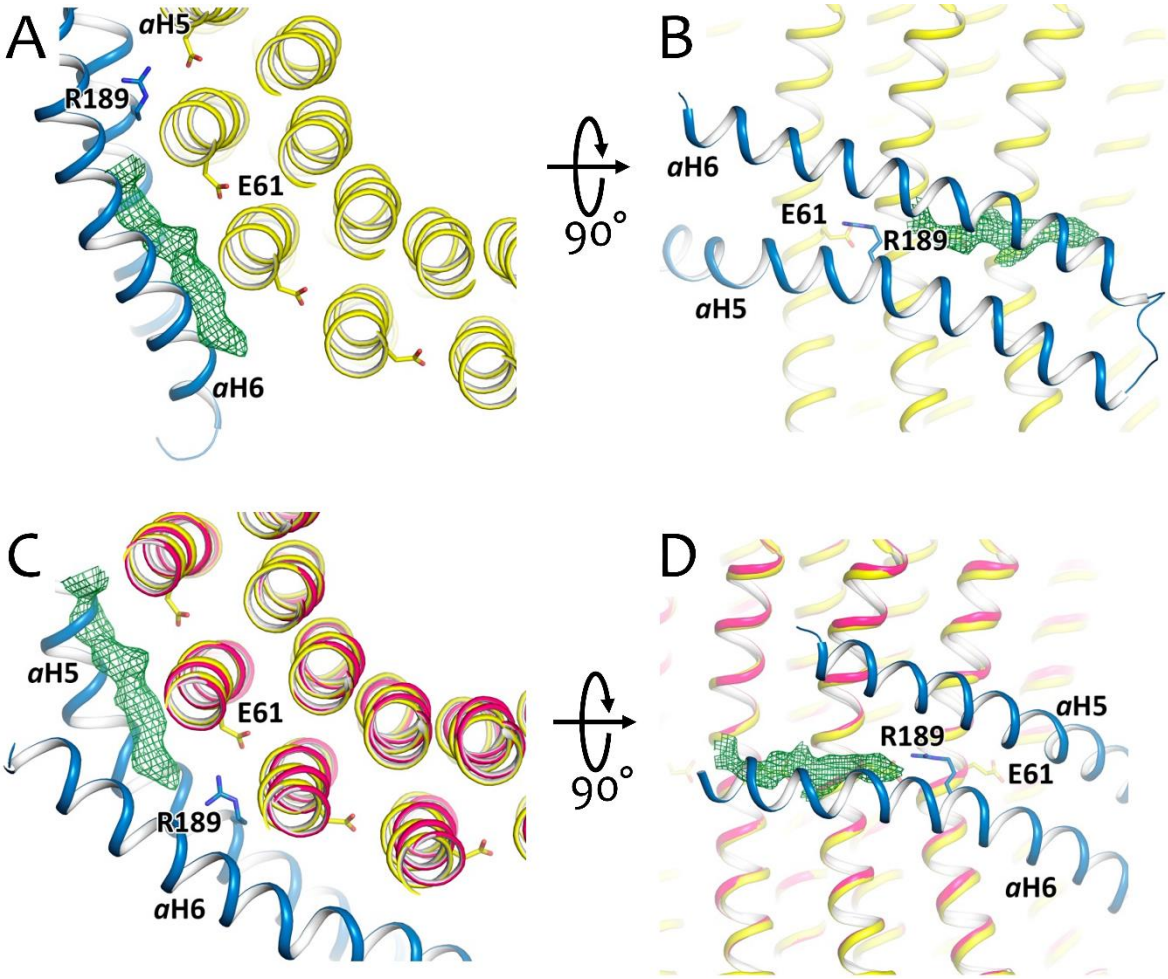

Fig. 5.37. Additional electron densities at the outside of the c-ring (6TQJ, obtained in this work) in context of a/c interface of the cF_OF_1 (6FKF) [11] from *Spinacia oleracea* (aH5 and aH6 are colored blue). The fit of the densities with aH6: **(A)** a view from F_1 part of the ATP synthase, **(B)**

a lateral view. The fit of the densities with aH5: **(C)** a view from F_1 part of the ATP synthase, **(D)** a lateral view. The additional electron densities are shown as a green mesh that corresponds to the Fo – Fc map at 3σ. The c-ring from the structure 6FKF (colored pink) was aligned to 6TQJ, obtained in this work (colored yellow). The figure was adapted from [26].

5.4. Hypothesis of isoprenoid quinones inside the c-ring

5.4.1. The basis of the hypothesis

The *summa* of the features mentioned above allowed us to suggest the possible composition of the "plug" inside the pore of the c-ring. First, analysis of literature and crystallization experiments showed that crystals of the c-ring of cF_OF_1 from *Spinacia oleracea* have a strong yellow-green color (Figs. 3.12 and 5.24) [25], [29], which implies the presence of pigments in the samples of solubilized c-ring, even at harsh conditions (1% NLS, 65 °C), and crystals. Second, the high-resolution structure of the c-ring obtained in this work showed strong circular densities exactly inside the pore of the c-ring (the densities outsied can hardly be assigned to pigments or lipid molecules). Third, a common character of circular electron densities placed in the proximity of the "grooves" of the VdW surface in the inner pore of c-rings from different species implies a presence of ubiquitous compounds that comprise the natural membranes of corresponding organisms, so that pigments described in [25] (beta-carotene and chlorophyll *a*) cannot fit the universality for the species from distant lineages. Fourth, the unusually large distances between inner p/a interfaces in almost all organisms with available high-resolution structures of their c-ring prompted that the universal compound varies in different species adjusting the thickness of hydrophobic area inside the corresponding c-ring, at the same time preserving the common character of the additional densities.

All mentioned observations above allowed us to suggest possible presence of isoprenoid quinones inside the inner pore of different c-rings and, in particular, a plastoquinone-9 (PQ-9) molecule in the c_{14}-ring from spinach chloroplasts. Isoprenoid quinones are amphiphilic molecules which have a polar moiety ("head") and a hydrophobic tail that composed of n-copies of isoprene. In living organisms there are naphthoquinones (for example, menaquinones) or benzoquinones (plastoquinones and ubiquinones) (Fig. 5.38). They are universal molecules comprising membranes of nearly all organisms from bacteria to eukaryotes functioning as electron or proton carriers in the respiratory chains of bacteria and eukaryotes or photosystems in chloroplasts and cyanobacteria, and are universal cofactors of a number of proteins [145].

The PQ-9 has a long hydrophobic tail ~ 45.3 Å (measured using PyMOL [144]) that fits the distance between inner p/a interfaces of the c_{14}-ring from spinach chloroplasts. The circles of the

densities are “fixed” in “grooves” of VdW surface (according to XRD crystalographic data) in the inner pore of the c-ring at the distance of ~5.4 Å – nearly the same as between side chain methyl gropus of the isoprene chain unit (~5.0 Å).

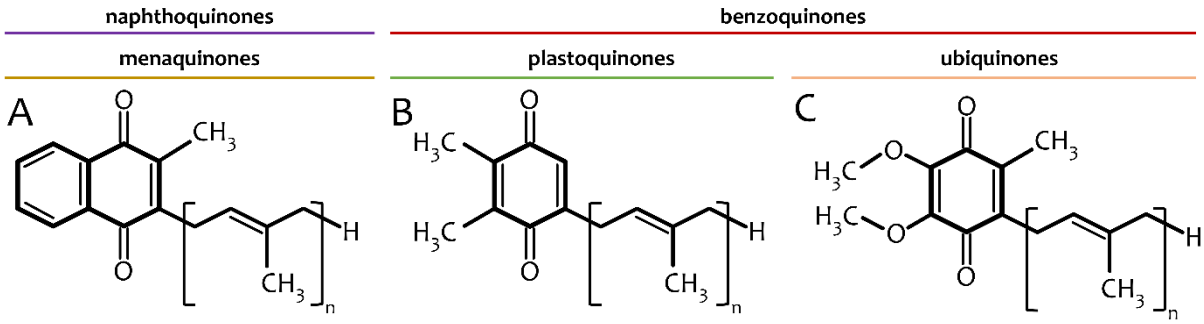

Figure 5.38. A short classification scheme of isoprenoid quinones present in living organisms – naphthoquinones and benzoquinones. Structural formulas of **(A)** menaquinone-n (MK-n), **(B)** plastoquinone-n (PQ-n), and **(C)** ubiquinone-n (UQ-n) are shown. All compounds are shown in oxidized form (two oxygens in quinone group).

For other species analogous isoprenoid quinones might be present inside their c-rings (such as ubiquinones ($UQ_{6\text{-}10}$ or $CoQ_{6\text{-}10}$ [145]) in case of eukaryotic mitochondria, or menaquinones in case of bacteria. For example, MK-6 or MK-7 was found in *Bacillus pseudofirmus* [146], [147]; and MK-9 (the other name is a vitamin K-9) was found in *Mycolicibacterium phlei* [148], – for these species the quinone molecules fit well the whole distance between inner p/a interfaces of their c-rings. Plastoquinones might present in c-rings of eukaryotic chloroplasts or in photosynthetic bacteria, e.g. cyanobacteria. PQ-9 was reported to be extracted from spinach chloroplasts [149] so it is definetely present in thylakoid membranes. PQ was also reported to present in a cyanobacteria *Arthrospira platensis* [150], however, at the moment there is no information about the exact number of isoprene units in its chain. Using the data from Table 5.5 and other knowledge, I speculate that PQ-7 might be present in c-rings of *Arthrospira platensis*. Actually, (the distance between inner p/a interfaces of a c-ring) / (the length of the hydrophobic chain of a corresponding isoprenoid quinone) (D_{in}/L_Q) ratio shows an unexpectedly strong correlation between the two values and equals almost 1/1 (1.00 – 1.08) for c-rings from bacteria and chloroplasts (Table 5.6).

The other result was obtained for c-rings from yeast mitochondria, where UQ-6 was found [145], however, the hydrophobic area inside the c-ring remains large (47.8 ± 0.3 Å). The D_{in}/L_Q ratio equals 1.56 in this case (Table 5.6). The length L_Q of UQ-6 is not enough to fit the whole hydrophobic area inside the c-ring of mtF_OF_1 from *Saccharomyces cerevisiae*. However, in eukaryotic mitochondria there are different interface contexts of corresponding c-rings. The ratio

D_{in}/L_Q = ~3/2 prompts that the other type of molecules migth coexist with UQ-6 in the inner pore of the c-ring from yeast mitochondria and together cover the hydrophobic/hydrophilic mismatch.

In addition, there is a similarity of mtF_OF_1 dimers between the representatives of Opisthokonta supergroup. The structure of dimeric mtF_OF_1 from *Sus scrofa* has an alpha helix 6.8PL inside the c-ring (Fig. 3.13) [13], and the structure of dimeric mtF_OF_1 from *Saccharomyces cerevisiae* [59], although does not allow to see the details of the c-ring inner pore, however, resolves the rest of the ATP synthase subunit machinery which is similar to that of the mtF_OF_1 dimer from *Sus scrofa*. Considering the facts mentioned above and the fact that *Saccharomyces cerevisiae* and *Sus scrofa* have the same (type I) organization of mtF_OF_1 dimers, I speculate that the interface context for the c-ring of *Saccharomyces cerevisiae* and *Sus scrofa* is similar and it may include a coexistence of UQ-6 and 6.8PL alpha helix in the inner pore of the c-ring from yeast mitochondria, creating a complex proteo-lipid (6.8PL) – lipid (UQ-6 and other lipids) – protein (inner surface of the c-ring) interaction interface in a rotating system.

The interface context of c-rings in chloroplasts and bacteria seems to be simpler and does not include protein peptides or proteo-lipids in their inner pore according to what is known. Thus, the presence of lipids that prevent ion leakage through the inner pore of a c-ring is vital for these organisms. Isoprenoid quinones are electron or proton carriers in respiratory chains of almost all species [145] and might create an effective barrier in comparison with common lipids (e.g. phospholipids).

Table 5.6. Comparison of the distance between inner p/a interfaces of a c-ring (D_{in}) with the length of the hydrophobic chain of a corresponding isoprenoid quinone (L_Q). L_Q was calculated using PyMOL [144].

№	**Origin, PDB ID(s)**	**Type of quinone**	**L_Q, Å**	**D_{in}, Å**	**D_{in}/L_Q**
1	*Spinacia oleracea*, (6TQJ)	PQ-9	45.3	45.8 ± 0.3	1.01
2	*Saccharomyces cerevisiae*, (5BPS, 4F4S)	UQ-6	30.6	47.8 ± 0.3	1.56
3	*Bacillus pseudofirmus*, (4CBK, 2X2V)	MK-7	35.5	35.4 ± 1.6	1.00
4	*Mycolicibacterium phlei*, (4V1H)	MK-9	45.3	47.8 ± 0.7	1.08
5	*Arthrospira platensis*, (2XQU)	PQ-7 (?)	35.5	38.2 ± 1.5	1.08

I also do not exclude the possible coexistence of isoprenoid quinones with other lipid molecules (e.g. beta carotene in a c-ring from spinach chloroplasts) that naturally compose lipid membranes of different organelles and organisms inside their c-rings. Moreover, considering the relevant works and preprints on the assembly processes of c-rings from protomers [24], [151] the lipids incorporated into corresponding membranes have to be one of the compounds of the “plug” inside

a c-ring, at least at the first step of ATP synthase assembly. It is possible that isoprenoid quinones might then substitute lipids and come to equilibrium (e.g. minimum of a free energy), because usually lipids in the membranes of different organelles and organisms have their hydrophobic parts ("tails") ~ 20 – 40% shorter than necessary to cover the whole hydrophobic area in the inner pore of corresponding c-rings (Table 5.5, D_{in}/D_{out} ratio for different organisms). The hydrophobic/hydrophilic mismatch might be a "motif force" of the substitution of lipids for ones with longer hydrophobic "tail". Taking into account the amount of isoprenoid quinones and the distribution of other types of lipids comprising corresponding membranes, it seems unlikely to find another lipid with similar length of "tails".

One more hint was found while analysing UV-Vis spectra of the samples of purified c_{14}-ring from spinach chloroplasts obtained in this work and available in literature UV-Vis spectra of dissolved crystals of c_{14}-ring from spinach chloroplasts [25] (Fig. 5.39). UV-Vis spectra were very similar except that our samples of the c_{14}-ring did not contain chlorophyll *a* molecules according to the UV-Vis spectra at ~670 nm.

The peak at ~335 nm present in the spectra of the c_{14}-ring obtained in this work and in [25] and is not associated with chlorophyll *a* or beta-carotene molecules that were reported to be tightly connected with the c-ring in [25]. Nevertheless, both samples contained a compound with the absorbance maximum at ~335 nm, which is not characteristic for carotenoids.

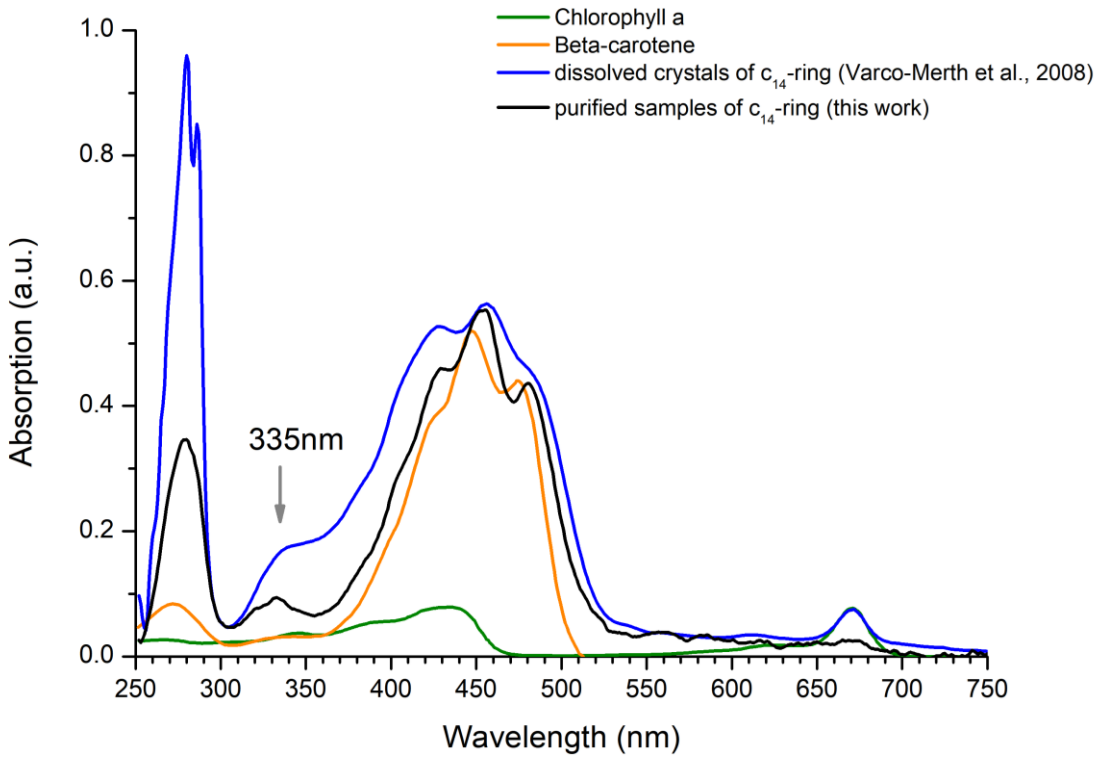

Figure 5.39. Comparison of UV-Vis spectra of the c_{14}-ring from spinach chloroplasts obtained in this work (purified samples) (black line) and available in literature UV-Vis spectra (dissolved

crystals) (blue line) [25]. The spectra of chlorophyll *a* (green line) and beta-carotene (orange line) are shown for reference and can be found anywhere in literature. The peak at ~335 nm in the spectra of the c_{14}-ring obtained in this work and in work [25] is marked with an arrow. The figure was adapted from [25].

Although nothing except chlorophyll *a* and beta-carotene was detected by reverse phase HPLC chromatography in the work [25] (Fig. 3.13I), but in that work the chromatograms are only shown for A_{480} and A_{665} (480 and 665 nm). PQ-9 in oxidized form (two oxygens are present as in Fig. 5.38) has a peak of absorption at 255 nm and cannot be detected at 480 – 665 nm range. Thus, there is no available HPLC chromatogram showing A_{255} for c_{14}-ring samples.

5.4.2. Differential UV-Vis spectroscopy of the c-ring samples

In order to provide more information on the problem of the interpretation of the densities I did differential UV-Vis spectroscopy with the samples of purified c_{14}-ring dissolved in EtOH as described in *Differential UV-Vis spectroscopy*, Materials and Methods. Briefly, the samples of purified c_{14}-ring in the buffer 50 mM NaCl, 10 mM HEPES, 2 mM 6AHA, 0.5 mM EDTA, 0.03% (w/v) DDM, pH 7.0, were concentrated and dissolved in pure EtOH ~1:30 (v/v) – this corresponds to the oxidized form of PQ-9. Then, several grains of $NaBH_4$ on the tip of a spatula were added to the solution and incubated for several minutes. Addition of $NaBH_4$ provides a qualitative reaction of reducing ketones and aldehydes to alcohols, therefore, quinones (if there are in the sample) of semiquinones (one oxygen and one OH^- group) would reduce to quinols (two OH^- groups) (reduced form of PQ-9 in our case). The UV-Vis spectra were measured before (oxidized form) and after addition of $NaBH_4$ (reduced form) and "oxidized" – "reduced" differential spectrum ("ox-redox") was calculated (Fig. 5.40A, B).

UV-Vis "ox-redox" differential spectra are unique fingerprints for detection of compounds containing quinone groups because their UV-Vis spectrum significantly changes when reducing oxygens to alcohols. Thus, as a reference a trimethyl benzoquinone (TMBQ) – a polar moiety of PQ-9 was taken. Differential UV-Vis "ox-redox" fingerprints of TMBQ and PQ-9 are the same if measured in the same solvent (Fig. 5.40D, E). This was the reason of high dilution factor of the c-ring samples in pure EtOH, which was ~1:30 (v/v) in order to eliminate the signal from a buffer of the c-ring samples. Due to high dilution and low concentration of compounds the difference signal is noisy however, the peaks could be clearly observed and are similar to the normalized difference spectrum of TMBQ (Fig. 5.40A). The control experiment was done with pure EtOH before and after addition of $NaBH_4$ and showed negligible difference between the two spectra (Fig. 5.40C).

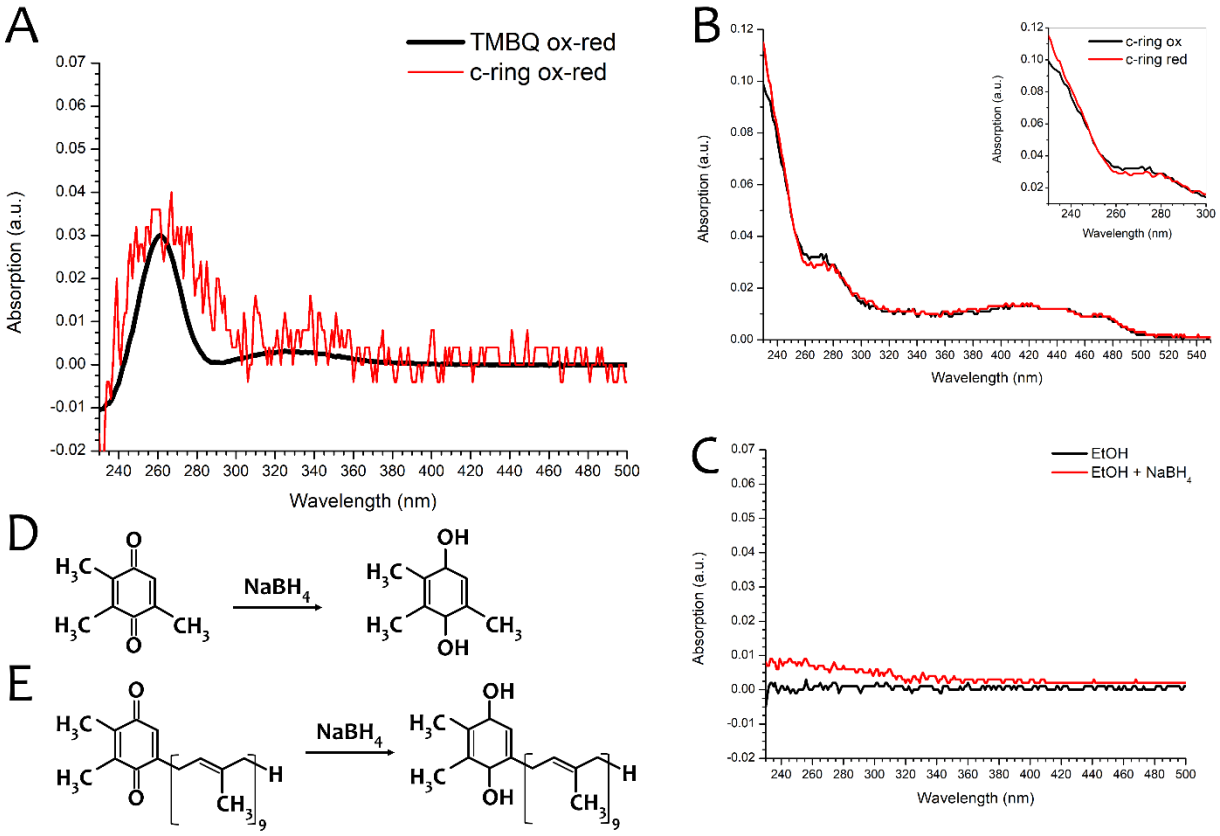

Figure 5.40. Differential UV-Vis spectroscopy of the c_{14}-ring samples dissolved in EtOH. **(A)** "Ox-redox" differential spectra of the c-ring samples and TMBQ (red and black lines, respectively). **(B)** UV-Vis spectra of the c-ring samples before (ox) and after addition of $NaBH_4$ (redox) (black and red lines, respectively). **(C)** A control experiment with pure EtOH before and after addition of $NaBH_4$ (black and red lines, respectively). Schemes of reducing **(D)** TMBQ to $TMBQH_2$ and **(E)** PQ_9 to PQ_9H_2.

Thus, I obtained one more experimental evidence of the presence of UV-Vis structural analogs of PQ-9 molecules in the samples of purified c-ring from spinach chloroplasts. However, this evidence is also indirect, it gives a strong argument that quinone-like compounds are present not only in thylakoid membranes of spinach chloroplasts but also are tightly bound to the c-ring after purification even at harsh detergent and temperature conditions (1% NLS, 65°C). All mentioned above points towards possible presence of isoprenoid quinones in the inner pore of a c-ring as one of the compounds and has the possible role of stabilizing a c-ring and prevent ion leakage through it.

5.4.3. New elements in the model of ATP synthase

One of the possible implications of all evidences mentioned before is a suggestion of a new feature of an ATP synthase, in particular, the presence of interaction interface between isoprenoid quinones and the inner surface of the c-ring. The rotating system of ATP synthase has to be stabilized against

ion leakage in order to avoid dissipation of ion motif force. In eukaryotic mitochondria even if the PL6.8 subunit is placed inside the c-ring it does not cover the whole area of the pore and there has to be a "buffer" compound between a fixed PL6.8 and a rotating c-ring.

Thus, I suggest the presence of the new element in the model of ATP synthase where isoprenoid quinones are universal cofactors of the enzyme, and are placed into the inner pore of the c-ring. I present (using the PyMOL [144]) the possible models of different c-rings with corresponding isoprenoid quinones inside their pores in Figure 5.41.

I suggest that for spinach chloroplasts ATP synthase a PQ-9 is placed in the inner pore of the c-ring comprising the lipid "plug" (Fig. 5.41A); for *Mycobacterium phlei* and *Bacillus pseudofirmus* the MK-9 and MK-7 are placed in corresponding c-rings (Fig. 5.41C, D); for *Arthrospira platensis* I speculate that PQ-7 might be placed inside the c-ring (Fig. 5.41E), although this should be verified by further experiments. I also speculate that in the mitochondria ATP synthase from *Saccharomyces cerevisiae* there is a complex interface c/UQ-6/6.8PL (Fig. 5.41B), however this is just a hypothesis and it should also be examined by further studies (e.g. new high-resolution structures of mtF_OF_1 dimers).

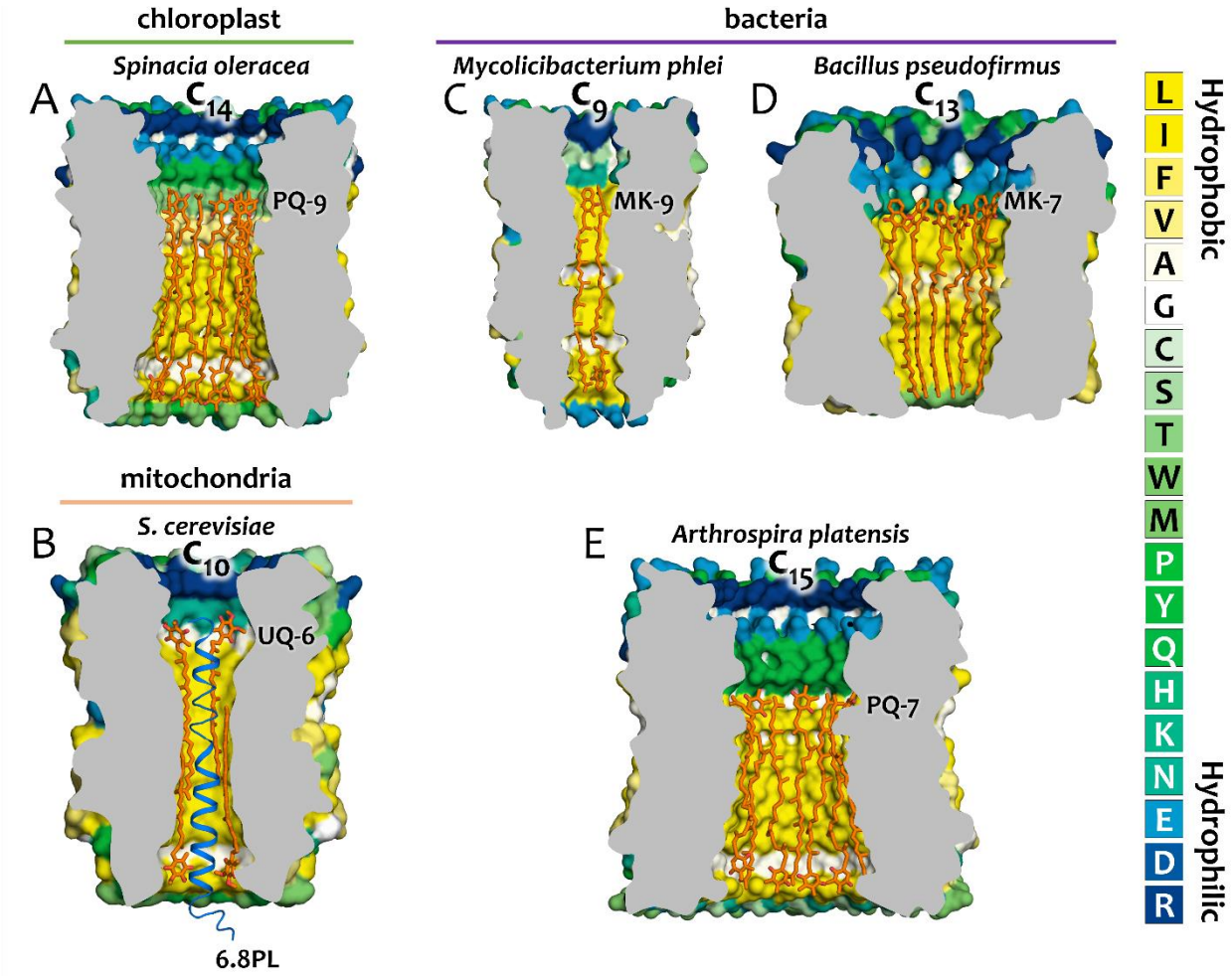

Figure 5.41. Schematic drawings showing the possible models of c-rings of F-ATP synthases from different organisms. Quinones are colored orange. **(A)** The c_{14}-ring of cF_OF_1 from *Spinacia oleracea* (6TQJ) [26] with corresponding PQ-9 molecules inside. **(B)** The c_{10}-ring of mtF_OF_1 from *Saccharomyces cerevisiae* (4F4S) [22] with corresponding UQ-6 and a possible 6.8PL subunit (colored blue) placed by alignment of the c-ring and 6.8PL subunit from the model 6J5K (tertamer of mtF_OF_1 from *Sus scrofa*) [13] with further centering of the aligned c-rings. **(C)** The c_9-ring of bF_OF_1 from *Mycolicibacterium phlei* (4V1H) [21] with corresponding MK-9 molecules. **(D)** The c_{13}-ring of bF_OF_1 from *Bacillus pseudofirmus* (4CBK) [21] with corresponding MK-7 molecules. **(E)** The c_{15}-ring of bF_OF_1 from *Arthrospira platensis* (2XQU) [19] with corresponding PQ-7 molecules. A lateral view on the clips of the c-rings so that their inner pores can be clearly seen. The c-rings oriented so that F_1 part of corresponding ATP synthases is on the top and C and N termini are one the bottom. Amino acids are colored according to their hydrophobicity (the legend is on the right). Panels A and D were adapted from [26].

To sum up, I recognize that all implications from our hypothesis mentioned above are only hypothetic models that have to be checked by additional experiments. However, our work presents strong evidences pointing towards the hypothesis. And finally, the hypothesis itself, although it seems attractive, has to be developed further to answer the questions that left out of the scope of this thesis, e.g.:

1. How exactly compounds of a “plug” interact with the inner surface of c-rings? The distances between the additional densities and the nearest residues are more than the length of a hydrophobic bond (as it is shown in Fig. 5.32C – E). When the c-ring is rotating does the composition of a “plug” changes and is there a dynamic equilibrium in rotating system?

2. How the length of the molecules inside the c-ring correlates with the hydrophobic area of its inner pore? Does it really remain a monolayer (as it is shown in Fig. 5.41A, C – E) or these molecules might have a non-linear conformation (e.g. bilayer, circles, etc.)?

3. What is a role of the “plug” in c-rings of ATP synthases? How it regulates the functions of the enzyme? What modification of the lipid “plug” may induce MPTP and further cell death?

These questions are open and make sense independently of the exact type of the molecules which hopefully will be found inside c-rings in the future. Answering them is necessary for deep understanding the mechanisms of working of ATP synthases.

6. Outlook

The first high-resolution structure of the c-ring from plant chloroplasts was obtained in our work by *in meso* crystallization and showed several new features which may improve our knowledge about not only c-rings from plant chloroplasts, but about ATP synthases in general. My thesis filled the gap in knowledge by presenting a high-resolution structure (2.3 Å) of a c-ring from spinach chloroplasts. The followed analysis of available structural data showed the presence of unusual additional electron densities that were not associated with protein in almost all high-resolution structures of bacterial, mitochondrial and, as I showed, chloroplast c-rings from different species. In my thesis experimental evidences are presented that isoprenoid quinones, such as plastoquinone-9 (PQ-9) in plant chloroplasts, ubiquinones in mitochondria, and corresponding quinones in other species might be candidates for explanation of new structural data and be universal cofactors of ATP synthases, preventing ion leakage through a c-ring and stabilizing it.

Due to the lack of high-resolution structures of the c-rings from plants there also was a "gap" in understanding of molecular mechanisms of a network of hydrogen bonds at c_1/c_1 interface. Other high-resolution structures of mitochondrial and bacterial c-rings allowed analyzing and comparing their c_1/c_1 interfaces with those of chloroplast c-rings. A net of hydrogen bonds was found to form c_1/c_1 interface where the role of G(A,S)xxxG(A,S) interlacing motifs and additional hydrogen bonds have been directly shown in the high-resolution crystallographic structure of the c-ring from spinach chloroplasts. Thus, in my thesis the molecular construction of c_1/c_1 interface is shown, which determines the angle between neighbor protomers and, therefore, the c-ring stoichiometry.

Contemporary models prompt that a "plug" inside c-rings might be organized differently in its composition for different types of ATP synthases. In my thesis I provide strong arguments in favor of the hypothesis that isoprenoid quinones well coincide with relevant structural data and might be present as one of compounds of the "plug", together with an alpha helix in animals and fungi or pigments in plant chloroplasts. Ubiquinones are universal compounds of cellular and organellar membranes involved in respiratory chain complexes and photosynthesis. Also, they are electron or proton carriers and have longer tails than average membrane lipids, which fit longer distance between polar/apolar interfaces inside a c-ring than outside (~1.2 – 1.4 times, as I showed in the present work).

All together shows that the nature of compounds in a c-ring inner pore and molecular mechanisms of their interaction with a c-ring might shed light on some biological questions, starting from prevention of ion leakage and stabilization of ATP synthases, and ending with the role of ATP synthases in a *phenomenon* of mitochondria permeability transition pore.

The hypothesis of isoprenoid quinones inside c-rings was not previously discussed in the literature. In my thesis strong experimental evidences are presented suggesting towards the hypothesis and isoprenoid quinones are suggested as a possible element of ATP synthases. The evidences are still indirect; therefore, additional experiments are required to clarify the composition of the c-ring "plugs" and solve this beautiful enigma of nature.

References

[1] H. Nuskova *et al.*, “Biochemical thresholds for pathological presentation of ATP synthase deficiencies,” 2019.

[2] P. Neupane, S. Bhuju, N. Thapa, and H. K. Bhattarai, “ATP Synthase: Structure, Function and Inhibition,” *Biomol. Concepts*, vol. 10, no. 1, pp. 1–10, 2019.

[3] R. Chen *et al.*, “Parkinson’s disease protein DJ-1 regulates ATP synthase protein components to increase neuronal process outgrowth,” *Cell Death Dis.*, vol. 10, no. 6, pp. 1–12, Jun. 2019.

[4] E. Gauba, H. Chen, L. Guo, and H. Du, “Cyclophilin D deficiency attenuates mitochondrial F1Fo ATP synthase dysfunction via OSCP in Alzheimer’s disease,” *Neurobiol. Dis.*, vol. 121, pp. 138–147, Jan. 2019.

[5] M. Jové, I. Pradas, M. Dominguez-Gonzalez, I. Ferrer, and R. Pamplona, “Lipids and lipoxidation in human brain aging. Mitochondrial ATP-synthase as a key lipoxidation target,” *Redox Biology*, vol. 23. Elsevier B.V., p. 101082, 01-May-2019.

[6] B. Zhu *et al.*, “F0F1 ATP synthase regulates extracellular calcium influx in human neutrophils by interacting with Cav2.3 and modulates neutrophil accumulation in the lipopolysaccharide-challenged lung,” *Cell Commun. Signal.*, vol. 18, no. 1, pp. 1–15, Feb. 2020.

[7] W. Kühlbrandt and K. M. Davies, “Rotary ATPases: A New Twist to an Ancient Machine,” *Trends in Biochemical Sciences*, vol. 41, no. 1. Elsevier Ltd, pp. 106–116, 01-Jan-2016.

[8] S. Schulz, M. Wilkes, D. J. Mills, W. Kühlbrandt, and T. Meier, “Molecular architecture of the N-type <scp>ATP</scp> ase rotor ring from *Burkholderia pseudomallei*,” *EMBO Rep.*, vol. 18, no. 4, pp. 526–535, Apr. 2017.

[9] H. Ueno, T. Suzuki, K. Kinosita, and M. Yoshida, “ATP-driven stepwise rotation of FoF1-ATP synthase,” *Proc. Natl. Acad. Sci. U. S. A.*, vol. 102, no. 5, pp. 1333–1338, Feb. 2005.

[10] W. Kühlbrandt, “Structure and Mechanisms of F-Type ATP Synthases,” *Annu. Rev. Biochem.*, vol. 88, no. 1, pp. 515–549, Jun. 2019.

[11] A. Hahn, J. Vonck, D. J. Mills, T. Meier, and W. Kühlbrandt, “Structure, mechanism, and regulation of the chloroplast ATP synthase.,” *Science*, vol. 360, no. 6389, p. eaat4318, May 2018.

[12] B. J. Murphy, N. Klusch, J. D. Langer, D. J. Mills, Ö. Yildiz, and W. Kühlbrandt, “Rotary substates of mitochondrial ATP synthase reveal the basis of flexible F1-Fo coupling,” *bioRxiv*, p. 543108, Feb. 2019.

[13] J. Gu *et al.*, “Cryo-EM structure of the mammalian ATP synthase tetramer bound with inhibitory protein IF1,” *Science (80-.).*, vol. 364, no. 6445, pp. 1068–1075, Jun. 2019.

[14] A. W. Mühleip, F. Joos, C. Wigge, A. S. Frangakis, W. Kühlbrandt, and K. M. Davies, “Helical arrays of U-shaped ATP synthase dimers form tubular cristae in ciliate mitochondria,” *Proc. Natl. Acad. Sci. U. S. A.*, vol. 113, no. 30, pp. 8442–8447, Jul. 2016.

[15] A. Mühleip, S. E. McComas, and A. Amunts, “Structure of a mitochondrial ATP synthase with bound native cardiolipin,” *Elife*, vol. 8, Nov. 2019.

[16] C. Gerle, “On the structural possibility of pore-forming mitochondrial FoF1 ATP synthase,” *Biochim. Biophys. Acta - Bioenerg.*, vol. 1857, no. 8, pp. 1191–1196, Aug. 2016.

[17] M. Carraro, A. Carrer, A. Urbani, and P. Bernardi, “Molecular nature and regulation of the

mitochondrial permeability transition pore(s), drug target(s) in cardioprotection," *J. Mol. Cell. Cardiol.*, vol. 144, pp. 76–86, Jul. 2020.

[18] J. E. Walker, J. Carroll, and J. He, "Reply to Bernardi: The mitochondrial permeability transition pore and the ATP synthase," *Proceedings of the National Academy of Sciences of the United States of America*, vol. 117, no. 6. National Academy of Sciences, pp. 2745–2746, 11-Feb-2020.

[19] D. Pogoryelov, A. Krah, J. D. Langer, Ö. Yildiz, J. D. Faraldo-Gómez, and T. Meier, "Microscopic rotary mechanism of ion translocation in the Fo complex of ATP synthases," *Nat. Chem. Biol.*, vol. 6, no. 12, pp. 891–899, Dec. 2010.

[20] L. Preiss, Ö. Yildiz, D. B. Hicks, T. A. Krulwich, and T. Meier, "A New Type of Proton Coordination in an F1Fo-ATP Synthase Rotor Ring," *PLoS Biol.*, vol. 8, no. 8, p. e1000443, Aug. 2010.

[21] L. Preiss *et al.*, "The c-ring ion binding site of the ATP synthase from *B acillus pseudofirmus* OF4 is adapted to alkaliphilic lifestyle," *Mol. Microbiol.*, vol. 92, no. 5, pp. 973–984, Jun. 2014.

[22] J. Symersky *et al.*, "Structure of the c10 ring of the yeast mitochondrial ATP synthase in the open conformation," *Nat. Struct. Mol. Biol.*, vol. 19, no. 5, pp. 485–491, May 2012.

[23] T. Meier, U. Matthey, F. Henzen, P. Dimroth, and D. J. Müller, "The central plug in the reconstituted undecameric c cylinder of a bacterial ATP synthase consists of phospholipids," *FEBS Lett.*, vol. 505, no. 3, pp. 353–356, Sep. 2001.

[24] O. Novitskaia, P. Buslaev, and I. Gushchin, "Assembly of Spinach Chloroplast ATP Synthase Rotor Ring Protein-Lipid Complex," *Front. Mol. Biosci.*, vol. 6, p. 135, Nov. 2019.

[25] B. Varco-Merth, R. Fromme, M. Wang, and P. Fromme, "Crystallization of the c14-rotor of the chloroplast ATP synthase reveals that it contains pigments," *Biochim. Biophys. Acta - Bioenerg.*, vol. 1777, no. 7–8, pp. 605–612, Jul. 2008.

[26] A. V. Vlasov *et al.*, "Unusual features of the c-ring of F1FO ATP synthases," *Sci. Rep.*, vol. 9, no. 1, p. 18547, Dec. 2019.

[27] M. Vollmar, D. Schlieper, M. Winn, C. Büchner, and G. Groth, "Structure of the c14 rotor ring of the proton translocating chloroplast ATP synthase.," *J. Biol. Chem.*, vol. 284, no. 27, pp. 18228–35, Jul. 2009.

[28] S. Saroussi, M. Schushan, N. Ben-Tal, W. Junge, and N. Nelson, "Structure and Flexibility of the C-Ring in the Electromotor of Rotary FoF1-ATPase of Pea Chloroplasts," *PLoS One*, vol. 7, no. 9, p. e43045, Sep. 2012.

[29] A. M. Balakrishna, H. Seelert, S.-H. Marx, N. A. Dencher, and G. Grüber, "Crystallographic structure of the turbine C-ring from spinach chloroplast F-ATP synthase.," *Biosci. Rep.*, vol. 34, no. 2, p. e00102, Apr. 2014.

[30] D. Pogoryelov *et al.*, "Engineering rotor ring stoichiometries in the ATP synthase," *Proc. Natl. Acad. Sci. U. S. A.*, vol. 109, no. 25, Jun. 2012.

[31] K. Lohmann, "Über die Pyrophosphatfraktion im Muskel," *Die Naturwissenschaften*, vol. 17, no. 31. Springer-Verlag, pp. 624–625, Aug-1929.

[32] H. Kalckar, "Phosphorylation in kidney tissue," *Enzymologia*, vol. 2, no. 4, pp. 47–52, 1937.

[33] V. A. Belitser and E. T. Tsybakova, "The mechanism of phosphorylation associated with respiration.," *Biochimiya*, vol. 4, pp. 516–534, 1939.

[34] F. Lipmann, “Role of phosphate in pyruvic acid dehydrogenation,” *Nature*, vol. 144, no. 3643. pp. 381–382, 1939.

[35] F. Lipmann, “Coupling between pyruvic acid dehydrogenation and adenylic acid phosphorylation,” *Nature*, vol. 143, no. 3616. p. 281, 1939.

[36] E. C. Slater, “Mechanism of Phosphorylation in the Respiratory Chain,” *Nature*, vol. 172, no. 4387, pp. 975–978, Nov. 1953.

[37] R. J. P. Williams, “Possible functions of chains of catalysts,” *J. Theor. Biol.*, vol. 1, no. 1, pp. 1–17, 1961.

[38] P. Mitchell, “Coupling of Phosphorylation to Electron and Hydrogen Transfer by a Chemi-Osmotic type of Mechanism,” *Nature*, vol. 191, no. 4784, pp. 144–148, Jul. 1961.

[39] E. A. Liberman, V. P. Topaly, L. M. Tsofina, A. A. Jasaitis, and V. P. Skulachev, “Mechanism of coupling of oxidative phosphorylation and the membrane potential of mitochondria,” *Nature*, vol. 222, no. 5198, pp. 1076–1078, 1969.

[40] L. I. Yaguzhinsky, L. S. Boguslavsky and A. B. Volkov, A. G. Rakhmaninova, “Synthesis of ATP coupled with action of membrane protonic pumps at the octane–water interface,” *Nature*, vol. 259, no. 5543, pp. 494–496, 1976.

[41] P. D. Boyer, R. L. Cross, and W. Momsen, “A new concept for energy coupling in oxidative phosphorylation based on a molecular explanation of the oxygen exchange reactions,” *Proc. Natl. Acad. Sci. U. S. A.*, vol. 70, no. 10, pp. 2837–2839, 1973.

[42] C. Kayalar, J. Rosing, and P. D. Boyer, “An alternating site sequence for oxidative phosphorylation suggested by measurement of substrate binding patterns and exchange reaction inhibitions,” *J. Biol. Chem.*, vol. 252, no. 8, pp. 2486–2491, 1977.

[43] G. Falk and J. E. Walker, “DNA sequence of a gene cluster coding for subunits of the F0 membrane sector of ATP synthase in Rhodospirillum rubrum. Support for modular evolution of the F1 and F0 sectors.,” *Biochem. J.*, vol. 254, no. 1, pp. 109–122, 1988.

[44] J. P. Abrahams, A. G. W. Leslie, R. Lutter, and J. E. Walker, “Structure at 2.8 Â resolution of F1-ATPase from bovine heart mitochondria,” *Nature*, vol. 370, no. 6491, pp. 621–628, 1994.

[45] “The Nobel Prize in Chemistry 1997.” [Online]. Available: https://www.nobelprize.org/prizes/chemistry/1997/summary/. [Accessed: 22-Jan-2020].

[46] H. Noji, R. Yasuda, M. Yoshida, and K. Kinosita, “Direct observation of the rotation of F1-ATPase,” *Nature*, vol. 386, no. 6622, pp. 299–302, Mar. 1997.

[47] D. Sabbert, S. Engelbrecht, and W. Junge, “Intersubunit rotation in active F-ATPase,” *Nature*, vol. 381, no. 6583, pp. 623–625, 1996.

[48] H. Itoh *et al.*, “Mechanically driven ATP synthesis by F1-ATPase,” *Nature*, vol. 427, no. 6973, pp. 465–468, Jan. 2004.

[49] A. V. Syroeshkin, E. A. Vasilyeva, and A. D. Vinogradov, “ATP synthesis catalyzed by the mitochondrial F1-F0 ATP synthase is not a reversal of its ATPase activity,” *FEBS Lett.*, vol. 366, no. 1, pp. 29–32, Jun. 1995.

[50] D. Stock, A. G. W. Leslie, and J. E. Walker, “Molecular architecture of the rotary motor in ATP synthase,” *Science (80-.).*, vol. 286, no. 5445, pp. 1700–1705, Nov. 1999.

[51] A. Dautant, J. Velours, and M. F. Giraud, “Crystal structure of the Mg·ADP-inhibited state of the yeast F 1c10-ATP synthase,” *J. Biol. Chem.*, vol. 285, no. 38, pp. 29502–29510, Sep. 2010.

[52] I. N. Watt, M. G. Montgomery, M. J. Runswick, A. G. W. Leslie, and J. E. Walker, "Bioenergetic cost of making an adenosine triphosphate molecule in animal mitochondria," *Proc. Natl. Acad. Sci. U. S. A.*, vol. 107, no. 39, pp. 16823–16827, Sep. 2010.

[53] M. F. Giraud, P. Paumard, C. Sanchez, D. Brèthes, J. Velours, and A. Dautant, "Rotor architecture in the yeast and bovine F 1-c-ring complexes of F-ATP synthase," *J. Struct. Biol.*, vol. 177, no. 2, pp. 490–497, Feb. 2012.

[54] K. M. Davies, C. Anselmi, I. Wittig, J. D. Faraldo-Gómez, and W. Kühlbrandt, "Structure of the yeast F1Fo-ATP synthase dimer and its role in shaping the mitochondrial cristae.," *Proc. Natl. Acad. Sci. U. S. A.*, vol. 109, no. 34, pp. 13602–7, Aug. 2012.

[55] A. Zhou *et al.*, "Structure and conformational states of the bovine mitochondrial ATP synthase by cryo-EM.," *Elife*, vol. 4, p. e10180, Oct. 2015.

[56] M. Allegretti, N. Klusch, D. J. Mills, J. Vonck, W. Kühlbrandt, and K. M. Davies, "Horizontal membrane-intrinsic α-helices in the stator a-subunit of an F-type ATP synthase," *Nature*, vol. 521, no. 7551, pp. 237–240, May 2015.

[57] M. Sobti *et al.*, "Cryo-EM structures of the autoinhibited *E. coli* ATP synthase in three rotational states," *Elife*, vol. 5, p. e21598, Dec. 2016.

[58] K. R. Vinothkumar, M. G. Montgomery, S. Liu, and J. E. Walker, "Structure of the mitochondrial ATP synthase from Pichia angusta determined by electron cryo-microscopy," *Proc. Natl. Acad. Sci. U. S. A.*, vol. 113, no. 45, pp. 12709–12714, Nov. 2016.

[59] H. Guo, S. A. Bueler, and J. L. Rubinstein, "Atomic model for the dimeric FO region of mitochondrial ATP synthase.," *Science*, vol. 358, no. 6365, pp. 936–940, Oct. 2017.

[60] A. P. Srivastava *et al.*, "High-resolution cryo-EM analysis of the yeast ATP synthase in a lipid membrane," *Science (80-.).*, vol. 360, no. 6389, May 2018.

[61] H. Guo, T. Suzuki, and J. L. Rubinstein, "Structure of a bacterial atp synthase," *Elife*, vol. 8, Feb. 2019.

[62] E. Morales-Rios, M. G. Montgomery, A. G. W. Leslie, and J. E. Walker, "Structure of ATP synthase from Paracoccus denitrificans determined by X-ray crystallography at 4.0 Å resolution," *Proc. Natl. Acad. Sci. U. S. A.*, vol. 112, no. 43, pp. 13231–13236, Oct. 2015.

[63] A. Hahn *et al.*, "Structure of a Complete ATP Synthase Dimer Reveals the Molecular Basis of Inner Mitochondrial Membrane Morphology," *Mol. Cell*, vol. 63, no. 3, pp. 445–456, Aug. 2016.

[64] E. Morales-Rios *et al.*, "Purification, characterization and crystallization of the F-ATPase from *Paracoccus denitrificans*," *Open Biol.*, vol. 5, no. 9, p. 150119, Sep. 2015.

[65] A. Stocker, S. Keis, J. Vonck, G. M. Cook, and P. Dimroth, "The Structural Basis for Unidirectional Rotation of Thermoalkaliphilic F1-ATPase," *Structure*, vol. 15, no. 8, pp. 904–914, Aug. 2007.

[66] M. Benvenuti and S. Mangani, "Crystallization of soluble proteins in vapor diffusion for x-ray crystallography," *Nat. Protoc.*, vol. 2, no. 7, pp. 1633–1651, Jun. 2007.

[67] M. Caffrey and V. Cherezov, "Crystallizing membrane proteins using lipidic mesophases.," *Nat. Protoc.*, vol. 4, no. 5, pp. 706–31, Jan. 2009.

[68] D. Li, S. T. A. Shah, and M. Caffrey, "Host Lipid and Temperature as Important Screening Variables for Crystallizing Integral Membrane Proteins in Lipidic Mesophases. Trials with Diacylglycerol Kinase.," *Cryst. Growth Des.*, vol. 13, no. 7, pp. 2846–2857, Jul. 2013.

[69] P. Ma *et al.*, “The cubicon method for concentrating membrane proteins in the cubic mesophase,” *Nat. Protoc.*, vol. 12, no. 9, pp. 1745–1762, Sep. 2017.

[70] A. Zabara *et al.*, “Design of ultra-swollen lipidic mesophases for the crystallization of membrane proteins with large extracellular domains,” *Nat. Commun.*, vol. 9, no. 1, pp. 1–9, Dec. 2018.

[71] M. J. Runswick, J. V. Bason, M. G. Montgomery, G. C. Robinson, I. M. Fearnley, and J. E. Walker, “The affinity purification and characterization of ATP synthase complexes from mitochondria,” *Open Biol.*, vol. 3, no. 2, p. 120160, Feb. 2013.

[72] S. A. Muñoz-Gómez, J. G. Wideman, A. J. Roger, and C. H. Slamovits, “The Origin of Mitochondrial Cristae from Alphaproteobacteria,” *Mol. Biol. Evol.*, vol. 34, no. 4, pp. 943–956, Jan. 2017.

[73] K. Eydt, K. M. Davies, C. Behrendt, I. Wittig, and A. S. Reichert, “Cristae architecture is determined by an interplay of the MICOS complex and the F1Fo ATP synthase via Mic27 and Mic10,” *Microb. Cell*, vol. 4, no. 8, pp. 259–272, Aug. 2017.

[74] R. Agarwala *et al.*, “Database Resources of the National Center for Biotechnology Information,” *Nucleic Acids Res.*, vol. 45, no. D1, pp. D12–D17, 2017.

[75] “Taxonomy browser (Eukaryota).” [Online]. Available: https://www.ncbi.nlm.nih.gov/Taxonomy/Browser/wwwtax.cgi. [Accessed: 25-May-2020].

[76] S. Rexroth, J. M. W. Meyer Zu Tittingdorf, H. J. Schwaßmann, F. Krause, H. Seelert, and N. A. Dencher, “Dimeric H+-ATP synthase in the chloroplast of Chlamydomonas reinhardtii,” *Biochim. Biophys. Acta - Bioenerg.*, vol. 1658, no. 3, pp. 202–211, Oct. 2004.

[77] H. J. Schwaßmann, S. Rexroth, H. Seelert, and N. A. Dencher, “Metabolism controls dimerization of the chloroplast FoF1 ATP synthase in Chlamydomonas reinhardtii,” *FEBS Lett.*, vol. 581, no. 7, pp. 1391–1396, Apr. 2007.

[78] A. V. Vlasov, Y. L. Ryzhykau, V. I. Gordeliy, and A. I. Kuklin, “Spinach ATP-synthases form dimers in nanodiscs. Small-angle X-ray and neutron scattering investigations,” *FEBS J.*, vol. 284, no. s1, p. 87, 2017.

[79] B. Böttcher and P. Gräber, “The structure of the H+-ATP synthase from chloroplasts and its subcomplexes as revealed by electron microscopy,” *Biochimica et Biophysica Acta - Bioenergetics*, vol. 1458, no. 2–3. Elsevier, pp. 404–416, 31-May-2000.

[80] B. Daum, D. Nicastro, J. Austin, J. Richard McIntosh, and W. Kühlbrandt, “Arrangement of photosystem II and ATP synthase in chloroplast membranes of spinach and pea,” *Plant Cell*, vol. 22, no. 4, pp. 1299–1312, Apr. 2010.

[81] R. R. Ishmukhametov, A. N. Russell, and R. M. Berry, “A modular platform for one-step assembly of multi-component membrane systems by fusion of charged proteoliposomes,” *Nat. Commun.*, vol. 7, no. 1, pp. 1–10, Oct. 2016.

[82] R. R. Ishmukhametov, M. A. Galkin, and S. B. Vik, “Ultrafast purification and reconstitution of His-tagged cysteine-less Escherichia coli F 1F o ATP synthase,” *Biochim. Biophys. Acta - Bioenerg.*, vol. 1706, no. 1–2, pp. 110–116, Jan. 2005.

[83] T. Suhai, N. G. Heidrich, N. A. Dencher, and H. Seelert, “Highly sensitive detection of ATPase activity in native gels,” *Electrophoresis*, vol. 30, no. 20, pp. 3622–3625, Oct. 2009.

[84] T. Suhai, N. A. Dencher, A. Poetsch, and H. Seelert, “Remarkable stability of the proton translocating F1FO-ATP synthase from the thermophilic cyanobacterium

Thermosynechococcus elongatus BP-1," *Biochim. Biophys. Acta - Biomembr.*, vol. 1778, no. 4, pp. 1131–1140, Apr. 2008.

[85] S. Fischer, C. Etzold, P. Turina, G. Deckers-Hebestreit, K. Altendorf, and P. Graber, "ATP Synthesis Catalyzed by the ATP Synthase of Escherichia coli Reconstituted into Liposomes," *Eur. J. Biochem.*, vol. 225, no. 1, pp. 167–172, Oct. 1994.

[86] A. Poetsch, S. Rexroth, J. Heberle, T. A. Link, N. A. Dencher, and H. Seelert, "Characterisation of subunit III and its oligomer from spinach chloroplast ATP synthase," *Biochim. Biophys. Acta - Biomembr.*, vol. 1618, no. 1, pp. 59–66, Dec. 2003.

[87] L. Preiss *et al.*, "Structure of the mycobacterial ATP synthase Fo rotor ring in complex with the anti-TB drug bedaquiline," *Sci. Adv.*, vol. 1, no. 4, pp. e1500106–e1500106, May 2015.

[88] P. Richard, J.-L. Rigaud, and P. Graber, "Reconstitution of CF0F1 into liposomes using a new reconstitution procedure," *Eur. J. Biochem.*, vol. 193, no. 3, pp. 921–925, Nov. 1990.

[89] N. Soga, K. Kimura, K. Kinosita, M. Yoshida, and T. Suzuki, "Perfect chemomechanical coupling of FoF1-ATP synthase," *Proc. Natl. Acad. Sci. U. S. A.*, vol. 114, no. 19, pp. 4960–4965, May 2017.

[90] I. Grotjohann and P. Gräber, "The H+-ATPase from chloroplasts: Effect of different reconstitution procedures on ATP synthesis activity and on phosphate dependence of ATP synthesis," *Biochim. Biophys. Acta - Bioenerg.*, vol. 1556, no. 2–3, pp. 208–216, Dec. 2002.

[91] H. Seelert, A. Poetsch, N. A. Dencher, A. Engel, H. Stahlberg, and D. J. Müller, "Proton-powered turbine of a plant motor," *Nature*, vol. 405, no. 6785, pp. 418–419, May 2000.

[92] M. Sobti *et al.*, "Cryo-EM structures provide insight into how E. coli F1Fo ATP synthase accommodates symmetry mismatch," *Nat. Commun.*, vol. 11, no. 1, pp. 1–10, Dec. 2020.

[93] H. P. Braun, "The Oxidative Phosphorylation system of the mitochondria in plants," *Mitochondrion*, vol. 53. Elsevier B.V., pp. 66–75, 01-Jul-2020.

[94] H. Seelert and N. A. Dencher, "ATP synthase superassemblies in animals and plants: Two or more are better," *Biochimica et Biophysica Acta - Bioenergetics*, vol. 1807, no. 9. Elsevier, pp. 1185–1197, 01-Sep-2011.

[95] E. A. Schon and N. A. Dencher, "Heavy Breathing: Energy Conversion by Mitochondrial Respiratory Supercomplexes," *Cell Metabolism*, vol. 9, no. 1. Cell Press, pp. 1–3, 07-Jan-2009.

[96] A. Urbani *et al.*, "Purified F-ATP synthase forms a Ca2+-dependent high-conductance channel matching the mitochondrial permeability transition pore," *Nat. Commun.*, vol. 10, no. 1, pp. 1–11, Dec. 2019.

[97] N. Mnatsakanyan and E. A. Jonas, "ATP synthase c-subunit ring as the channel of mitochondrial permeability transition: Regulator of metabolism in development and degeneration," *J. Mol. Cell. Cardiol.*, vol. 144, pp. 109–118, Jul. 2020.

[98] J. Carroll, J. He, S. Ding, I. M. Fearnley, and J. E. Walker, "Persistence of the permeability transition pore in human mitochondria devoid of an assembled ATP synthase," *Proc. Natl. Acad. Sci. U. S. A.*, vol. 116, no. 26, pp. 12816–12821, Jun. 2019.

[99] M. Wu, J. Gu, S. Zong, R. Guo, T. Liu, and M. Yang, "Research journey of respirasome," *Protein and Cell*, vol. 11, no. 5. Higher Education Press, pp. 318–338, 01-May-2020.

[100] F. Krause, N. H. Reifschneider, D. Vocke, H. Seelert, S. Rexroth, and N. A. Dencher, "'Respirasome'-like supercomplexes in green leaf mitochondria of spinach," *J. Biol.*

Chem., vol. 279, no. 46, pp. 48369–48375, Nov. 2004.

[101] H. Eubel, J. Heinemeyer, and H. P. Braun, "Identification and characterization of respirasomes in potato mitochondria," *Plant Physiol.*, vol. 134, no. 4, pp. 1450–1459, Apr. 2004.

[102] H. Eubel, L. Jänsch, and H. P. Braun, "New insights into the respiratory chain of plant mitochondria. Supercomplexes and a unique composition of complex II," *Plant Physiol.*, vol. 133, no. 1, pp. 274–286, Sep. 2003.

[103] H. Eubel, J. Heinemeyer, S. Sunderhaus, and H. P. Braun, "Respiratory chain supercomplexes in plant mitochondria," *Plant Physiology and Biochemistry*, vol. 42, no. 12. Elsevier Masson SAS, pp. 937–942, 01-Dec-2004.

[104] T. Briston, D. L. Selwood, G. Szabadkai, and M. R. Duchen, "Mitochondrial Permeability Transition: A Molecular Lesion with Multiple Drug Targets," *Trends in Pharmacological Sciences*, vol. 40, no. 1. Elsevier Ltd, pp. 50–70, 01-Jan-2019.

[105] J. Šileikytė *et al.*, "Second-Generation Inhibitors of the Mitochondrial Permeability Transition Pore with Improved Plasma Stability," *ChemMedChem*, vol. 14, no. 20, pp. 1771–1782, Oct. 2019.

[106] G. Bhosale and M. R. Duchen, "Investigating the Mitochondrial Permeability Transition Pore in Disease Phenotypes and Drug Screening," *Curr. Protoc. Pharmacol.*, vol. 85, no. 1, Jun. 2019.

[107] S. Nesci, "The mitochondrial permeability transition pore in cell death: A promising drug binding bioarchitecture," *Med. Res. Rev.*, vol. 40, no. 2, pp. 811–817, Mar. 2020.

[108] M. A. Neginskaya *et al.*, "ATP Synthase C-Subunit-Deficient Mitochondria Have a Small Cyclosporine A-Sensitive Channel, but Lack the Permeability Transition Pore," *Cell Rep.*, vol. 26, no. 1, pp. 11-17.e2, Jan. 2019.

[109] J. He *et al.*, "Assembly of the membrane domain of ATP synthase in human mitochondria," *Proc. Natl. Acad. Sci. U. S. A.*, vol. 115, no. 12, pp. 2988–2993, Mar. 2018.

[110] J. Benkert *et al.*, "Cav2.3 channels contribute to dopaminergic neuron loss in a model of Parkinson's disease," *Nat. Commun.*, vol. 10, no. 1, pp. 1–11, Dec. 2019.

[111] T. Meier, A. Krah, P. J. Bond, D. Pogoryelov, K. Diederichs, and J. D. Faraldo-Gómez, "Complete Ion-Coordination Structure in the Rotor Ring of Na+-Dependent F-ATP Synthases," *J. Mol. Biol.*, vol. 391, no. 2, pp. 498–507, Aug. 2009.

[112] J. Symersky, D. Osowski, D. E. Walters, and D. M. Mueller, "Oligomycin frames a common drug-binding site in the ATP synthase.," *Proc. Natl. Acad. Sci. U. S. A.*, vol. 109, no. 35, pp. 13961–5, Aug. 2012.

[113] D. Pogoryelov, Ö. Yildiz, J. D. Faraldo-Gómez, and T. Meier, "High-resolution structure of the rotor ring of a proton-dependent ATP synthase," *Nat. Struct. Mol. Biol.*, vol. 16, no. 10, pp. 1068–1073, Oct. 2009.

[114] T. Meier *et al.*, "Evidence for structural integrity in the undecameric c-rings isolated from sodium ATP synthases," *J. Mol. Biol.*, vol. 325, no. 2, pp. 389–397, Jan. 2003.

[115] S. Schulz *et al.*, "A New Type of Na+-Driven ATP Synthase Membrane Rotor with a Two-Carboxylate Ion-Coupling Motif," *PLoS Biol.*, vol. 11, no. 6, p. e1001596, Jun. 2013.

[116] D. Matthies *et al.*, "High-resolution structure and mechanism of an F/V-hybrid rotor ring in a Na+-coupled ATP synthase," *Nat. Commun.*, vol. 5, no. 1, p. 5286, Dec. 2014.

[117] T. Meier, S. A. Ferguson, G. M. Cook, P. Dimroth, and J. Vonck, “Structural investigations of the membrane-embedded rotor ring of the F-ATPase from Clostridium paradoxum,” *J. Bacteriol.*, vol. 188, no. 22, pp. 7759–7764, Nov. 2006.

[118] T. Meier, P. Polzer, K. Diederichs, W. Welte, and P. Dimroth, “Structure of the rotor ring of F-Type Na+-ATPase from Ilyobacter tartaricus.,” *Science*, vol. 308, no. 5722, pp. 659–62, Apr. 2005.

[119] D. Pogoryelov, J. Yu, T. Meier, J. Vonck, P. Dimroth, and D. J. Muller, “The c $_{15}$ ring of the *Spirulina platensis* F-ATP synthase: F $_{1}$ /F $_{0}$ symmetry mismatch is not obligatory,” *EMBO Rep.*, vol. 6, no. 11, pp. 1040–1044, Nov. 2005.

[120] T. Meier and P. Dimroth, “Intersubunit bridging by Na+ ions as a rationale for the unusual stability of the c-rings of Na+-translocating F1F0 ATP synthases,” *EMBO Rep.*, vol. 3, no. 11, pp. 1094–1098, Nov. 2002.

[121] T. Meier, J. Yu, T. Raschle, F. Henzen, P. Dimroth, and D. J. Muller, “Structural evidence for a constant c11 ring stoichiometry in the sodium F-ATP synthase,” *FEBS J.*, vol. 272, no. 21, pp. 5474–5483, Nov. 2005.

[122] T. Krebstakies, I. Aldag, K. Altendorf, J. C. Greie, and G. Deckers-Hebestreit, “The stoichiometry of subunit c of Escherichia coli ATP synthase is independent of its rate of synthesis,” *Biochemistry*, vol. 47, no. 26, pp. 6907–6916, Jul. 2008.

[123] B. Ballhausen, K. Altendorf, and D. H. Gabriele, “Constant c10 Ring Stoichiometry in the Escherichia coli ATP Synthase Analyzed by Cross-Linking,” *J. Bacteriol.*, vol. 191, no. 7, pp. 2400–2404, Apr. 2009.

[124] D. J. Müller *et al.*, “ATP synthase: Constrained stoichiometry of the transmembrane rotor,” in *FEBS Letters*, 2001, vol. 504, no. 3, pp. 219–222.

[125] W. Laubinger, P. Dimroth, G. Deckers-Hebestreit, and K. Altendorf, “A Hybrid Adenosinetriphosphatase Composed of F1 of Escherichia coli and F0 of Propionigenium modestum Is a Functional Sodium Ion Pump,” *Biochemistry*, vol. 29, no. 23, pp. 5458–5463, Jun. 1990.

[126] G. A. Davis and D. M. Kramer, “Optimization of ATP Synthase c–Rings for Oxygenic Photosynthesis,” *Front. Plant Sci.*, vol. 10, p. 1778, Jan. 2020.

[127] H. Seelert, N. A. Dencher, and D. J. Müller, “Fourteen Protomers Compose the Oligomer III of the Proton-rotor in Spinach Chloroplast ATP Synthase,” *J. Mol. Biol.*, vol. 333, no. 2, pp. 337–344, Oct. 2003.

[128] H. Seelert, A. Poetsch, M. Rohlfs, and N. A. Dencher, “Dye-ligand chromatographic purification of intact multisubunit membrane protein complexes: application to the chloroplast H+-FoF1-ATP synthase.,” *Biochem. J.*, vol. 346 Pt 1, no. 1, pp. 41–4, Feb. 2000.

[129] U. Pick and E. Racker, “Purification and reconstitution of the N, N’-dicyclohexylcarbodiimide-sensitive ATPase complex from spinach chloroplasts,” *J. Biol. Chem.*, vol. 254, pp. 2793–2799, 1979.

[130] W. D. Frasch, C. R. Deluca, M. J. Kulzick, and B. R. Selman, “A quantitative estimation of chloroplast thylakoid-bound coupling factor 1 by rocket immunoelectrophoresis,” 1980.

[131] R. J. Porra, W. A. Thompson, and P. E. Kriedemann., “Determination of accurate extinction coefficients and simultaneous equations for assaying chlorophylls a and b extracted with four different solvents: verification of the concentration of chlorophyll standards by atomic absorption spectroscopy.,” *Biochim. Biophys. Acta (BBA)-Bioenergetics*, vol. 975, no. 3, pp. 384–394, 1989.

[132] T. C. Taylor and I. Andersson, “Structure of a product complex of spinach ribulose-1,5-bisphosphate carboxylase/oxygenase,” *Biochemistry*, vol. 36, no. 13, pp. 4041–4046, Apr. 1997.

[133] D. Franke *et al.*, “ATSAS 2.8: a comprehensive data analysis suite for small-angle scattering from macromolecular solutions,” *J. Appl. Cryst*, vol. 50, pp. 1212–1225, 2017.

[134] D. V Zabelskii *et al.*, “Ambiguities and completeness of SAS data analysis: investigations of apoferritin by SAXS/SANS EID and SEC-SAXS methods,” *J. Phys. Conf. Ser.*, vol. 994, no. 1, p. 012017, Mar. 2018.

[135] W. Kabsch, “*XDS*,” *Acta Crystallogr. Sect. D Biol. Crystallogr.*, vol. 66, no. 2, pp. 125–132, Feb. 2010.

[136] M. D. Winn *et al.*, “Overview of the *CCP* 4 suite and current developments,” *Acta Crystallogr. Sect. D Biol. Crystallogr.*, 2011.

[137] A. Vagin and A. Teplyakov, “Molecular replacement with *MOLREP*,” *Acta Crystallogr. Sect. D Biol. Crystallogr.*, vol. 66, no. 1, pp. 22–25, Jan. 2010.

[138] G. N. Murshudov *et al.*, “REFMAC5 for the refinement of macromolecular crystal structures.,” *Acta Crystallogr. D. Biol. Crystallogr.*, vol. 67, no. Pt 4, pp. 355–367, Apr. 2011.

[139] P. Emsley and K. Cowtan, “Coot: model-building tools for molecular graphics,” *Acta Crystallogr. Sect. D Biol. Crystallogr.*, vol. 60, no. 12, pp. 2126–2132, Dec. 2004.

[140] N. M. Kurbatov *et al.*, “DDM solubilization-based protocol for isolation and purification of spinach chloroplast ATP synthase,” *J. Bioenerg. Biomembr.*, vol. 50, no. 6, p. 555, 2018.

[141] T. N. Murugova *et al.*, “Low resolution structural studies of apoferritin via SANS and SAXS: The Effect of concentration,” *J. Optoelectron. Adv. Mater.*, vol. 17, no. 9–10, pp. 1397–1402, 2015.

[142] G. M. Cooper, “10. The Chloroplast Genome,” in *The Cell: A Molecular Approach*, 2nd edition., Sinauer Associates, 2000.

[143] M. A. Lomize, I. D. Pogozheva, H. Joo, H. I. Mosberg, and A. L. Lomize, “OPM database and PPM web server: resources for positioning of proteins in membranes,” *Nucleic Acids Res.*, vol. 40, no. D1, pp. D370–D376, Jan. 2012.

[144] W. L. DeLano, “Pymol: An open-source molecular graphics tool.,” *CCP4 Newsl. protein Crystallogr.*, vol. 40, no. 1, pp. 82–92, 2002.

[145] B. Nowicka and J. Kruk, “Occurrence, biosynthesis and function of isoprenoid quinones,” *Biochimica et Biophysica Acta - Bioenergetics*, vol. 1797, no. 9. Elsevier, pp. 1587–1605, 01-Sep-2010.

[146] I. Yumoto, K. Yamazaki, M. Hishinuma, Y. Nodasaka, N. Inoue, and K. Kawasaki, “Identification of facultatively alkaliphilic Bacillus sp. strain YN-2000 and its fatty acid composition and cell-surface aspects depending on culture pH,” *Extremophiles*, vol. 4, no. 5, pp. 285–290, 2000.

[147] H. Takami, · Terry, and A. Krulwich, “Reidentification of facultatively alkaliphilic Bacillus firmus OF4 as Bacillus pseudofirmus OF4,” 2000.

[148] P. H. Gale, B. H. Arison, N. R. Trenner, A. C. Page, K. Folkers, and A. F. Brodie, “Characterization of Vitamin K9(H) from Mycobacterium phlei,” *Biochemistry*, vol. 2, no. 1, pp. 200–203, Jan. 1963.

[149] M. Malferrari and F. Francesco, “Isolation of plastoquinone from spinach by HPLC,” *J.*

Chromatogr. Sep. Tech., vol. 5, no. 5, p. 1, 2014.

[150] M. Ruengjitchatchawalya *et al.*, “Higher plant-like fluorescence induction and thermoluminescence characteristics in cyanobacterium, Spirulina mutant defective in PQH2 oxidation by cytb6/f complex,” *J. Plant Physiol.*, vol. 162, no. 10, pp. 1123–1132, Oct. 2005.

[151] H. Bahri *et al.*, “TMEM70 promotes ATP synthase assembly within cristae via transient interactions with subunit c,” *bioRxiv Cell Biol.*, p. 2020.04.03.023861, Apr. 2020.

Appendix

ATP synthesis rate formula

$$S = \frac{\left(\frac{dU}{dt}\right)_0 V_{st} C_{st} V_1}{V_L (V_1 + V_{st}) C_E \Delta mV}$$

where S is an ATP synthesis rate (ATP/cF$_O$F$_1$/sec); $\left(\frac{dU}{dt}\right)_0$ is a slope at the beginning of exponential growth; V_{st} and C_{st} – a volume and concentration of ATP standard, respectively; ΔmV is the difference between the plateau value and when adding the ATP standard; V_L is a volume of a solution of proteoliposomes; V_1 is a volume of L1 and L2 buffers + V_L + a volume of luciferase reagent; C_E is the final concentration of ATP synthase in the solution (Fig. S1).

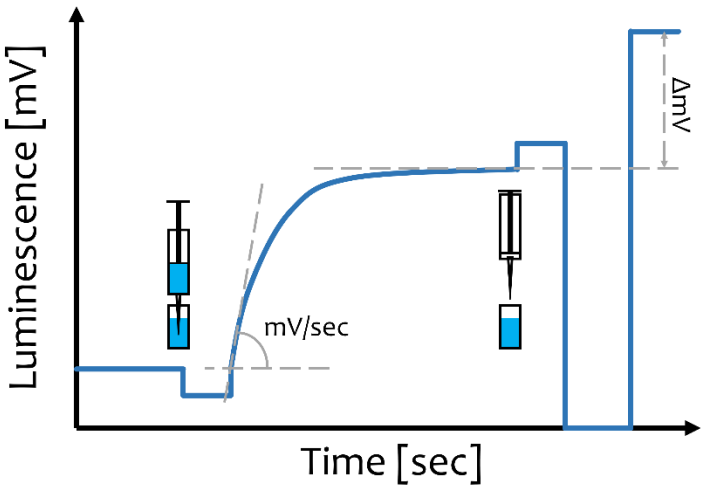

Figure S1. A schematic plot of luminescence signal *vs.* time is shown. At the beginning – background signal; then proteoliposomes are inserted in a cuvette via a cannula, that causes a slight signal decrease; after that there is an exponential growth of the signal due to ATP synthesis until the plateau is reached. When removing the cannula, there is a slight increase of the signal; then – the ATP standard is added. The slope at the beginning of the exponential growth (mV/sec) and the difference between the plateau value and when adding the ATP standard (ΔmV) are required to calculate the rate of the ATP synthesis (ATP/sec/enzyme).

Scoring tables for VD plates

VD plates were scored and conditions where crystals have grown are shown with scores 5 or 6 (Fig. S2).

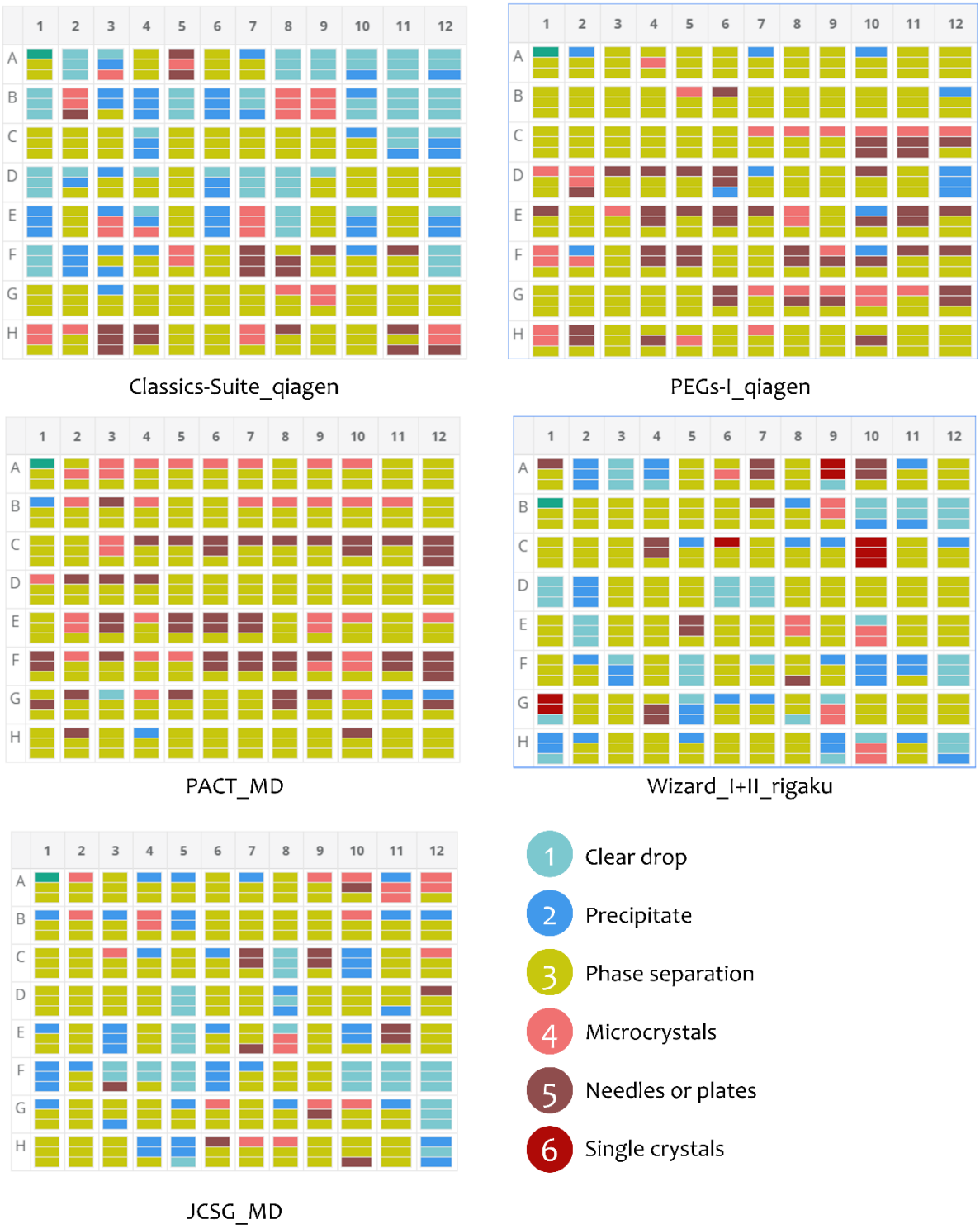

Figure S2. Scoring of VD crystallization plates. Crystallization kits are shown on the bottom of each scoring table.

Extended table of c-ring structures

Table S1. Extended list of c-rings from different species (not only high-resolution structures).

Type	Cn	Origin	Year	Method	Res., Å	PDB ID	Active center
H^+	**14**	***Spinacia oleracea***	**2019**	**XRD**	**2.3**	**6TQJ**	**E61**
	14	*Spinacia oleracea*	2014	XRD	6.0	4MJN	E61
	14	*Pisum sativum*	2012	XRD	3.4	3V3C	E61
	14	*Spinacia oleracea*	2009	XRD	3.8	2W5J	E61
	9	*Mycolicibacterium phlei*	2016	XRD	1.8	4V1H	E65
	9	*Mycolicibacterium phlei*	2015	XRD	1.7	4V1F	E65
	9	*Mycolicibacterium phlei*	2015	XRD	1.55	4V1G	E65
	10	*Saccharomyces cerevisiae*	2015	XRD	2.1	5BPS	E59
	10	*Saccharomyces cerevisiae*	2015	XRD	2.3	5BQ6	E59
	10	*Saccharomyces cerevisiae*	2015	XRD	2.1	5BQA	E59
	10	*Saccharomyces cerevisiae*	2015	XRD	2.1	5BQJ	E59
	10	*Saccharomyces cerevisiae*	2012	XRD	1.9	4F4S	E59
	10	*Saccharomyces cerevisiae*	2012	XRD	2.0	3U2F	E59
	10	*Saccharomyces cerevisiae*	2012	XRD	2.5	3U2Y	E59
	10	*Saccharomyces cerevisiae*	2012	XRD	2.0	3U32	E59
	10	*Saccharomyces cerevisiae*	2012	XRD	2.0	3UD0	E59
	12	*Bacillus pseudofirmus OF4* mutant	2013	XRD	4.1	3ZO6	E54
	13	*Bacillus pseudofirmus OF4*	2014	XRD	2.8	4CBJ	E54
	13	*Bacillus pseudofirmus OF4*	2014	XRD	2.42	4CBK	E54
	13	*Bacillus pseudofirmus*	2010	XRD	2.5	2X2V	E54
	15	*Arthrospira platensis*	2010	XRD	3.0	2XQS	E62
	15	*Arthrospira platensis*	2010	XRD	2.2	2XQT	E62
	15	*Arthrospira platensis*	2010	XRD	1.84	2XQU	E62
	15	*Arthrospira platensis*	2009	XRD	2.13	2WIE	E62
Na^+	$9_F/1_V$	*Acetobacterium woodii*	2014	XRD	2.1	4BEM	E_F62, E_V79, Q_V162
	11	*Fusobacterium nucleatum*	2013	XRD	2.2	3ZK1	E65
	11	*Fusobacterium nucleatum*	2013	XRD	2.63	3ZK2	E65
	11	*Ilyobacter tartaricus*	2009	XRD	2.35	2WGM	E65
	10	*Enterococcus hirae*	2006	XRD	2.8	2CYD	E54
	11	*Ilyobacter tartaricus*	2005	XRD	2.4	1YCE	E65

Another representation of phylogenetic tree showing c-ring stoichiometries

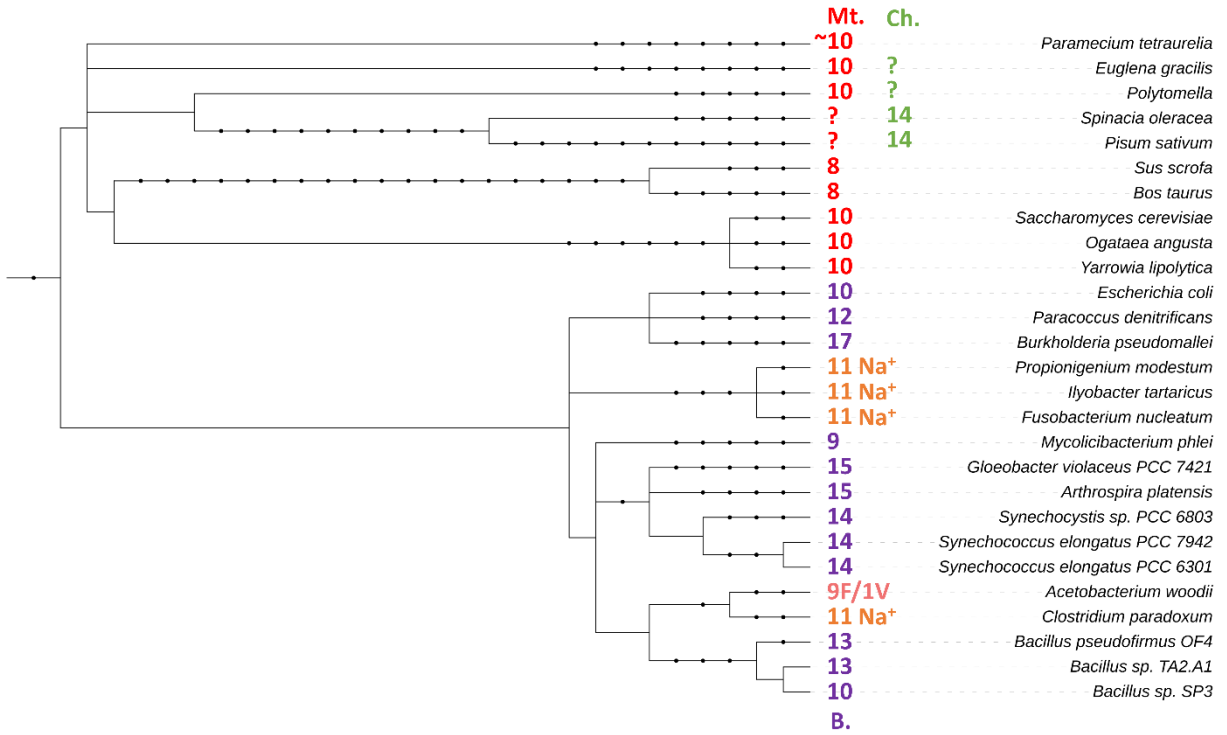

Figure S3. A phylogenetic tree of different species with available number of c-subunit copies in corresponding ATP synthases. Numbers of the copies are shown. Eukaryotes with available data of corresponding H^+ mtF_OF_1 are colored red, and H^+ cF_OF_1 – green; bacteria with corresponding H^+ bF_OF_1 are colored purple, and Na^+ bF_OF_1 – orange. *Acetobacterium woodii* is colored pink because it has a Na^+ c-ring of a hybrid F/V type with a stoichiometry of $9_F/1_V$. The symbol "~" means that the number of copies was suggested, however, was not proven experimentally.

Acknowledgements

"If I have seen further it is by standing on ye sholders (the shoulders) of Giants" (Isaac Newton)

During my PhD project I worked in a team of professionals, who gave me an amazing opportunity to learn from them and work together trying to convey their unique experience. Owing to these great people who made this history possible I am here where I am and it would be hard for me to imagine encompassing so many fields of knowledge without their help. They encouraged me not to give up when difficulties arise and continue working on the project. My great acknowledgements and big thanks to the following people:

Prof. Dr. Valentin Gordeliy for wise supervision of my PhD project, for opportunity of working in a team of professionals and for fruitful discussions that formed a pattern of thoughts which helped me for data analysis and systematization, and for his idea that isoprenoid quinones might be present inside c-rings of different organisms;

Prof. Dr. Norbert Dencher for conveying experience of working with thylakoid membranes, protocols of isolation and purification of intact ATP synthase from spinach chloroplasts, and for a lot of time spent for fruitful detailed discussions that really helped to work on the project;

Dr. Alexander Kuklin for teaching me small-angle X-ray scattering and smart administration of my working processes, for supporting me during any difficulties and for a strong belief in my future scientific career;

Prof. Dr. Georg Büldt, Dr. Ivan Gushchin, Dr. Vitaly Polovinkin, Dr. Ekaterina Round, and Dr. Sven Marx for their invaluable help with experiments and data treatment;

Dr. Taras Balandin for teaching me expression of recombinant proteins in *E.coli* cells, and biochemical methods of isolation and purification of membrane proteins, and for quick response in helping me with problems of any kind;

Nikolay Tsoy for helping me a lot with development of ATP synthase purification protocols and invaluably helped me with experiments at the beginning of the project;

Alexander Kazantsev for helping with automatization of SAXS data treatment and with biochemical experiments at the beginning of the project;

Stepan Osipov for helping with development of c-ring purification protocols and UV-Vis spectroscopy, and invaluably helped me with experiments at the final part of the project;

Yury Ryzhykau for helping with SAXS data analysis and long hours spent for fruitful discussions;

Danylo Komisar for helping with UV-Vis spectroscopy of c-ring samples;

My colleagues and friends: Prof. Dr. Ilya Manukhov, Prof. Dr. Vladimir Chupin, Dr. Valentin Borshchevskiy, Dr. Andrey Rogachev, Dr. Pavel Kuzmichev, Dr. Alexey Mishin, Christian Baeken, Ivan Okhrimenko, Sergei Bazhenov, Nina Maliar, Kirill Kovalev, Egor Zinovev – all these people significantly contributed to the project;

My colleagues and friends who ever helped me with preparing of spinach leaves;

And, special thanks to Prof. Dr. Norbert Dencher and Taisia Bazhina for helping with German language.

Finally, my mother Iraida Vlasova and my stepfather Alexander Deineko for their belief in me, their support, love and patience; my wife Anastasia Vlasova for her love, infinite patience, strong support and invaluable help at any problem; and my son Petr Vlasov for motivating me doing my PhD, with a hope that these words will motivate him doing his PhD in the future.

Abstract

ATP synthase is an enzyme that catalyzes the synthesis of adenosine triphosphate (ATP) – the molecule which supplies energy for vital biochemical reactions in almost all living organisms. F-type ATP synthases are spread in bacteria cellular membranes, thylakoid membranes of chloroplasts and mitochondria inner membranes of eukaryotes. F-type ATP synthase is a membrane protein complex with a large non-membrane part F_1 and a membrane part F_O. Being so widely spread in different species, ATP synthases have conserved parts responsible for their major functions: ATP synthesis/hydrolysis and transmembrane ion transport in F_1 and F_O regions, respectively. At the same time their subunit organization and composition are highly variable, especially for mitochondrial F-type ATP synthase dimers in eukaryotes (four different types were found up to date). Bacterial ATP synthases are found in monomeric state as well as chloroplast ATP synthases, which are also predominantly monomers, however, there are protein pairs and oligomers of ATP synthases in chloroplasts according to the literature. At the moment the physiological role of such oligomers is discussed.

One of the most important and unknown parts of ATP synthases – the membrane F_O region, in particular, a rotary part (c_n-ring), which consists of n copies of protomers (c_1-subunits) that are assembled in a circle. Being coupled with the a-subunit, c-ring establishes a transmembrane ion transport, rotates γ-subunit and drives ATP synthesis. Despite the fact that ATP synthase was in a focus of interest for the last decades and resulted in a huge progress in its' structural and functional studies, a number of key details remained unknown. High-resolution structures (better than 3 Å) were obtained for c-rings from bacterial and mitochondrial ATP synthases, however, the gap of the knowledge of a c-ring from chloroplasts was not filled.

Another open question relates to molecular composition of the inner pore of c-rings. Literature data showed at least four different types of interaction interfaces of c-rings in a context of assembled ATP synthase dimers in mitochondria of eukaryotes. In all these cases, additional subunits interacting with a c-ring except a and γ subunits are also involved into dimerization F_O/F_O interface between two monomers of ATP synthase. However, in case of monomeric bacterial and chloroplast ATP synthases, no additional machinery, which could provide a similar stabilization of a c-ring, was found in F_O part. The question of molecular composition of the inner pore of c-rings from different organisms, e.g. bacteria and chloroplasts, was not deeply discussed in literature. In the literature it was shown that pigments, e.g. chlorophyll *a* and beta carotene, are tightly connected to a c-ring from spinach chloroplasts and might be compounds of a lipid "plug" inside its' inner pore, however, due to the absence of a c-ring structure it was not proven that the pigments were exactly inside the c-ring.

In the present work the high-resolution structure (2.3 Å) of a c-ring of F-type ATP synthase from spinach chloroplasts was obtained. This is the first high-resolution structure of a c-ring from plant chloroplasts and the first subunits of any ATP synthase that were crystallized by *in meso* method. The present work fills the gap in knowledge of c-rings from plant chloroplasts and provides a complete c_1/c_1 interaction interface formed by a net of hydrogen bindings between amino acids of neighbor protomers. The role of the motifs G(A,S)xxxG(A,S) was theoretically predicted in literature to be key determinants of c-ring stoichiometry in different organisms. In my thesis, it is directly shown that the motifs G(A,S)xxxG(A,S) occurred to be only partially involved in a network of hydrogen bonds at the c_1/c_1 interface. It was also demonstrated that the complete network of hydrogen bonds includes the motifs G(A,S)xxxG(A,S) and other amino acids which determine the c_1/c_1 interface and, therefore, a stoichiometry of the c-ring.

I found additional positive electron densities inside the c-ring. They were not associated with the c-subunits. I found similar densities during analysis of high-resolution structures of c-rings from different organisms, e.g. bacteria and mitochondria of eukaryotes. It was not previously discussed in the literature. The distances between polar/apolar interfaces were calculated and showed

significant difference between inside the inner pore and outside of the c-ring. The hydrophobic length inside the c-ring was found to be ~1.4 times larger than in the membrane bilayer outside the c-ring. A similar difference (~1.2 – 1.4 times) was found for all c-rings with available high-resolution structures. Our hypothesis is that isoprenoid quinones inside the inner pore of c-rings may explain our and literature data. We suggest that these molecules are present in all c-rings (e.g. plastoquinone-9 (PQ-9) in a c-ring from spinach chloroplasts, menaquinones in bacteria, ubiquinones in mitochondria of eukaryotes).

I tested the hypothesis by UV-Vis differential spectroscopy of the c-ring samples using a qualitative reaction of reducing ketones and aldehydes to alcohols by $NaBH_4$, and showed the presence of the compounds with quinone group similar to trimethyl benzoquinone – a polar moiety of PQ-9. Thus, this presents, although indirect, arguments towards the hypothesis that isoprenoid quinones might be universal cofactors of ATP synthases, preventing ion leakage through a c-ring and stabilizing it.

In addition, I studied the structure of ATP synthase. In the work, small-angle X-ray scattering (SAXS) of purified intact ATP synthase from spinach chloroplasts reconstituted into POPC/MSP1E3D1 nanodiscs was performed and showed the low-resolution structure that has a form-factor similar to that of V-shape dimers of mitochondrial ATP synthases. It rises questions of possible physiological role of such oligomers of chloroplast ATP synthases.

Understanding of ATP synthase in details is extremely important. ATP synthase is a part of oxidative and photophosphorylation systems and relevant studies reveal hidden connections of ATP synthase in different biochemical processes. Dysfunctions of this enzyme lead to a number of severe diseases, e.g. as diabetes, severe metabolic and mitochondrial disorders, dysfunctions of tissues and organs, neurodegenerative and age-associated diseases. At the same time, ATP synthase, due to being significantly variable in details in organisms from distant lineages, might become a target for structure-based design of new antibacterial drugs. Thus, new insights on its' structural and functional features are important for pharmacology and applied medicine, for development of different therapies and structure-based drug design as well as for fundamental biology. I believe that this work is contributing to better understanding of this molecular machine.

Abstrakt

ATP-Synthase ist ein Enzym, das die Synthese von Adenosintriphosphat (ATP) katalysiert - dem Molekül, das Energie für lebenswichtige biochemische Reaktionen in fast allen lebenden Organismen liefert. ATP-Synthasen vom F-Typ sind in Bakterienzellmembranen, Thylakoidmembranen von Chloroplasten und Mitochondrien-Innenmembranen von Eukaryoten verbreitet. Die ATP-Synthase vom F-Typ ist ein Membranproteinkomplex mit einem großen Nichtmembranteil F_1 und einem Membranteil F_O. ATP-Synthasen sind in verschiedenen Spezies so weit verbreitet, dass sie konservierte Teile erhalten haben, die für ihre Hauptfunktionen verantwortlich sind: ATP-Synthese/Hydrolyse und Transmembranionentransport in F_1- bzw. F_O-Regionen. Gleichzeitig sind ihre Organisation und Zusammensetzung der Untereinheiten sehr variabel, insbesondere für mitochondriale ATP-Synthase-Dimere vom F-Typ in Eukaryoten (vier verschiedene Typen wurden bisher gefunden). Bakterielle ATP-Synthasen liegen im monomeren Zustand vor. Chloroplasten-ATP-Synthasen sind ebenfalls überwiegend Monomere, es gibt jedoch Dimere und Oligomere laut Literatur. Derzeit liegt die physiologische Rolle solcher Oligomere wird diskutiert.

Einer der wichtigsten und unbekanntesten Teile von ATP-Synthasen ist die eine Membran-F_O-Region, insbesondere ein rotierender Teil (c_n-Ring), der aus n Kopien von Protomeren (c_1-Untereinheiten) besteht, die in einem Kreis angeordnet sind. In Verbindung mit der a-Untereinheit ermöglicht der c-Ring einen Transmembranionentransport, dreht die γ-Untereinheit und treibt die ATP-Synthese an. Trotz der Tatsache, dass die ATP-Synthase in den letzten Jahrzehnten im Mittelpunkt des Interesses stand und in ihren strukturellen und funktionellen Studien ein enormer Fortschritt erzielt wurde, blieben einige wichtige Details unbekannt. Die hochauflösenden Strukturen (besser als 3 Å) wurden für c-Ringe aus bakteriellen und mitochondrialen ATP-Synthasen erhalten, die Wissenslücke bestand jedoch für den c-Ring aus Chloroplasten, z.B. Schlüsseldeterminanten der c-Ring-Stöchiometrie waren unbekannt.

Eine weitere offene Frage betrifft die molekulare Zusammensetzung der inneren Pore von c-Ringen. Die Literaturdaten zeigten mindestens vier verschiedene Arten von Interaktionsschnittstellen von c-Ringen im Zusammenhang mit zusammengesetzten ATP-Synthase-Dimeren in Mitochondrien von Eukaryoten. In all diesen Fällen sind zusätzliche Untereinheiten, die mit einem c-Ring außer a- und γ-Untereinheiten interagieren, ebenfalls an der Dimerisierungs-F_O/F_O-Schnittstelle zwischen zwei Monomeren der ATP-Synthase beteiligt. Im Fall von monomeren Bakterien- und Chloroplasten-ATP-Synthasen wurde im F_O-Teil jedoch keine zusätzliche Maschinerie gefunden, die eine ähnliche Stabilisierung eines c-Rings bewirken könnte. Die Frage der molekularen Zusammensetzung der inneren Pore von C-Ringen aus verschiedenen Organismen, z.B. Bakterien und Chloroplasten wurde in der Literatur nicht ausführlich diskutiert. In der Literatur wurde gezeigt, dass Pigmente, z.B. Chlorophyll a und Beta-Carotin eng mit einem c-Ring aus Spinat-Chloroplasten verbunden sind und könnten in Verbindungen mit einem postulierten Lipid-Pfropfen in seiner inneren Pore sein. Aufgrund des Fehlens einer c-Ring-Struktur konnte jedoch nicht nachgewiesen werden, dass die Pigmente sich im c-Ringkanal befanden.

In der vorliegenden Arbeit wurde die hochauflösende Struktur (2,3 Å) eines c-Rings der ATP-Synthase vom F-Typ aus Spinatchloroplasten erhalten. Dies ist die erste hochauflösende Struktur eines c-Rings aus pflanzlichen Chloroplasten und die ersten Untereinheiten einer ATP-Synthase, die mit der Meso-Methode kristallisiert wurden. Die vorliegende Arbeit füllt die Wissenslücken über c-Ringe aus pflanzlichen Chloroplasten und bietet eine vollständige c_1/c_1-Interaktionsschnittstelle, die durch ein Netz von Wasserstoffbrücken zwischen Aminosäuren benachbarter Protomere gebildet wird. Die Rolle der Motive G(A,S)xxxG(A,S) wurde in der Literatur theoretisch als Schlüsselfaktoren der C-Ring-Stöchiometrie in verschiedenen Organismen vorhergesagt. In meiner Arbeit wird direkt gezeigt, dass die Motive G(A,S)xxxG(A,S)

nur teilweise an einem Netzwerk von Wasserstoffbrückenbindungen an der c_1/c_1-Schnittstelle beteiligt sind. Es wurde auch gezeigt, dass das vollständige Netzwerk von Wasserstoffbrückenbindungen der Motive G(A,S)xxxG(A,S) enthält und anderer Aminosäuren, die die c_1/c_1-Schnittstelle und damit eine Stöchiometrie des c-Rings bestimmen.

Ich fand zusätzliche positive Elektronendichten im c-Ring. Sie waren nicht mit den c-Untereinheiten assoziiert. Ich fand ähnliche Dichten während der Analyse hochauflösender Strukturen in der Literatur von c-Ringen aus verschiedenen Organismen, z.B. Bakterien und Mitochondrien von Eukaryoten. Sie wurde bisher in der Literatur nicht diskutiert. Die Abstände zwischen polaren/unpolaren Schnittstellen wurden berechnet und zeigten einen signifikanten Unterschied zwischen der inneren Pore und der Außenseite des c-Rings. Die hydrophobe Länge innerhalb des c-Rings war ~ 1,4-mal größer als in der Membrandoppelschicht außerhalb des c-Rings. Ein ähnlicher Unterschied (~ 1,2 – 1,4-fach) wurde für alle c-Ringe von Literaturdaten mit verfügbaren hochauflösenden Strukturen gefunden. Unsere Hypothese ist, dass Isoprenoidchinone in der inneren Pore von c-Ringen unsere und Literaturdaten erklären können. Wir schlage vor, dass diese Moleküle in allen c-Ringen vorhanden sind (z. B. Plastochinon-9 (PQ-9) in einem c-Ring aus Spinatchloroplasten, Menachinonen in Bakterien, Ubichinonen in Mitochondrien von Eukaryoten).

Ich habe die Hypothese getestet durch UV-Vis-Differentialspektroskopie der c-Ring-Proben unter Verwendung einer qualitativen Reaktion der Reduktion von Ketonen und Aldehyden zu Alkoholen durch $NaBH_4$ und zeigten das Vorhandensein von Verbindungen mit einer Chinongruppe ähnlich Trimethylbenzochinon - einer polaren Einheit von PQ-9. Dies liefert, obwohl indirekt, Argumente für die Hypothese, dass Isoprenoidchinone universelle Cofaktoren von ATP-Synthasen sein könnten, die das Austreten von Ionen durch einen c-Ring verhindern und diesen stabilisieren.

Zusätzlich untersuchte ich die Struktur der gesamten ATP-Synthase. In der vorliegenden Arbeit wurde eine Kleinwinkel-Röntgenstreuung (SAXS) von gereinigter intakter ATP-Synthase aus Spinat-Chloroplasten, rekonstituiert in POPC/MSP1E3D1-Nanoplatten durchgeführt. Die Struktur mit niedriger Auflösung hat einen ähnlichen Formfaktor wie die V-förmigen Dimere mitochondrialer ATP-Synthasen. Sie wirft Fragen nach einer möglichen physiologischen Rolle solcher Oligomere von Chloroplasten-ATP-Synthasen auf.

Das Verständnis der ATP-Synthase im Detail ist äußerst wichtig. Die ATP-Synthase ist Teil von oxidativen und Photophosphorylierungssystemen, und relevante Studien zeigen verborgene Verbindungen der ATP-Synthase in verschiedenen biochemischen Prozessen auf. Funktionsstörungen dieses Enzyms führen zu einer Reihe schwerer Krankheiten, z. B. Diabetes, schwere Stoffwechsel- und Mitochondrienstörungen, Funktionsstörungen von Geweben und Organen, neurodegenerative und altersbedingte Erkrankungen. Gleichzeitig könnte die ATP-Synthase aufgrund ihrer signifikanten Detailvariabilität in Organismen aus entfernten Abstammungslinien ein Ziel für das strukturbasierte Design neuer antibakterieller Arzneimittel werden. Daher sind neue Erkenntnisse über seine strukturellen und funktionellen Merkmale für die Pharmakologie und angewandte Medizin, für die Entwicklung verschiedener Therapien und das strukturbasierte Wirkstoffdesign sowie für die Grundlagenbiologie wichtig. Ich glaube, dass unsere Arbeit zu einem besseren Verständnis dieser molekularen Maschine beiträgt.